# Design, Analysis, Measurement and Control of a New Disc-type Ultrasonic Motor System

Thesis submitted for the degree of

Doctor of Philosophy

At the University of Leicester

by

**Puu-An Juang**

Department of Engineering

University of Leicester

**October 2005**





ProQuest LLC
789 East Eisenhower Parkway
P.O. Box 1346
Ann Arbor, MI 48106-1346

# Design, Analysis, Measurement and Control of a New Disc-type Ultrasonic Motor System

**By**

**Puu-An Juang**

## Abstracts

An ultrasonic motor (UM) uses ultrasonic vibration to obtain a driving force by means of friction. Ultrasonic motors can produce larger torque at low speed with higher efficiency, in comparison with normal electromagnetic DC motors. No gears are used in a UM and, therefore, direct drive is possible. A UM has good control characteristics, high precision in positioning and no EM interference. Ultrasonic motor can be used as actuators for robots as well as for many household appliances.

In this thesis, a novel disc-type ultrasonic motor stator is investigated. The stator has an asymmetrical structure (120°-90°-150° support boundary configuration) on its surface. The advantages of this structure include a single electrical phase driving, multiple-resonant-modes driving, rotational direction changes by modulation of driving frequencies, single contact point, and simple driving electrical circuit.

With the setup of a precision laser vibrometer measurement experiment, mode motions and wave propagations of the UM are analyzed. The model is further verified by using finite element simulations where a 3-dimensional mechanical element with an extra electrical degree of freedom is used and then electrical impedance response, phase response and mechanical frequency response of the UM are studied. Furthermore, a transfer function model and equivalent circuit model of the UM in terms of radial and tangential displacement components are established for control objectives and for certification of dynamic characteristic parameters. The equivalent circuit model verifies radial, tangential and couple vibration modes once more and is used in search of resonance frequencies. The PSPICE has been used to simulate the equivalent circuit components. Finally, a speed control scheme is implemented by using current modulation and commercial DSP technique, in order to keep the revolution speed constant.

The proposed ultrasonic motor system has proven good dynamic behaviours with the driving frequency range of 65k-100kHz and reaches a maximum revolution speed of 600rpm.

To my parents,

My wife, Mi-Ning

and

My children

# Acknowledgement

I wish to express my appreciation to Dr. Da-Wei Gu, my dissertation supervisor, for his guidance and encouragement during my staying at Department of Engineering, University of Leicester. Without his great patience and understanding, the route to my doctorate degree would not have been a wonderful journey in my life. I would also like to thank Dr. Paul W. Lefley, my dissertation co-supervisor, for his expert suggestions in my dissertation. I would also like to thank Professor Minsun Oyang (National Tsing Hua University, Taiwan) for providing his patent(502488) in my prototyping motor.

I would also like to thank Professor Hans-Jürgen Hardtke for his help and valuable advice. I would also like to express my appreciation to Dr. Dietrich Pawandent for helping me set up the experimental devices, Dr. Joachim Gier and Mr. Hans-Joachim Beer assisting me in several experiments at TU, Dresden Germany. I very appreciate Associate Professor Dr. Guo-Shing Huang at Department of Electronic Engineering National Chin-Yi Institute of Technology Taiping, Taichung, Taiwan to lend the DSP PC-based digital servo control system for my speed control test.

Finally, I would like to express my deepest respect and thanks to my parents who have brought up me through a great hardship and to my wife who took the responsibility of taking care of my parents and two children when I was at UK.

# Table of Contents

# Notations and Symbols

## Mathematical notations

| | |
|---|---|
| $A_i$ | transfer factor |
| $A_r$ | transfer factor |
| $A_V$ | transfer factor |
| $B_u$ | product of differential-operating matrix |
| $c$ | Young's Modulus |
| $C_d$ | piezoceramic clamp capacitance |
| $C_{eq}$ | total equivalent capacitor |
| $C^E$ | 6x6 elasticity matrix |
| $C_i$ | equivalent capacitance of stator |
| $C_{mr}$ | equivalent capacitor of radial vibration |
| $C_{m\theta}$ | equivalent capacitor of tangential vibration |
| $C_s$ | compensation capacitor |
| $C_\theta$ | equivalent capacitor |
| $d$ | piezoelectric strain constant |
| $dr$ | radius of a piece |
| $d\theta$ | circumferential angle of a piece |
| $d_{33}$ | piezoelectric strain constant in $z$ direction |
| $D$ | 3x1 electrical displacement vector |
| $D_r$ | direction restriction |
| $e$ | 3x6 piezoelectric matrix |
| $e^T$ | $e$ transpose |

| | |
|---|---|
| $e_{ss}$ | error function |
| $E$ | 3x1 electrical field vector |
| $E_c$ | coercive electric field |
| $E_z$ | electric field in $z$ direction |
| $f_b$ | body force |
| $f_c$ | concentrated force |
| $f_s$ | surface force |
| $\vec{F}_d$ | a contact force |
| $F^p$ | mechanical force vector |
| $F_r$ | radial force |
| $F_\theta$ | tangential force |
| $g$ | voltage output constant |
| $g_{31}$ | voltage output constant in $x$ direction |
| $g_{33}$ | voltage output constant in $z$ direction |
| $h$ | thickness of ceramic |
| $i_{in}$ | measured input current |
| $i_{out}$ | measured output current |
| $J$ | rotor moment of inertia |
| $k$ | coupling coefficient |
| $K$ | transfer coefficient |
| $K_G$ | constant gain |
| $K_I$ | integral gain |
| $K_P$ | proportional gain |
| $K_{uu}^p$ | elastic stiffness matrix |
| $K_{u\phi}^p$ | piezoelectric coupling matrix |
| $K_{\phi\phi}^p$ | dielectric stiffness matrix |

| | |
|---|---|
| $K_T$ | force factor |
| $L_{eq}$ | total equivalent inductor |
| $L_{mr}$ | equivalent inductor of radial vibration |
| $L_{m\theta}$ | equivalent inductor of tangential vibration |
| $L_r$ | equivalent inductor of rotor |
| $L_\theta$ | equivalent inductor |
| $m$ | mass of rotor |
| $M^p$ | stator mass matrix |
| $n$ | transfer ration |
| $N_u$ | interpolation function for the variable of $u$ |
| $N_\phi$ | interpolation function for the variable of $\phi$ |
| $p$ | piezoelectric ceramic |
| $P$ | electrical charge vector |
| $P_{out}$ | motor output power |
| $q_c$ | point charge |
| $q_s$ | surface charge |
| $Q$ | mechanical quality factor |
| $Q_s$ | plate stiffness |
| $r$ | radius of rotor |
| $R$ | equivalent resistor of stator |
| $R_{eq}$ | total equivalent resistor |
| $R_{mr}$ | equivalent resistor of radial vibration |
| $R_{m\theta}$ | equivalent resistor of tangential vibration |
| $R_r$ | equivalent resistor of rotor |
| $R_\theta$ | equivalent resistor |
| $s$ | disc |
| $S$ | 6x1 strain vector |

| | |
|---|---|
| $S_1$ | area where mechanical forces are applied |
| $S_2$ | area where electrical charges are applied |
| $S_{31}$ | strain in the *x* direction |
| $S_{33}$ | strain in the *z* direction |
| $T$ | 6x1 stress-vector |
| $T_d$ | Fourier transforms of $\tau_d$ |
| $u$ | displacement vector |
| $u_r$ | radial displacement |
| $u_\theta$ | circumferential displacement |
| $V_{in}$ | measured input voltage |
| $V_{out}$ | measured output voltage |
| $VP$ | pre-force |
| $Y_d$ | damped admittance |
| $Y_{seq}$ | equivalent dynamic admittance |
| $\alpha$ | damping coefficient |
| $\beta^p$ | damping coefficient |
| $\beta^s$ | damping coefficient |
| $\varepsilon$ | permittivity of ceramics |
| $\varepsilon_0$ | permittivity of free space |
| $\varepsilon^S$ | 3x3 dielectric matrix |
| $\phi$ | electric potential |
| $\eta$ | Rayleigh coefficient |
| $\lambda$ | Rayleigh coefficient |
| $\nu$ | Poisson ratio |
| $\nu^E$ | Poisson ratio in constant electric field |
| $\rho$ | density |
| $\tau_d$ | applied torque |

| | |
|---|---|
| $\mu$ | kinetic friction coefficient |
| $\omega$ | angular velocity |
| $\omega_a$ | anti-resonance frequency |
| $\omega_0$ | resonance frequency |
| $\omega_R$ | revolution speed |
| $\Delta$ | variation |
| $\Delta\theta$ | phase shifter |
| $\Theta$ | Fourier transforms of $\theta$ |
| $\wedge$ | nodal value |

## Substitutions

| | |
|---|---|
| $C = C^p + C^s$ | stator structure damping computation |
| $C^p = \eta M^p + \lambda K^p_{uu}$ | piezoelectric ceramic structure damping computation |
| $C^s = \eta M^s + \lambda K^s_{uu}$ | disc structure damping computation |
| $E = -\nabla\phi$ | electric field $E$ is related to electric potential $\phi$ |
| $G(S)\big\|_{S=j\omega} \cong K_G$ | transfer function approximation |
| $J = mr^2/2$ | rotor moment of inertia computation |
| $S = B_u\hat{u}$ | strain-displacement in terms of nodal displacement |

# List of Figures

# List of Tables

# Chapter 1 Introduction

## 1.1 Role of Ultrasonic Motors

An ultrasonic motor is defined as a motor that fully uses ultrasonic vibration, *i.e.*, a kind of elastic vibration, and a driving force to drive the motor. In general, an ultrasonic motor consists of a stator and a rotor. This concept is equivalent to the traditional electromagnetic motor.

Ultrasonic motors have been widely used in industry due to the following advantages:

(1). Low speed and high torque under direct drive;
(2). Fast response and wide velocity range;
(3). Hard brake but no backlash;
(4). Fine position resolution and easy to control;
(5). High performance under high power/weight ratio;
(6). Very low noise during driving;
(7). Lightweight and min-size;
(8). Simple design structure and easy production procedures;
(9). Low external magnetic and radioactive field interferences.

However, they also have the following disadvantages:

1. A higher frequency power supply required;
2. Low durability due to the contacted friction;
3. Nonlinear torque-speed characteristics.

At the beginning of this dissertation, we shall review the history and

classification of ultrasonic motors as well as their features in detail.

## 1.2 History and Classification of Ultrasonic Motors

Electromagnetic motors were invented more than a hundred years earlier than the first, practical ultrasonic motor was proposed by Barth [1]. Conventional electromagnetic motors are difficult to be minimized to under 1 $cm^3$ in size yet with sufficient energy efficiency. Thus, the ultrasonic motor, which fully explores electromechanic interactive energy transformation (i.e., electronic to ultrasonic energy), is proposed and considered in industry. In general, an ultrasonic motor consists of a high frequency power supply, a stator and a rotor. Furthermore, the stator is usually composed of a piezoelectric driving actuator and an elastic metal part, and the rotor is composed of a movable part and a friction coat, as shown in Figure 1.1.

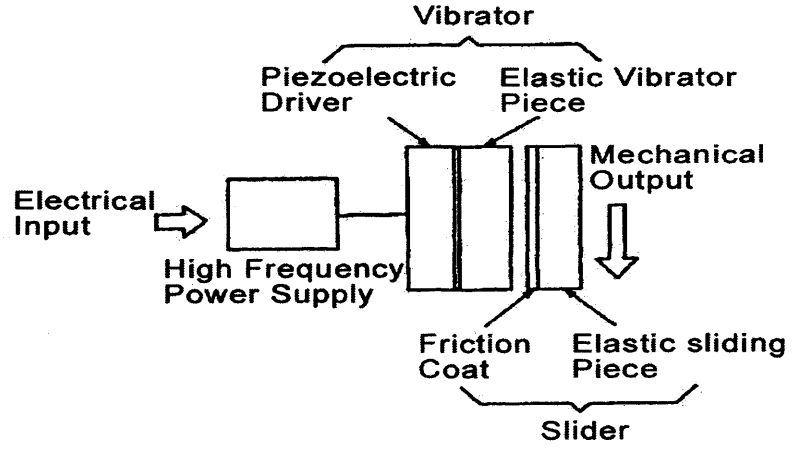


Figure 1.1 Fundamental structure of ultrasonic motors [1], [12].

The stator of an ultrasonic motor is made mainly by piezoelectric material, which will affect the final performance of the motor. So, the principle of piezoelectric material property should be considered in

prototyping an ultrasonic motor. The relevant detail of piezoelectric material is introduced in Appendix B.

In general, ultrasonic motors are classified [2]-[3] according to the following categories:

(1). Classification by motor function (rotary type or linear type); further the rotary motors fall into:

(a) Continuous rotary motors;

(b) Motors rotating in one direction;

(c) Stepping rotary motors;

(d) Rotary motors for heavy or light load use.

(2). Classification by motor structure:

* *Ultrasonic motors using a disk or ring vibrator*: (Figure 1.2-1.4 are standard expressions in ultrasonic motor area. To show their vibration characteristics, it needs to express them in different forms.)

(a) Bending motions vibrating in the direction perpendicular to the plane face, as shown in Figure 1.2, where two degenerate resonance modes of the same form are used. The vibrations are in the direction perpendicular to its surface and the vibration modes are represented as $B_{mn}$, where m is the number of nodal circles and n is that of nodal diameters. (It will be not clear if shown in (+,-), but it is very clear to express in nodal line and circles. For example for $B_{02}$, we can see two nodal lines but no circle on the disk.)

(b) Flexural motions vibrating in the horizontal face, as shown in Figure 1.3, where resonance modes of the same form are used. They are non-axisymmetric contours and the displacement is in its plane. The modes are represented as ((n, m)), where n is the circular order relative to axis of symmetry in a resonance mode

and m is the radial harmonics (the *m*th eigenvalue).

(c) Radial and flexural vibrations in the horizontal face, as shown in Figure 1.4, where modes of different forms are used. They are expressed in deformation form in radial and flexural vibrations to emphasize non-axisymmetric contours.

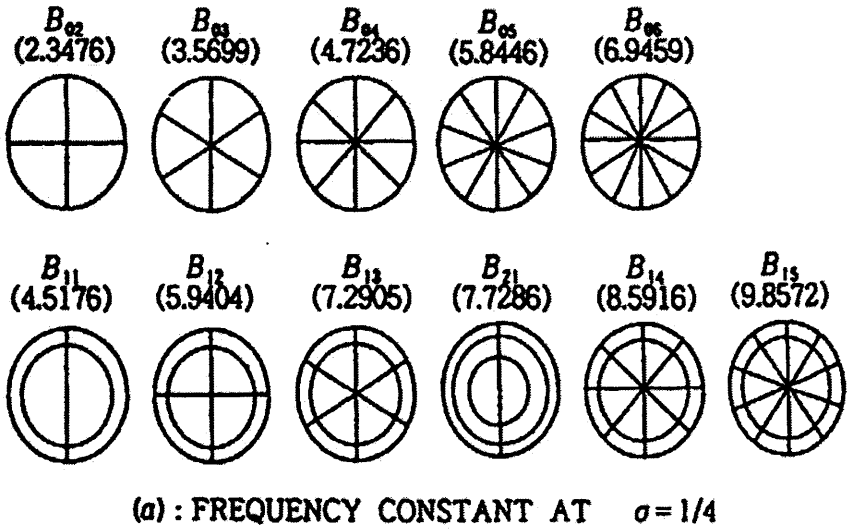


Figure 1.2. Resonance modes and frequency constants of a disk in bending vibration [2].

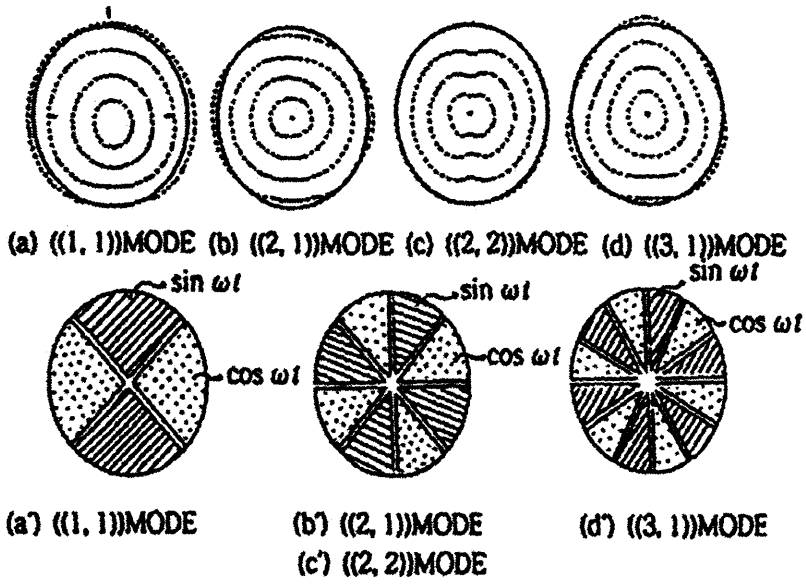


Figure 1.3. Non-axisymmetric modes and excitation of two-phase drive [2], [12].

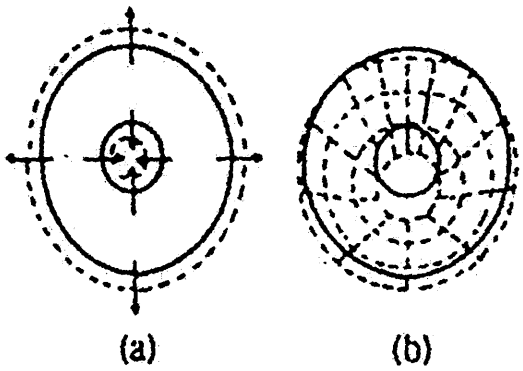


Figure 1.4. An annular plate ultrasonic motor using radial and non-axisymmetric vibration [2].

* *Ultrasonic motors using a rod vibrator*:

(a) Flexural vibrations with degenerate resonance modes of the same form;

(b) Longitudinal and torsional vibrations, as shown in Figure 1.5, with resonance modes of differing forms.

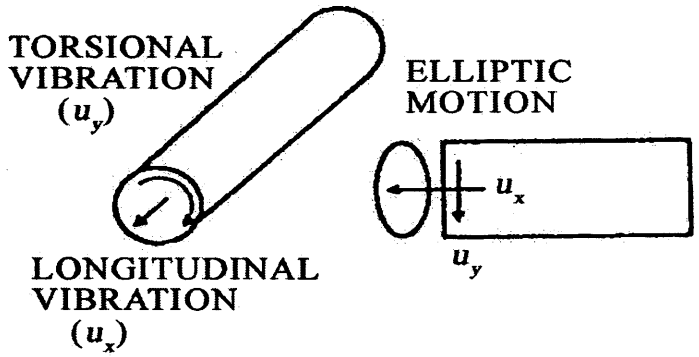


Figure 1.5. Longitudinal and torsional modes and their elliptical motion [2].

* *Ultrasonic motors using a thin plate of rectangular form*:

(a) Longitudinal and bending vibrations, as shown in Figure 1.6, resonance modes of differing forms used;

(b) Flexural vibrations, as shown in Figure 1.7-1.11, resonance modes of the same or differing form used.

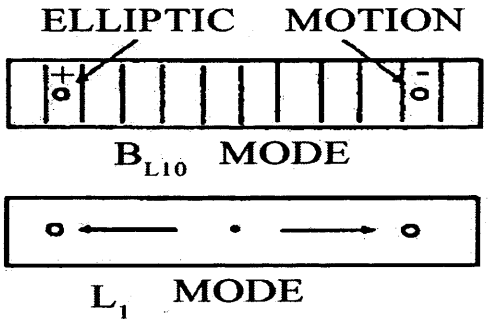


Figure 1.6. A rectangular plate motor using longitudinal and bending vibrations [2].

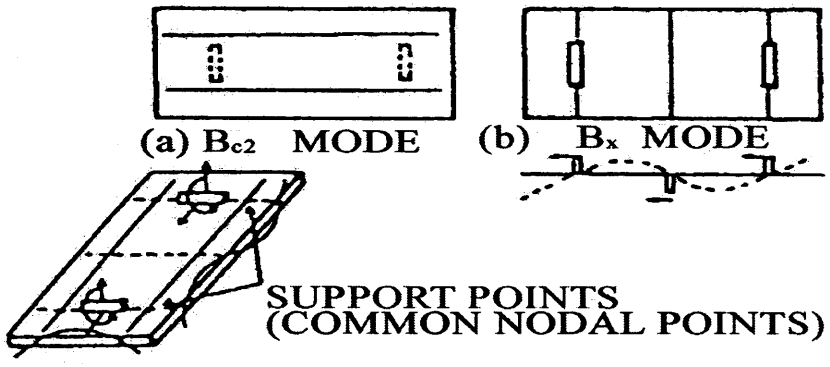


Figure 1.7. A rectangular plate motor using two bending vibrations [2].

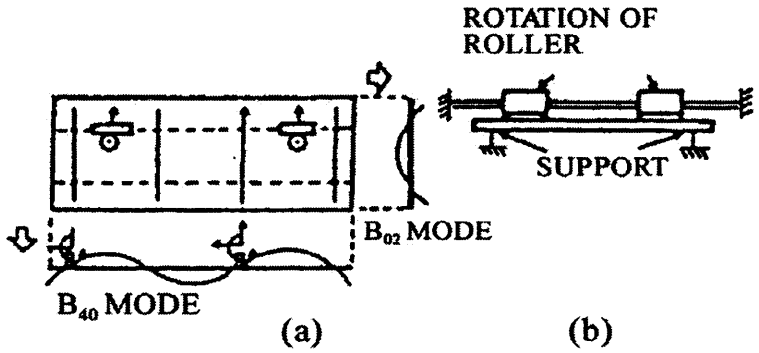


Figure 1.8. An alternative rectangular plate motor using two bending vibrations [2].

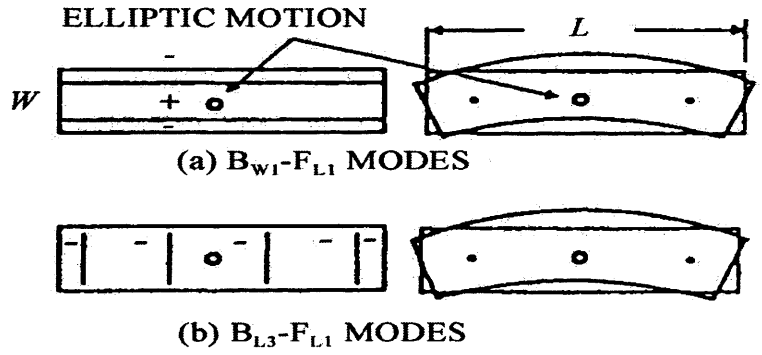


Figure 1.9. A rectangular plate motor using bending and flexural vibrations [2].

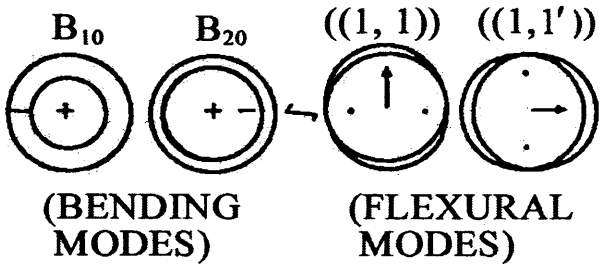


Figure 1.10. A disk motor using bending and flexural vibrations [2].

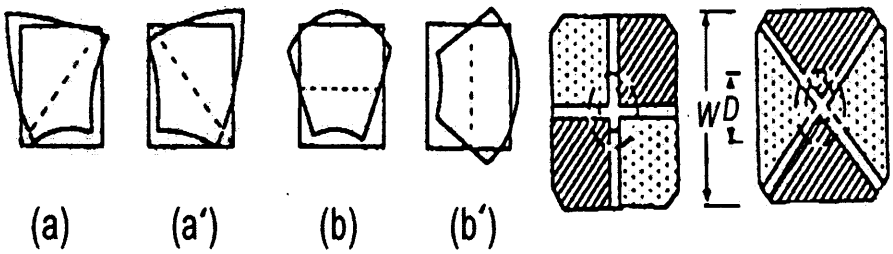


Figure 1.11. A square plate motor using degenerate flexural vibrations [2].

(3). Classification by operating principles; the driving force for the ultrasonic motor could be:

(a) By electrical excitation of the stator through another transducer;

(b) By mechanical excitation of the stator through another transducer as shown in Figure 1.12.

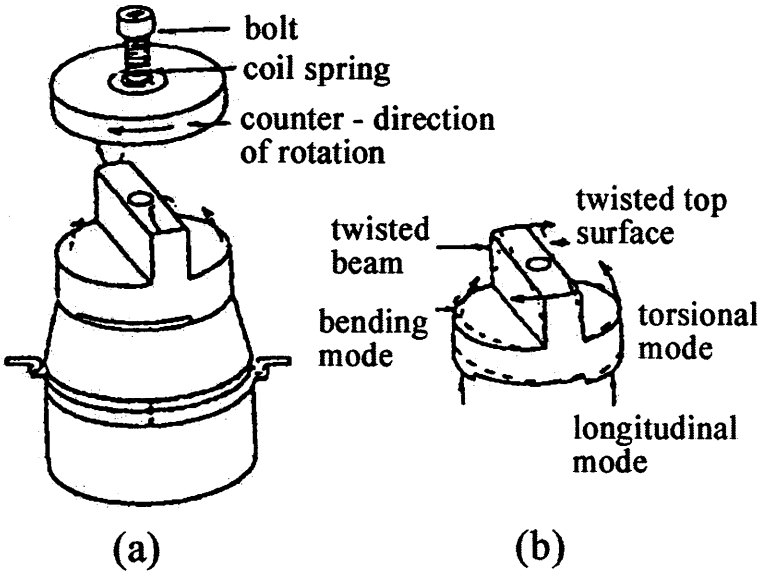


Figure 1.12. Kumada's motor using a single-resonance-mode vibration [2].

## 1.3 Features of Ultrasonic Motors

The unique features of ultrasonic motors can be distinguished by wave type, reliability (heat generation, frictional coating and lifetime) and drive/control. In this section, we will discuss these features using simple theoretic descriptions and explanations of functions.

### 1.3.1 Wave Types

#### 1.3.1.1 Standing-wave Type

A standing wave generated by an ultrasonic motor can be expressed by

$$u_s(x,t) = A\cos kx\cos \omega t . \tag{1.1}$$

A standing wave type is sometimes considered as a vibrator-coupler type, where a vibrator piece is connected to a piezoelectric driver and its tip can generate elliptical movement, as shown in Figure 1.13. Sashida [4]

has proposed this type of motor. When a displacement

$$u_x = u_0 \sin(\omega t + \alpha) \tag{1.2}$$

is excited at a piezoelectric vibrator attached to a rotor with a slight cant angle $\theta$, the vibratory piece will generate bending due to restriction by the rotor. The tip moves along the rotor face between A→B and freely between B→A.

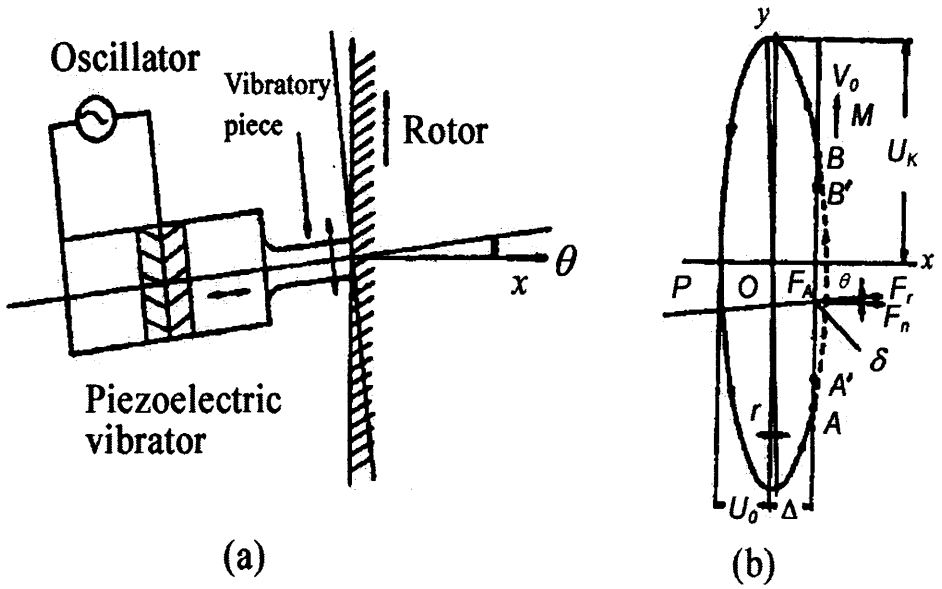


Figure 1.13. (a) Vibratory coupler type motor (b) its tip locus [4], [12].

### 1.3.1.2 Propagating-wave type

The propagating wave is expressed as

$$u_p(x,t) = A\cos(kx - \omega t), \tag{1.3}$$

using a trigonometric relation, (1.3) can be transformed as

$$u_p(x,t) = A\cos kx \cos \omega t + A\cos(kx - \pi/2)\cos(\omega t - \pi/2). \tag{1.4}$$

This leads to an important result, i.e., a propagating wave can be generated by superposition of two standing waves whose phases differ

from each other by 90° both in time and in space. This principle is necessary to generate a propagating wave on a limited volume/size substance, because only standing waves can be excited stably in a finite size. This superposition principle is shown in Figure 1.14. A surface particle of the elastic body draws an elliptic locus due to the coupling of longitudinal and transverse waves. This type requires, in general, two vibration sources to generate one propagating wave, leading to low efficiency, but it is controllable in both rotational directions.

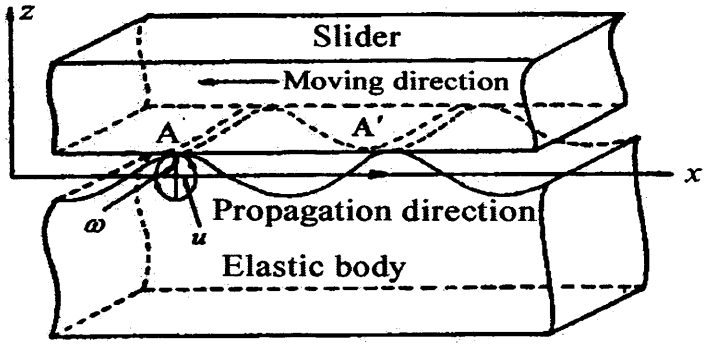


Figure 1.14. Principle of the propagating-wave type motor [12].

## 1.3.2 Ultrasonic Motor Types

### 1.3.2.1 Rotary Motors

Sashida [4] proposed a rotary type motor. This type of ultrasonic motor contains four vibratory pieces mounted onto the edge face of a cylindrical vibrator and pressed onto the rotor. Many present prototypes of ultrasonic motors follow and develop further on this type. This rotary motor can provide a revolution speed of 1500rpm, torque of 0.008N-m, output of 12W, and efficiency of 40% under 35kHz excitation and 30W input. It will obtain a much higher speed than the inchworm types due to its high frequency and the amplified vibration displacement at its resonance frequency. Hitachi Maxel [5] used a torsion coupler to replace

Sashida's vibratory pieces and increase the pressing force with a bolt; therefore its torque and efficiency would be significantly improved. Its configuration is shown in Figure 1.15(a). It usually consists of two legs that transfer longitudinal vibration generated by a Langevin vibrator to a bending mode of the knob disk and the vibratory extruder. The extruder must be aligned with a certain cant angle to the legs transferring the bending to the torsion vibration. The transverse moment coupled with the bending up down motion leads to an elliptical motion on its tip portion, as Figure 1.15(b) illustrates. If the elliptic locus is reduced by about half, the optimum pressing force for the maximum thrust can be acquired. For example, a $30 \times 60mm^2$ motor with a $20-30^\circ$ cant angle between the leg and the vibratory piece can provide up to 1.3N-m torque and 80% efficiency. Its main merit is that its rotation output is quite smooth—even its drive is intermittent. This is because of the inertia of its rotor. However, its drawback is that it only provides unidirectional rotation.

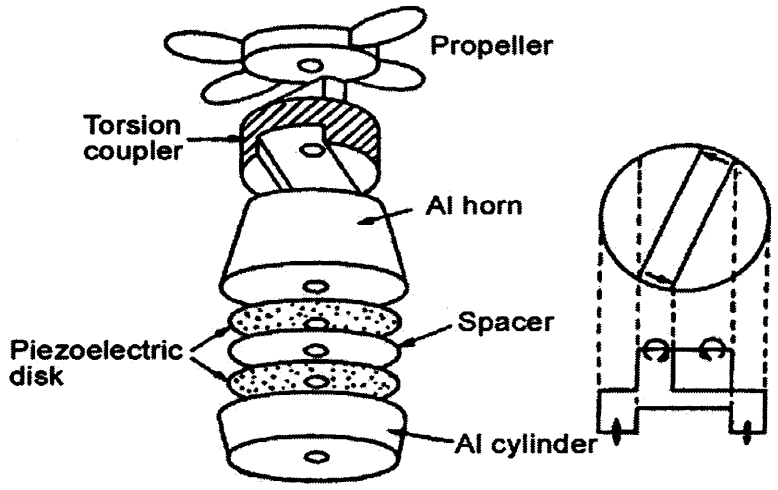


Figure 1.15. (a) Torsional coupler ultrasonic motor (b) the motion of the torsional coupler [5], [12].

In addition, Penn State University invented a tiny 3mm diameter ultrasonic motor [12]. It is shown in Figure 1.16. Its stator consists of a piezoelectric ring and two concave/convex metal end-caps with windmill shaped slots bonded together. It can generate an up-down and torsional type of coupled vibration, and has a maximum revolution speed of 600rpm and a maximum torque of 1mNm at a 160kHz driving frequency. Tokin [6] has used an interdigital type electrode pattern printed with a 45° cant angle on a piezoelectric ceramic cylinder as a torsional vibrator. It is shown in Figure 1.17. Ueha also developed a two-vibration-mode coupled type [7]. It used a torsional Langevin vibrator with three multilayer actuators to allow its stator to generate larger longitudinal and transverse surface displacement. This is shown in Figure 1.18. Its rotational direction can be changed by controlling the phase difference.

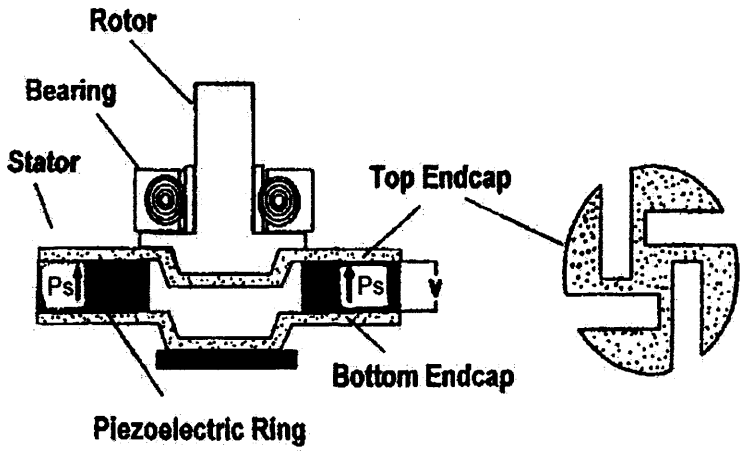


Figure 1.16. 'Windmill' motor with a disk-shaped torsional coupler [12].

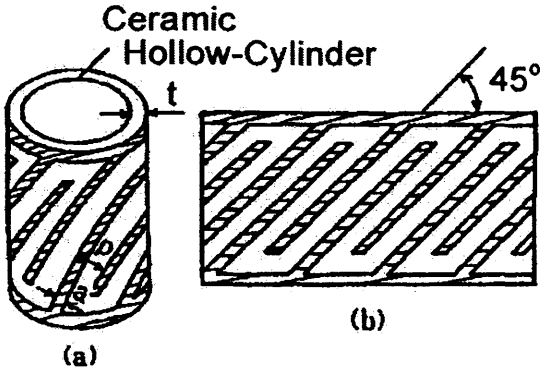


Figure 1.17. (a) Piezoelectric cylinder torsional vibrator (b) electrode pattern [6], [12].

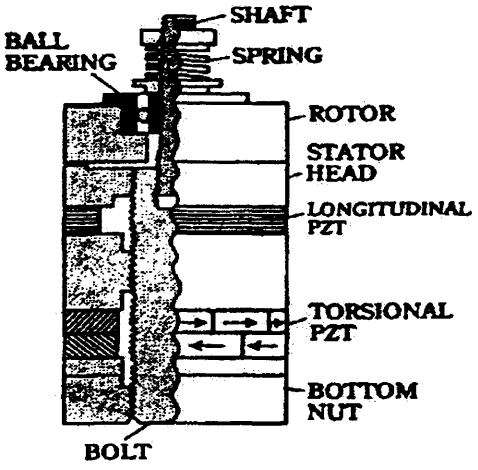


Figure 1.18. Two-vibration-mode coupled type motor [7].

### 1.3.2.2 Linear Motors

K.Uchino [8] developed a $\pi$-shaped linear motor, as shown in Figure 1.19. It is implemented with a multilayer piezoelectric actuator and fork-shaped metallic legs. Changing its driving frequency due to a slight difference in the mechanical resonance frequency between the two legs can control the phase difference between the bending vibrations of both legs. A prototype motor $20 \times 20 \times 5mm^3$ driven at 98kHz with a 0.7W input power will have a maximum speed of $20cms^{-1}$, a maximum thrust of 0.2kgf and a maximum efficiency of 20%. The characteristics of the

linear motor are shown in Figure 1.20. This type of motor is usually employed in a precision X-Y stage.

Another type of linear motor is Tomikawa's rectangular plate motor [9], as shown in Figure 1.21. The first longitudinal mode, $L_1$ mode, and the eighth bending mode, $B_8$, with the same resonance frequencies are made by applying voltages with a $90^{\circ}$ phase difference to form an elliptical displacement motion on the plate surface. Ueha et al. [10] developed a kind of linear motor using a bending vibration, as shown in Figure 1.22. The two piezoelectric vibrators mounted at both ends of the transmittance steel rod will become excited and will receive the travelling transverse wave in the asymmetric fundamental Lamb wave mode. Adjusting the load resistance in the receiving vibrator produces a travelling wave. A reverse motion can be achieved by exchanging the roles of exciting and receiving piezo-components.

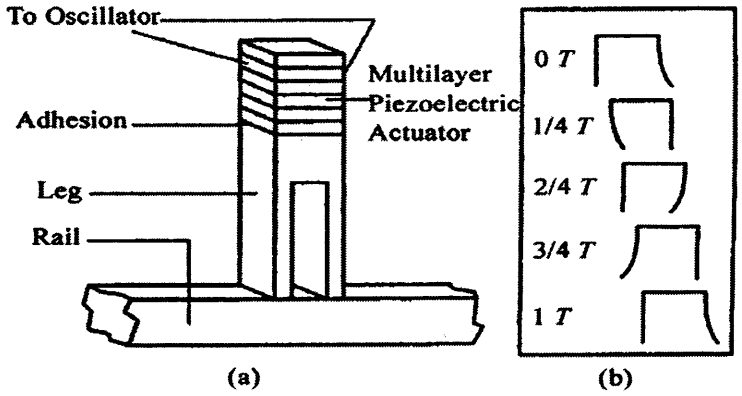


Figure1.19. (a) $\pi$-shaped linear ultrasonic motor (b) walking principle [8], [12].

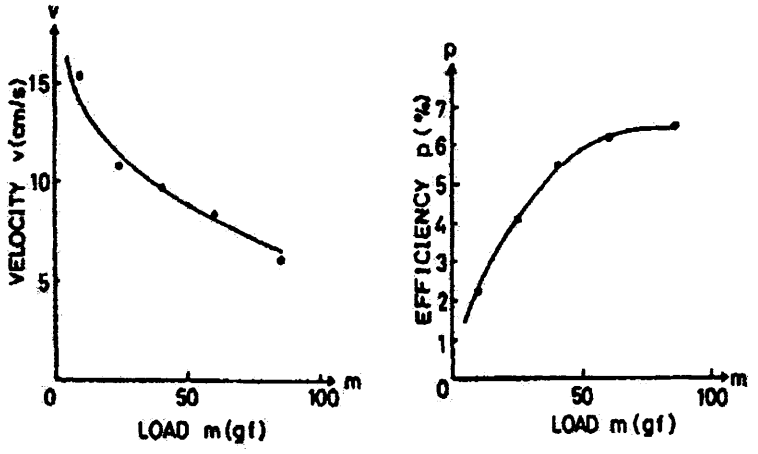


Figure 1.20. Motor characteristics of the $\pi$-shaped linear ultrasonic motor [8], [12].

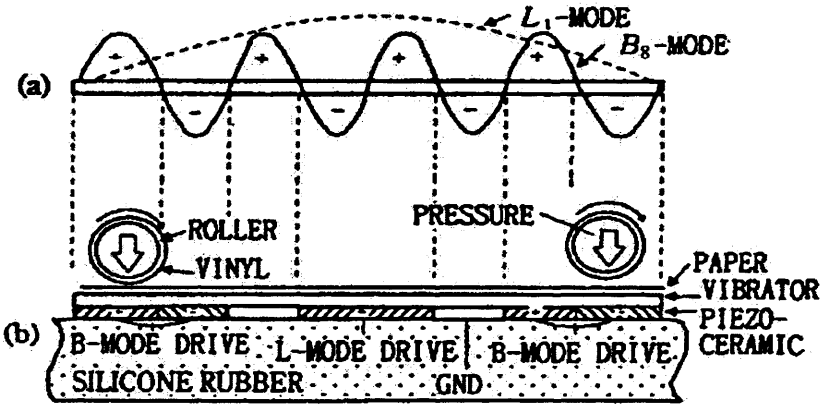


Figure 1.21. $L_1$ and $B_8$ double-mode vibrator motor [9], [12].

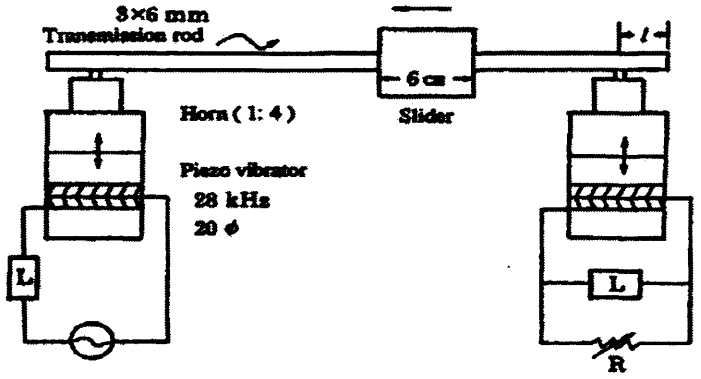


Figure 1.22. Linear motor using a bending vibration [10], [12].

### 1.3.2.3 Surfing Type

When a stator is driven at one position on a closed ring at a resonance frequency, a standing wave is excited. The vibration waves will interfere with each other due to the propagation outward to random direction from the vibration source. All the waves induced by the vibration source can be superimposed; they will produce a standing-wave rotation in the ring. When a vibration source of $A\cos\omega t$ is located on the point $\theta = 0$ of the closed ring, the nth standing wave can be written as

$$u(\theta,t) = A\cos n\theta\cos\omega t \tag{1.5}$$

and the travelling wave as

$$u(\theta,t) = A\cos(n\theta - \omega t), \tag{1.6}$$

where n is the nth mode. Using the superposition method, the travelling wave can be formulated as

$$u(\theta,t) = A\cos n\theta\cos wt + A\cos(n\theta - \pi/2)\cos(wt - \pi/2). \tag{1.7}$$

It reveals that the travelling wave is formed by two standing waves with a phase shift of 90° in any direction. In general, the phase shift can be arbitrary except $0, -\pi, \pi\phi$, but the phase shift must occur in the same space and time. Figure 1.23 illustrates this shift. Basically, for generating

a travelling wave, there only needs to occur an excitation in two parts of the ring. However, to increase the mechanical output, there needs to be as many vibration sources as possible. Therefore, we need to consider the symmetry of the electrode on the closed ring, that is, it is depending on the mode order to be excited. The main reason is that in the condition, some standing-waves will be produced and all the waves induced by these vibration sources can be superimposed maximally, then it can create maximal electrical-mechanical transfer energy and efficiency, so the mechanical output can be increased.

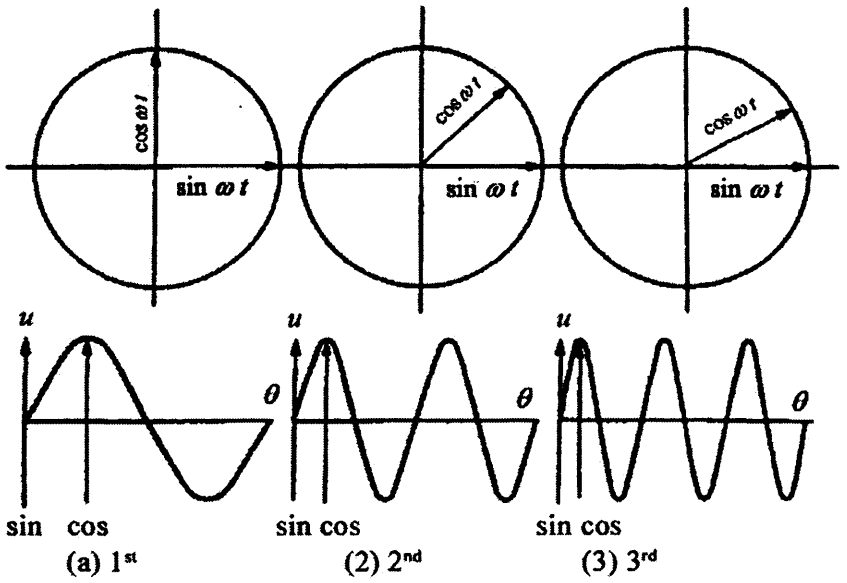


Figure 1.23. Vibration source position for generating a propagating wave in a ring [12].

The Sashida type ultrasonic motor [11] is illustrated in Figure 1.24. Most ultrasonic motor systems in Japan and the US are modification of the Sashida type, for example, the exchange lens of Canon's EOS camera series uses the type for its ultrasonic motor mechanism. In practice, it operates by using travelling wave induced by a thin piezoelectric ring. The slider makes contact with the rippled surface of the elastic body bonded onto the piezoelectric ring driven in both directions by

exchanging the sine and cosine inputs. Its advantage is its thin design, which can serve as an automatic focusing device in cameras. The piezoelectric ring has 16 pairs of positive and negative poled regions and two asymmetric electrode gap regions (the poled pairs will determine the excited mode form and driving frequency), which can generate the ninth mode propagating wave at 44 kHz. The prototype consists of a brass ring of 60mm in outer diameter, 45mm in inner diameter and 2.5mm in thickness, bonded onto a piezoelectric ring of 0.5mm in thickness with divided electrodes on the back side. The rotor is polymer material coated with hard rubber or polyurethane. Sashida's motor characteristics are illustrated in Figure 1.25.

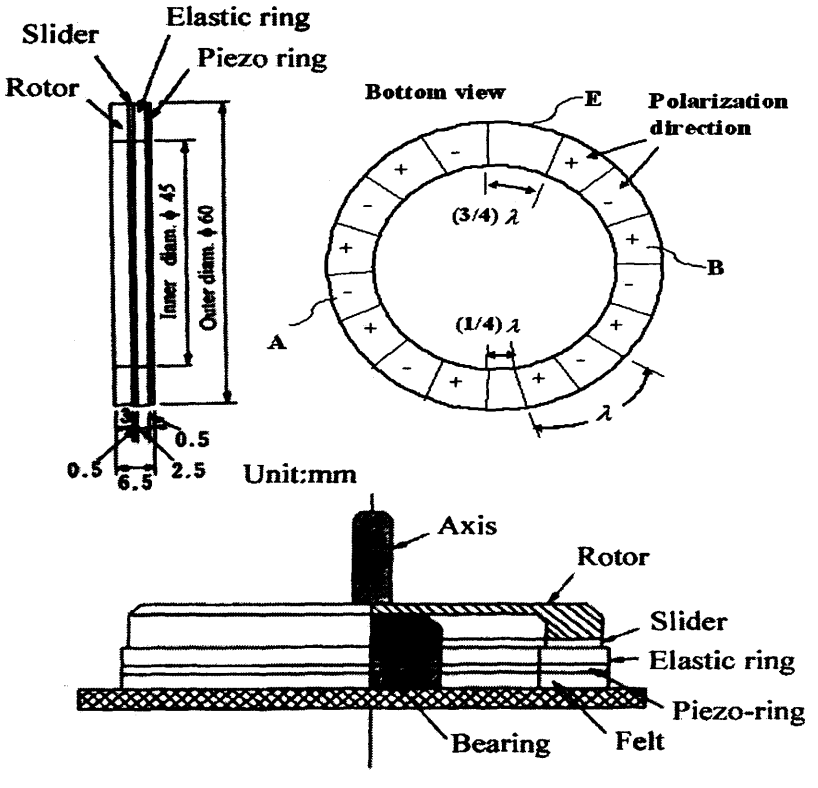


Figure 1.24. Stator structure of Sashida's motor [11], [12].

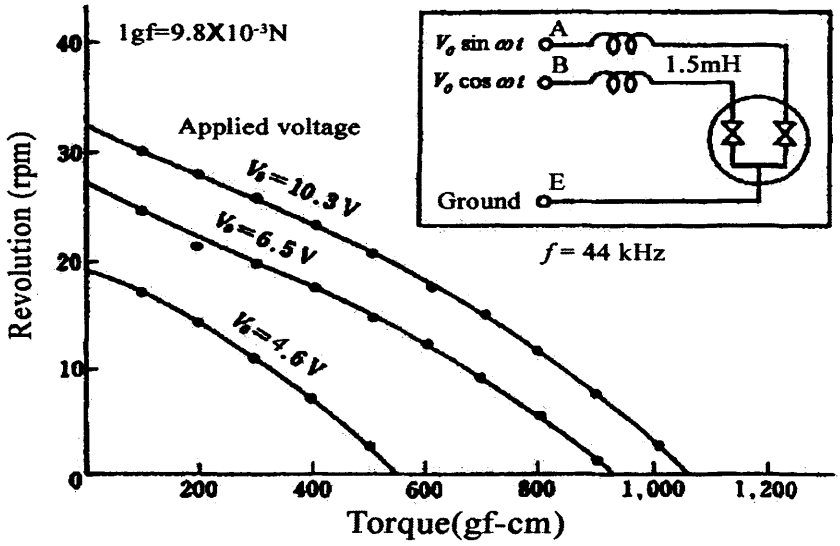


Figure 1.25. Motor characteristics of Sashida's motor [11], [12].

A Cannon camera is another example of a surf motor used for a camera's automatic focusing mechanism. It can compactly install the ring motor into the lens frame. Because the closed ring has many teeth, it can magnify the transverse elliptical displacement and promote the speed. The lens position can be moved back and forth by regulating a screw mechanism.

Although the surfing motor has some advantages such as a silent drive due to the ultrasonic frequency drive with no gear mechanism, and thin motor design with no gear mechanism which leads to the saving of space and energy, these type of motors usually encounter a problem relating to the support of the closed ring. For the standing wave motor, the nodal points or lines are generally supported, which may have minimal effect on the resonant vibration. However, the surfing type does not have steady nodal points or lines. Therefore, these problems must be deal with. Figure 1.24 shows that the stator is fixed along the axial direction so as not to reduce its' vibration. The stop pins latch onto the stator teeth only for the purpose of high rigidity against the rotation.

Figure 1.26(a) shows the stator structure proposed by Matsushita Electric [12], who used a nodal line method supported by a higher order vibration mode [see Figure 1.26(a)]. The ring is supported at the nodal circular line and the teeth are arranged on the maximum amplitude circle to obtain a larger revolution.

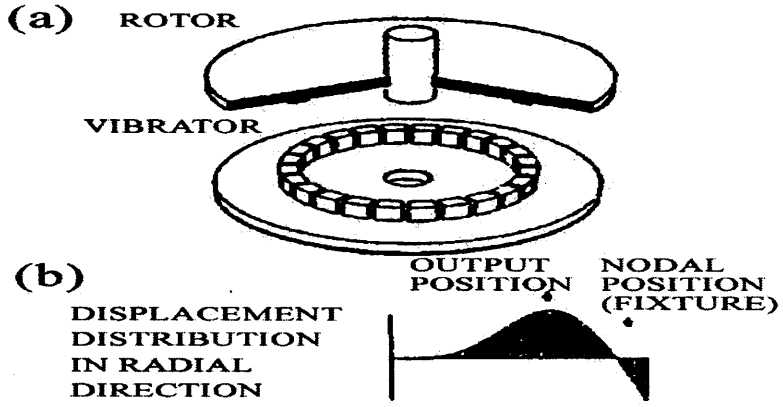


Figure 1.26. (a) Tooth shaped stator (b) a higher order vibration mode with a nodal line for fixing [12].

Figure 1.27 shows the construction of a small motor with a $10mm$ diameter and $4.5mm$ thickness proposed by Seiko Instruments, which can miniaturize the ultrasonic motor a to 10 mm in diameter [12]. This small motor can provide $6000rev\,\min^{-1}$ and a torque of $0.1mNm$ under driving a voltage of 3V and a current of $60mA$. Allied-Signal proposed an ultrasonic motor similar to Shinsei's type that can be used as mechanical switches for launching missiles [12].

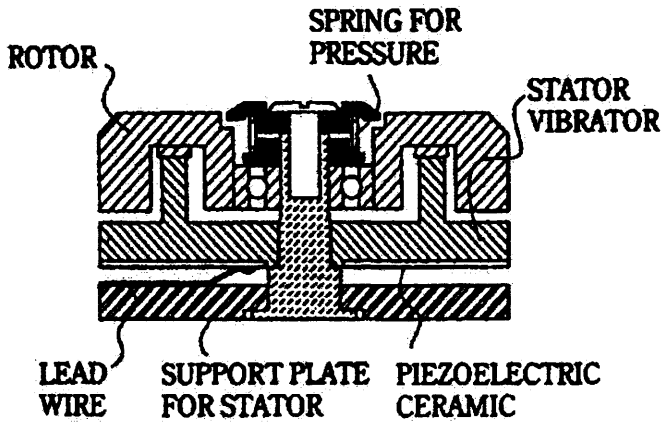


Figure 1.27. Construction of Seiko's motor [12].

Tokin [13] proposed another special design called a 'plate-spinning' type motor, as shown in Figure 1.28. Its operating principle involves the use of a mixture of sine and cosine signals to excite a piezoelectric rod, and then it rotates a cup contacting the 'spinning' rod by the internal face.

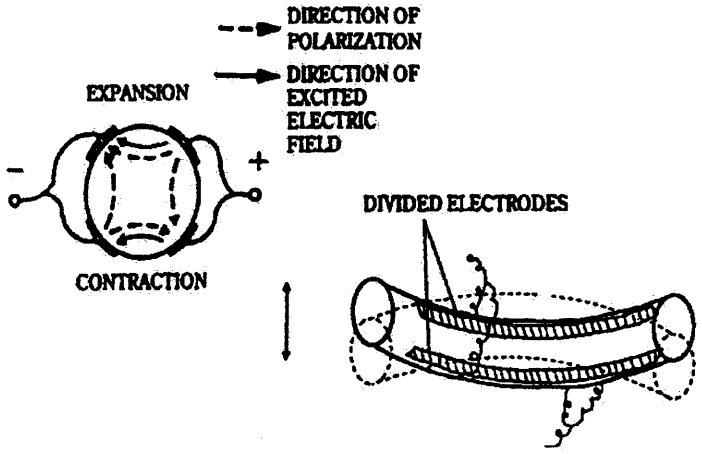


Figure 1.28. Plate-spinning type motor by Tokin [12], [13].

### 1.3.2.4 Vibration Coupler Type

Here, the compliant slider-rigid stator model is introduced. As shown in Figure 1.29, the horizontal and vertical displacements of the rigid

stator are given by

$$a = a_0 \cos \omega t \tag{1.8}$$

$$b = b_0 \sin \omega t . \tag{1.9}$$

Thus the horizontal velocity becomes

$$v_h = (\partial a / \partial t) = -a_0 \omega \sin \omega t . \tag{1.10}$$

We usually employ the following three hypotheses [12] for further calculations:

Hypothesis 1. Normal force is given as follows, using a characteristic angle $\phi$ between $P_1$ and $P_2$:

$$n = N[\sin \omega t - \cos(\phi / 2)] .$$

for $(\pi / 2 - \phi / 2) < \omega t < (\pi / 2 + \phi / 2)$ (in contact)

$$n = 0$$

for $0 < \omega t < (\pi / 2 - \phi / 2), (\pi / 2 + \phi / 2) < \omega t < 2\pi$ (out of contact). (1.11)

Hypothesis 2. The slider speed is constant ($V_0$).

Hypothesis 3. The dynamic friction constant gives the maximum thrust $\mu_d$:

$f = -\mu_d n$ Accelerating force for $(\pi / 2 - \psi / 2) < \omega t < (\pi / 2 + \psi / 2)$

$f = \mu_d n$ dragging force for $(\pi / 2 - \phi / 2) < \omega t < (\pi / 2 - \psi / 2)$,

$$(\pi / 2 + \psi / 2) < \omega t < (\pi / 2 + \phi / 2) . \tag{1.12}$$

The main results are summarized. If we know $\phi$ experimentally under a certain normal force N, we can calculate the no-load speed $V_0$ from (no-load condition, no slip, $V_0 = v_h$ see Figure 1.29)

$$V_0 = v_h = -a_0 \omega \sin \omega t = -a_0 \omega \sin(\pi / 2 - \psi / 2) = -a_0 \cos(\psi / 2) , \tag{1.13}$$

and no-slip position angle $\psi$ (small angle) from the following relation

$$\cos(\psi / 2) = \sin(\phi / 2) / (\phi / 2) . \tag{1.14}$$

Equation (1.14) is obtained by trigonometric approximation relationship ( $\sin(\phi/2)=(\phi/2)=\tan(\phi/2)$ ). According to Hypothesis 1(normal force, in contact and out of contact period) and Hypothesis 3(acceleration force and dragging force period), with further simplifications made by the author in [12], the thrust can be obtained as follows:

$$F=\mu_d N\{1-2[\sin(\psi/2)-(\psi/2)\cos(\phi/2)]/[\sin(\phi/2)-(\phi/2)\cos(\phi/2)]\} \quad (1.15)$$

The two cases of $\phi=0,\psi=0,V_0=-a_0\omega$, $F=-0.155\mu_d N$, and $\phi=\pi$, $\cos(\psi/2)=2/\pi$, $V_0=-(2/\pi)a_0\omega$, $F=-0.542\mu_d N$ can be verified by Equation (1.15). We also find that with an increasing contact period of the vibratory piece, the thrust F will be increased at the expense of reducing the speed.

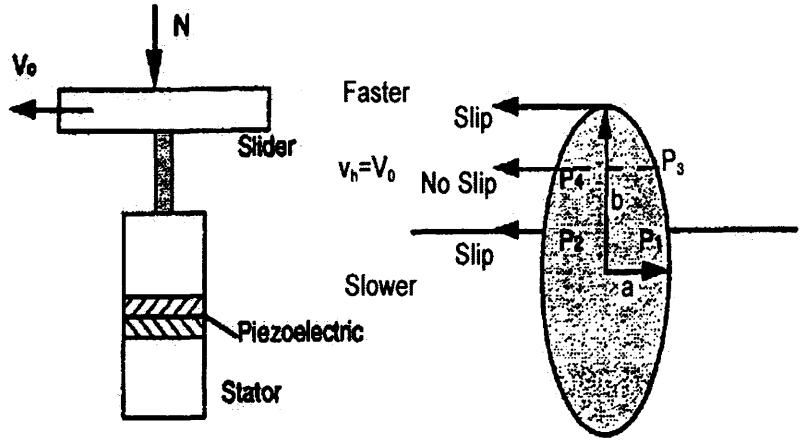


Figure 1.29. Compliant slider and rigid stator model [12].

## 1.3.3 Reliability of Ultrasonic Motors

When discussing reliability of ultrasonic motor, the following issues should be considered:

(1). Measuring methods—high-field electromechanical couplings.

(2). Material development– low loss.

(3). Piezoelectric actuator designs.

(a) Heat generation mechanism.

(b) Degradation mechanisms.

(c) New multilayer actuator designs.

(4). USM designs.

(a) Displacement magnification mechanisms.

(b) USM type.

(c) Frictional contact part.

(5). Drive/control.

(a) High frequency/high power supply.

(b) Resonance/anti-resonance usage.

There are some important factors such as heat generation, frictional coating and lifetime that affect the reliability of the ultrasonic motor. These factors are described in the following section.

### 1.3.4 Heat Generation

Heat generation is a major problem with ultrasonic motors that causes a serious degradation of the motor characteristics, especially if its temperature gets up to 120°C. Therefore, the ultrasonic motor is required to have a very hard type piezoelectric material with a high mechanical quality factor Q, which can reduce heat generation. In addition, Q value is related to the actual mechanical vibration amplitude at the resonance frequency.

Figure 1.30 [14] shows mechanical Q versus basic composition x at

effective vibration velocity $v_0$=0.05 $ms^{-1}$ and 0.5 $ms^{-1}$ for $Pb(Zr_xTi_{1-x})O_3$ doped with 2.1 at. % of Fe. The results reveal that the mechanical Q is slightly decreased with an increase of vibration level around the rhombohedral- tetragonal morphotropic phase boundary (52/48). The worst material at a small vibration level becomes the best at a high vibration level, which is not relevant to high power materials from the conventional impedance analyzer.

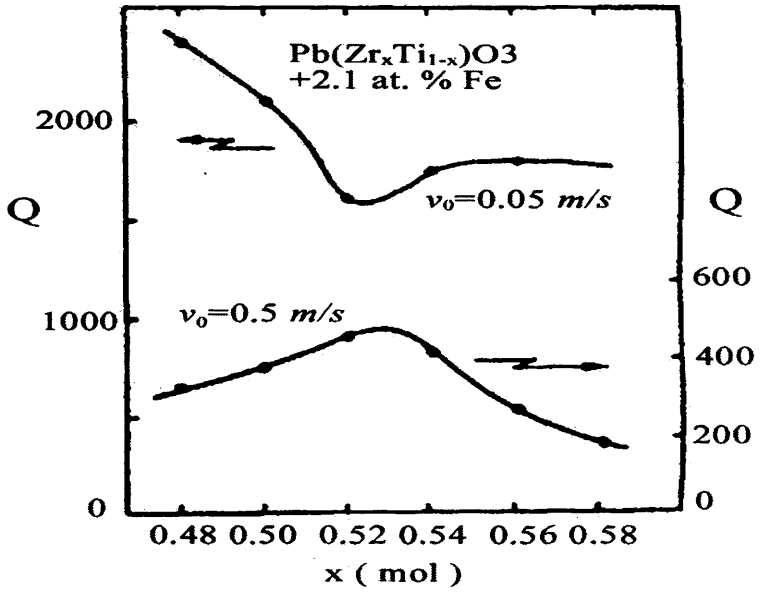


Figure 1.30. Mechanical quality factor Q against basic composition x at vibration velocity $v_0 = 0.005$ and $0.5ms^{-1}$ for $Pb(Zr_xTi_{1-x})O_3$ +2.1 at. % Fe ceramics [12], [14].

Another problem relating heat generation is resonance loss, referencing [15], as shown in Figure 1.31. From the relationship between the resistances $R_d$, $R_m$ in the equivalent electrical circuit and vibration velocity, it reveals that $R_m$ is mainly related to the mechanical loss and insensitive to the vibration velocity, while $R_d$ is related to the dielectric loss and changes significantly around a certain critical vibration

velocity. The resonance loss at a small vibration velocity is mainly determined by the mechanical loss, and with increasing vibration velocity; the dielectric loss contribution significantly increases. For the ultrasonic motor, dielectric loss dominates heat generation.

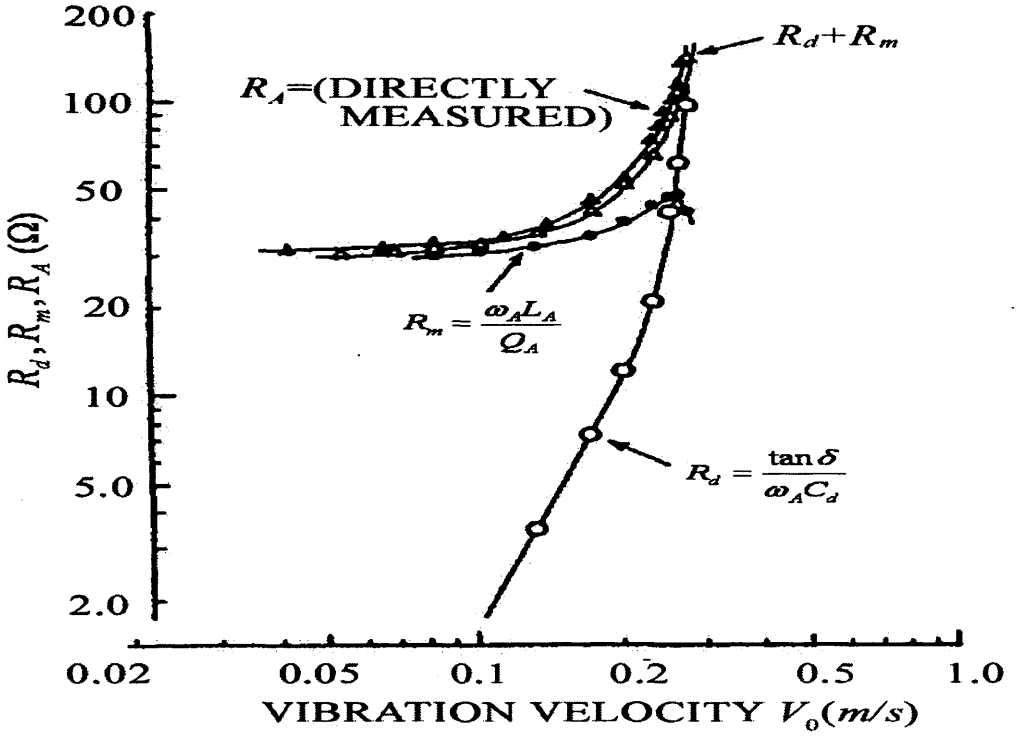


Figure 1.31. Vibration velocity dependence of resistances $R_d$ and $R_m$ in the equivalent electric circuit [12], [15].

Uchino [12] reported the heat generation from various sizes of multi-layer type piezoelectric ceramic actuators. The temperature change was monitored in the actuators when driven at 3kV $mm^{-1}$ and 300 Hz, and Figure 1.32 plots the saturated temperature as a function of $v_e / A$, where $v_e$ is the effective volume and A is the surface area. This linear relation is reasonable because the volume $v_e$ generates the heat and this heat is dissipated through the area A. Thus, if one needs to suppress the heat, a

small $v_e / A$ design is preferred.

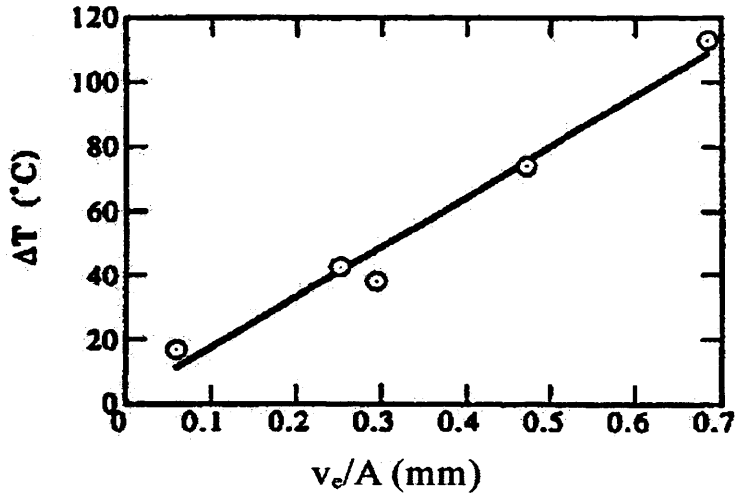


Figure 1.32. Temperature rise versus $v_e / A$ (3kV $mm^{-1}$, 300kHz), where $v_e$ is the effective volume generating the heat and A is the surface area dissipating the heat [12].

### 1.3.5 Frictional Coating and Lifetime

Figure 1.33 plots the efficiency and maximum output of various friction materials [12]. High-ranking materials include PTFE (polytetrafluoroethylene, Teflon), PPS (Ryton), PBT (polybutyl terephthalate) and PEEK (polyethylethylketone). In practical motors, Econol (Sumitomo Chemical), carbon fiber reinforced plastic (Japan Carbon); PPS (Sumitomo Bakelite) and polyimide have been widely used. Figure 1.34 shows the wear and driving period for CFRP, which indicates that 0.5mm thick coating corresponds to 6000-8000 hours of life [12]. Although the lifetime of the ultrasonic motor is limited by the characteristics of the friction material, in some case this problem has been nearly solved in practice. For example, in these experiments, the

thickness of the frictional material was kept constant at 0.2mm, its contact surface was polished with fine abrasive (no. 2000), the thrust on the material was 160N and driving frequency of the motor was 40kHz. From these results, we can conclude that the features required in a frictional material are as follows. A certain amount of defacement is allowable, as long as each particle dislodged is small and significant recombination of the particles does not readily occur. In addition, the dislodged particles must be easily eliminated from the motor. Frictional material that suffers breakage of large particles by friction is not suitable for an ultrasonic motor. The material of group C in Figure 1.33 are considered to suffer from this defect; that is, large dislodged particles and portions where the compound is broken away are deemed to prevent effective conversion of vibration energy from the stator to rotor. Here the durability test of the Shinsei motor is shown below.

(1). Continuous drive (CW 1 min and CCW 1 min) with a revolution of 250 rpm and a load of 0.5 kg-cm.

(2). After 2000 hours, the revolution change is less than 10%.

(3). Intermittent drive (CW 1 rotation and CCW 1 rotation) under no load.

(4). After 250 million revolutions, there is no degradation in motor characteristics.

Taking into account the usual lifetime specifications, e.g., 2000-3000 hours for VCRs, the lifetime of the ultrasonic motor is no longer a problem.

There is no doubt that the lifetime of the motor itself is not identical to the lifetime when installed in a device system. We need further clarification on this issue under severe drive conditions such as large load and high temperature and humidity.

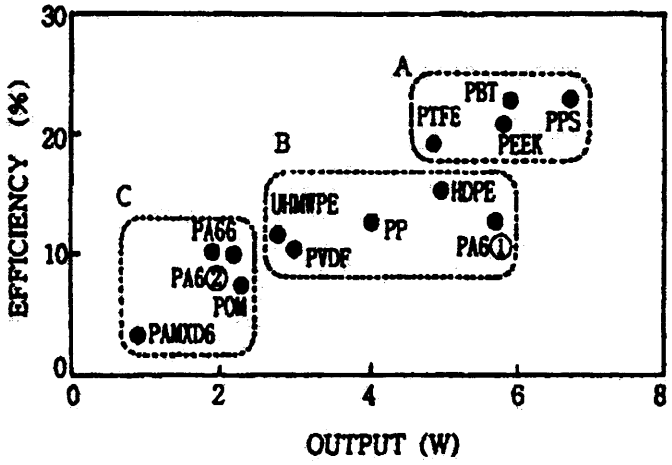


Figure 1.33. Efficiency and maximum output of the Shinsei ultrasonic motor for various friction materials [12].

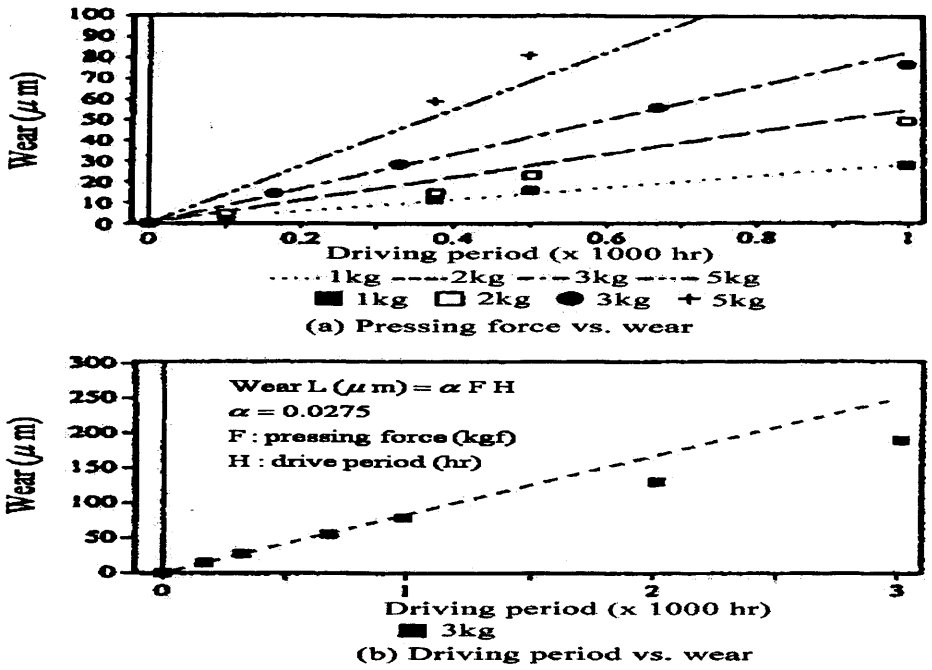


Figure 1.34 Wear and driving period of the ultrasonic motor for CFRP friction material [12].

## 1.3.6 Drive/Control Technique

Driving the ultrasonic motor at the resonant and anti-resonant

frequency is also a special technique to reduce the load on the piezoceramic and the power supply. Why do we drive the motor at the resonant and anti-resonant frequency, the reason is that usually, in order to achieve high efficiencies of ultrasonic motor, it should be driven at or close to the frequency that will create resonance, however, temperature rise is occasionally observed particularly when the motor is driven cyclically at resonant frequency, this is due to the imbalance between heat generation caused by dielectric hysteretic loss and heat dissipation determined by the device size. The heat generated attributes to the low efficiency of the motor as the mechanical vibration transform into heat energy through friction. So, usage of anti-resonant frequency is suggested for improving the efficiency of an ultrasonic motor when the motor is driven cyclically because anti-resonant frequency reveals much mechanical quality factor and low heat generation than resonant status. Mechanical quality factor $Q_m$ and temperature rise have been investigated on a PZT ceramic rectangular bar, and the results for the fundamental resonance (A-type) and anti-resonance (B-type) modes are plotted in Figure 1.35 as a function of vibration velocity. It [16] is recognized that $Q_B$ is higher than $Q_A$ over the entire vibration velocity range. The anti-resonance mode can provide the same mechanical vibration level without generating heat. Moreover, the usage of 'antiresonance', whose admittance is very low, requires low current and high voltage for driving, in contrast to high current and low voltage for 'resonance'. This means that a conventional inexpensive power supply may be utilized to drive the ultrasonic motor.

For the rotor used in the high-speed rotation experiment, we need to take into account the controllability and efficiency. A specific drive circuit or control technique is required. Figure 1.36 displays most of the control methods of ultrasonic motors. The main control techniques include: (1)

voltage control (voltage change/modulation), its major disadvantage is not sensitive to slow motion due to piezoelectric ceramic fast response to voltage variation (2) frequency control (frequency change/modulation), its major disadvantage is also not sensitive to slow motion due to piezoelectric ceramic fast response at resonance frequency (3) phase control (phase change/modulation), its major disadvantage is low efficiency due to piezoelectric ceramic existing dielectric loss (4) pulse width modulation(PWM) control, it is the most popular adaptive control technique for ultrasonic motor, its major advantage is the efficiency can be kept at maximal and constant value by regulating adaptive duty ratio. Most of existing control strategies are similar to EM motor except the stator material and energy transformation. To take a two-phase-driving ultrasonic motor as a general example [2], the common requirements of its driving and control are as follows.

1. Two-phase-driving pulse signals with a duty ration of 50% and $\pi/2$ phase difference are used. Driving the motor clockwise or counter-clockwise is performed by electrical switching of the phase difference of the two pulse signals by a circuit composed of a TTL.
2. A rotary encoder is used to detect the angular displacement of the motor.
3. A PC based DSP system is used for driving and controlling the motor movement.

Various IC packages are commercially available for driving EM motors in stepping movement, therefore, if IC packages exclusive to the ultrasonic motor are also made available, they must favour wide use of ultrasonic motor. The following specifications are required for an IC package for an ultrasonic motor:

(1). Two-phase pulse driving of the motor must be possible and additionally the followings are required:

(a) switching of the phase difference, 0° and 90°;

(b) switching of single and push-pull driving;

(c) direct driving of motor by MOSFET.

(2). Individual control of pulse-width modulation two-phase-driving is expected.

(3). Frequency range: 1-500kHz.

(4). On/OFF and CW/CCW operation are made possible by logic signal control.

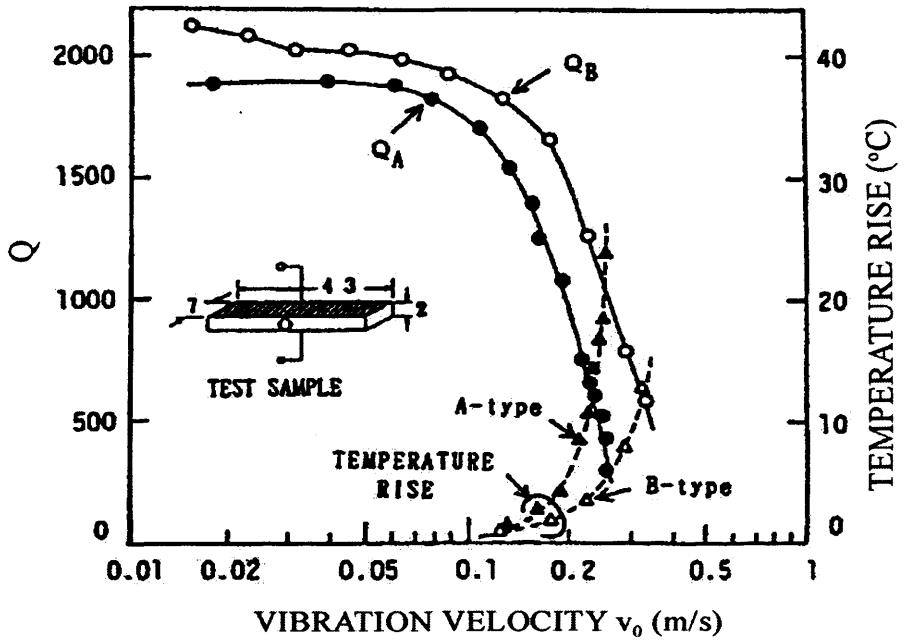


Figure 1.35. Vibration velocity dependence of the quality factor Q and temperature rise for both A (resonance) and B (anti-resonance) type resonances of a longitudinally vibrating PZT rectangular transducer through $d_{31}$ [12], [16].

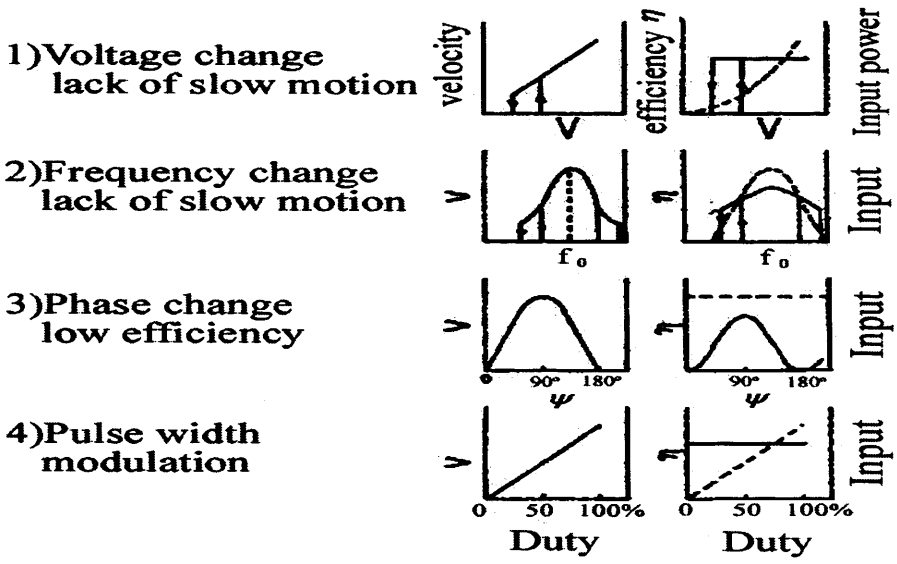


Figure 1.36. Control methods of ultrasonic motors [12].

## 1.4 Overview

In the dissertation, we use a novel disc-type stator proposed by a published patent [17] (Prof. Minsun Ouyang, National Tsing Hua University, Taiwan) for the ultrasonic motor. The stator has an asymmetrical simple-support boundary configuration (120°-90°-150°) on its surface. The advantages of this motor system are that one single electrical phase driving instead of usually two electrical phases driving, multiple-resonant-modes driving instead of single- resonant-mode driving, clockwise rotation (CW) and counter-clockwise rotation (CCW) change by driving frequency modulation instead of by phase shifter, single contact instead of area contact, and simple driving electrical circuit instead of usually complicated driving electrical circuit. The multiple-resonant modes were performed by an external perturbation with constraint technique on the stator rather than cutting off the edge of a stator. The cutting edge method was also applied for application to an electromechanical filter as a communication frequency element. This

constraint technique is a completely different principle from a conventional multi-electrode ultrasonic motor. Using the controlled mode shapes in a single-phase driving power for one set of electrode, a stator vibrator can be possibly expected to rotate the rotor in both directions of CW and CCW. The detail about the disc-type ultrasonic motor structure and operation principle will be described at Chapter 2. To explore the characteristics of the motor, this dissertation includes the following research tasks:

(1). Description of the disc-type piezoelectric ultrasonic motor.

(2). Finite element analysis for the ultrasonic stator.

(3). Transfer function of the ultrasonic motor.

(4). Equivalent circuit estimation of the ultrasonic motor.

(5). Speed control of the ultrasonic motor by using a current controller.

In Chapter 2, first it is mainly focused on description of the disc-type ultrasonic motor structure and operation principle from the published patent [17]. Then according to the patent's modal analysis and test, and add our laser vibrometer measurement of mode motion and wave propagation concept, the asymmetrical simple-support boundary configuration (120°-90°-150°) for an adaptive mechanism was proven. The relationship between contact point (rotor location) and CW and CCW rotation, and the relationship between frequency and CW and CCW rotation were proven by finite element mode interaction together with real inspection. The driving circuit and measurement instrument for the motor system are also discussed.

Chapter 3 is concerned with the finite element model of the disc-type piezoelectric ultrasonic stator. Linear piezoelectric, mechanical and piezoelectro-mechanic behaviors of a metal disc structure embedded with piezoelectric actuator are considered. Using finite element method, a dynamic formulary is modeled for the disc-type piezoelectric ultrasonic

stator. In this model, a 3-dimensional (D) mechanical element with an extra electrical degree of freedom is used to simulate dynamic vibration modes and analyze characteristic responses such as electrical impedance response, phase response and mechanical frequency response for the new disc-type piezoelectric ultrasonic stator. An adaptive boundary condition, simple support condition with three nonequal-triangular fixed points near the stator edge is defined in the finite element model. The finite element results have been compared with the experimental measurements. As a result, the analysis model seems to be similar to the real condition.

The focus of Chapter 4 is the issue of the transfer function of the disc-type ultrasonic motor. The transfer function model is derived from the piezoelectric constitutive laws in terms of radial and tangential displacement components for control application and for the certification of dynamic characteristic parameters. The relative response characteristics including frequency response, phase response, transient response, stability diagram (bode diagram and Nyquist path), speed-current, speed-torque and voltage-torque are obtained from the transfer function analysis.

The issue of simulating equivalent circuit models for the disc-type ultrasonic motor system is considered in Chapter 5. The equivalent circuit models cover radial vibration mode, tangential vibration mode and coupling vibration mode but are applied to search for the possible resonance frequency. The resonance frequency is examined by using the frequency response measurement. The PSPICE is used to build up the equivalent circuit models and simulate the equivalent circuit components. Some effects are revealed from the comparison between the analysis and the experiment.

The rotational speed of an ultrasonic motor is related to the vibration speed of its stator. Because drift of the piezostator characteristics will

cause variation of the motor speed, a controller is thus necessary in order to produce a constant output speed. Variations of the motor output characteristics will also make it very difficult to obtain the efficiency of the motor. Chapter 6 points out the origins of possible drifts in the disc-type piezoelectric ultrasonic motor. The frequency behaviour of the proposed motor and its consequences on speed control scheme are discussed. The speed control scheme is implemented by using current modulation and commercial DSP technique, so the revolution speed will be kept constant.

Conclusions derived from the results of the dissertation research are summarized and future research directions also indicated in Chapter 7.

A supplementary explanation is given at Appendix A. Some axial vibration measurements are made to investigate levitation motion on the stator surface and explore its possible application on the linear, surfing and shaft types of bearingless ultrasonic motor.

# Chapter 2 Description of a New Disc-type Piezoelectric Ultrasonic Motor

## 2.1 Introduction

For piezoelectric ceramics applied to most ultrasonic transducers, the design of a single-frequency piezoelectric resonator [18]-[19] is very important. In the case of the resonator, the requirements [20] include (1) an assurance of the specified mechanical resonance frequency; (2) an absence of spurious resonances close to the working frequency; (3) a high quality factor including minimum energy dissipation in the material and in the attachment. For example, a transducer for most acoustic wave generation applications is required to oscillate in the piston mode. However, the design of a multi-driving frequency piezoelectric stator/vibrator becomes critically important for ultrasonic motor application; the main reason is to satisfy the feature of ultrasonic motor in multi-mode vibrator and one single-phase driving power, in addition, CW and CCW can be changed by switching driving frequency instead of a phase shifter, its driving circuit will be able to be simplified. The multi-driving-frequency design is essentially related to resonance frequency, vibration mode and electromechanical coupling factor, i.e., EMCC, which measures how strong the excitation of a specific resonant mode is in the transducer response [21]-[22]. All of these parameters depend on many factors, however the topology/shape [23]-[25] and material property are the most important. In general, the resonance frequency and EMCC are dependent upon the size and shape of piezoelectric transducers. Thus, optimizing dimension or boundary

condition is one of the most important problems in piezoelectric engineering. Challande [21] and Sato et al. [22] have presented the optimization of the dimension ratio of a piezoelectric element with a parallelepipedic shape that maximizes the EMCC for a specific mode. The main problems with size and shape are solving eignvalue optimization. Diaz and Kikuchi [23] used the homogenization method to solve the shape and topology eigenvalue optimization problem. Meric and Sagal [24] analyzed the shape sensitivity of piezoelectric structures by using the adjoint variable method. In our study, by making the boundary condition of the stator into an asymmetrical configuration, we can adapt the configuration into an adaptive ultrasonic motor.

For an ultrasonic motor, it is powered by the rotational motion from the transformational vibration mode and wave motion in the stator coming into with the contact frictional force from the rotor. TWUM (travelling-wave type) [26]-[28], HTUSM (hybrid type) [29] and RUM (rotary type) [30]-[32] are the most popular application in ultrasonic motor. Hirata and Ueha [26], [28] proposed a design method based on two vibration modes for prototyping TWUM and estimating its dynamic characteristics. Hosoe [27] applied TWUM to the automatic focusing lenses of cameras. Iwamatsu et al. [30] and Ise [31] employed two degenerate flexural vibration modes, which are spatially orthogonal with each other to establish RUM. Iula et al. [32] developed RUM using mode rotation. The rotating wave is generated by the combination of two standing natural flexural waves whose phases differ by 90°, both spatially and temporally. They have promoted the driving frequency of RUM to ultrasonic frequency range by using axial vibration.

In our studying, the contact frictional force is divided into tangential force and radial force, as shown in Figure 2.1. An elliptical motion of the material points of the stator edge generates these force components.

These forces are related to the frictional process in the contact area. The contact mechanics of piezoelectric ultrasonic motors determines the operational characteristics such as revolution speed, torque, transmitted power and efficiency. In addition, wear properties and the lifetime of piezoelectric ultrasonic motors are also determined by contact mechanics. In general, ultrasonic motors have two-stage energy conversion [33]. In the first stage, piezoelectric elements convert electric energy into high frequency mechanical oscillations. Depending on the geometry of the vibrator and the piezoelectric excitation, two orthogonal and coupled vibration modes (tangential, radial and coupled modes) are superposed onto an elliptical motion of the surface. In the second stage, the high oscillatory vibration is rectified into the macroscopic unidirectional rotary or the linear motion of a driven component. The second energy conversion is based on contact mechanisms occurring at the interface between the stator and rotor. The contact mechanics can be divided into two groups according to [34]. One is the travelling-wave contact type where the distributed contact area between the stator and rotor moves along with a travelling-wave on the stator. The second is an intermittent contact type where the contact occurs at the same, small area of the stator. In this dissertation, the proposed motor belongs to the intermittent contact type. Although the smooth contact of the first group seems to be quite different from the impact-like contact of the second group, many similarities exist between both types and their overall behavior is comparable if proper interpretations of parameter and processes are adopted. The mathematical modeling of contact mechanics [35] and the optimization of lifetime and operational characteristics of ultrasonic motors by a proper choice of contact materials and design parameters have been significant topics in the research of ultrasonic motors. Hagoog and McFaland [35] calculated the modal forces and formulated a

mathematical model that enables us to investigate the overall travelling wave motor system behavior including the stator/rotor contact. In their analysis, the normal pressure was obtained from an elastic foundation model including a rigid body displacement of the rotor and the tangential stresses were calculated using Coulomb's friction law together with the assumption of the complete slip in the whole contact area. However, the investigation was limited to the case of a perfect travelling wave with prescribed form but undetermined amplitude. Analytical, numerical and experimental methods have been employed in the investigations [36]-[62].

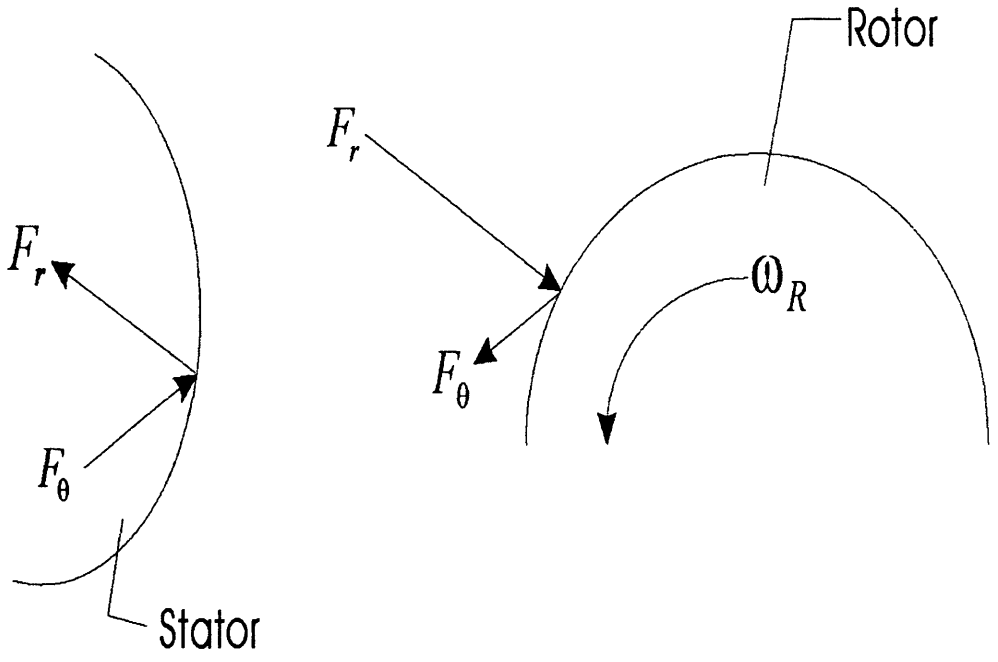


Figure 2.1. Expression of the contact force between stator and rotor.

In general, the area of contact is subdivided into adhesion and slips zones, whose distribution is complex due to its variable nature and inherent nonlinearity. One of the first systematic studies of intermittent contact type motors is Marth [36]. A strong influence of the contact material on the resulting motor characteristics was observed and

experiments were performed in order to validate a simple model for contact mechanics. Further models for the contact mechanics of intermittent contact type motors are discussed by Ragulskis [37]. They are used to investigate torque-speed characteristics and the stability of the operation of piezomotors with oblique impact in different regimes. Fleischer [38] discussed the contact process for an intermittent contact type motor. He emphasized that the impact oscillations of the rotor and a corresponding shock wave can be minimized by a proper choice of beveling angle. In order to prevent wear, protective layers like sputtered TiN was investigated, resulting in drastic improvements of the motor's lifetime. Nakamura [39] reported a simple contact model for intermittent contact type motors and applied it to the simulation of a hybrid ultrasonic motor. One of the earliest studies of the contact mechanics of the travelling wave ultrasonic motor was done by Endo and Sasaki [40] who experimentally investigated the influence of the physical characteristics of the frictional material on the performance of a linear travelling-wave motor. They experimentally confirmed that a linear relationship exists not only between the vibration amplitude of the travelling wave and the on-load speed of the motor but also between the normal pressing force and the obtained driving force. A strong influence of the material hardness on the operational characteristics was observed and some general guidelines for the choice of contact materials were given.

Kamano [41] found that a certain vibration amplitude must be obtained before the motor starts to operate. This non-linear dead-band behavior makes it difficult to control the operation of ultrasonic motors at low rotational speeds, as pointed out in detail by Furuya [42]. Kato [43] discussed the influence of surface roughness, normal force, sliding velocity and local plastic deformations as well as damage and wear of the contact surface. He gave a critical discussion of the coefficients of static

and dynamic friction and pointed out that due to the tangential elasticity of the contacting micro-asperties a coefficient of static friction, strictly speaking, does not exist. Maeno [44]-[45] analyzed the rotor/stator contact of a ring-type ultrasonic travelling-wave motor. He used the finite-element method to calculated displacements and velocities of the stator and rotor and the distribution of stick and slip areas in the contact surface respectively. Normal and tangential deformations of the rotor, constructed as a flange shaped spring, were taken into account. The authors also studied the influence of initial deformations of stator or rotor geometry due to production tolerances. Their analysis, based on the finite-element method, showed that the initial deformation led to asymmetric normal pressure distributions, resulting in torque-speed curves lower than those obtained for perfect geometry. Maeno and Bogy [46] used a refined model in the finite element analysis. Again, they observed that tangential stresses can have an influence on the distribution of the normal pressure. Flynn [47] compared several models for the contact mechanics of travelling-wave ultrasonic motors and discussed torque-speed curve as well as mechanical power flow and conversion efficiency of the frictional interface. Zharii [48]-[50] approximated analytical solutions of dynamic contact problems that were given by subdividing the coupled contact problem into two parts. First, the influence of tangential stresses on the size of the contact area and on the normal stress distribution was ignored and the contact problem was solved for $\mu=0$. In the second step, the solutions for normal stresses and tangential velocity were used to find the tangential stresses. Buchaillot [51] has given a detailed analysis of the contact mechanics of the travelling-wave type of ultrasonic motor. In his study, the influence of the normal pre-load on the static normal pressure distribution takes the rotor and the stator deflections into account.

Kawai [52] presented experimental results obtained for travelling-wave ultrasonic motors of different diameters. He found good agreement between the measured no-load speed and the calculated one, which was estimated under the assumption of point contact between the stator and rotor. He also investigated the influence of the rotor vibrations on the motor characteristics. It was observed that maximum torque, output power and efficiency of the motor was obtained if the normal vibration amplitude of the rotor was half as large as the normal vibration amplitude of the stator, this is a special case, not a common example because maximum torque, output power and efficiency are strongly depended on stator configuration, frictional material, rotor size and pre-load, it is just for the researcher's type. If the rotor was designed correctly, high amplitude levels could be obtained without audible squeal noise. If the friction contact layer between the stator and rotor is to be optimized, a detailed description of its dynamic behavior is necessary, including the effects of tangential stiffness, damping, layer thickness and other design parameters of the frictional interface. Cao and Wallaschek [53] presented a contact model including normal and tangential stiffness and dissipation of the contact layer as a viscoelastic foundation model. Interesting stick-slip phenomena, similar to those observed by [44] were found. Cao and Wallaschek [54] studied the stick-slip behaviour in detail and it was indicated that there exist three different slip and two different stick zones according to the kinematics of the stator and rotor. Guyomar [55] developed a travelling-wave type ultrasonic motor that operates at very high vibration amplitudes of the stator. His results indicate that the effect of rotor vibration and the observed phase shift should be considered in the modeling of the stator/rotor contact of ultrasonic motors.

Schmidt [56] used the same viscoelastic foundation model for the description of the contact layer as that of [53]-[54]. However, the coupled

dynamic contact problem was solved by using a Fourier expansion method. Hagedorn [57] extended this contact model by taking the bending vibrations of the rotor into account. It was shown that a spatial phase shift between the vibrations of the stator and rotor existed in the general case and that the contact mechanics might be much more complicated than suggested by simple models, which neglect the rotor's dynamics. In the modeling of the overall motor behavior, the impact of the normal and tangential stresses on the amplitude of the stator vibration must be taken into account. Maas [58] extended this model for the general case of a non-perfect travelling wave and studied the effect of various asymmetrical modes of operation. In another paper [59], he showed that the special case of a perfect travelling wave is indeed the best operation mode for a travelling-wave ultrasonic motor.

Ishii [60] experimentally investigated the wear behaviour of fibre orientation. He measured specific wear rates and developed a model for the calculation of the long-term wear behavior. Compared to the experimental results his model under-estimated the lifetime, which might be due to the fact that the change of thickness of the contact layer during service was not taken into account. For constant normal force the contact length became smaller for the worn contact layer and this led to less wear than was predicted by the model with constant thickness of the contact layer. Adachi [61] presented experimental results obtained by a special test ring simulating the contact conditions of intermittent contact type motors. He investigated the microscopic force transfer mechanism and proposed a modified Coulomb friction law, where the coefficient of friction depends on the relative local displacement of contact asperities. Rehbein and Wallaschek [62] used a special test ring for high frequency fretting to study the high frequency friction behavior as well the wear characteristics of several polymer and ceramic materials with respect to

their application as contact material in the travelling wave and micro-push motors. They experimentally supported the hypotheses that the wear resistance of polymer materials can be improved by adding short fibres and solid lubrication.

Ultrasonic motors are usually analyzed in two steps. First the vibrating structure is designed to achieve the required vibration modes, operational frequency and amplitudes. Then, the contact mechanics are studied under the assumption that the contact process does not affect the vibration characteristics of the resonating structure. The contact mechanics will be detailed in this chapter. Strictly speaking, such a separation is not accurate, because the motion of the vibrating structure depends on the forces generated at the frictional interface, and the whole system, including the rotor and other structural parts, should be considered as a coupled dynamic structure. However, the separation of the analysis process simplifies the investigation considerably and quite often results in a good description of motor behavior. In this dissertation, the contact type of the studied ultrasonic motor is a point-contact type. The rotor is rigid and that the interface forces do not change the stator bending profile. The stator and rotor only come into contact at the peaks of the travelling wave, as shown in Figure 2.1. The radial and tangential forces describe the interaction between the stator and the rotor. The friction is assumed to be Coulomb friction in the proposed ultrasonic motor system. The contact force/driving force is from $r$ and $\theta$ direction displacements. The derivation of driving force equation may follow up classic plate and shell theory [63]-[64]. The mechanically active forces are induced from the lateral elliptic motion displacement and the driving force is dependent upon the radial and tangential vibration amplitudes of the stator

In order for the ultrasonic motor to be widely used, it is necessary

that the required characteristics of the studied motor are realized. Thus, the author follows up a new design method [17] by that can realize its practical use. Prof. Minsun Ouyang got the patent earlier than dissertation author; in addition, the author has stayed his group for half year, so in order to respect his help, the author still needs to state "follow up". In fact, the research works are undertaken independently, dissertation author left there after two years, then the patent (120°-90°-150°) was found. The purpose of this chapter is to analyze the novel boundary configuration for the studied motor by mode concept and physical behaviors. This chapter is organized in the following way. First the mechanism for realizing the required characteristics is described; second is the description of relative design consideration; third the adaptive boundary configuration is proven; forth the driving principle is discussed. Then, a drive circuit used in the research work for high speed rotation and stable operation is described. Lastly, the measurement instruments are introduced and some motor characteristic measurements are displayed. In the next several chapters, we will use the stator for further research: finite element analysis, transfer function model, equivalent circuit analysis and speed control. These relative characteristic parameters including driving frequencies, driving force, load characteristics and dynamic response will also be acquired from these analyses and experiments.

## 2.2 The Structure of the Motor

### 2.2.1 Structure and Dimension of the Disc-type Stator

This study is related to an ultrasonic motor using piezoceramic-driving element, wherein a main sliver electrode is covered at the lowest end of the piezoceramic and the uppermost end of

piezoceramic is adhered to a metal sheet. In operation, an AC power is inputted between the main electrode and the metal sheet. The piezoelectric ceramic will generate a pull or push motion due to the converse piezoelectric effect and a metal sheet is driven to vibrate in the air to emit sound waves. The original operating frequency used is under 20kHz. But, in this study, a piezoceramic-driving element is used as a stator in which its operating frequency launched is over 20 kHz. Thus, the generated mechanical flexural waves are transferred along radial or transverse directions. In transferring the waves, a reflecting point can be formed by using a screw as a constraint. By setting up three reflecting points on three peripheral constraints, the flexural wave of different direction is generated on the metal sheet at its outer edge. One of the reflecting waves is used to provide a torque to rotate the rotor. Therefore, the location of constraints shall be considered. Normally, the diameter of the screw is 2 mm. To assure the reflection of the waves on metal sheet, the screw must be locked tightly.

According to the actuating principle, the studied disc-type structure is classified into the quasi-hybrid one, in which one standing wave is the propelling source merged functional reflection waves or deflection waves. The structure of stator includes three fundamental elements: (1) the membrane of piezoceramics; (2) the elastic metal sheet of nickel alloy; (3) the covered with its diameter of 24.5 mm sliver sol–gel membrane used as an electrode. The thin-disk structure is a piezoceramic membrane boned on a Ni-alloy sheet with its diameter 41 mm. Its total thickness is 0.23 mm and its thickness of metal sheet is 0.10 mm. Actually, the stator is a commercial piezoelectric buzzer bought from a local company (OBO Corp.) in Taiwan, with its dimension specification as shown in Figure 2.2

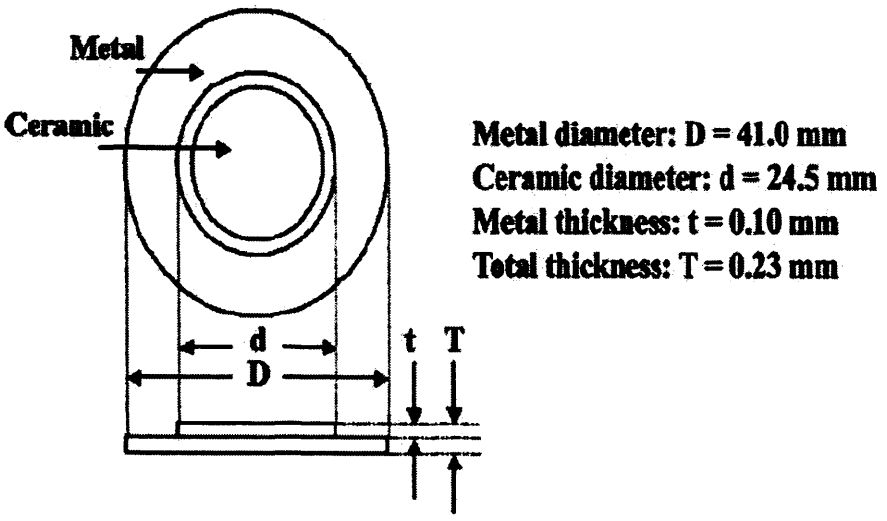


Figure 2.2. The structure of piezoelectric membrane.

## 2.2.2 Geometry Description and Design Consideration

For PZT disc-type structure vibration in ultrasonic frequency, piezoceramic plays the driving source to generate the high frequency extended-shrunk motion of metal sheet. The metal sheet plays the amplifier of vibrating magnitude and constructs the desired mode shapes. The minimum deformation located at central portion but larger deflection near outer edge of metal sheet. Contradictorily, metal stiffness of sheet also constrains the piezoceramic, and limits the PZT dynamic response to electric power. Only in suitable power entry matching resonant frequency, metal stiffness would be overcome by piezoceramic to produce the optimal efficiency. Thus, the resonant deformation of metal sheet always well-being follows the flexural-like vibrating of piezoelectric ceramic, called as mechanical flexural wave, that the phenomena is existed especially in ultrasonic frequency. Furthermore, if it were used as an actuator, we only need to directly observe the resonant mode shapes. Then, ultrasonic driving mechanism was roughly configured. Therefore, realizing vibration mode of PZT disc-type structure is the first step for a

future application. In this study, a piezoceramic stator (simple support structure with three fixed points) is fixed to a movable base which is linked to a pair of spring for a preload control mechanism, as shown in Figure 2.3 (the photo figure of the real ultrasonic motor). The preload mechanism is conformed to the movable actuator and fixed rotor may contact anytime and can increase the friction between the stator and the rotor and increase the torque. And, a good insulation must be formed between the fixing aluminum plate and the piezoceramic assuredly. It is major purpose to avoid the wire of the driving power to be shorted as connected to it. As considering the precise in finishing and the balance of the rotor, the rotor is a fixed rotary component. The body of the rotor is a rigid steel (diameter 26mm and thickness 16mm). The rotor surface was attached a white mark for measuring the rotor speed using photo detector. Table 2.1 lists these parameters for the construction of the motor.

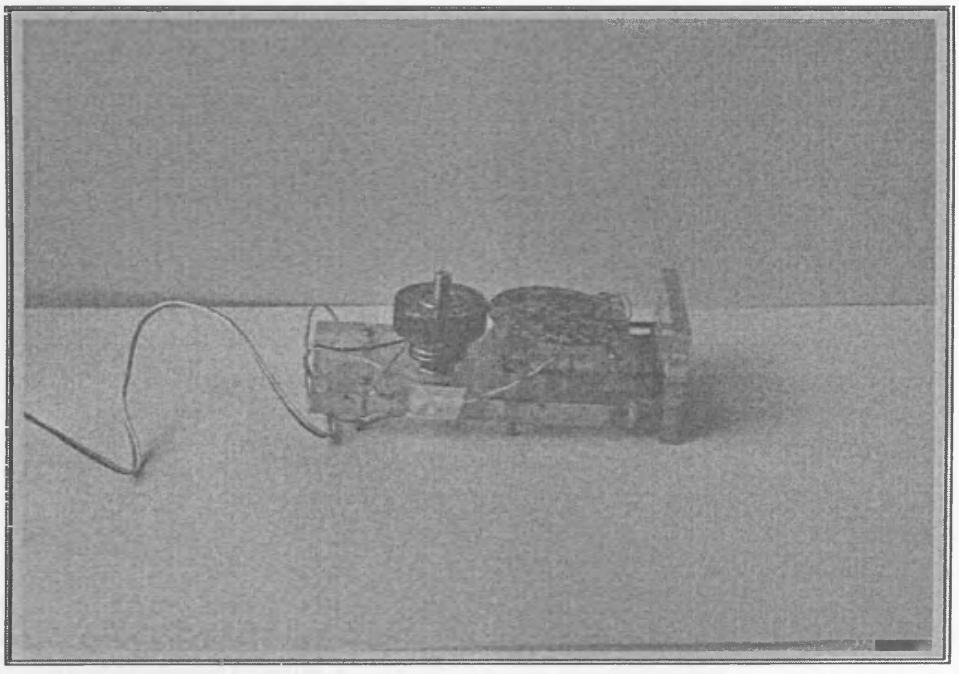

(a)

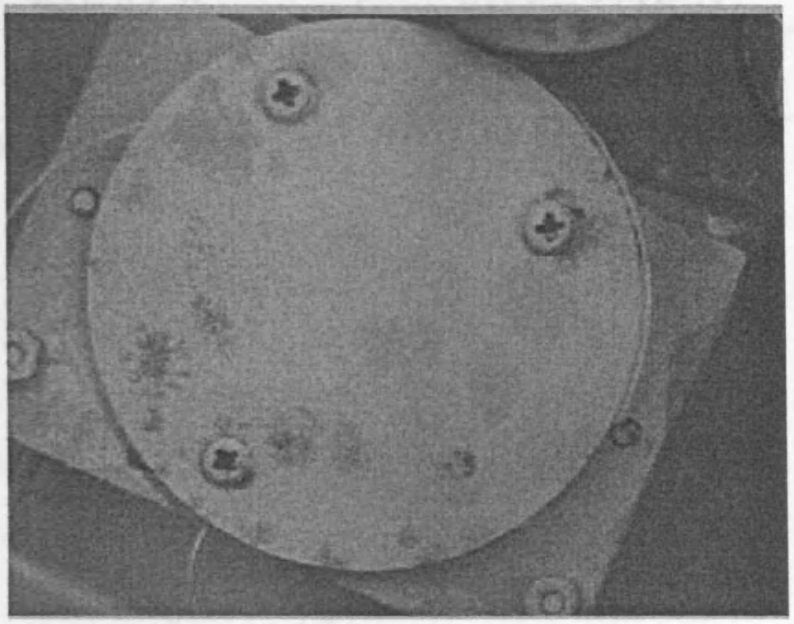

(b)

Figure 2.3. (a) Side views of the real ultrasonic motor (b) top views of the real ultrasonic stator.

Table 2.1. Parameters for constructing LEMUM.

| | Values used for motor system |
|---|---|
| Piezoelectric membrane: | |
| material | PZT-5H |
| diameter (mm) | 24.5 |
| thickness (mm) | 0.13 |
| Young's modulus | 65GPa |
| density (kg $m^{-3}$) | 7500 |
| $C_d$ ($10^3$ pF) | 77 |
| $\varepsilon_{33}^T$ | $3400\,\varepsilon_0$ |
| $s_{11}^E$ ($10^{-12}\ m^2/N$) | 16.5 |
| $s_{12}^E$ ($10^{-12}\ m^2/N$) | -4.78 |
| $d_{31}$ ($10^{-12}\ m/volt$) | -274 |
| Poisson's ratio | 0.34 |
| Metal back plate: | |
| material | Ni-alloy |
| diameter (mm) | 41 |
| thickness (mm) | 0.1 |
| Young's modulus | 170GPa |
| density (kg $m^{-3}$) | 8800 |
| Poisson's ratio | 0.35 |
| Rotor: | |
| material | steel |
| diameter (mm) | 26 |
| thickness (mm) | 16 |
| Young's modulus | 190GPa |
| density (kg $m^{-3}$) | 7850 |
| Poisson's ratio | 0.27 |

### 2.2.3 The Description of (120°-90°-150°) Simple Support Behavior on Metal Sheet

In the ultrasonic motor system, we used the type of simple support with three non-equal-triangular (120°-90°-150°), as shown in Figure 2.4, fixed points near the edge for the stator, the patent [17] was found by test and trial. The author of the dissertation also found it by test in the past. But there exists some common concept: we fixed two points "120°" and increase/decrease 30° step by step for the rest point to explain) is symmetric, so only exists radial force and no tangential force which will rotate the rotor, 120°-180°-60° will cause cancellation effect from two fixed point with 180° and the rest fixed point will not be reflected by edge, so will not occur a standing wave which forms elliptical motion for driving, as shown in Figure 2.5, and other configurations are similar to two fixed points, it shall be noted that there are at least three fixed points for a stable plate structure.

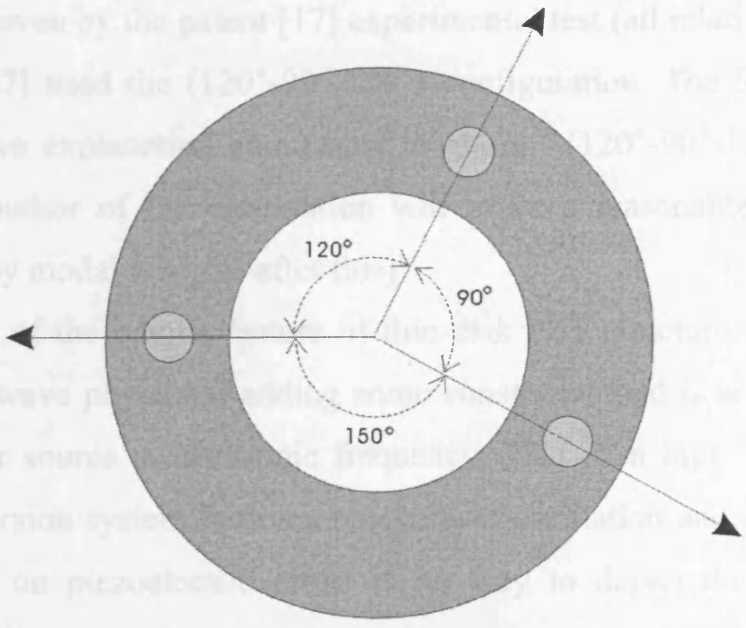


Figure 2.4. The non-equal-triangular (120°-90°-150°) boundary condition [17].

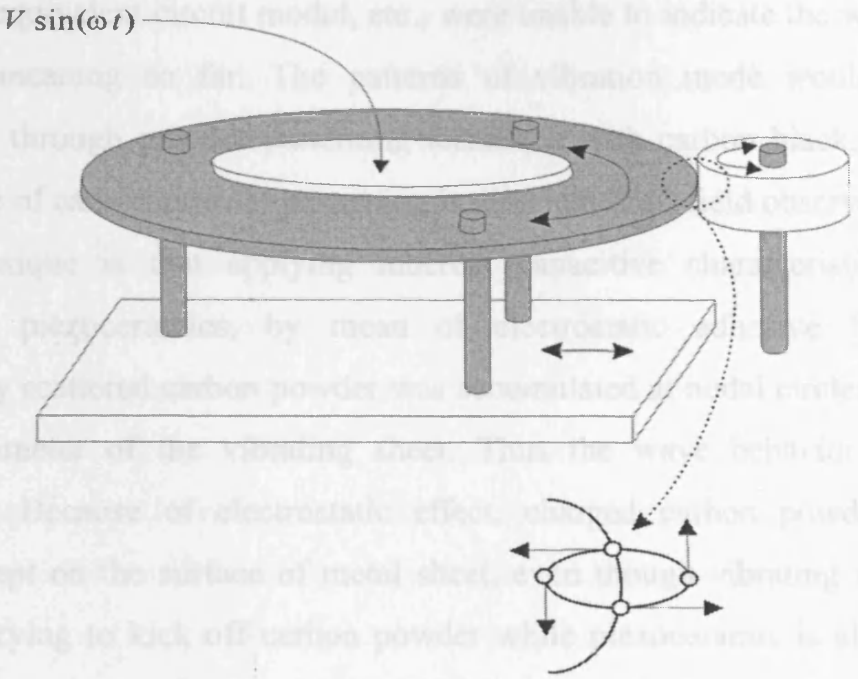


Figure 2.5. Operation expression of the ultrasonic motor.

In the past test and trial, we conclude that the motor can not be rotate by all other boundary configuration except (120°-90°-150°) configuration, it also was proven by the patent [17] experimental test (all relative reports written by [17] used the (120°-90°-150°) configuration. The followings are the relative explanation about how to chose (120°-90°-150°) from [17] (* the author of the dissertation will make a reasonable physical explanation by modal analysis after this):

Because of the unique feature of thin-disk PZT structure, it is very complicated wave physics if adding some constraints and is actuated by an AC power source at ultrasonic frequency. That is, a high frequency energy conversion system between mechanical oscillation and electricity power based on piezoelectric effect is no way to depict the physical propagation model of flexural wave, although many papers related to mathematical equations had been issued for PZT structures. But, the past experimental methods for vibration mode, such as modal testing and

analysis, equivalent circuit model, etc., were unable to indicate the whole physical meaning so far. The patterns of vibration mode would be portrayed through powder patterning technique with carbon black. The advantage of carbon powder patterning is direct and full-field observation. The technique is that applying inherent capacitive characteristic of polarized piezoceramics, by mean of electrostatic adhesive force. Uniformly scattered carbon powder was accumulated at nodal circles and nodal diameter of the vibrating sheet. Thus the wave behavior was observed. Because of electrostatic effect, charged carbon powder is always kept on the surface of metal sheet, even though vibrating metal sheet is trying to kick off carbon powder while piezoceramic is always tracking the input electric field and forced oscillation at ultrasonic frequency. Hence, wave propagation on metal sheet would be portrayed via carbon powder accumulation so that wave bands and nodal patterns would be directly observed.

Flexural wave proven by experimental patterns has useful driving mechanism. There were two vibrating direction of flexural wave: one in radial (also called in-plane) direction, another in normal (also called out-of-plane) direction. In physical textbook, out-of-plane vibration mode shapes are generally defined as a term symbol $B_{nm}$, where $n$ is nodal circle; and $m$ is nodal diameter line. But, in this study, the in-plane vibration is major consideration, vibrating in thickness direction is neglected. Ultrasonic resonant mode shapes of PZT disc-type structure will be great different to sonic mode shape of drum membrane or thin film. According to ANSYS (finite element theory will be individually discussed at Chapter 3) simulations and further experimental evidence, nodal diameter line did not appear on the vibration modes of disc-type structure when existing somewhat modified in boundary constraints. Through the boundary modification of a PZT disc-type structure; for example, edge

bounded or located harder screws on a metal disk, the specific vibration mode could be controllable. From ANSYS simulations, while a positive voltage was input, apparently a PZT thin-disk was extended forcedly in radial direction. Similarity, if negative voltage was supplied, due to converse piezoelectric effect, forced shrinkage should be occurred in the opposite radial direction. Thus, the periodical phenomenon of extended-shrunk motion was existed in radial direction while the PZT thin-disk structure was input a sinusoidal signal. At the same circumstance, nodal circles were obviously displayed due to flexural bending wave of metal sheet based on Poisson's ratio. By spot clamping at disk edge or fixed constraints on the metal disk, one desired mode shape could be appeared nearby the resonant frequency while the flexural wave propagation was influenced. One of purpose to locate the fixed screws on metal sheet as a constraint is the nodal effect and specific boundary condition. A fixed steel screw is also a reflecting point for flexural wave. In ANSYS simulations, the degree of freedom was assumed to zero at meshing nodes for the fixed screw position on a metal disk. It is composed of flexural wave from bending deformation of metal in θ (transverse) direction and from extended-shrunk deformation in $R$ (radial) direction. The vibration at the edge of metal sheet from flexural wave can therefore be used to produce the elliptical displacement motion. The different elliptical locus is decided by the combination in amplitude and phase of flexural waves. Owing to the actuating principle of ultrasonic actuators completely based on location arrangement of fixed screws, the following figures demonstrate the diverse geometric arrangement of fixed screws. Several simulations and experimental results are explained corresponding to the simulating conditions of AC power 20 $V_{p-p}$ (if for one single input driving, the input voltage can be 20V, if for sweeping input, the input voltage must be 10V due to power

limit) frequency range from 65 (* the patent [17] may use two buzzer together or add some other mechanical load, so its first driving is 65kHz, our studying the first driving is 75kHz) to 75 kHz, compound PZT thin-disk structure placed one, two, and three constraints called as (($B_m$,1)), (($B_m$,2)), and (($B_m$,3)). For easier explanation, the notation (($B_m$,$N$)) is used to catalogue the variation of vibrating modes; where $m$ is radial harmonic extended-shrunk motion, $N$ is screw amount as constraint.

(($B_3$,1)) mode: Placing one fixed screw (constraint) onto a metal disk, simulating deformed vectors were divided into three portions. That is, three separated spreads of deflection in 120° arc was constituted when 65 kHz voltage was inputted, here called as (($B_3$,1)) mode, as shown in Figure 2.6. Carbon pattern is noticed that carbon powder is roughly scattered to three 120° arc placement, but not clear, as shown in Figure 2.6(b). Thus, via one fixed screw settlement, (($B_3$,1)) mode was gradually produced at 65 kHz frequency or higher frequency.

(($B_3$,2)) mode in pitched 120 angle: At 65 kHz, nodal effect obviously appeared onto (($B_3$,1)) mode caused by one fixed screw in which a screw plays a reinforce element in structure with less flexural deformation. Later, one more fixed screw was added to an adjacent 120° position, then we called (($B_3$,2)) mode will be formed. Deformed vectors of disk still be distributed in three regions, but they are more concentrated in comparison to (($B_3$,1)) mode, as shown in Figure 2.7. From carbon powder patterns, an ultrasonic mode shape consists of three regions: powder scattered in radial direction at first, second, third region, but there was not only powder located in radial direction but also pushed in transverse component, detailed in Figure 2.7(c). Because of steel screws enhanced the sheet strength as well as limited the disk deflection, the major deformed vectors shown on the simulations were located on the

opposite 120° area, that is the rest 240° arc area. In other word, the average deformation rate of constraint area between the two screws is less than that of rest area on the metal disk, because of sheet stiffness intensified. Asymmetric flexural deformation on metal sheet was formed due to the difficulty oscillation of piezoelectric membrane and metal sheet. In contrast, the rest 240° arc area of metal sheet was inherently flexible. Thus, the extended-shrunk motion of metal sheet is large than that of constraint area (120° arc area). Furthermore, the propagation of flexural wave was interfered by screws. If screws were adequately arranged, the wave energy would be appropriately driving some objects. According to above results, although the deformation vectors of sheets were limited between two constraints, some special mode shapes could be produced through fixed screws. For instances, the deformed vectors are point to the different direction in $R$ and $\theta$ component at constraint region implied such PZT thin-disk structure that could be designed as one "edge-driving" mode as the driving torque for a rotor running in which a rotor was directly contacted to thin-disk actuator. Under well assembly with mechanical elements, it also is an excellent fundamental of rotary mechanism for an ultrasonic actuator.

($(B_3,3)$) mode in pitched 90, 120, 150 angle respectively: For guiding the wave energy concentrated in somewhere of disk edge, it is necessary to construct asymmetrically boundary conditions (constraints). The fixed screws are individually arranged in 90°, 120°, and 150° arc location. At particularly input frequency of 67 and 75 kHz, the oscillation wave on disk edge of metal sheet would appear, resulting from converse piezoelectric effect. These harmonic motions in circumference are the principal propelling basis for ultrasonic actuator. From simulations shown in Figure 2.8, at 90° arc edge region, the deformation vectors have different directions in both of radial and transverse components when the

voltage frequencies of 67 and 75 kHz were individually input. The variation of the deformation would be enlarged with the higher voltage. When a rotor is tightly against the driving point, as the frequency is at 67 kHz, the rotor will be driven to rotate in counterclockwise; as the frequency is at 75 kHz, the rotor will move in clockwise. Thus, edge contact of 90° arc region could push the rotor to turn in clockwise and counterclockwise respectively via metal sheet deflection. That is, some definite region on the metal sheet could be suitable as a driving point to rotate the movable mechanical element. For ultrasonic actuating in PZT thin-disk structure, a 3-mode is used to get a maximum lateral motion effect. The simulations of Figure 2.8 represent (($B_3$,3)) mode, one of worth modes in driving mechanism.

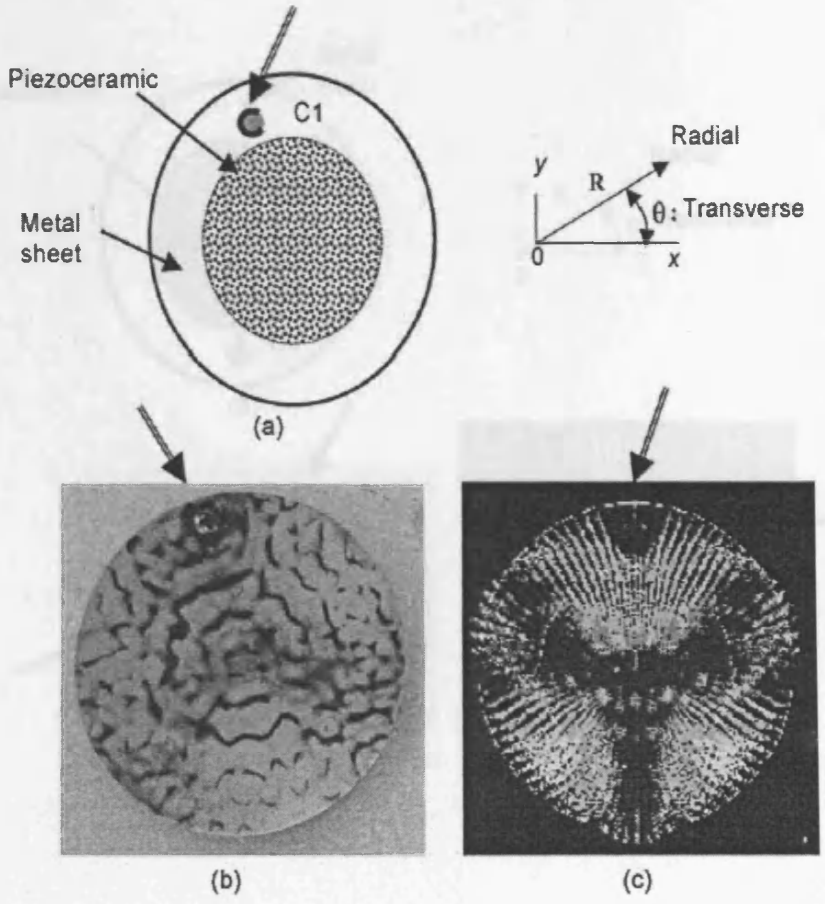


Figure 2.6. (($B_3$,1)) mode: (a) scheme with one constraint placed top location; (b) carbon powder pattern; (c) simulation at 65 kHz. Arrows point to the constraint points [17].

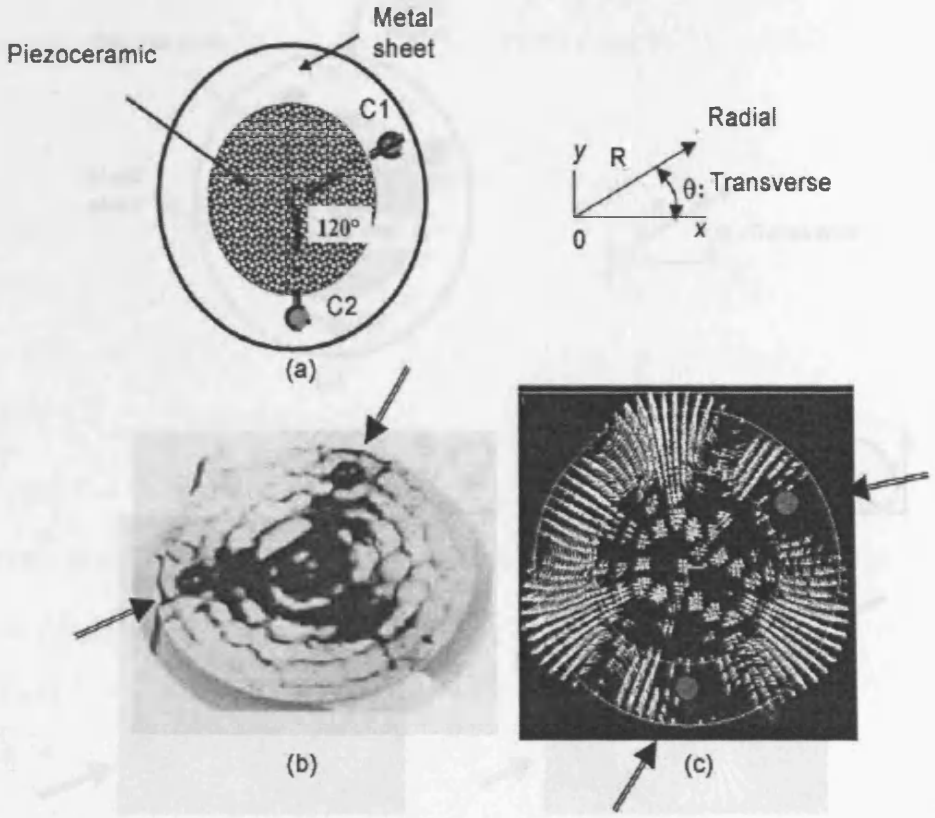


Figure 2.7. Modes of two constraints with carbon patterns and ANSYS simulations: (a) two constraints placed scheme; (b) carbon pattern; (c) deformation vectors (($B_3$,2)) mode at 65 kHz;. Arrows point to the constraint points [17].

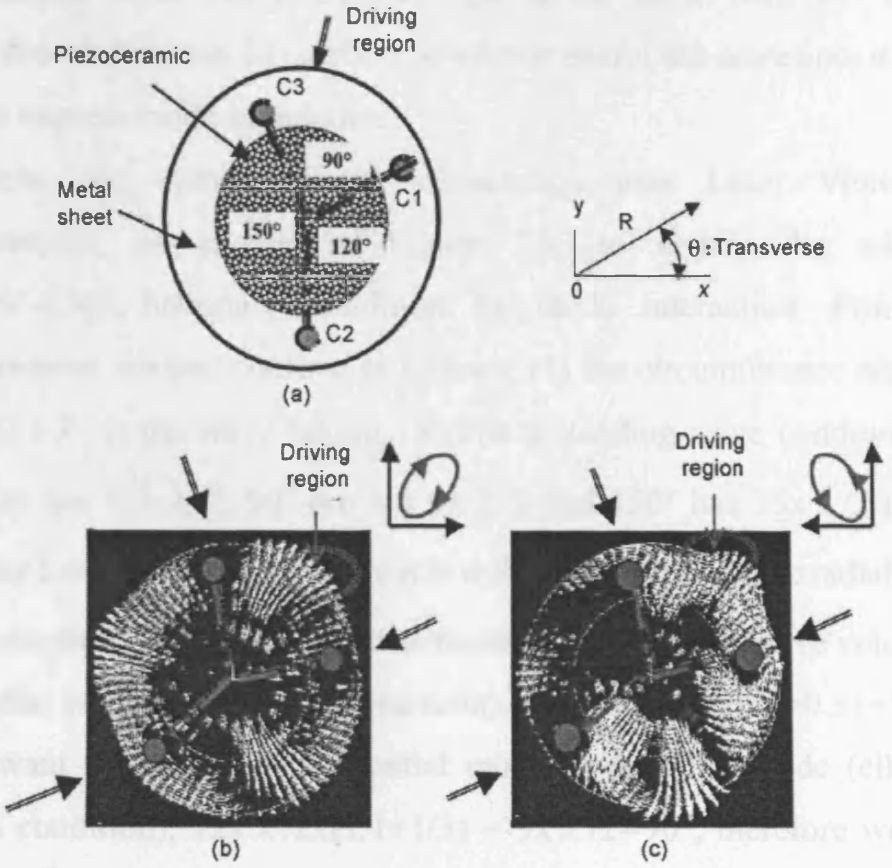


Figure 2.8. (($B_3$,3)) mode: (a) scheme with three constraints placed 90°, 120°, 150° arc location; (b) simulation at 67 kHz; (c) simulation at 75 kHz. Arrows point to the constraint points [17].

### 2.2.4 Proof of Adaptive (120°-90°-150°) Simple Support Configuration

From above the patent experiment test, we found as follows: (1) 120° arc just has radial displacement but no tangential displacement, however, 120° arc is a necessary condition for radial mode occurring (2) 90° arc has both radial and tangential displacement, apparently, 90° arc reflects radial mode (coupled from 120°) and tangential mode

(degenerated from 120°) (3) 150° arc is the same with 90° except displacement direction (4) carbon powder is useful but sometime it is not clear to express mode interaction.

Now, the author of the dissertation uses Laser Vibrometer measurement, as shown in Figure 2.9, to certify the adaptive 120°-90°-150° boundary condition by mode interaction. From the measurement, we can confirm as follows: (1) the circumference edge has 36x $\lambda/2$ ( $\lambda$ is the wave length, $\lambda/2$ is a standing-wave condition), so 120° arc has 12x $\lambda/2$, 90° arc has 9x $\lambda/2$ and 150° has 15x $\lambda/2$ (2) the diameter has 12x $\lambda/2$, apparently it is reflected from 120° arc radial mode *(3) according to wave propagation theory, the tangential wave velocity = (the radial velocity x 1/(1+Poisson ratio), and Poisson ratio =0.33=1/3, so if we want to induce the tangential mode from radial mode (elliptical motion condition), 12x $\lambda/2$x(1/1+1/3) = 9x $\lambda/2$--90°, therefore we need to has 90° arc. 120° arc and 90° arc have been confirmed, the rest arc is =360°-120°-90°=150°. So, the 120°-90°-150° for the adaptive configuration has been proven. This is for 75kHz driving frequency and its mode form is $B_{618}$ ($B_{mn}$, m is nodal circle and n is nodal line, in this case m=12/2=6, n=36/2=18), the above analysis from the patent [17] did not exactly evaluate the mode form. For the other driving frequencies, their mode form theory is similar to 75kHz, however, due to high frequency decay (see Figure A.5(b)-(c)), it is very difficult to tell the exact mode form.

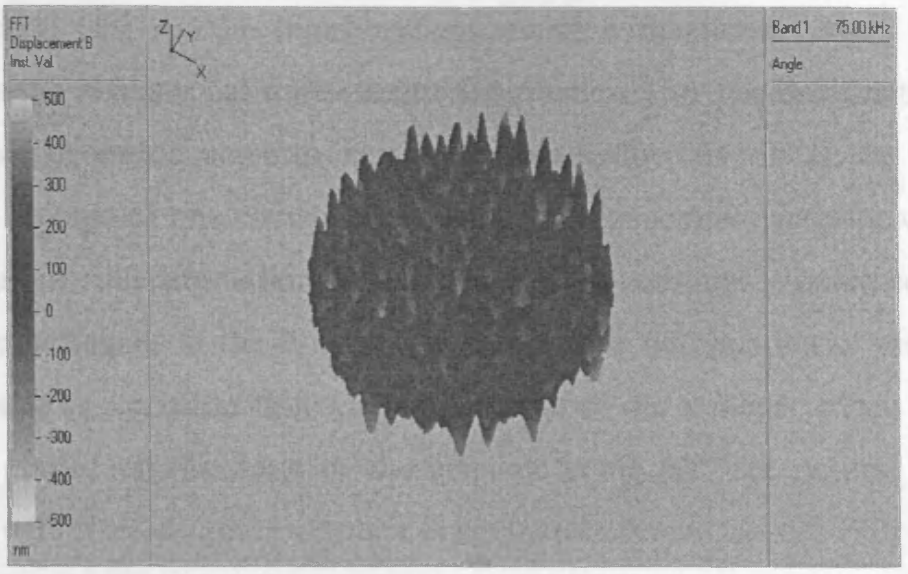


Figure 2.9. Laser Vibrometer measurement of mode interaction for proof of 120°-90°-150° configuration (it is identical to Figure A.5(a) for convenient explanation).

### 2.2.5 The principle of driving mechanism

When a periodic voltage is input, the actuator will have a periodic deformation. According to converse piezoelectric effect, the input power at positive half period or negative half period of sinusoidal voltage, then, the deformation orientation of the metal sheet is opposite. Therefore, in position voltage of one sinusoidal period, as illustrated in Figure 2.10(a), four points (i), (ii), (iii), and (iv) represent checking points for periodic deformation. When the peak–peak voltage $V_{p-p}$ ($=2V_m$) was input at 67 kHz, the periodic deformation according to the amplitude of AC power is: (i), (ii), (iii), and (iv) sequence; the deformation vectors of the ultrasonic actuator are illustrated in Figure 2.10(b). The sequence of the actuator deformation also is: (i), (ii), (iii), and (iv). Where (i) represents that the voltage is input initially ($V$=0+); (ii) represents that the input voltage is enlarged gradually ($V$=1/2$V_m$) and the piezoceramic actuator is also

deformation; (iii) As the input voltage attains a maximum value, the piezoceramic actuator has a maximum deformation; (iv) The deformation of the piezoceramic actuator is reduced gradually ($V$=1/2$V_m$). In the negative voltage of one sinusoidal period, the piezoceramic actuator was shrunk. From the simulation, at 90° arc region, actuator's outer edge would be deformed in the $R$ and θ directions. The deformation of metal edge would be variation following the change of the voltage. When the rotor is placed on the edge of the actuator being 90° arc region, the actuator will push the rotor to rotate in counterclockwise. At the 120° arc region, the deformation of the actuator is toward the two screws. At the 150° arc region, the deformation of the actuator is toward the middle portion of the two screws. From above analysis of vibrating mode through ANSYS simulations and powder patterns, it is appreciated that the displacement of the ultrasonic actuator in this study is determined according to the amplitude of the sinusoidal voltage applied to the piezoceramic. And the rotational orientation is determined by the frequency of the sinusoidal voltage. The deformation procedure for 75kHz is similar to above that of 67kHz.

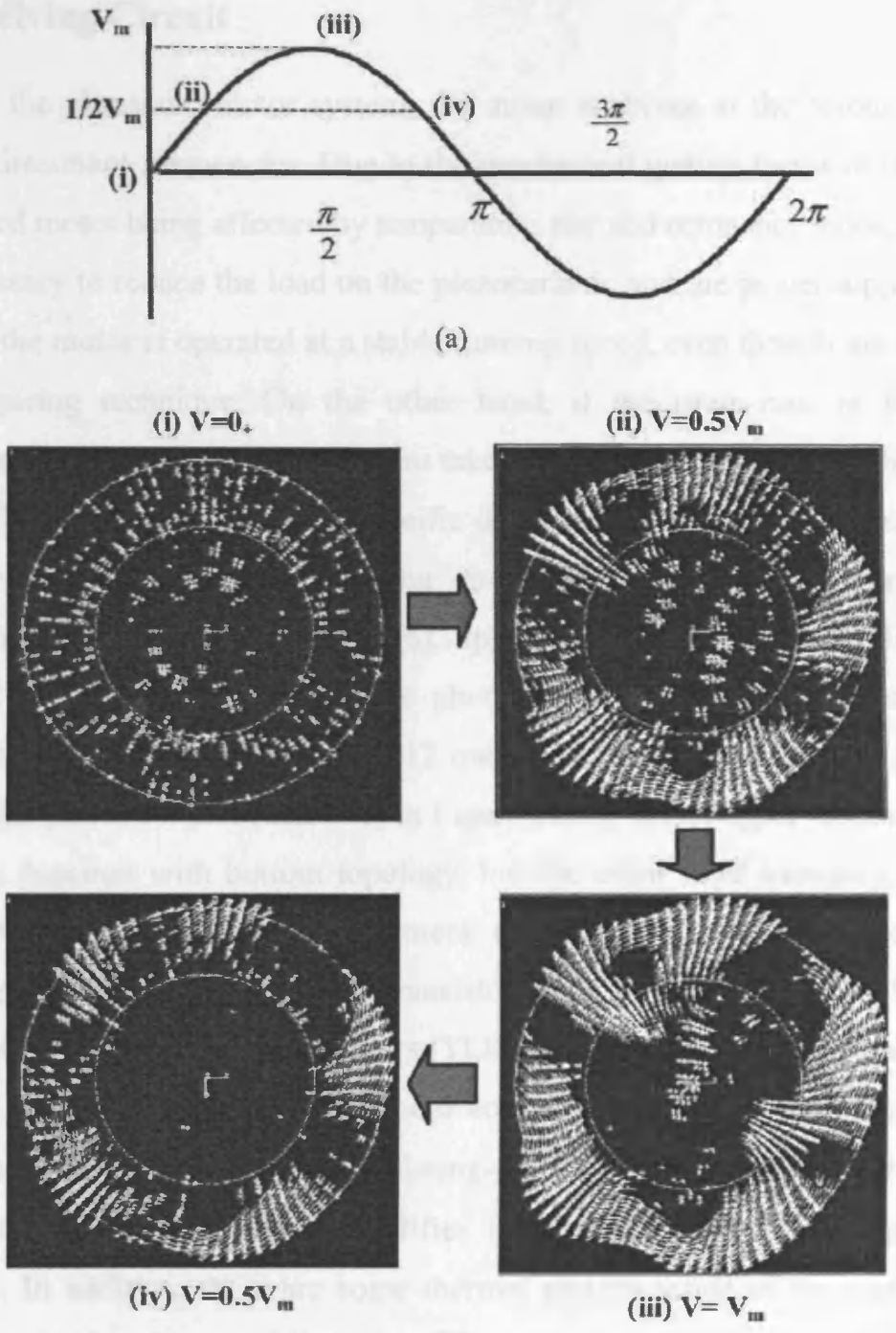


Figure 2.10. Vibration mode with ANSYS simulations of three fixed screws placed 90°, 120°, 150° arc location: (a) schematic view showing the input sinusoidal voltage; (b) simulation of a PZT actuator extending in counterclockwise (at 67 kHz) [17].

## 2.3 Driving Circuit

In the ultrasonic motor system, the motor is driven at the resonant and antiresonant frequencies. Due to the mechanical quality factor of the proposed motor being affected by temperature rise and resonance mode, it is necessary to reduce the load on the piezoceramic and the power supply so that the motor is operated at a stable running speed, even though this is a conspiring technique. On the other hand, if the rotor runs in the high-speed rotation status, we need to take into account its controllability and efficiency and therefore, a specific drive circuit is required. Figure 2.11(a)-(b) shows a specific driving circuit diagram, there are three different topologies in Figure 2.11(a), upper topology with two parallel 7812IC for providing +12V to one photo coupler (TLP250) in Figure 12(b), bottom topology with one 7812 transistor also for providing +12V to another photo coupler (TLP250) in Figure 12(b), in fact upper topology is same function with bottom topology, but the extra 7812 transistor of upper topology is just for supplement enhancement, and the middle topology with two serial 7812 transistor and 7805 transistor is for providing +5V to two photo couplers (TLP250) in Figure 12(b). In Figure 2.11(b), there are two TLP250 photo couplers for gaining high input frequency signal. So, this is an isolating-resistant type driving circuit—its source supply and signal amplifier is separated to stabilize input voltage. In addition, there are some thermal sinkers inside of the signal amplifier to dispel heat while it is running. In fact, this is an inverter single-phase AC-DC conversion driving circuit which will be applied to current controller for the speed control of the motor system in Chapter 6. The driving circuit diagram was advised by Associate Professor Dr. Guo-Shing Huang at Department of Electronic Engineering National Chin-Yi Institute of Technology Taiping, Taichung, Taiwan, and made by

the author himself.

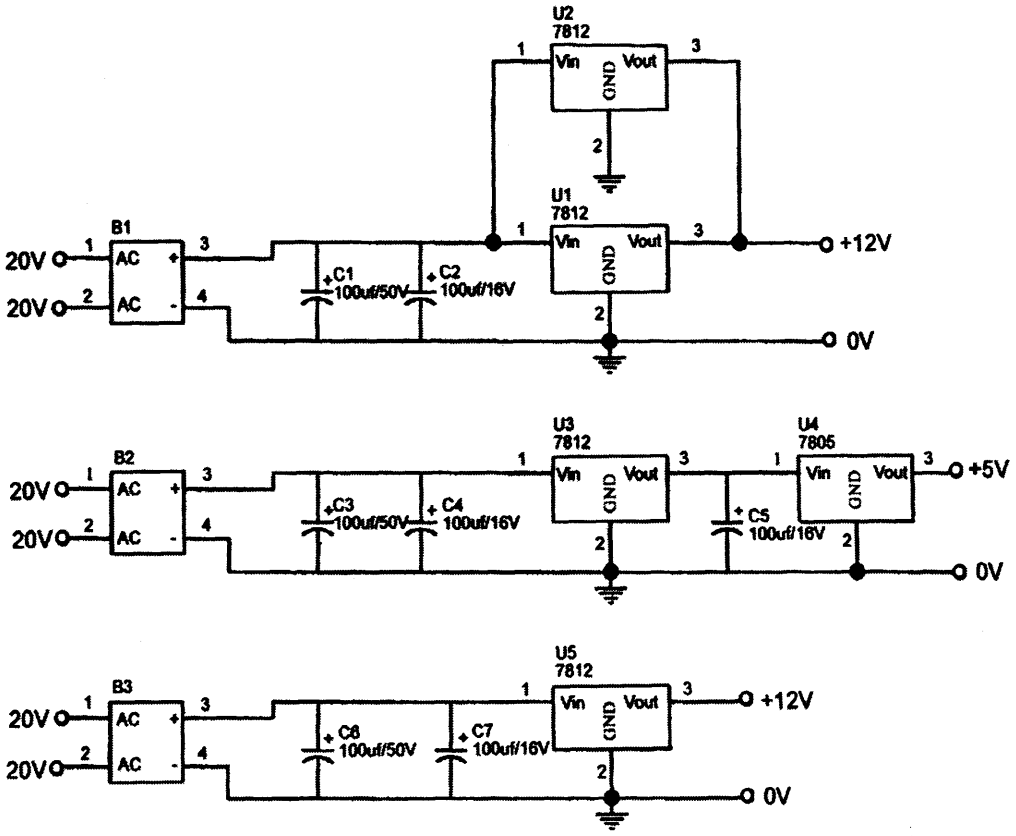


(a)

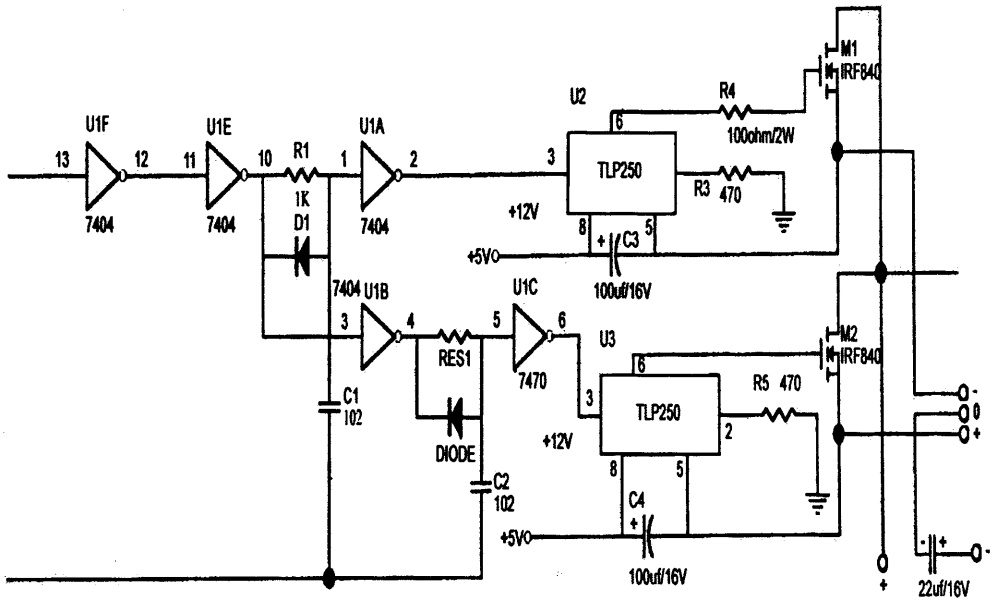


(b)

Figure 2.11. The isolating-resistant type driving circuit (a) source supply (b) signal amplifier.

## 2.4 Measured Characteristics

The new disc- type ultrasonic motor was experimentally built and measured to validate the analysis model according to Table 2.1 and the design rule. In addition to the dynamic analyzer, power meter and photometer, the laser vibrometer (the detail laser measurement is discussed at Appendix A) shown in Figure 2.11 was also used to check the analysis model. Here, the input voltage is 20V (if for one single input driving, the input voltage can be 20V, if for sweeping input, the input voltage must be 10V due to power limit).

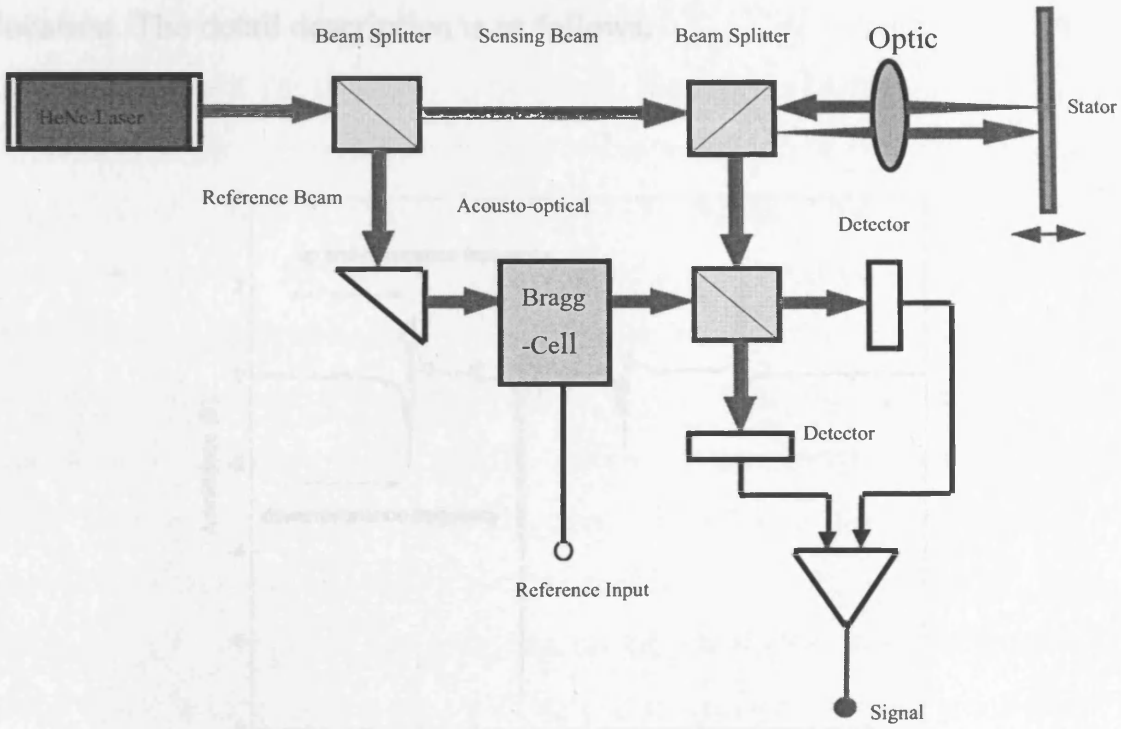


Figure 2.12. Laser vibrometer schematic view.

Figure 2.13 shows the electrical admittance response of the stator (z dir.), there is higher response near 74kHz, 84kHz, 93kHz and 103kHz from the response result. A very significant resonant response occurs close to 84kHz. These are the driving frequencies for the ultrasonic motor since the rotor can only be rotated near these frequencies, including resonant and anti-resonant frequency. Why to drive the motor at the resonant and anti-resonant frequency has been discussed at Chapter 1.3.6. However, it shall be noted that from above modal analysis and operation principle, the driving frequency is not only depended on resonant and anti-resonant frequency but also depended on mode rotation and rotor location. The detail description is as follows.

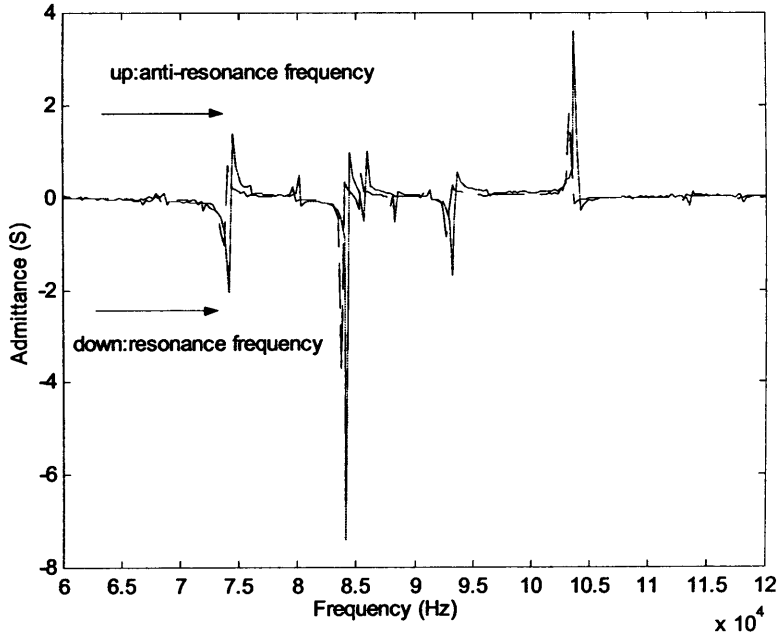


Figure 2.13. The electrical admittance response of the stator (z dir., it is identical to Figure 3.1(a) for convenient explanation).

Figure 2.14 is the phase response of the stator obtained by superposing the desired frequency range, phase degree 180° is a reference, up 180° is CW and down 180° is CWW, it shall be noted that CW and CCW depend on driving frequency, mode rotation and rotor location together, not individually. The phase response is measured from z (transverse) direction, it has no direct relation with the lateral elliptical motion direction phase (radial and tangential displacement, their phase can not be measured), however it is defined by real test inspection. For discussion the relationship between frequency and CW and CCW rotation (Figure 2.14), it has to together with discussion the relationship between contact point (rotor location) and CW and CCW rotation (Figure 2.15(a)-(c)), then we can fully understand. First, from Figure 2.15(a), the input frequency is 75kHz, the displacement vector flow (mode rotation) shows the elliptical motion direction is CCW, we fixed the rotor location on the middle of 90° arc, so the rotor rotation direction is CW (it is reverse with elliptical motion), the region of 90° arc just exists a type of displacement vector flow and 75kHz is the first driving frequency, therefore we define it as initial CW on the phase response figure. Then, from Figure 2.15(b), the input frequency is 83kHz, the displacement vector flow shows two elliptical motion directions, CW (down 90° arc area) and CCW (up 90° arc area) but no elliptical motion at the middle place (rotor location), it means that we can not rotate the rotor at 83kHz, but when we shift down to 83.13kHz, then the elliptical motion CW follows to shift to the middle place, so the rotor is rotated at CCW, therefore we define 83.13kHz as CCW, if we shift up to 85.81kHz, then the elliptical motion CCW follows to shift to the middle place, so the rotor is rotated at CW, therefore we define 85.81KHz as CW, because the second driving frequency 84kHz is arrange 83.13kHz-85kHz, it is CCW (real condition). Finally, from Figure 2.15(c), the input frequency is

98kHz, the displacement vector flow (mode rotation) shows the elliptical motion direction is CW near middle place and up 90° arc (the finite element analysis has some little difference with real condition, which 98kHz, the elliptical motion direction CW is location near the middle place, it may be mode degradation with frequency increase in real condition), so the rotor is rotated at CCW, therefore we define 98kHz as CCW, 98kHz is also the third driving frequency, if we shift up to 103kHz, then the elliptical motion CCW follows to shift to middle place, so the rotor is rotated at CW, therefore we define 103kHz as CW.

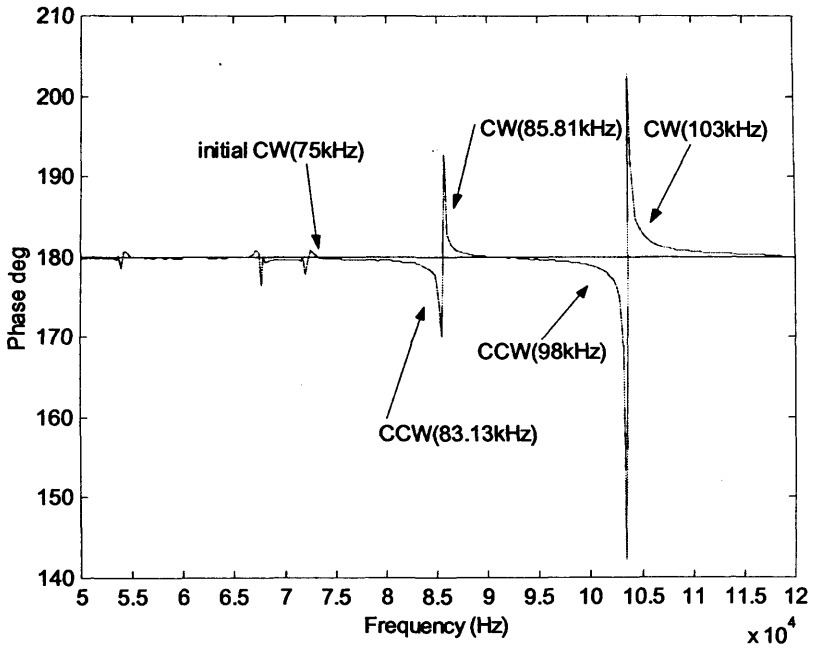


Figure 2.14. Phase response of the stator in z dir. (it is identical to Figure 3.1(b) for convenient explanation).

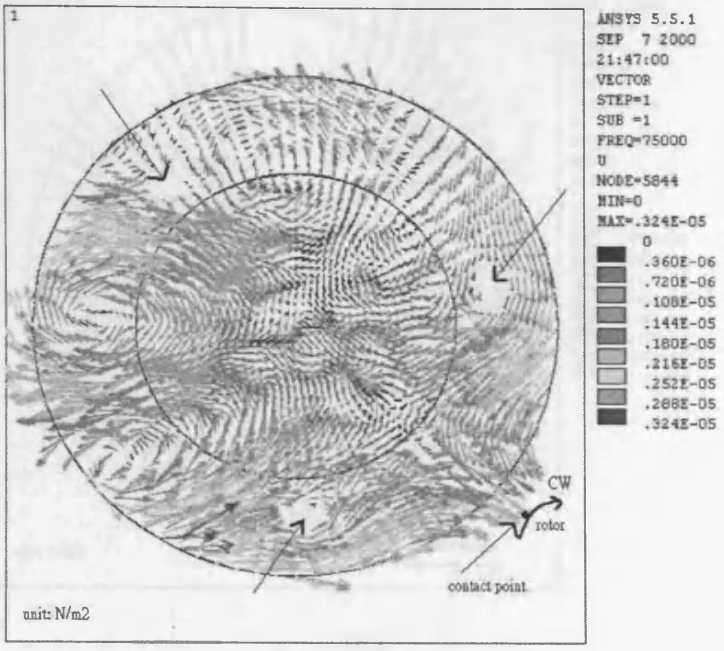
1
ANSYS 5.5.1
SEP 7 2000
21:47:00
VECTOR
STEP=1
SUB =1
FREQ=75000
U
NODE=5844
MIN=0
MAX=.324E-05
0
.360E-06
.720E-06
.108E-05
.144E-05
.180E-05
.216E-05
.252E-05
.288E-05
.324E-05
CW
rotor
contact point
unit: N/m2

(a)

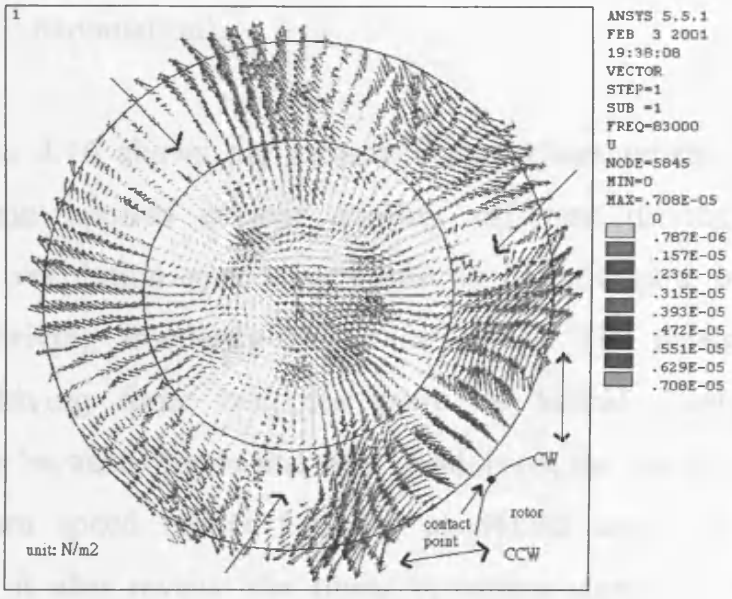
1
ANSYS 5.5.1
FEB 3 2001
19:38:08
VECTOR
STEP=1
SUB =1
FREQ=83000
U
NODE=5845
MIN=0
MAX=.708E-05
0
.787E-06
.157E-05
.236E-05
.315E-05
.393E-05
.472E-05
.551E-05
.629E-05
.708E-05
CW
rotor
contact point
CCW
unit: N/m2

(b)

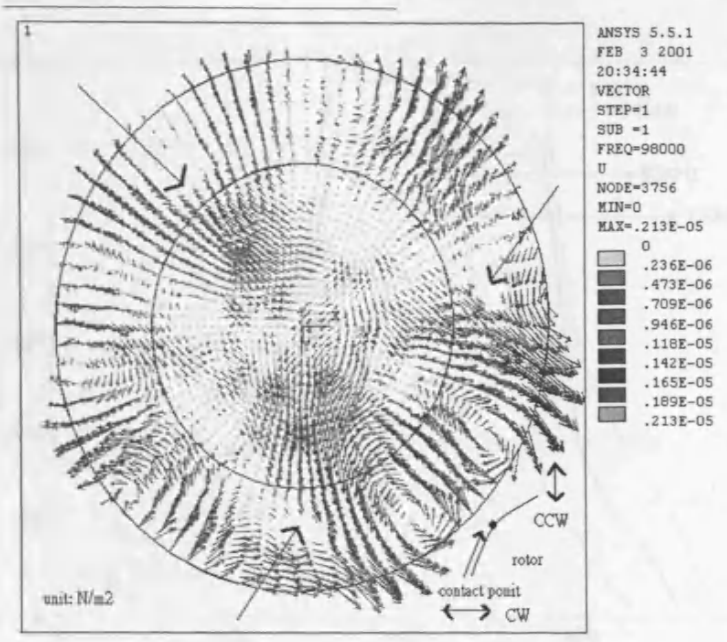


(c)

Figure 2.15. The explanation of CW and CCW on the lateral edge (a) 75kHz, (b) 83kHz and (c) 98kHz ($\rightarrow$ indicates fixed-point location, it is identical to Figure 3.6 for convenient explanation).

Figure 2.16 shows the measured load characteristic of revolution speed again applied current at four different driving frequencies. Basically, revolution speed increases as current gain increases at a constant driving frequency before saturation. The reason is that the friction driving force becomes more as lateral displacement gets amplifying because of gain increase. In addition, the result shows there is a maximum speed (about 580rpm) at 84kHz under same operation condition, it also reveals the linear operation current is about 70mA. Other characteristics of the motor will be shown and discussed next few chapters.

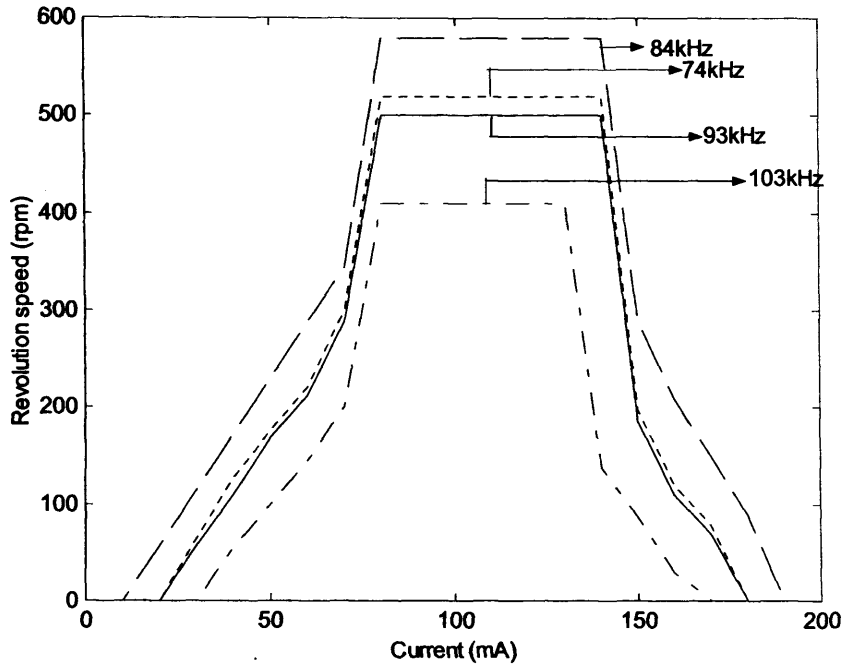


Figure 2.16. Revolution speed vs. applied current at four different driving frequencies.

# Chapter 3 Finite Element Analysis for the Ultrasonic Stator

## 3.1 Introduction

In the last few decades, a finite element method has been well developed and has become widely used in solid mechanics. Several papers address the use of this method to analyze devices fabricated from piezoelectric materials [65]-[73]. The main reasons for its use are that the finite element method is very useful for an analysis of mechanical structures with different geometry and materials and it is very useful for studying the coupling effect between the actuator and test structure [74]-[79]. A number of papers use the finite element method to analyze the characteristics of piezoelectric transducers/actuators. Most of them will be discussed in what follows.

Varadon et al. [80] presented an example where they observed an improvement of design time and cost by introducing a hybrid finite element into the simulation model of the moony transducer. The actuator and sensor function of this type transducer [81]-[83], such as the admittance spectrum and the voltage sensitivity, were acquired from finite element analysis. Lim et al. [79] reported a finite element model with Guyan's reduction scheme to deal with the transient problems of the micro-electromechanical sensor [84]. Further, Kim et al. [85] also conducted numerous studies on the numerical aspects of modeling electric boundary conditions, the treatment of electrodes as equipotential surfaces, the optimal placement of sensors and actuators on a structure and other aspects using finite element modeling. Lerch [72] studied a

simulation of piezoelectric devices using the finite element method that included time domain modeling.

Seshu [86] and Naganathan et al. [92] researched the strain transfer of extension and bending type actuation from the adhesive layer by using a two-dimensional nine-node Lagrangian finite element. The finite element method can also be employed to study the feedback control of the piezo-actuator-structure [87]-[92]. Lim et al. [87], [91] described a numerical closed loop finite element investigation of the active damping of a structure using an appropriate feedback circuit. The finite element simulations demonstrate the attenuation produced by active damping in the time domain. The model also indicates that the use of direct voltage control is more effective than charge control. In one of these papers [88], the feedback forces induced by piezoelectric actuators were taken as external forces at appropriate degrees of freedom of the structures. Varadan et al. [89] analyzed the frequency response of a beam structure with active constrained layer damper. In their study, the exciting control charge force acted on the piezo-actuator using a constant velocity for the active constrained layer damper, purely active damping and purely passive damping. Ha [90] proposed utilizing feedback voltage as the only voltage input at actuator degrees of freedom and neglect considering the electric charge on the actuator.

Bernadou and Haenel [93] dealt with the modelization of piezoelectric materials through a system of general curvilinear coordinate. They specialized these equations to the case of a piezoelectric thin shell and derived a set of two-dimensional equations formulated upon the middle surface of the shell. The equations were used to model the case of a thin shell made of a classical material actuated by several piezoelectric patches. Their research emphasizes the existence and uniqueness of solutions, approximations by finite element methods and validation

through numerical experiment. Krome and Wallaschek [94] investigated the influence of the shape of the ceramics on the vibration of the stator by using finite element methods. Their model takes into account the piezoelectric effect in the actuators as well as the exact geometry of the stator used to calculate the transfer function between the electric excitation and the mechanical vibrations of the stators. Kadokura et al. [95] proposed the simplified equivalent circuit of quartz resonators by using finite element methods. The clamped capacitance, the motional inductance and the capacitance were also calculated using finite element analysis. Kim et al. [96] proposed a hybrid element method using 3D elements for the piezoelectric device region to obtain sufficient detail, i.e., plate elements for the structure to reduce numerical stiffening, and developed transition elements at the interface of 3D piezoelectric elements and plate elements. Boucher et al. [97] proposed a three-dimensional finite element method for the determination of the eigenmodes of vibration in piezoelectric transducers. They promoted the computation accuracy by introducing piezoelectricity as perturbation.

Kagawa et al. [98] presented a piezoelectric three-dimensional finite element code including transient response calculations to simulate the dynamic behavior of ultrasonic motors and actuators. The time response was solved by using the Nemark- $\beta$ integration scheme. Fung and Tseng [99] proposed a new hybrid Laplace transform/finite element method to solve the dynamic problems of bimodal ultrasonic motors excited by longitudinal and flexural modes. The new hybrid Laplace transform/finite element method can greatly increase the simulation speed for the variational principle. Sze and Pan [100] employed hybrid variational principles for piezoelectric finite element formulation. They used hybrid eight-node hexahedral finite element models in electric displacement, stress and coupled displacement- stress formulations. Following up Allik

and Haghes [65], all of the authors [101]-[108] who later performed research in this area presented their finite element models including displacement and electric displacement derived from displacement and electric potential. However, the number of field variables cannot be further reduced, i.e., they are irreducible. The irreducible piezoelectric elements are often too stiff and are susceptible to mesh distortion and aspect ration. Tzou [109]-[111] made use of bubble/incompatible displacement modes to improve the eight-node hexahedral element and triangle shell element. Pian and Tony [112] and Yang [113] successfully used the bubble/incompatible displacement method of hybrid variational principles to enhance the element accuracy and circumvent various locking phenomena. Using the research of Allik and Hughes as a guide, Ghandi and Hagood [114] proposed a piezoelectric hybrid tetrahedral finite element model where electric displacement, electric potential and displacement are assumed. Their model is markedly superior to the irreducible model.

The authors of [77] used the finite element method to study the dynamic characteristics of a piezoceramic disc. In their research, the electrical term was considered as an extra mechanical degree of freedom for solving the eigenvalue problem. Then a modal analysis using the Lanczos method was run to acquire steady-state response functions such as vibration modes and natural frequencies in mechanical response and electrical impedance function. In this case, $r$ modes were the majority of types considered. However, this research focused on transducer application. Meanwhile, an adhesive layer under the piezoceramic disc such as a metal back-plate was not included in the finite element analysis. In our study, we referred to this analysis model for the piezoelectric membrane and considered the adhesive metal plate. The piezoceramic itself served as an actuator in our case.

A finite element analysis of the stator (actuator) is very important for the disc-type ultrasonic motor [78] because it will be able to offer us some information such as possible driving frequency and rotational direction of the motor. To make the analysis clear, before the analysis of the stator, we shall review the motor, as shown in Chapter 2, the schematic view of the motor. It includes the disc-type piezoelectric ultrasonic stator, a rotor, a movable base and a driving function.

The motor characteristics focus on the lateral force motion of the stator and a single contact point, which is totally different from all of the other proposed ultrasonic motors. To express the operational principle of the motor, a simple support condition with three nonequal-triangular (120°-90°-150°) [17] fixed points near the edge of the stator was used. Tthere exists some common concept: we fixed two points "120°" and increase/decrease 30° step by step for the rest point to explain) is symmetric, so only exists radial force and no tangential force which will rotate the rotor, 120°-180°-60° will cause cancellation effect from two fixed point with 180° and the rest fixed point will not be reflected by edge, so will not occur a standing wave which forms elliptical motion for driving, and other configurations are similar to two fixed points, it shall be noted that there are at least three fixed points for a stable plate structure. In the past test and trial, we conclude that the motor can not be rotate by all other boundary configuration except (120°-90°-150°) [17] configuration, the detail about investigation of location has been discussed at Chapter 2. When a sinusoidal input is applied to the stator, it induces a lateral elliptical motion and generates a torque to rotate the rotor. The mechanical design of the stator will enlarge the lateral elliptical motion between two fixed points with a 90° included angle. The desired vibration modes can be concentrated at 75kHz, 83.13kHz and 98kHz [see Figure 3.1], respectively.

The study aim of this chapter is to establish the dynamic model of the new piezoelectric ultrasonic stator by the finite element method: modal analysis and harmonic analysis, then evaluates its response characteristics, including electrical impedance response, phase response and mechanical frequency response. These modal shape patterns are also acquired through them. Some experiment measurements were made by the dynamic analyzer and the laser vibrometer to check the predicted results. These analysis results would be a good reference for future work on a more advanced design of a new disc-type piezoelectric ultrasonic motor.

## 3.2 Finite Element Model

The finite element theoretical derivation was carried out by commercially available finite element (FEM) ANSYS5.51/ Multiphysics software, which provides structure analysis with piezoelectric effect. The simulating model consists of eight-nodes SOLID5 structure element to model the elastic-metal-back plate and coupling element for a piezoelectric membrane. In ANSYS software, the SOLID5 structure element with four degree of freedom at each node is solved for the nodal displacement in X, Y, and Z axes plus electrical potential (see Introduction to ANSYS for Revision 5.51 and Dynamics User's Guide for Revision 5.51). Under fitting mechanical and electrical boundary conditions, ANSYS FEM code to get the relative simulation graphs of displacement, stress and electrical potential for the elastic-metal-back plate and piezoelectric membrane. The detail finite element theoretical derivation is described as follows:

### 3.2.1 The Formulae

A circular piezoelectric ceramic is bonded to the disc structure with an optima boundary condition, which forms the piezoelectric actuator. Shear forces are transferred to the disc when voltages are applied to the surface of the circular piezoelectric ceramic. Furthermore, except for dielectric stiffness it will induce the added stiffness, called piezoelectric stiffness, and the modal force. The linear constitutive equation expressing the coupling between the elastic field and the electric field for the piezoelectric actuator will be given by [79]

$$\begin{aligned} T &= C^E S - e^T E \\ D &= eS + \varepsilon^S E \end{aligned}, \tag{3.1}$$

where $T$: 6x1 stress-vector, $D$: 3x1 electrical displacement vector, $S$: 6x1 strain vector, and $E$: 3x1 electrical field vector respectively, $C^E$: 6x6 elasticity matrix, e: 3x6 piezoelectric matrix and $e^T$ is its transpose, and $\varepsilon^S$: 3x3 dielectric matrix.

The electric field $E$ is related to the electric potential $\phi$ by $E = -\nabla\phi$. The displacement and potential for each element can be expressed, respectively, as

$$\begin{aligned} u &= N_u \hat{u} \\ \phi &= N_\phi \hat{\phi} \end{aligned}, \tag{3.2}$$

where $u$ is the displacement vector, $N_u$ and $N_\phi$ the interpolation function for the variables of $\phi$ and $u$, and ^ denotes the nodal values.

To put the strain-displacement relation in terms of the nodal displacement yields $S = B_u \hat{u}$. Here, $B_u$ is the product of the differential-operating matrix relating $S$ to the shape function matrix $N_u$. Similarly, let $E = -\nabla\phi = -\nabla N_\phi \hat{\phi} = -B_\phi \hat{\phi}$ [87].

In this chapter, we use the finite element method to study the

different aspects of behavior in the piezoelectric stator. In this code, a multi-field solid element and a standard isotropic solid element are involved in modeling the piezoelectric ceramic and disc base, respectively. They are both eight-node brick elements and three spatial degree nodal displacements for the degrees of freedom. In addition, each node has voltage as an extra degree of freedom in the multifield elements.

The governing dynamic equation of the new disc-type piezoelectric stator in matrix form for the piezoelectric ceramic phase [65] is as follows:

$$\begin{aligned} &M^p\ddot{u}^p + K_{uu}^p u^p + K_{u\phi}^p \phi = F^p \\ &K_{u\phi}^p u + K_{\phi\phi}^p \phi = P \end{aligned}, \tag{3.3}$$

where $M^p$, $K_{uu}^p$, $K_{u\phi}^p$, $K_{\phi\phi}^p$, $F^p$ and $P$ are mass matrix, elastic stiffness matrix, piezoelectric coupling matrix, dielectric stiffness matrix, mechanical force vector and electrical charge vector, respectively. The superscript p denotes the piezoelectric ceramic. These relative substitutive variables are given, respectively, by:

$$\begin{aligned} M^p &= \int \rho N_u^T N_u dV, \\ K_{uu}^p &= \int B_u^T C^E B_u dV, \\ K_{u\phi}^p &= \int B_u^T e^T B_\phi dV, \\ K_{\phi\phi}^p &= -\int B_\phi^T b^s B_\phi dV, \\ F^p &= \int_V N_b^T f_b dV + \int_{S_1} N_{S_1}^T f_S dS_1 + N_u^T f_c, \\ P &= -\int_{S_2} N_{S_2}^T q_S dS_2 - N_\phi^T q_c, \end{aligned} \tag{3.4}$$

where $f_b$ is the body force, $f_s$ is the surface force, $f_c$ is the concentrated force, $q_s$ is the surface charge, $q_c$ is the point charge, $S_1$ is

the area where mechanical forces are applied and $S_2$ is the area where electrical charges are applied.

For the disc base, the electrical effects are ignored and the finite element equation is given by:

$$M^s\ddot{u}^s + K_{uu}^s u^s = F^s, \tag{3.5}$$

where the superscript s denotes the disc. In general, all structures are slightly damped due to structure damping. Thus, equation (3.3) and (3.5) can be modified to

$$\begin{aligned} &M^p\ddot{u}^p + C^p\dot{u}^p + K_{uu}^p u^p + K_{u\phi}^p \phi = F^p \\ &K_{u\phi}^p u + K_{\phi\phi}^p \phi = P \end{aligned} \tag{3.6}$$

$$M^s\ddot{u}^s + C^s\dot{u}^s + K_{uu}^s u^s = F^s, \tag{3.7}$$

where $C^p = \eta M^p + \lambda K_{uu}^p$ and $C^s = \eta M^s + \lambda K_{uu}^s$ [79], where $\eta$ and $\lambda$ are Rayleigh coefficients. It shall be noted that the damping matrix in ANSYS implements, $C = \beta^p K_{uu}^p + \beta^s K_{uu}^s$ where $\beta^p$ and $\beta^s$ are the damping coefficients associated with piezoelectric ceramic and disc material, cannot model dielectric losses but does not allow the two attenuation mechanisms to differ due to being normally insignificant to structural damping. To evaluate the influence of damping loss, harmonic analysis was run to predict the electrical impedance of the stator as a function of frequency. Harmonic analysis (ANSYS code) allows incorporation of loss within a medium by use of damping factors for any operating frequency. The damping is usually adjusted following the experimental test until a reasonable match is found.

The electric field boundary condition requires that the electrode surface is an equipotential one and the summation of the nodal electric charges on it should be zero as shown in the following:

$$\hat{\Phi}_i = \hat{\Phi}_{i+1} = \ldots = \text{constant} \quad \text{or} \quad \sum Q_i = 0. \tag{3.8}$$

The adhesive layer between the piezoelectric ceramic and the disc base will be ignored in the finite element analysis.

### 3.2.2 Analysis

To analyze the steady-state response characteristics of the new disc-type piezoelectric stator, first modal response analysis has to be made to determine the mode shape and the natural frequency of the piezoelectric stator. In modal analysis, it should be noted that the extra voltage degrees of freedom in the finite element equation have to be condensed using Guyan reduction. Then the modal frequencies and associated mode shapes can be found using Householder-Bisection inverse iteration. Additionally, because the electrical degrees of freedom do not have mass associated with them, the mass matrix may not be positive definite and the stiffness matrix would be non-positive definite due to the negative dielectric.

When the eigenequations are solved using modal analysis, the steady-state characteristics can be analyzed using the eigenvalues. First the electrical frequency response can be obtained in eigenvector form as follows:

$$\frac{P}{\phi} = -\sum_{r=1}^{N} \frac{H_r^2}{\omega_r^2 - \omega^2} + H_{gg} \ . \tag{3.9}$$

The substitutive variables $H_r$ and $H_{gg}$ are given by

$$H_r = K_{u\phi}^T K_{uu}^T \tag{3.10}$$

$$H_{gg} = K_{\phi\phi}^p - K_{\phi u}^{p\,T} K_{uu}^{p\,-1} K_{\phi u}^p \ . \tag{3.11}$$

In this case, $\phi$ is the electrical potential of the electrode on the top surface of the piezoelectric ceramic.

If damping is considered, (3.9) becomes as the following:

$$\frac{P}{\phi} = -\sum_{r=1}^{N} \frac{H_r^2}{\omega_r^2 - \omega^2 + iC\omega_r} + H_{99}, \tag{3.12}$$

where $C = C^p + C^s$. Using (3.12) and differentiating the electrical charge, the electrical impedance response is obtained as follows:

$$Z(\omega) = \phi / i\omega P. \tag{3.13}$$

Meanwhile under voltage excitation, the mechanical frequency response can also be obtained as follows:

$$\frac{u_r}{\phi} = -\sum_{r=1}^{N} \frac{H_r}{\omega_r^2 - \omega^2}. \tag{3.14}$$

If the damping term is included, (3.14) becomes the following:

$$\frac{u_r}{\phi} = -\sum_{r=1}^{N} \frac{H_r}{\omega_r^2 - \omega^2 + iC\omega_r}, \tag{3.15}$$

where subscript $r$ denotes $r$-th mode of the stator. In this study, the lateral elliptical motion is mainly used so the radial direction response is mainly considered.

## 3.3 Results and Discussions

According to these methods developed above, we can analyze the vibration characteristics of the piezoelectric ultrasonic stator. Using (3.13) and (3.15), we can search the possible types of resonant and antiresonant modes of the new disc-type piezoelectric stator in the desired frequency range. But we can also predict the possible natural frequencies that may be driving frequencies to rotate the rotor. In this study, all steady-state response analyses will be added to the structure damping, that is, $\eta$ and $\lambda$. We assumed $\eta = 7.5$ and $\lambda = 2 \times 10^{-5}$ [79], internal damping and

Poisson's ratio of the passive metal disc base influence the damping loss of the ultrasonic stator considerably. To make reasonable correction between theory and experiment, the surface displacement was measured using a laser vibrometer system and the damping was maintained constant for the stator material during supplementary theoretical analysis. The soft metal disc base with almost unimodal behavior usually is predicted quite well by the finite element theory. Additionally, we defined the boundary condition of the piezoelectric ultrasonic stator as a simple support condition with three nonequal-triangular (120°-90°-150°) fixed points near the edge. Then we used ANSYS code to run all response analyses.

To test the accuracy of the finite element model, we used the dynamic analyzer to make the relative experiment measurement within the desired frequency range. Then we made a comparison between these experimental results regarding electrical impedance response and mechanical frequencies with the analysis values from the theoretical model. Figure 3.1(a) shows the electrical impedance responses from analysis and experimental results, the detail has been discussed at Chapter 2. Figure 3.1(b) is the phase response of the stator obtained by superposing the desired frequency range, phase degree 180° is a reference, up 180° is CW and down 180° is CWW, it shall be noted that CW and CCW depend on driving frequency, mode rotation and rotor location together, not individually. The phase response is measured from z (transverse) direction, it has no direct relation with the lateral elliptical motion direction phase (radial and tangential displacement, their phase can not be measured), however it is defined by real test inspection. For discussion the relationship between frequency and CW and CCW rotation (Figure 3.1(b)), it has to together with discussion the relationship between contact point (rotor location) and CW and CCW rotation (Figure 3.6(a)-(c)), the detail has been discussed at Chapter 2. Figure 3.2 shows

the mechanical response (z dir.) from the analysis and experimental results, the applied voltage (10V) is fixed for all of the desired frequency ranges, and the place of measurement is located around the circumferential (90° included angle section) edge. It reveals that second-harmonic waves occur between 70-120kHz and wave mixtures are concentrated upon this region. The major reason is that the three nonequal-triangular (120°-90°-150°) fixed points induce standing waves but let traveling waves generated from the input signal be partly reflected and mixed near the stator edge.

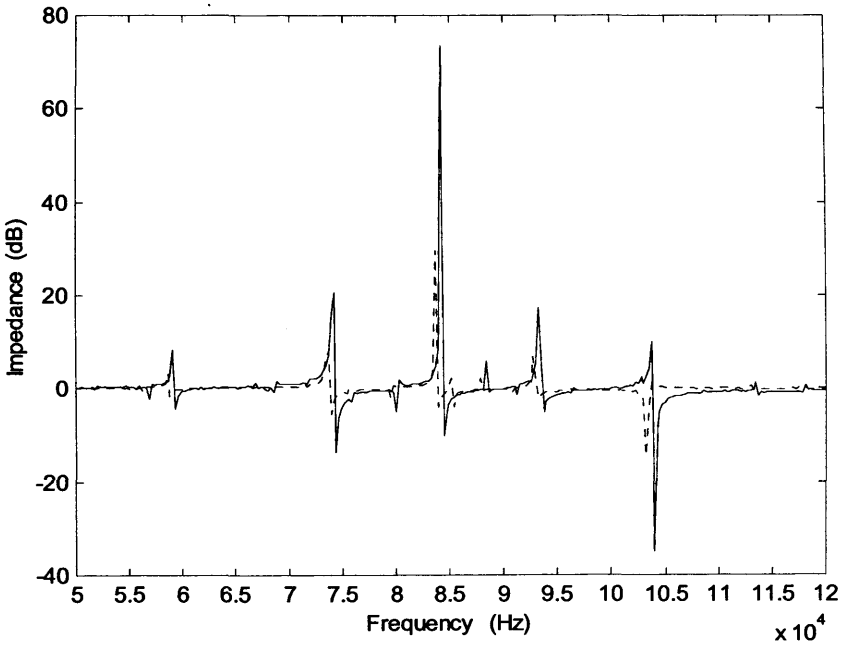


(a)

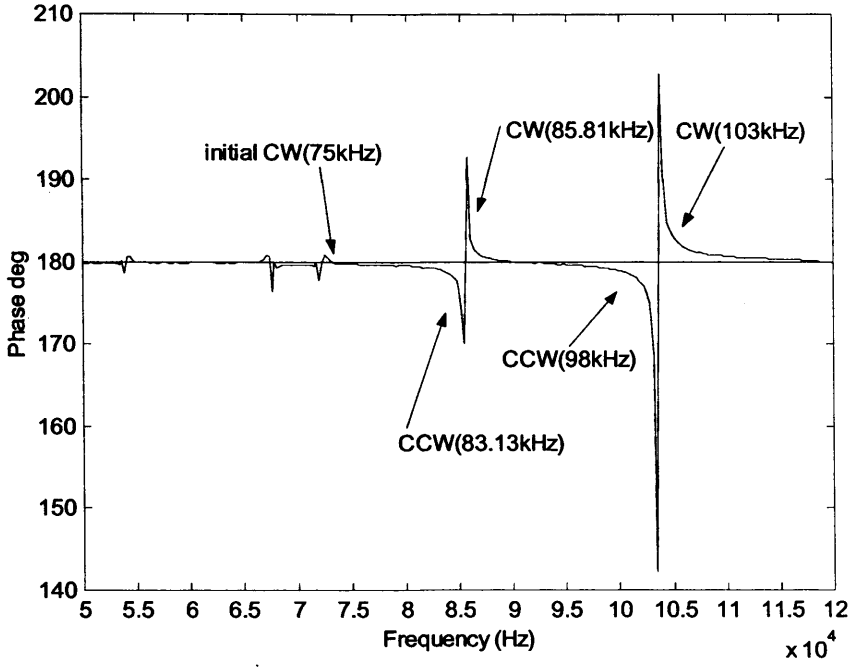


(b)

Figure 3.1. (a) The electrical impedance response from analysis and experimental results (—, experiment; ---, analysis), and (b) The phase response.

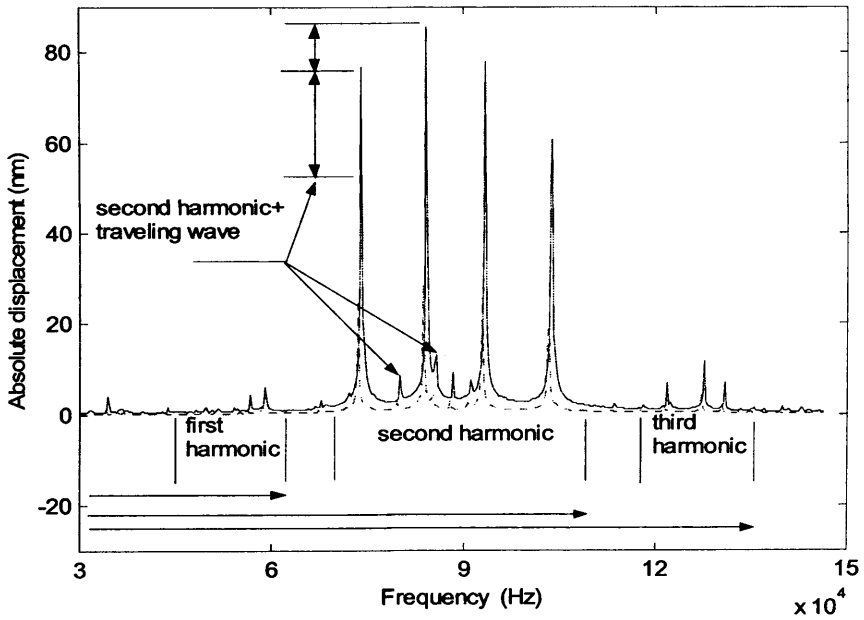


Figure 3.2. The mechanical response (z dir., 10V input voltage) from analysis and experimental results (—, experiment; ---, analysis).

To check the 3-D dynamic displacement profile, an experimental set-up was arranged. Figure 3.3 is a laser vibrometer set-up schematic. The 3-D displace profile, frequency response and phase response can be acquired from the measurement. Figure 3.4(a)-(c) contains the measurement results under a 20V input signal at 75kHz, 83.13kHz and 98kHz, respectively. Furthermore, harmonic analyses were run at the same frequency and applied voltage. Figure 3.5(a)-(c) is the analysis results at the same frequencies and input signals. The displacement patterns from Figure 3.4(a)-(c) and Figure 3.5(a)-(c) are obtained from the vertical direction (z. dir.). They show very similar displace patterns to each other. The finite element model has been approved to be correct from the comparisons.

To clarify that the mechanism of the piezoelectric ultrasonic stator is adaptive for the best output performance of the ultrasonic motor, we ran an analysis of displacement vector flow at its lateral edge for a 75kHz, 20V input signal. Figure 3.6(a)-(c) shows that lateral elliptical motions are induced at the stator edge, and that they confirm the operation principle in Chapter 2. The maximal displacement around the edge occurs in a 90° included angle section. It is the optimal output location for rotating the rotor. The results of the mode shape in Figure 3.7(a)-(c) (75kHz, 20V) show that the standing waves are compassed between two fixed points. They can be checked using a 3D displacement profile with a laser vibrometer [see Figure 3.8]. Here, 75kHz was used just for explanation. It shows that maximal and steady energy exists at the stator edge. Figure 3.9(a)-(e) shows the z direction displacement profile under harmonic excitation. The exciting frequencies are at an audible frequency range of 1k-20kHz. Compared with Figure 3.5(a)-(c), the results reveal that the stator has no significant standing wave that exists, especially at

the stator edge. As we know, the standing wave transfers most driving energy into the rotor. However, obviously there is not much useful transformational energy at an audible frequency range. So, the proposed motor cannot operate at an audible frequency range. The authors of [119] indicate that their motor (axial rotor) can be driven at 3.5kHz. Figure 3.10(a)-(e) shows the displacement vector flow under audible frequency driving at 1k-20kHz. The results show that there is no lateral elliptical motion that exists. It proves again that audible frequency is not adaptive for LEMUM. Figure 3.11 shows the z direction displacement profile under lower ultrasonic frequency excitation: 35kHz, 45kHz, 55kHz and 65kHz. The results show that there are more significant standing waves that exist at lower ultrasonic frequency driving. There is a more stable and a more dense standing-wave pattern at 65kHz. Figure 3.12 shows the displacement vector flow under lower ultrasonic frequency excitation: 35kHz, 45kHz, 55kHz and 65kHz. Lateral displacement motions have become very significant at 55kHz and 65kHz. However, the maximum lateral motions are not located in the 90° included angle section. The lateral displacement patterns are much more non-uniform at 55kHz and 65kHz than at 75kHz, 83kHz and 98kHz. In a real test, the proposed motor can be driven at 45kHz, 55kHz and 65kHz using the isolating-resistant type driving circuit described in Chapter 2. However, the vibration patterns at 45kHz, 55khz and 65kHz can be acquired from the laser vibrometer due to input voltages being limited using the isolating-resistant type driving circuit and in contrast, input signals being too weak without the driving circuit. Therefore, we can conclude that the stator will be able to drive the rotor, at least, at 75kHz, 83kHz and 98kHz.

By modeling the dynamic formulary of the new disc-type piezoelectric stator in the finite element method, the eigenvalue can be obtained. The electrical term is treated as an extra mechanical degree of

freedom. The mechanical responses are exactly acquired under constant voltage excitation and the electrical impedance response. An experimental measurement was also made to verify the response characteristics of the new disc-type piezoelectric stator formulated by the finite element analysis.

It has been shown that the theoretical model is very exact in examining the piezoelectric influence on a disc-type piezoelectric ultrasonic stator. It has great potential to serve as a design guideline for possible use in practical stator design, especially in the stator of an ultrasonic motor using its lateral elliptical motion. Boundary condition design is the successful key because it will induce a standing wave but let travelling wave be partly reflected and mixed. It is very helpful in rotating the rotor.

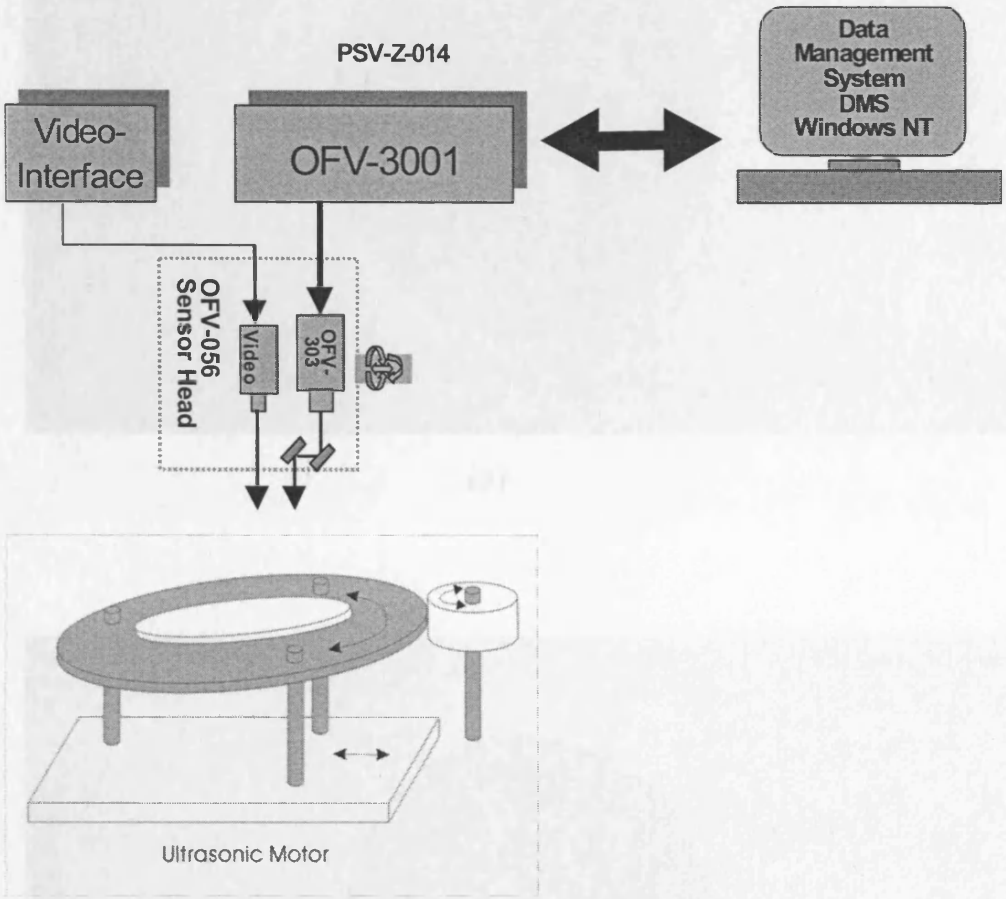


Figure 3.3. Laser vibrometer configuration.

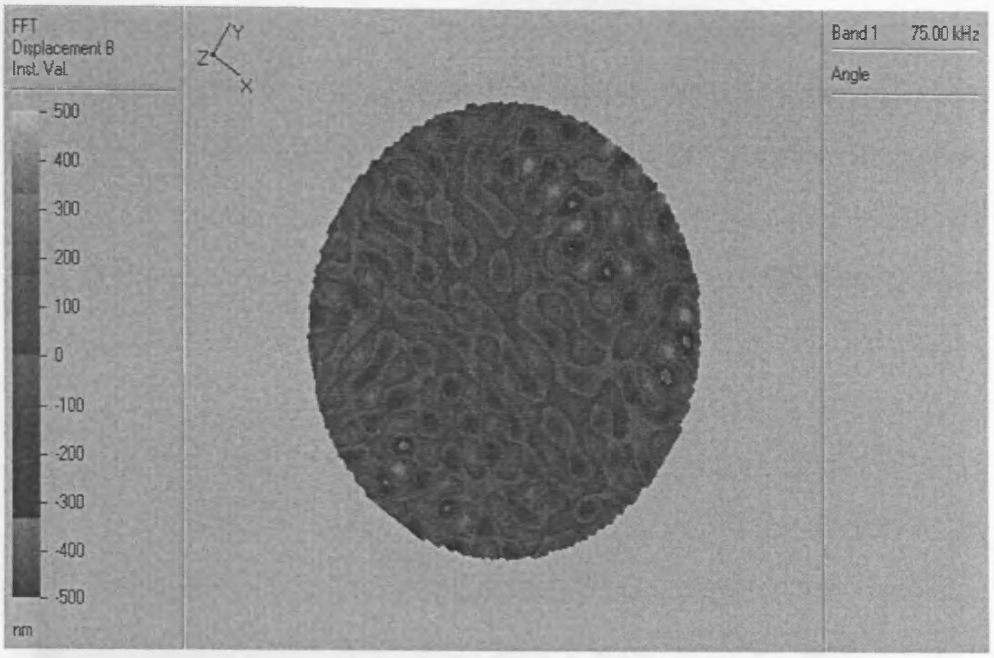
FFT
Displacement B
Inst. Val.
500
400
300
200
100
0
-100
-200
-300
-400
-500
nm
Y
Z
X
Band 1 75.00 kHz
Angle

(a)

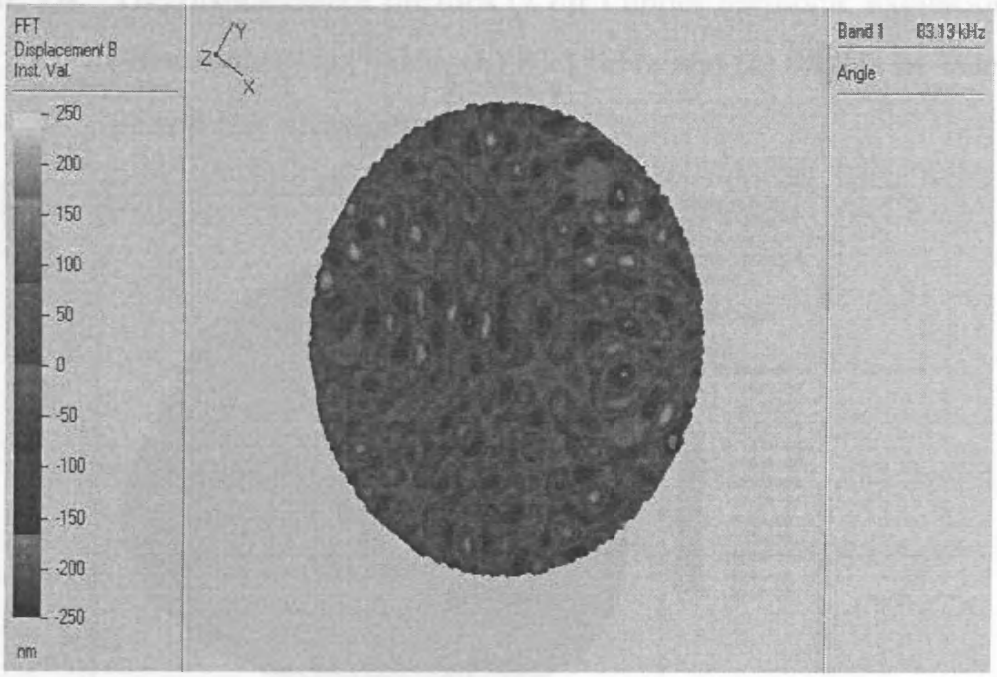
FFT
Displacement B
Inst. Val.
250
200
150
100
50
0
-50
-100
-150
-200
-250
nm
Y
Z
X
Band 1 83.13 kHz
Angle

(b)

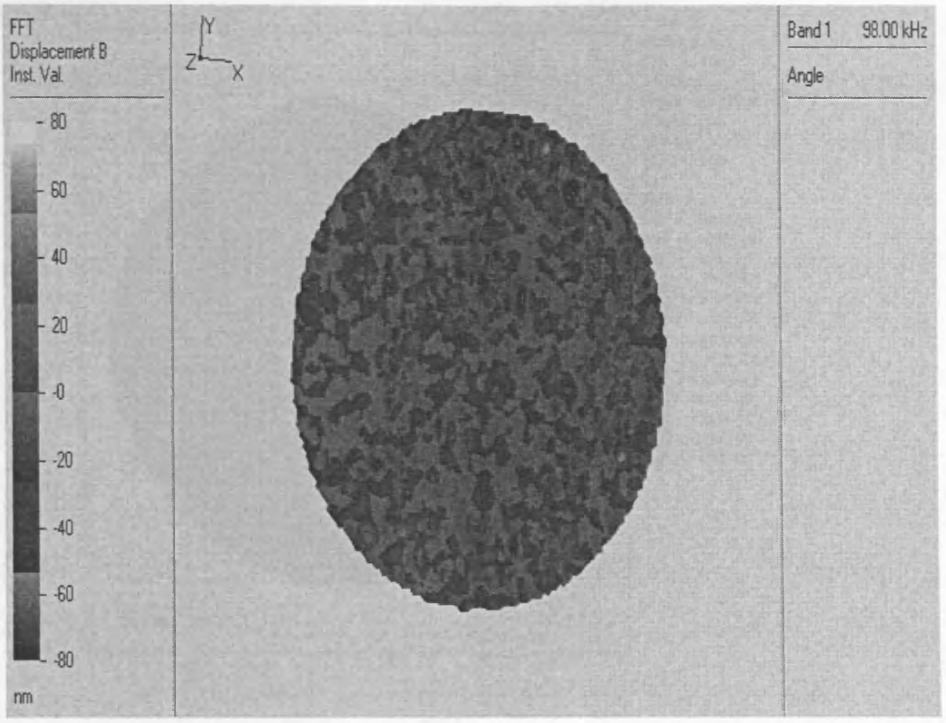


(c)

Figure 3.4. The displacement profiles (z dir.) under harmonic excitation (20V input) (a) 75kHz, (b) 83.13kHz and (c) 98kHz by laser vibrometer measurement.

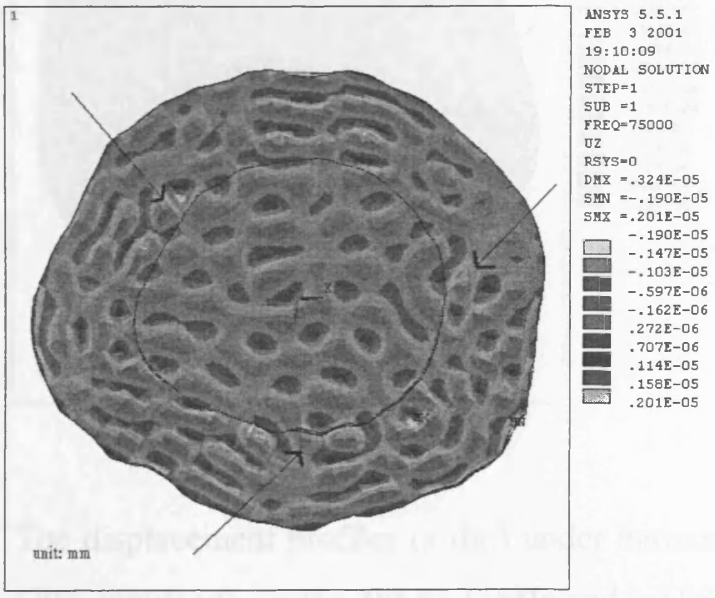


(a)

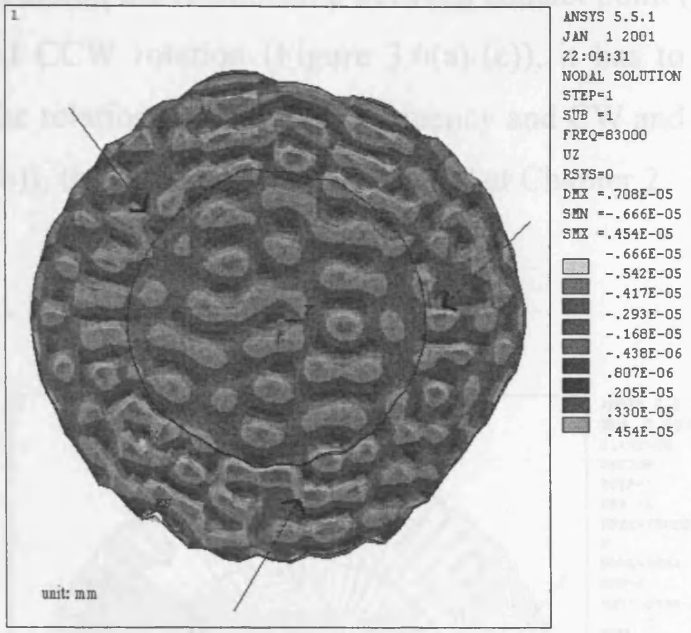


(b)

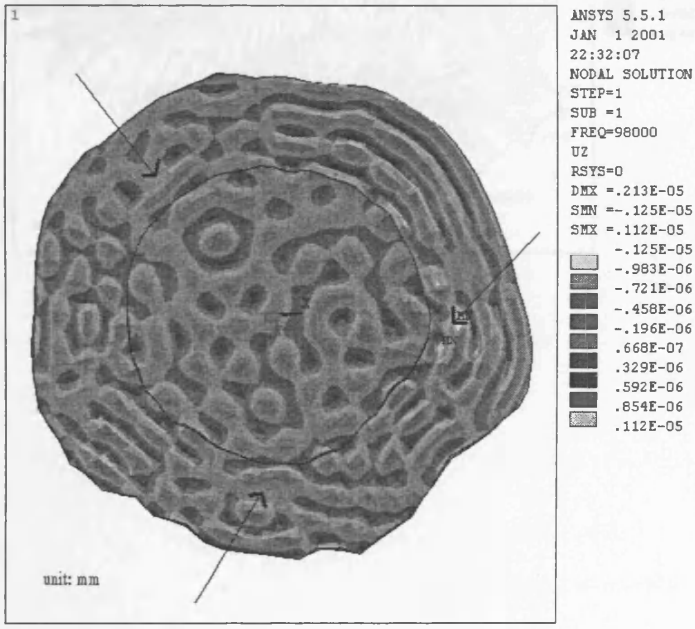


(c)

Figure 3.5. The displacement profiles (z dir.) under harmonic excitation (20V input) (a) 75kHz, (b) 83.13kHz and (c) 98kHz by finite element analysis (→indicates fixed-point location).

For discussion the relationship between contact point (rotor location) and CW and CCW rotation (Figure 3.6(a)-(c)), it has to together with discussion the relationship between frequency and CW and CCW rotation (Figure 3.1(b)), the detail has been discussed at Chapter 2.

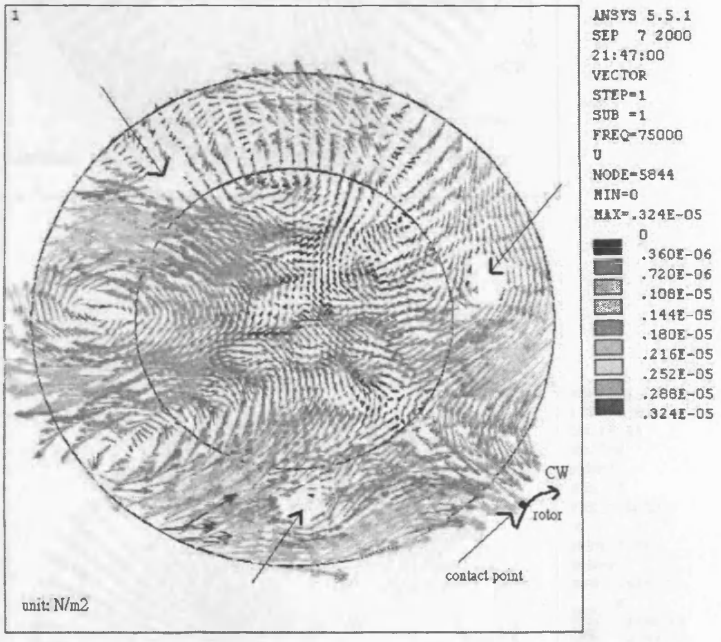


(a)

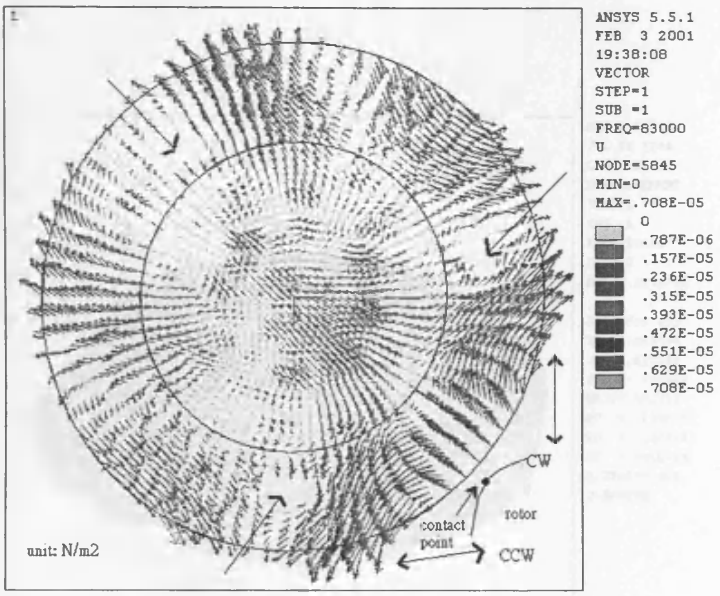


(b)

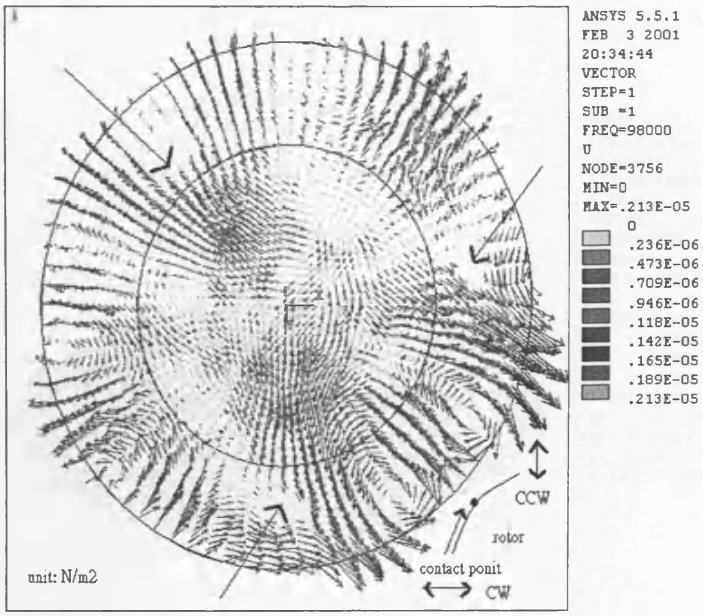


(c)

Figure 3.6. The displacement vector flow at the lateral edge under harmonic excitation (20V input) (a) 75kHz, (b) 83.13kHz and (c) 98kHz by finite element ($\rightarrow$ indicates fixed-point location).

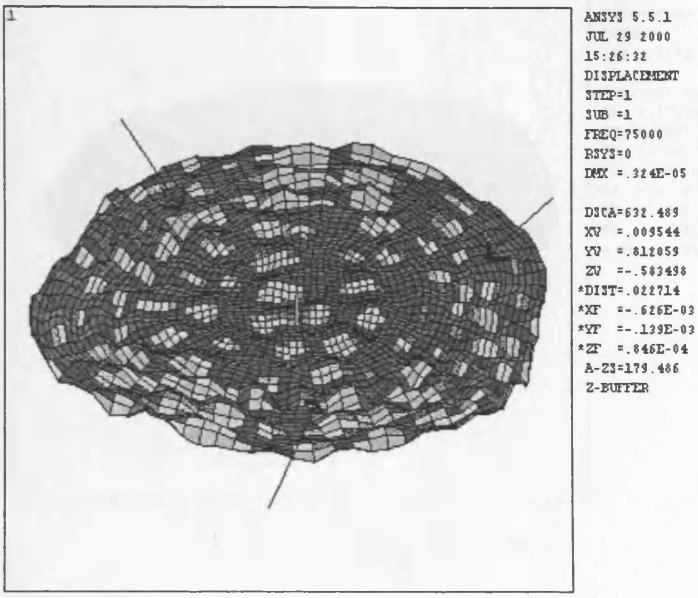
1
ANSYS 5.5.1
JUL 29 2000
15:26:32
DISPLACEMENT
STEP=1
SUB =1
FREQ=75000
RSYS=0
DMX =.324E-05
DSCA=632.489
XV =.009544
YV =.812059
ZV =-.583498
*DIST=.022714
*XF =-.626E-03
*YF =-.139E-03
*ZF =.846E-04
A-ZS=179.486
Z-BUFFER

(a)

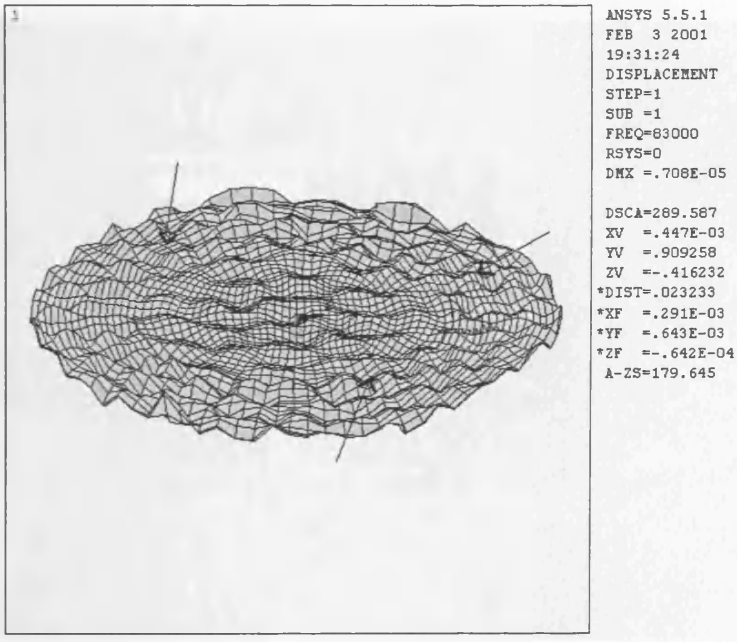
1
ANSYS 5.5.1
FEB 3 2001
19:31:24
DISPLACEMENT
STEP=1
SUB =1
FREQ=83000
RSYS=0
DMX =.708E-05
DSCA=289.587
XV =.447E-03
YV =.909258
ZV =-.416232
*DIST=.023233
*XF =.291E-03
*YF =.643E-03
*ZF =-.642E-04
A-ZS=179.645

(b)

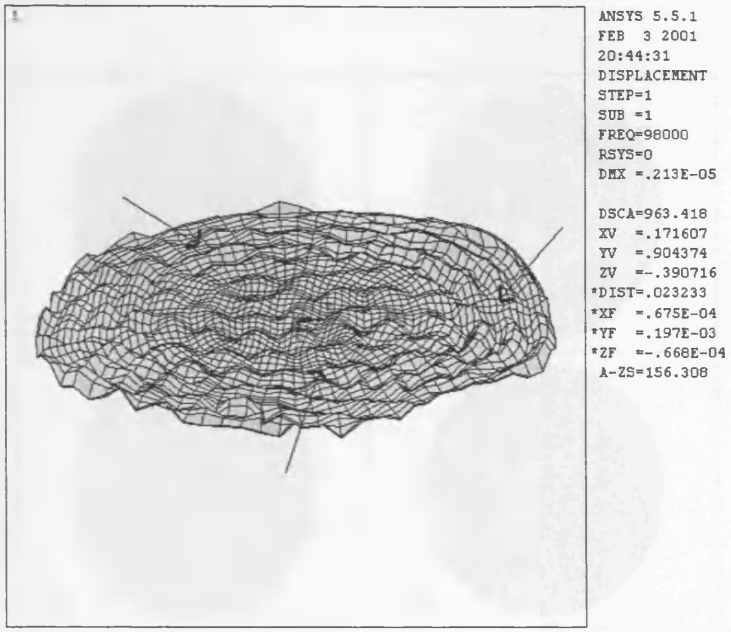


(c)

Figure 3.7. The mode shape under harmonic excitation (20V input) (a) 75kHz, (b) 83.13kHz and (c) 98kHz (→indicates fixed-point location).

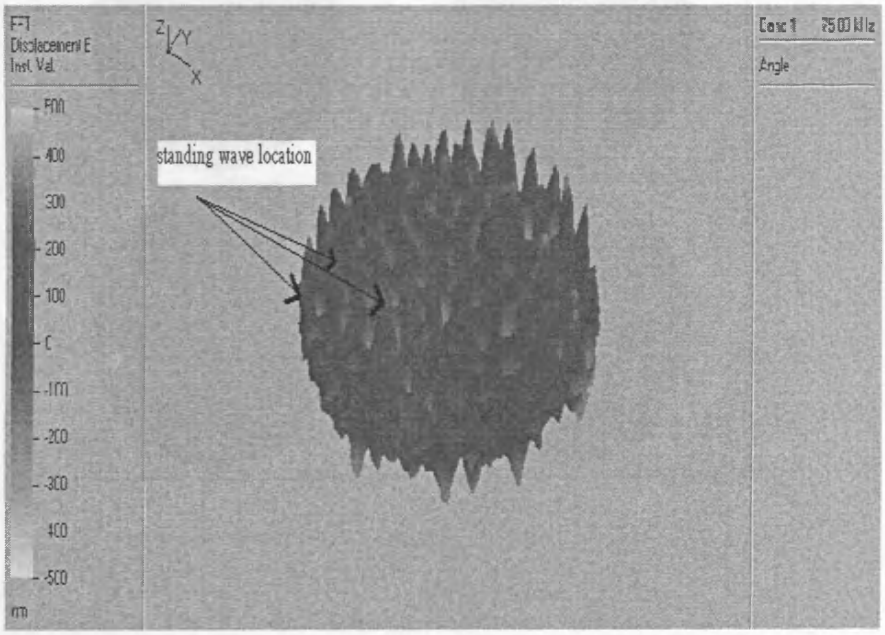


Figure 3.8. The 3-D displacement profiles for checking standing wave existence (it is identical to Figure A.5(a) for convenient explanation).

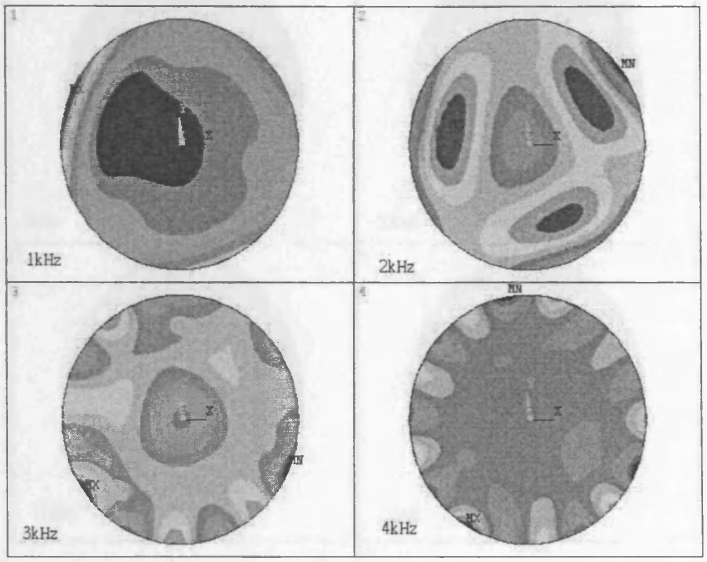


(a)

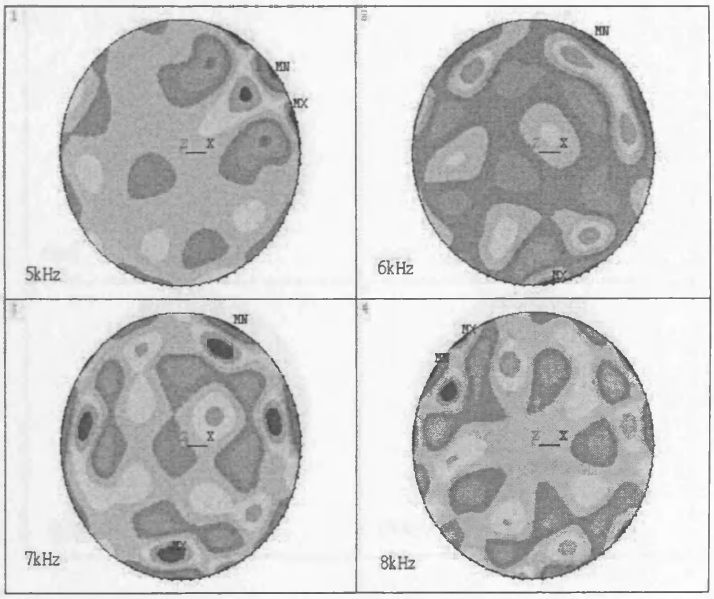


(b)

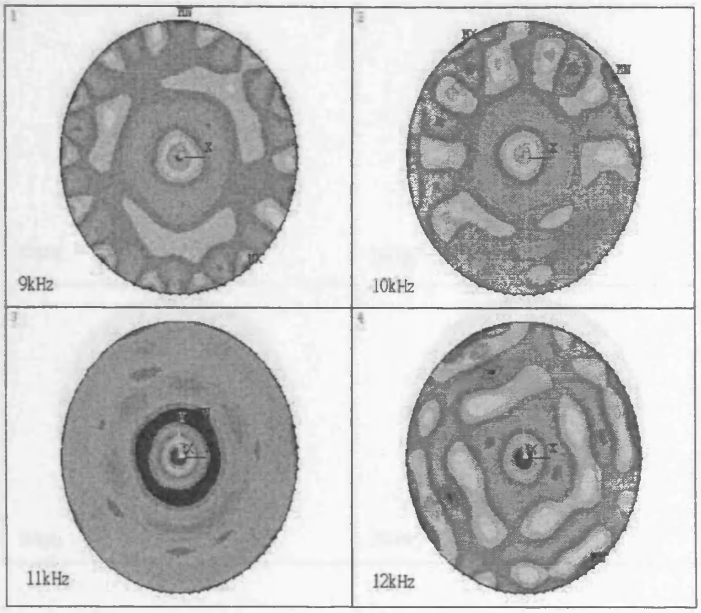


(c)

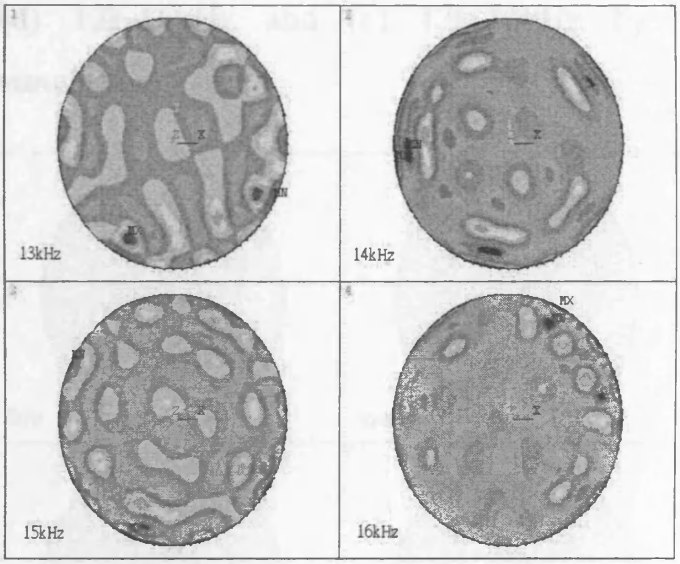


(d)

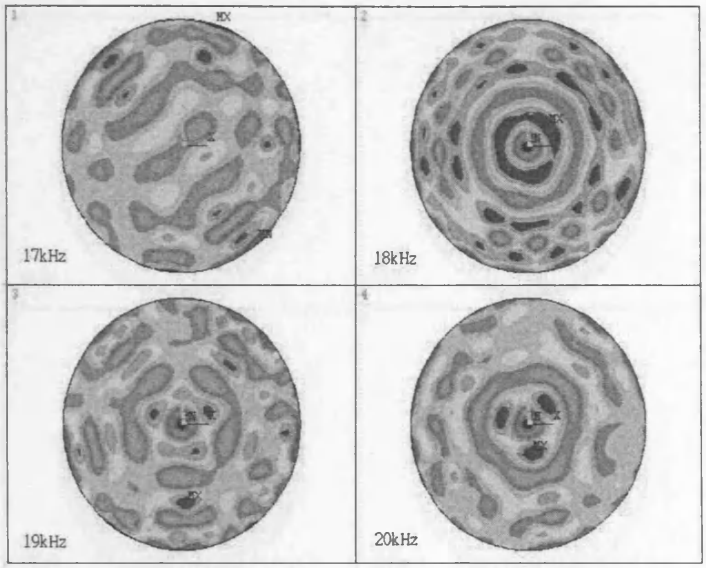


(e)

Figure 3.9. The displacement profiles (z dir. view) under audible frequency excitation (a) 1k-4kHz, (b) 5k-8kHz, (c) 9k-12kHz, (d) 13k-16kHz and (e) 17k-20kHz by finite element simulation.

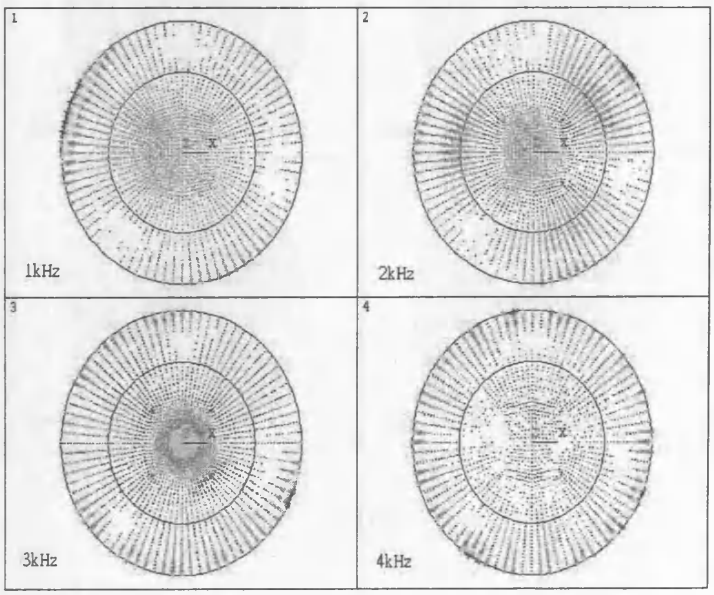


(a)

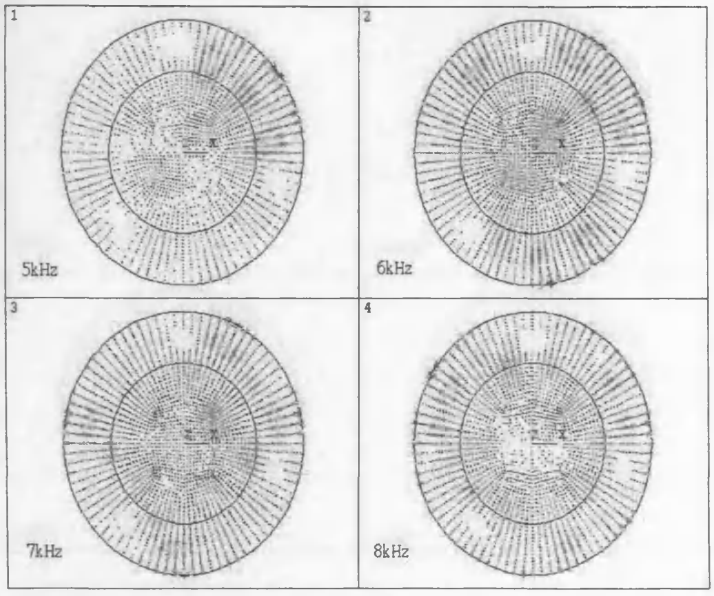


(b)

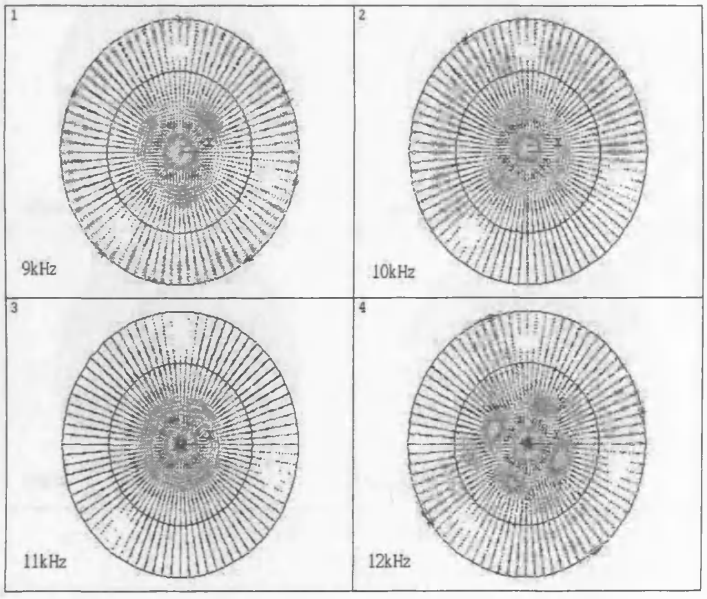


(c)

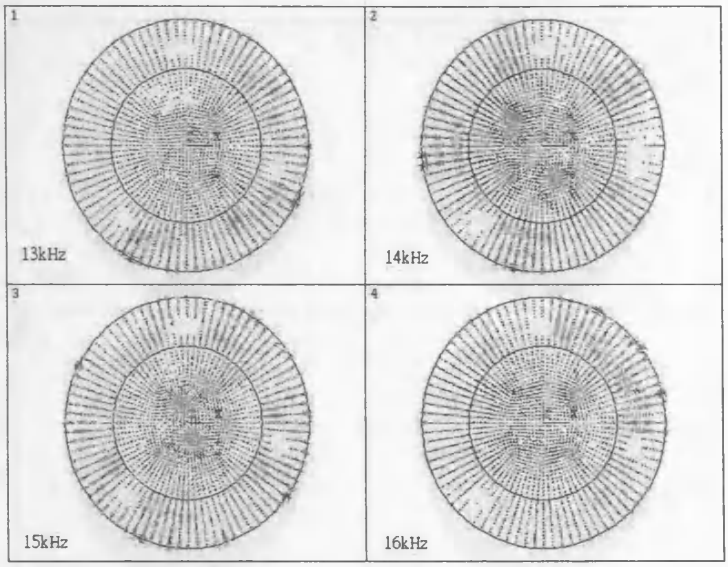


(d)

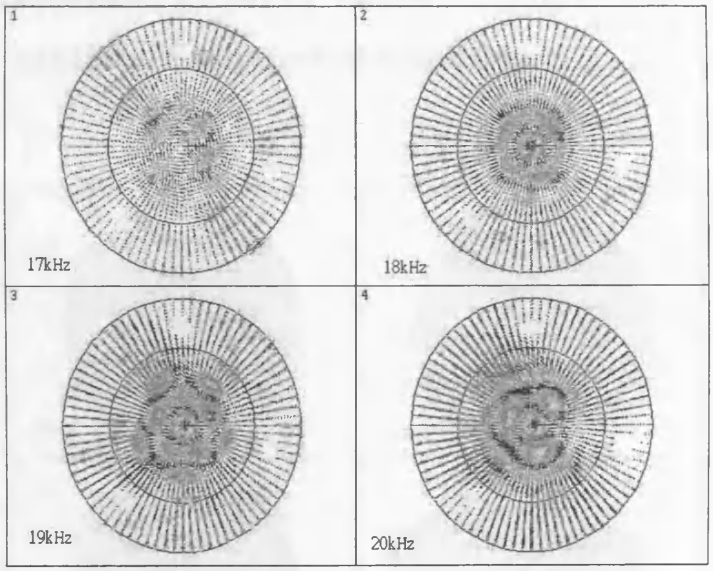


(e)

Figure 3.10. The displacement vector flow under audible frequency excitation (a) 1k-4kHz, (b) 5k-8kHz, (c) 9k-12kHz, (d) 13k-16kHz and (e) 17k-20kHz by finite element simulation.

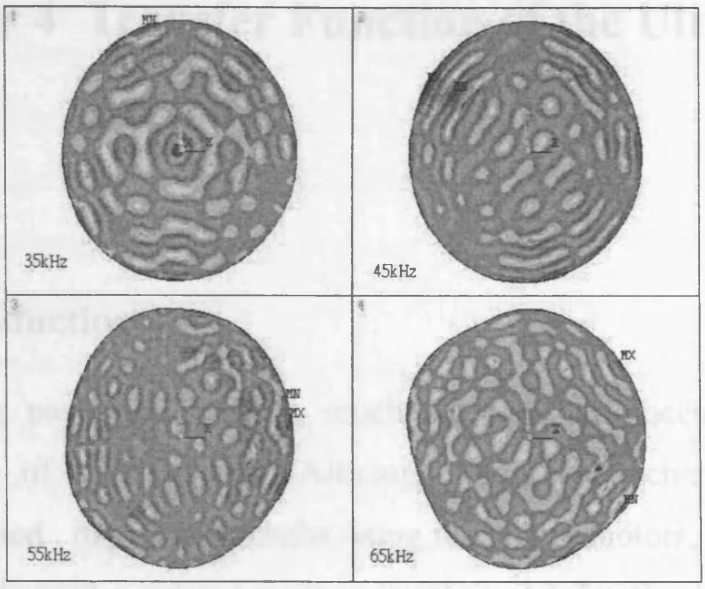


Figure 3.11. The displacement profiles (z dir. view) under lower ultrasonic frequency excitation: 35kHz, 45kHz, 55kHz and 65kHz by finite element simulation.

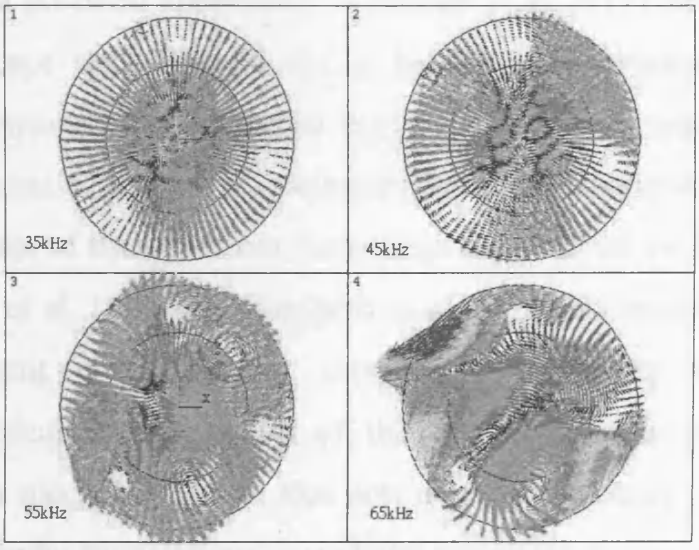


Figure 3.12. The displacement vector flow under lower ultrasonic frequency excitation: 35kHz, 45kHz, 55kHz and 65kHz by finite element simulation.

# Chapter 4 Transfer Function of the Ultrasonic Motor

## 4.1 Introduction

In the past two decades, much attention has been paid to the application of piezomotors. Although many researchers [115]-[119] have obtained impressive results using ultrasonic motors, they have not explicitly derived a related mathematical model for the motor. Im and Atluri [144] developed several analyses and numerical models to analyze the integrated structures. Most of the numerical models were based on simplified structures under simple loading conditions. Tomikawa et al. [116] were the first to turn a prototype of a traveling-wave-type ultrasonic motor into a practical application. Fleischer et al. [117] developed a new motor concept that allowed for a bi-directional piezoelectric single voltage. However, they presented the basic design concept based on the ideal formation of a stator tip trajectory without considering the dynamic characteristics of the stator and the contact behavior of the bimodal motor. Carotenuto et al. [118] and Lamberti et al. [119] presented a new motor with different energy-transfer mechanisms that can transform the antisymmetrical rotating strain of the central plate in a processional motion of a mechanical axial that acts as a displacement amplifier. The analytical model for rotational speed and torque prediction was simplified without considering piezoelectro-mechanical interaction. Two-stage energy conversion is a common feature in piezomotor applications. First, the piezoelectric actuator converts electrical energy into high-frequency mechanical vibration. Usually, there are some coupling vibrational modes

that exist in this stage. Second, the oscillatory energy is transferred into the rotary or linear motion of a driven part. The energy transformation is based on the contact interface between stator and rotor. Thus, a transfer function of the contact interface must be modeled to obtain a true state of energy transformation.

The transfer function analysis [120]-[121] of a stator (actuator) is a very important task in modifying a prototype ultrasonic motor because it will produce response information and a control rule [122]-[123], [128]-[135]. Hagood et al. [120] modeled a type of rotary ultrasonic motor for the purpose of predicting motor performance as a function of design parameters. The Rayleigh-Ritz method, a mode energy method, was used to mode the distributed piezoceramics and the traveling-wave dynamics of the stators. The forcing function, including non-linear normal and tangential interface forces between stator and rotor, was established to acquire the relative dynamic characteristics. Hargerdon and Wallaschek [121] have taken into account how the interfaces between the stator and rotor affect the amplitude of the traveling-wave within the stator. This amplitude determines the torque and speed characteristics of a stator. Lin et al. [127] modeled the transfer function of PZT phase modulators used in optical fiber sensors. The transfer function included the interaction between the vibration mode of a PZT ceramic shell and the sensing mechanism of the optical fiber. The frequency response, phase delay and output voltage were obtained by deriving the transfer function. Yang and Mote [122] proposed an approach for stabilizing flexible structures with non-collocated sensor-actuator pairs by introducing a time delay element into the transfer function of the controller. Yang and Mote [123] used the transfer function to design a controller for active vibration control of an axially moving string. They showed that by introducing a specific time delay into the transfer function of the controller structure, all

the vibratory modes can be stabilized and spillover instability can be avoided. Chung and Tan [128] proposed controlling the transverse vibration of an axially moving structure by using transfer function and wave cancellation concepts. Datko et al. [129] investigated the effects of time delays in boundary feedback stabilization schemes for the transfer function of a control system. Wie and Bryson [130] studied the effect of actuator and sensor location on the transfer functional zeros using uniform bars and beams as generic models of flexible space structures. Alli and Singh [131] used information about the poles of the open-loop transfer function of the wave equation to design the exact time-optimal controller. Pan and Chao [132] proposed a technique for generation of the root-loci of a distributed actuator and sensor system. Alli and Singh [133] developed a technique for determination of the optimum gain, which results in the close-loop poles being located at the extreme left of the root locus. This technique was used to select a gain that minimizes a quadratic cost. Schulte and Frohleke [134] presented a parameter-identification method based on the transfer function of traveling-wave type ultrasonic motors for output control. Mass et al. [135] presented a complete model-based and cascaded bending-wave control scheme for traveling-wave-type ultrasonic motors. The principle of the new control scheme serves to control a resonant system related to the amplitude and relative temporal phase shift of the fundamental oscillation. In this chapter, the dynamic and contact models of [124]-[125] that used in development of a bimodal ultrasonic motor are followed, but a disc plate was used instead of a beam. We must emphasize the fact that the contact model of ultrasonic motors is rather complicated as many parameters must be taken into account. Thus, the transfer functions depend on the form, frequency and amplitude of the stator vibration, the stiffness and damping of the contact layer, the flexibility of the rotor, the normal

pre-load force, the static deflection of the stator and rotor, and frictional characteristics of the contact materials as well as the their surface topology and microstructure. Furthermore, most material properties strongly depend upon temperature and manufacturing tolerances concerning the flatness and alignment of the contact surface. Apparently, it is very difficult to include all of these aspects in a single, general contact model. Therefore, one of the most important questions relating to modeling the transfer function is how much force and power can be delivered and what form the torque curve will take. So, in deriving the transfer function of the proposed motor, our emphasis will focus on the estimation of these dynamic characteristics.

This chapter deals with the transfer functions of the ultrasonic motor: stator and stator-rotor energy transformation. The objective is to initiate a mode that can produce certain relative dynamic responses in the proposed motor. The emphasis is still on the asymmetrical simple support (120°-90°-150°) [17] boundary condition of the stator, which induces a lateral elliptical motion and generates torque [see Figure 4.1] to rotate the rotor. The performance will be parameterized by system inputs in an attempt to obtain an optimal operation configuration. The transfer function model of the piezoelectric ultrasonic stator based on the lateral elliptical motion is derived for the control application and certification of its load-characteristic parameters and also predicts the motor performance. On this basis, we can determine whether the output of the motor will be stable. The contact-dynamic behaviors of the stator are also studied. These derived formulations in this chapter are based on the general concept of the constitutive laws governing piezoelectric materials which permit the introduction of kinetic energy, electrical energy, and geometric constraints relating to the deformation variables.

The transfer function models of the piezoelectric ultrasonic stator

are to be derived by using the piezoelectric constitutive laws, with the intention of establishing a control scheme and evaluating its relative response characteristics. These characteristics include frequency response, phase response, transient response, stability diagram, speed-torque and torque-voltage. Some experimental measurements were made to check these analyses. The transfer function model would be a good reference for future prototypes of piezoelectric ultrasonic motors.

## 4.2 Transfer Function Model

### 4.2.1 Transfer Function of the Stator

For transfer function derivation, we assume that the electrode surface forms an equal potential surface in a thin ceramic disc bonded to the disc metal structure. In this condition, $E_3 = E$, $T_3 = 0$, $T_1 = \sigma_\theta$, $T_2 = \sigma_r$. In cylindrical coordinates, the piezoelectric linear constitutive equation [126] for the radial expansively coupled vibration of the stator is as follows:

$$S_1 = c_{11}^E T_1 + d_{31} E_3 \tag{4.1}$$

$$D_3 = d_{31} T_1 + \varepsilon_{33}^T E_3, \tag{4.2}$$

where $S_1$ and $T_1$ are the strain and stress in the circumferential direction, $D_3$ and $E_3$ the electrical displacement and electrical field in the radial direction, $c_{11}^E$ the compliance coefficient at a constant electrical field, $d_{31}$ the piezoelectric constant, and $\varepsilon_{33}^T$ the dielectric constant. Furthermore, from the force diagram [see Figure 4.2], we have

$$F_r = 2F_\theta(\frac{1}{2}d\theta) = F_\theta d\theta = T_1 h dr d\theta, \tag{4.3}$$

where $F_\theta$ is a tangential force acting on the circumferential direction of the ceramic, $F_r$ a radial force, h the thickness of the ceramic, $dr$ the radial of a piece of the ceramic and $d\theta$ the circumferential angle of a piece of the ceramic. According to Newton's second law

$$\rho hrdrd\theta \frac{\partial^2 u_r}{\partial t^2} = -T_1 hdrd\theta, \tag{4.4}$$

where $\rho$ is the density of the stator, r the mean radius and $u_r$ the radial displacement. In the tiny angular displacement change situation, the circumferential strain is similarly equal to

$$S_1 = \frac{u_r}{r} + \frac{1}{r}\frac{\partial u_r}{\partial \theta} \cong \frac{u_r}{r}. \tag{4.5}$$

After some manipulation from (4.1), (4.4) and (4.5), the motion equation for the radial displacement under an applied electrical field can be expressed as follows:

$$\frac{\partial^2 u_r}{\partial t^2} + \frac{1}{\rho r^2 c_{11}^E} u_r = \frac{d_{31}}{\rho r c_{11}^E} E_3. \tag{4.6}$$

If the damping effect is considered, then equation (4.6) becomes

$$\frac{\partial^2 u_r}{\partial t^2} + \frac{\alpha}{\rho}\frac{\partial u_r}{\partial t} + \frac{1}{\rho r^2 c_{11}^E} u_r = \frac{d_{31}}{\rho r c_{11}^E} E_3, \tag{4.7}$$

where $\alpha$ is a damping coefficient of the stator. In equation (4.7), let $E_3 = 0$ will be applied to the disc metal structure. We assume that the driving field is excited harmonically, then $u_r$ is time dependence as $u_r e^{-i\omega t}$ where $\omega$ is angular velocity. Consequently, the steady-state solution of (4.7) may be written as

$$u_r = \frac{d_{31} E_3}{(\omega_0^2 + i\frac{\omega\alpha}{\rho} - \omega^2)\rho r c_{11}^E}. \tag{4.8}$$

The substitutive variable $\omega_0$ is the resonant angular frequency,

given as

$$\omega_0 = \sqrt{\frac{1}{\rho r^2 c_{11}^E}}. \tag{4.9}$$

We also define the mechanical quality factor as

$$Q = \frac{\omega_0 \rho}{\alpha}. \tag{4.10}$$

In the equal potential condition, that is

$$E_3 = V/h, \tag{4.11}$$

where V is applied voltage. Then from (4.8), (4.10) and (4.11), we have

$$\frac{u_r}{V} = \frac{d_{31}}{(\omega_0^2 + i\frac{\omega\alpha}{\rho} - \omega^2)\rho r c_{11}^E h}. \tag{4.12}$$

The delay angle of the stator phase response can be obtained from the complex term of (4.12) as follows:

$$\tau = -\tan^{-1}\frac{\omega\omega_0}{Q(\omega_0^2 - \omega^2)}. \tag{4.13}$$

The transfer function of the stator can be obtained by replacing $i\omega$ with S into (4.12) as follows:

$$G(S) = \frac{d_{31}}{(S^2 + \frac{S\alpha}{\rho} + \omega_0^2)\rho r c_{11}^E h}. \tag{4.14}$$

The circumferential displacement $u_\theta$, can be obtained from the lateral elliptical motion equation [63]

$$u_\theta = (\overline{U}_\theta)\sqrt{1 - \left[\frac{u_r}{(\overline{U}_r)}\right]^2}. \tag{4.15}$$

The substitutive variables, $\overline{U_r}$ and $\overline{U_\theta}$, are given as

$$\left(\overline{U}_r\right)=\left(A\frac{\partial J_n(lr)}{\partial r}+nB\frac{J_n(kr)}{r}\right)$$
$$\left(\overline{U}_\theta\right)=-\left(nA\frac{J_n(lr)}{r}+B\frac{\partial J_n(kr)}{\partial r}\right) \tag{4.16}$$

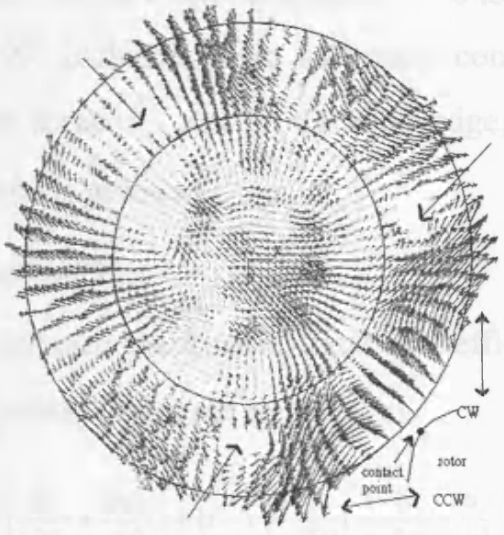


Figure 4.1. The operational principle explanation ( → indicates fixed-point location, it is identical to Figure 3.6(b) for convenient explanation).

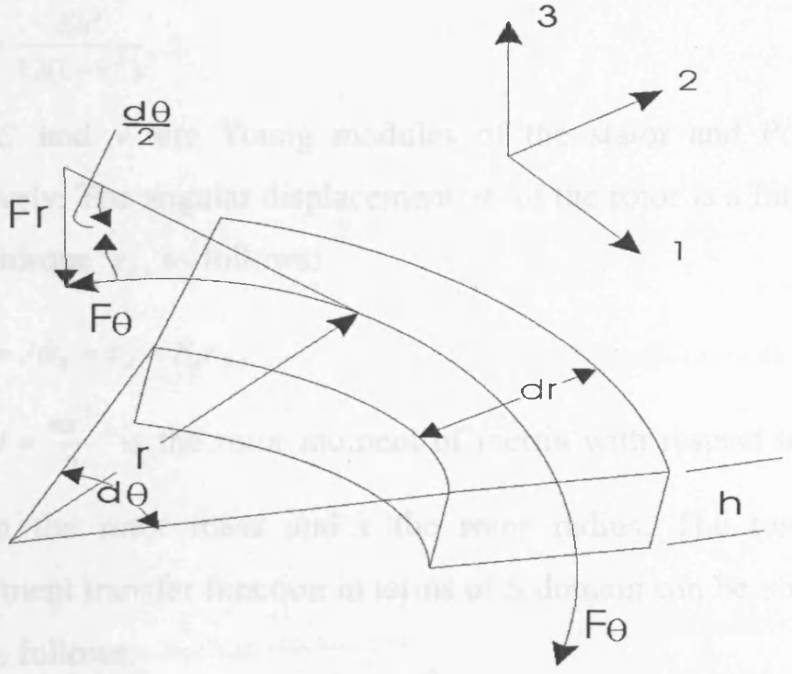


Figure 4.2. Force diagram of the stator.

### 4.2.2 Model of the Rotor-Stator Energy Transfer

Applying a traveling-wave to the stator, the rotor of the motor will be animated in a lateral elliptical motion. Due to the induced motion, the region with a 90° included angle will make contact with the rotor. As a result, a contact force $\vec{F}_d$ acts on the rotor edge, as shown in Figure 2.9. The contact force is given as

$$F_d = V_\theta + \mu(V_r + VP), \tag{4.17}$$

where $\mu$ and $VP$ are the kinetic friction coefficient and pre-force. The radial and tangential forces are as follows:

$$\begin{aligned} V_r &= Q_s\left\{\frac{\partial}{\partial r}\left(\frac{\partial u_r}{\partial r}+\frac{\partial u_\theta}{\partial \theta}\right)+(1-\nu)\frac{1}{r}\frac{\partial}{\partial \theta}\left(\frac{1}{r}\frac{\partial u_r}{\partial \theta}-\frac{u_r}{r^2}\right)\right\} \\ V_\theta &= Q_s\left\{\frac{1}{r}\frac{\partial}{\partial \theta}\left(\frac{\partial u_r}{\partial r}+\frac{\partial u_\theta}{\partial \theta}\right)+(1-\nu)\frac{\partial}{\partial r}\left(\frac{1}{r}\frac{\partial u_r}{\partial \theta}-\frac{u_r}{r^2}\right)\right\} \end{aligned}. \tag{4.18}$$

where the plate stiffness $Q_s$ is given as

$$Q_s = \frac{Eh^3}{12(1-\nu^2)}, \tag{4.19}$$

where $E$ and $\nu$ are Young modules of the stator and Poisson ratio, respectively. The angular displacement $\theta$ of the rotor is a function of the applied torque $\tau_d$, as follows:

$$J\ddot{\theta} = J\dot{\omega}_R = \tau_d = F_d r, \tag{4.20}$$

where $J = \frac{mr^2}{2}$ is the rotor moment of inertia with respect to its central axial, m the rotor mass and r the rotor radius. The torque-angular displacement transfer function in terms of S domain can be obtained from (4.20) as follows:

$$\frac{\Theta}{T_d} = \frac{1}{JS^2}, \tag{4.21}$$

where $\Theta$ and $T_d$ are Fourier transforms of $\theta$ and $\tau_d$, respectively. According to (4.15), (4.17) and (4.18), $\tau_d$ can be further simplified as

$$\tau_d = K_T u_r, \tag{4.22}$$

so that

$$T_d(S) = K_T u_r(S), \tag{4.23}$$

then

$$T_d(S) = K_T G(S) V(S), \tag{4.24}$$

where $K_T$ is assumed as force factor. When (4.14), (4.21) and (4.23) are involved in the control system of the motor, we can obtain the control scheme for the motor, as shown in Figure 4.3, where $\omega_R$ is the revolution speed of the rotor. The control system can be input voltage control, input current control, and input frequency control.

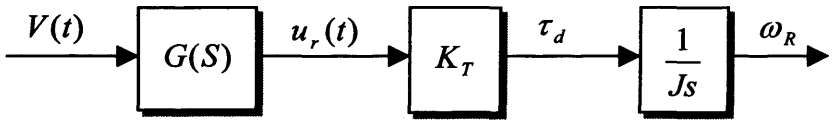


Figure 4.3. Control scheme of the ultrasonic motor.

## 4.3 Verification of the Model

Table 2.1 was again used to check the performance response of the prototype ultrasonic motor, and Figure 2.1, the configuration of the disc-type ultrasonic motor set up. A displacement meter was installed into

the movable base to measure the radial dynamic displacement, $u_r$, and the pre-pressure acting on the rotor, as shown in Figure 4.4.

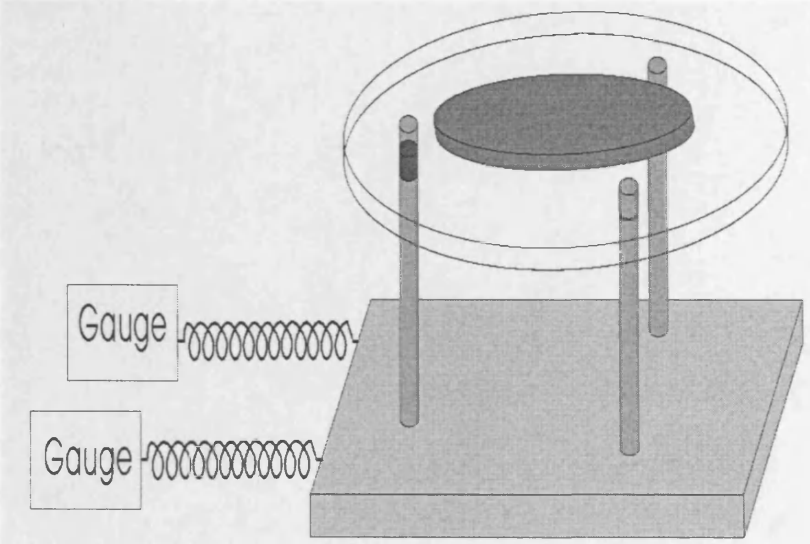


Figure 4.4. Configuration of the lateral displacement measurement.

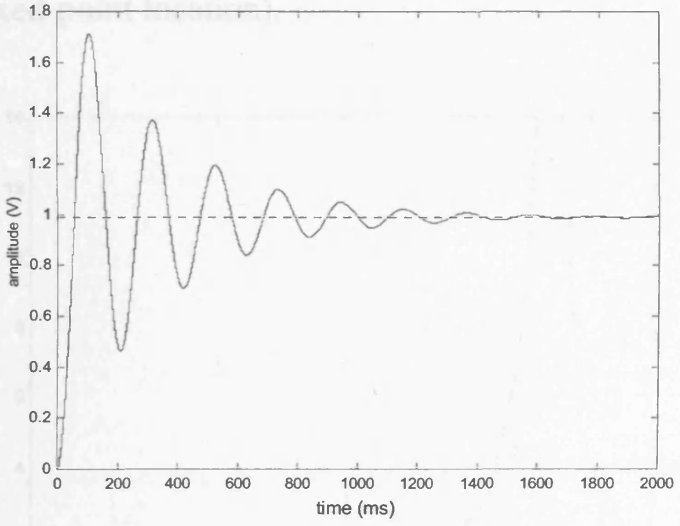


Figure 4.5. Transient response of the stator at 74kHz.

In the first tests, the transient responses of the stator were simulated by applying voltage at a 74 kHz driving frequency and 10V input voltage. The result is shown in Figure 4.5, from which the damping ratio of the

stator was estimated to be about 0.2. For other driving frequencies, it near 0.18.

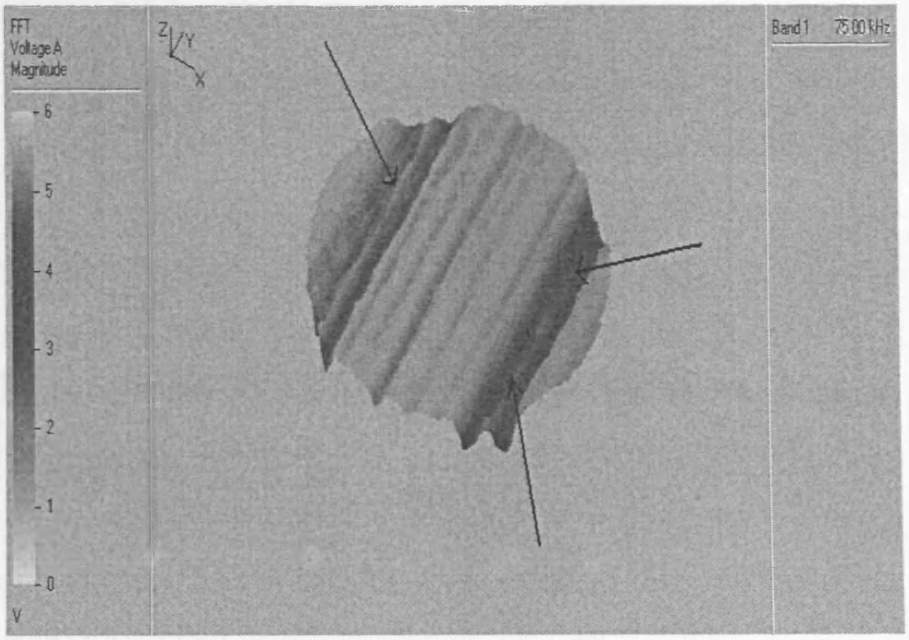


Figure 4.6. Voltage response in the whole stator at 74kHz (→ indicates fixed-point location).

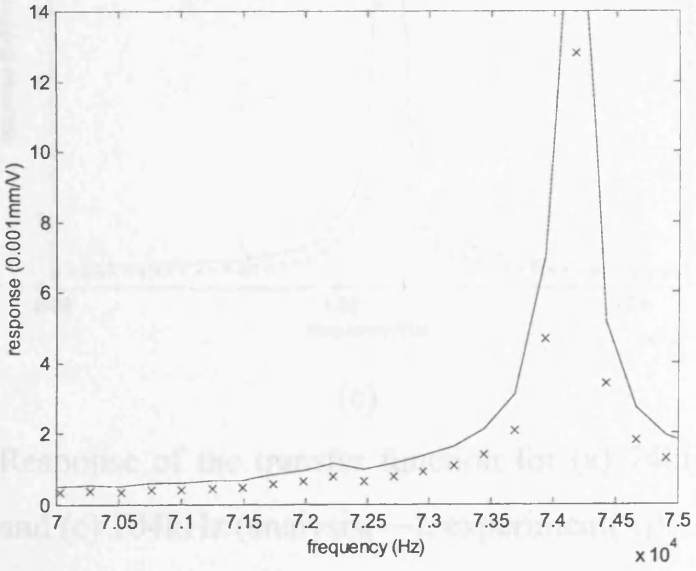


(a)

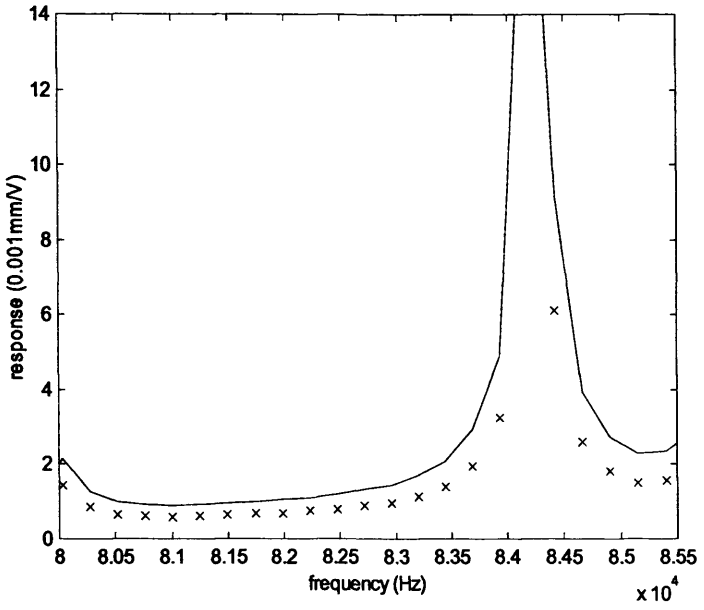


(b)

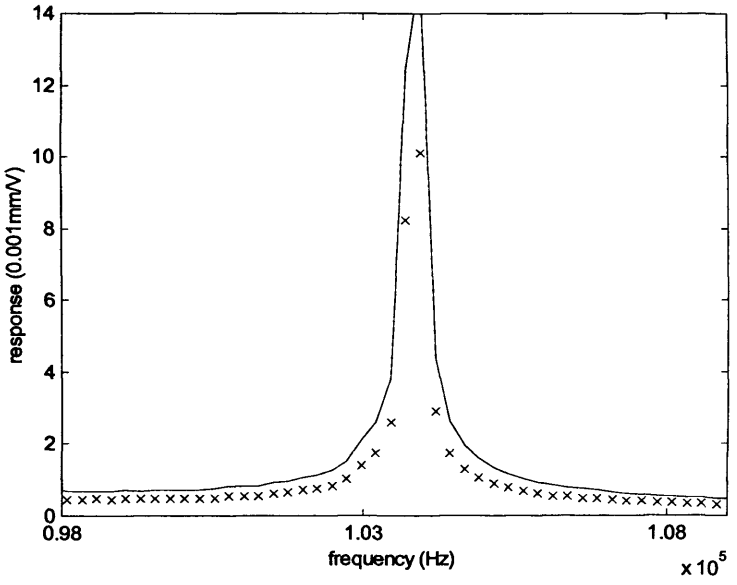


(c)

Figure 4.7. Response of the transfer function for (a) 74kHz, (b) 84kHz and (c) 104kHz (analysis(—); experiment(×)).

For the second tests, the steady-state responses of the stator were analyzed. The laser vibrometer was used to realize voltage response of

the stator, as shown in Figure 4.6. The result reveals that voltage response is uniform around the stator. However, the displacement drops are significant among its fixed points. Especially, there exist two fixed points with a 90° included angle. In this case, only 74kHz was tried. In fact, there would be the same voltage response at other driving frequencies. Figure 4.7 (a)-(c) shows the results from experimental data and theoretically calculated data at 74kHz, 84kHz and 104kHz three different resonant frequencies for the transfer function of the stator, equation (4.14). The results for 74kHz, 84kHz and 104kHz show a great deal of correspondence between experiment and theory. Thus, we confirm that the ultrasonic motor can be driven at 74kHz, 84kHz and 104kHz, that is, the outputs including revolution speed, output current and efficiency are at optimum. Figure 4.8 is the phase response of the stator obtained by superposing the desired frequency range, the detail discussions about the relationship between frequency and CW and CCW rotation has been done at Chapter 2. We also discovered that changing the exciting frequency, amplitude and phase will yield better performance.

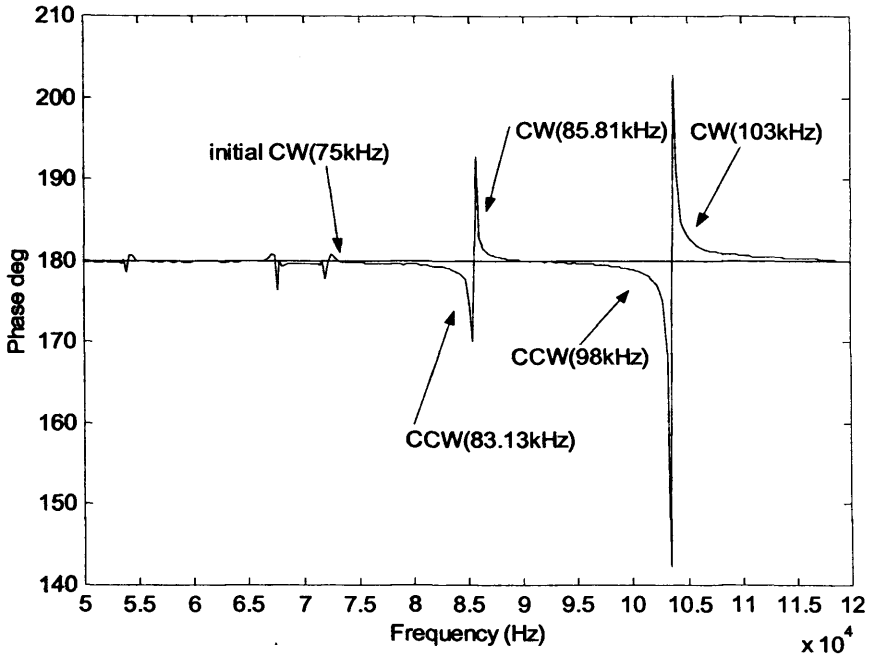


Figure 4.8. Phase response of the stator by superposing the desired frequency range (y-axial is the z dir. phase response degree of the stator, it is identical to Figure 3.1(b) for convenient explanation).

Thirdly, the time responses of the stator and rotor by applying a unit step input (74kHz) to the transfer functions of the stator and rotor were tested and these results are shown in Figure 4.9 and Figure 4.10. The results show that the maximum overshoot, peak time, rise time, and setting time of the stator are 36%, 55ms, 40ms and 220ms. On the contrary, the rotor's are 2.48%, 3.94ms, 2.198ms and 5ms. Figure 4.9 reveals that the stator output is stable at specified driving frequencies. There would be similar results for the other two driving frequencies. Thus, we are sure that the ultrasonic motor will have good performance at 74kHz, 84kHz and 104kHz. Figure 4.11 shows the time responses of the transfer function combining the stator with the rotor, that is the motor. The results show that the stator dominates the ultrasonic motor. The

reason is that the rotor is fixed except for its rotation, and it interacts with the stator at a contact point only. Figure 4.12 is the bode diagram of the transfer function for the motor. The result shows that its gain margin and phase margin are 25dB and $30^{\circ}$, respectively, and that a PI controller will be required to compensate for the revolution-speed error of the ultrasonic motor. It shall be emphasized that because tangential displacement $u_{\theta}$ and force $F_{\theta}$ of the stator can not be measured, they must be acquired from theoretical formulae when these radial displacement $u_r$ and force $F_r$ are measured and put into it. So, these responses of Figure 4.9-4.12 are these results of experiment(measurement) with theoretical model(prediction). These measurement data were put into model and fed into "Matlab tool box" to get the response result.

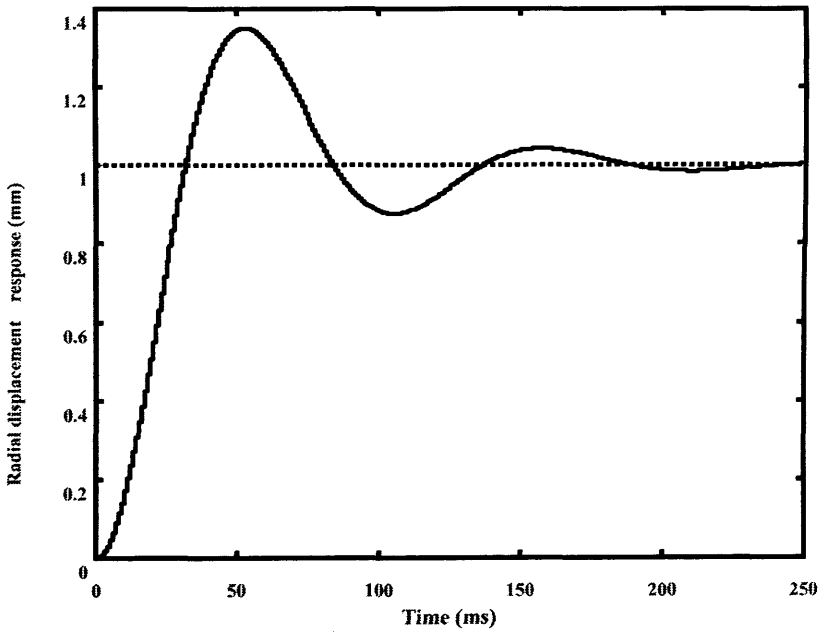


Figure 4.9. Step response of the stator at 74kHz(the result is measurement combining with theoretical model fed into Matlab).

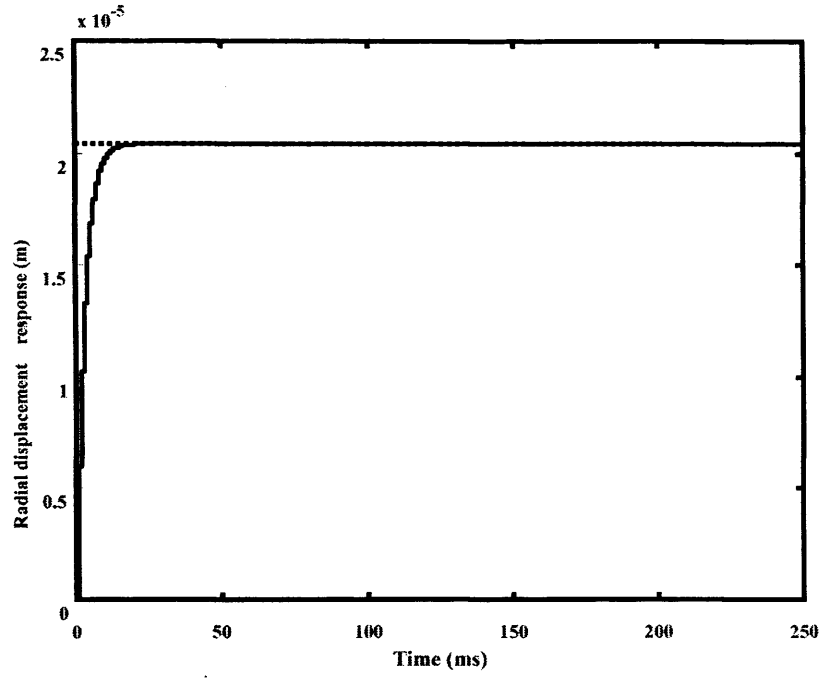


Figure 4.10. Step response of the rotor at 74kHz(the result is measurement combining with theoretical model fed into Matlab).

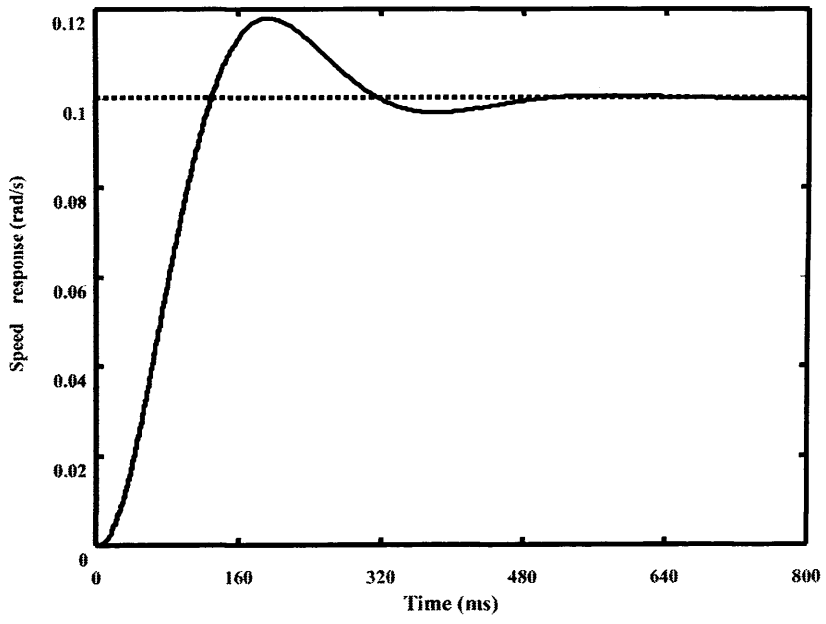


Figure 4.11. Step response of the ultrasonic motor(revolution speed response) at 74kHz(the result is measurement combining with theoretical model fed into Matlab).

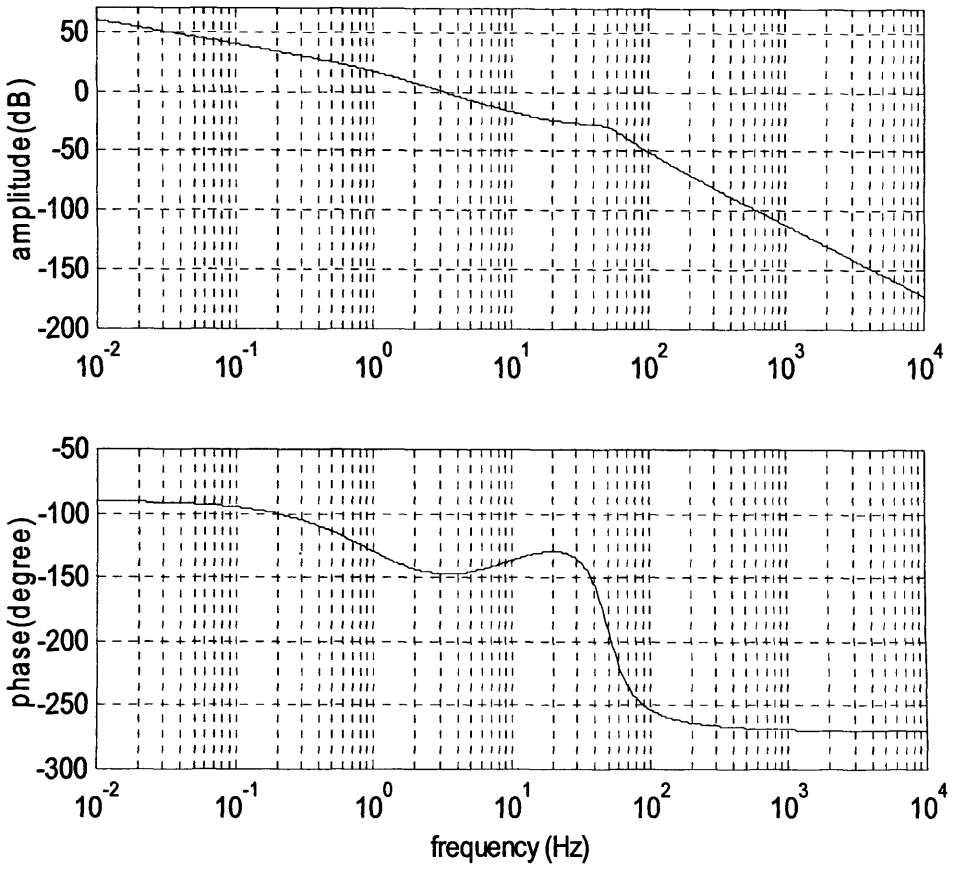


Figure 4.12. Bode diagram of the transfer function for the ultrasonic motor(the result is measurement combining with theoretical model fed into Matlab).

Finally, in order to check the operation performance, the same driving condition as was used in the preview was created to study the contact dynamic behaviors between the stator and rotor. The ultrasonic motor used only one power amplifier to drive the rotor. Figure 4.13(a)-(c) shows the radial amplitude of the steady-state response. The maximum amplitude is about 7 $\mu$ m. The rotor is placed at a position where the stator has a 1mm static deflection. Figure 4.14 shows the contact point trajectory of the stator using laser-vibrometer measurement for 74kHz.

Initially, we marked the contact point in a static condition. It was shown that there exists a clearance between the stator and rotor during a motion period. The normal contact force in Figure 4.15 shows that the stator does not make contact with the rotor in each oscillating period.

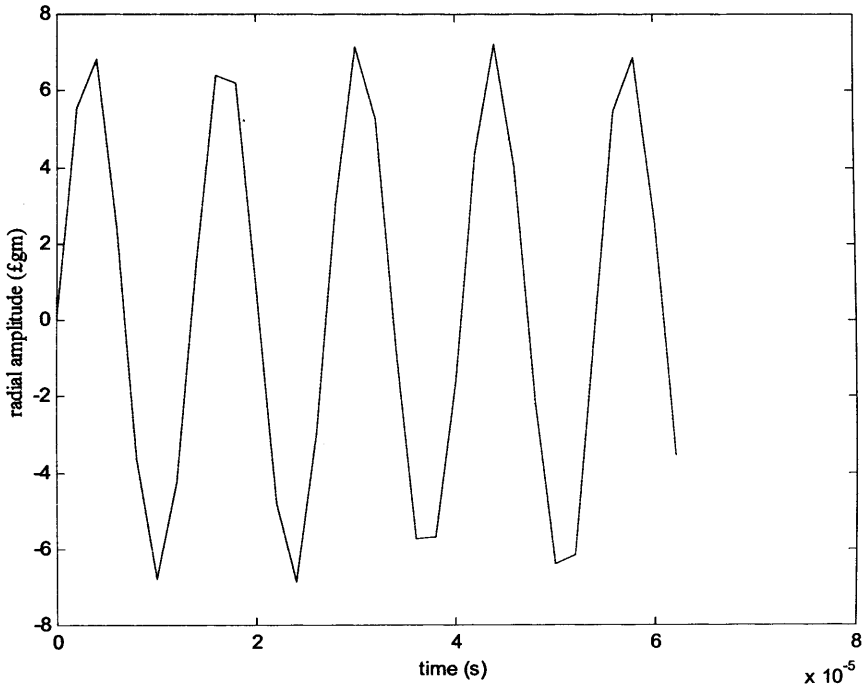


(a)

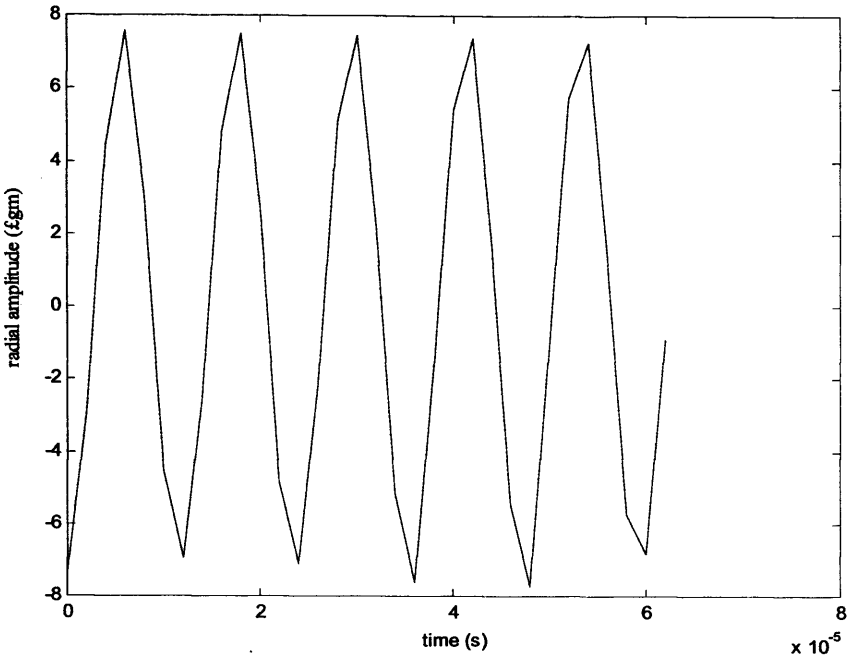


(b)

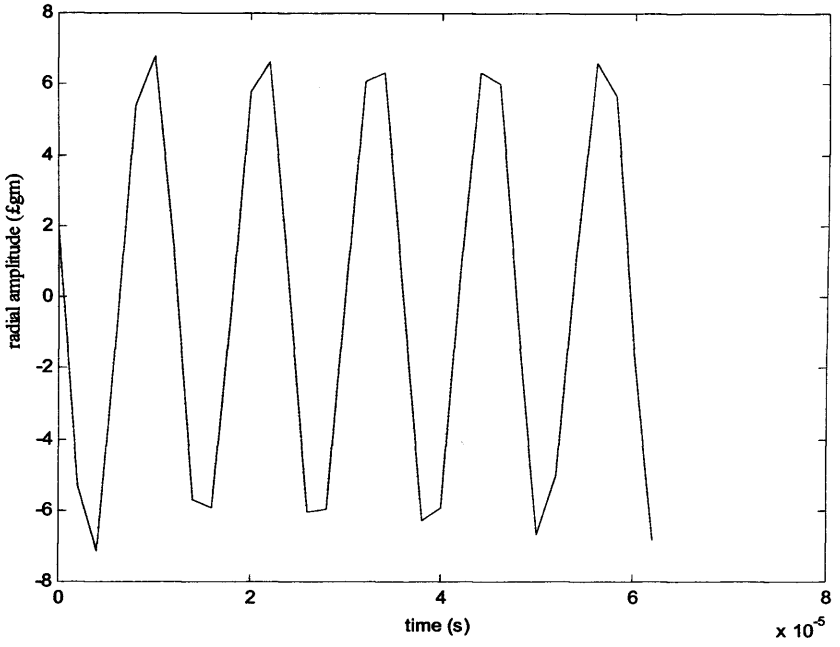


(c)

Figure 4.13.Radial amplitude of the steady state response at (a) 74kHz, (b) 84kHz and (c) 104kHz.

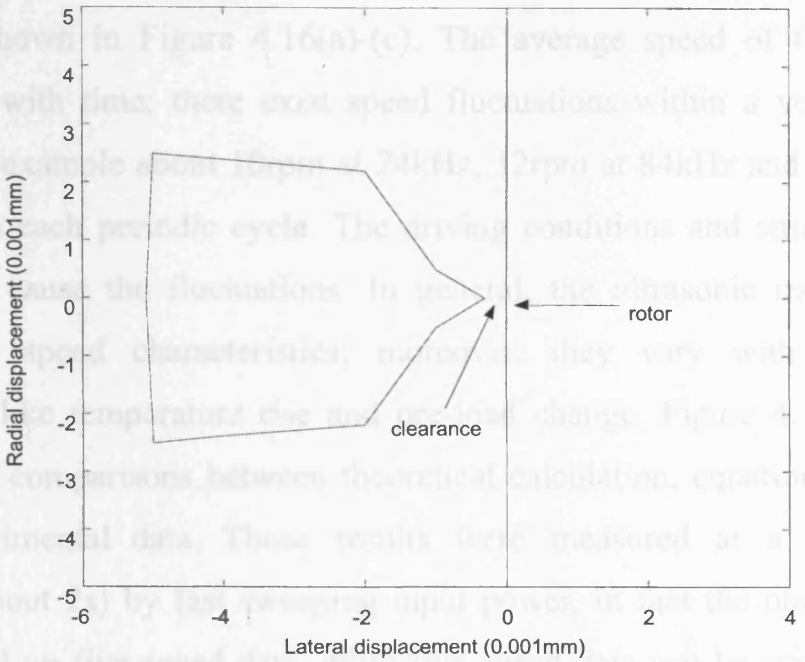


Figure 4.14. Trajectory of the contact point at the stator for 74kHz.

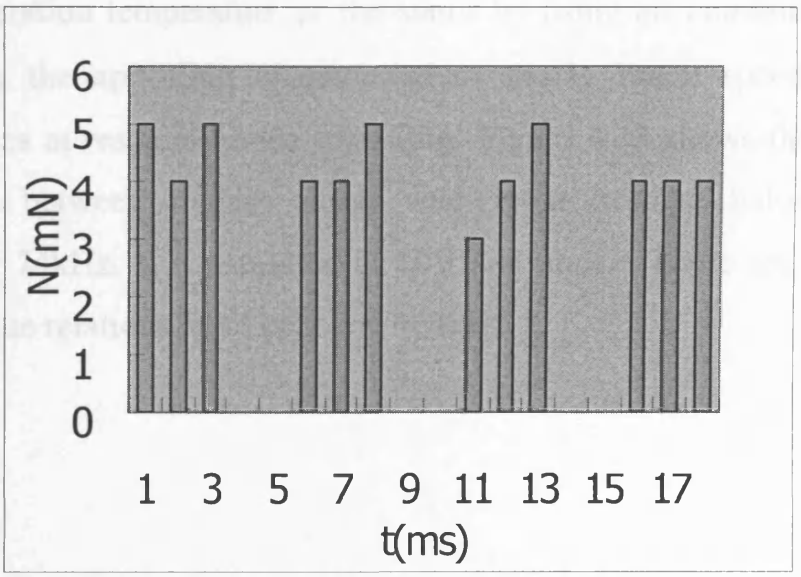


Figure 4.15. The radial contact force.

The rotor velocity performance derived through contact-friction force is shown in Figure 4.16(a)-(c). The average speed of the rotor decreases with time; there exist speed fluctuations within a very wide range, for example about 10rpm at 74kHz, 12rpm at 84kHz and 8rpm at 104kHz in each periodic cycle. The driving conditions and structure of the stator cause the fluctuations. In general, the ultrasonic motor has non-linear speed characteristics; moreover, they vary with driving condition like temperature rise and pre-load change. Figure 4.17(a)-(c) shows the comparisons between theoretical calculation, equation (4.20), and experimental data. These results were measured at a constant interval(about 2s) by fast sweeping input power, in fact the photometer just picked up five speed data, other five speed data can be approached interpolatively. The reason for setting 2s test interval is the speed fast fluctuation and decay after the interval, if the test interval took longer, the real data would far escape to follow the theoretical model. In fact, if we cool the operation temperature of the stator by using air condition, they would have the appealing characteristics—nearly linear speed-torque characteristics at resonant mode operation. Figure 4.18 shows the linear relationship between output torque and input voltage below 10V operation at 74kHz. It is saturated at 10V and above. There are similar voltage-torque relations at 84 kHz and 104kHz.

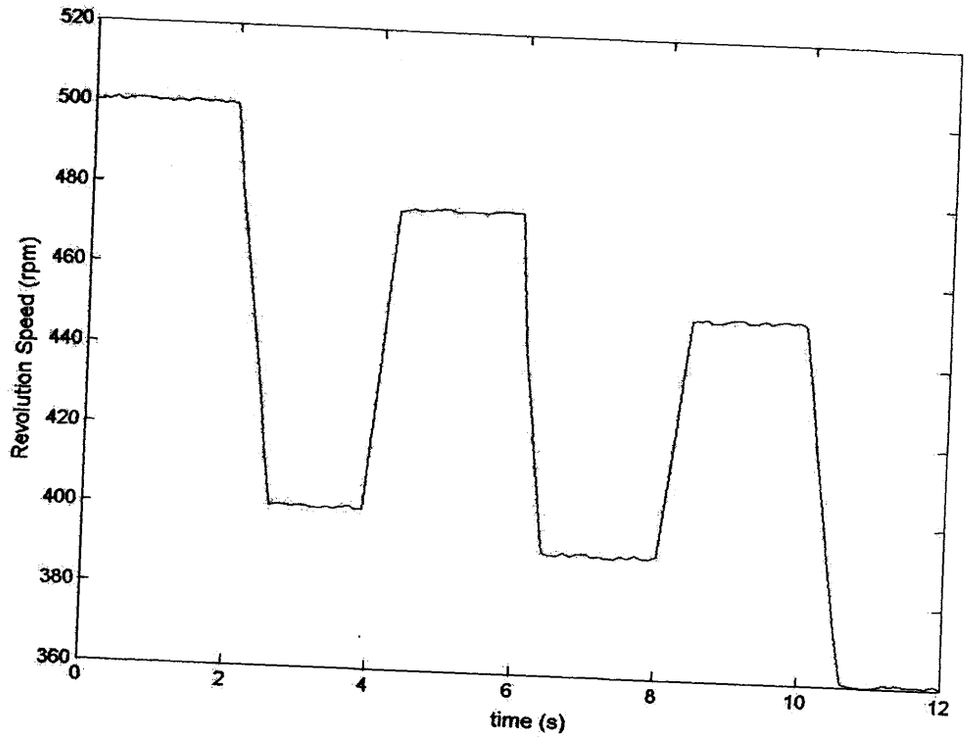
Revolution Speed (rpm)
520
500
480
460
440
420
400
380
360
0
2
4
6
8
10
12
time (s)

(a)

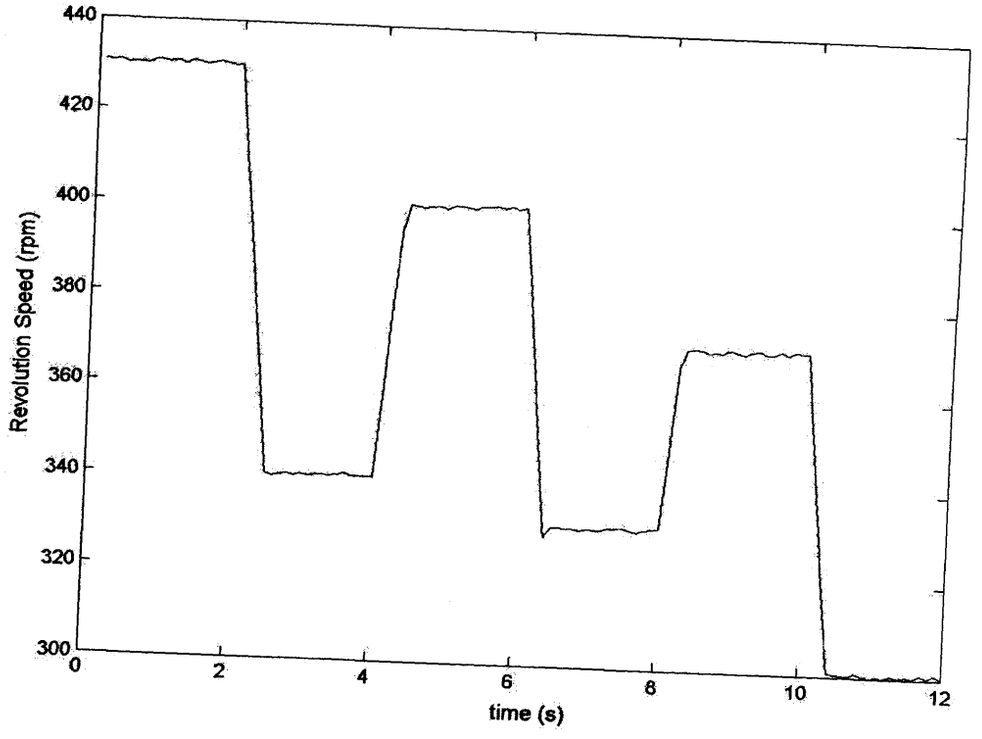
Revolution Speed (rpm)
440
420
400
380
360
340
320
300
0
2
4
6
8
10
12
time (s)

(b)

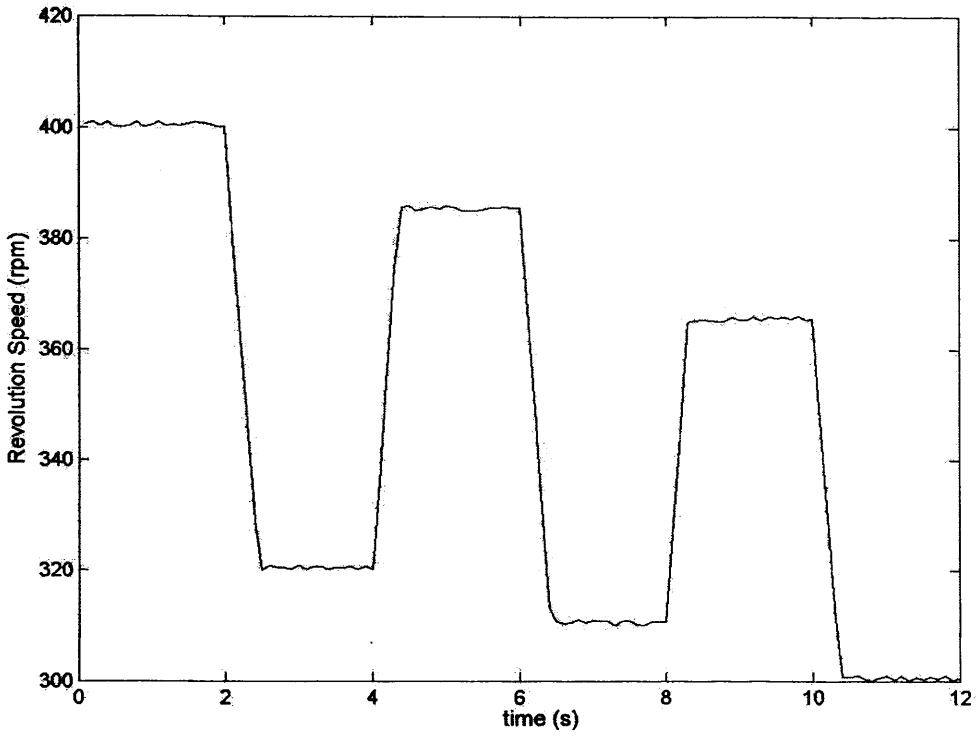


(c)

Figure 4.16. The rotor velocity at (a) 74kHz, (b) 84kHz and (c) 104kHz.

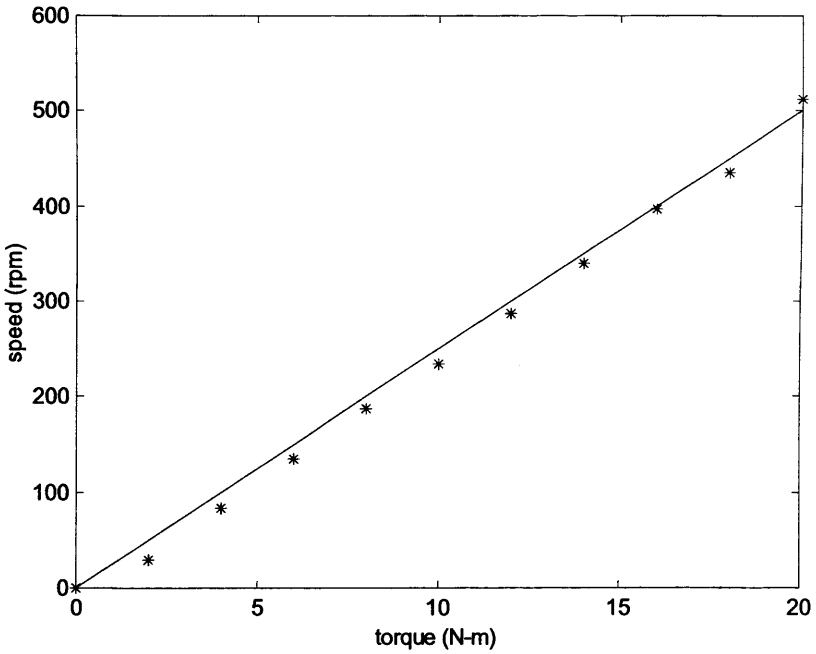


(a)

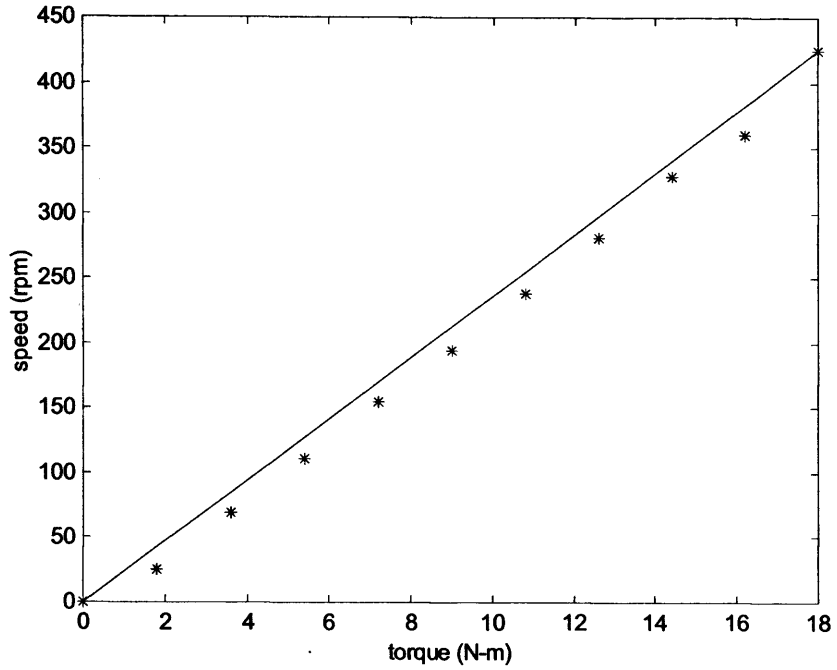


(b)

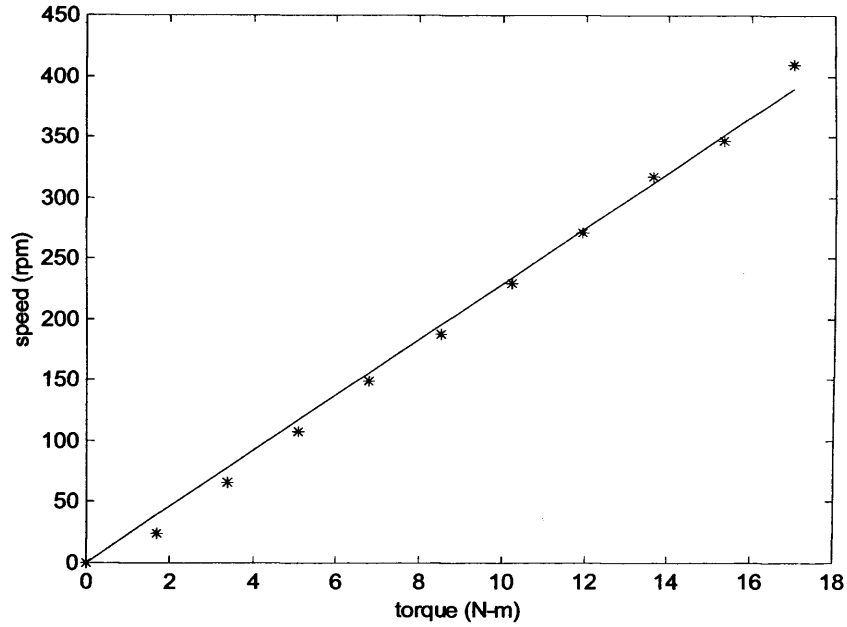


(c)

Figure 4.17. Comparisons of theoretical calculation and experimental data for speed-torque characteristic at (a) 74kHz, (b) 84kHz and (c) 104kHz (analysis(—); experiment(×), the initial test interval is 2s).

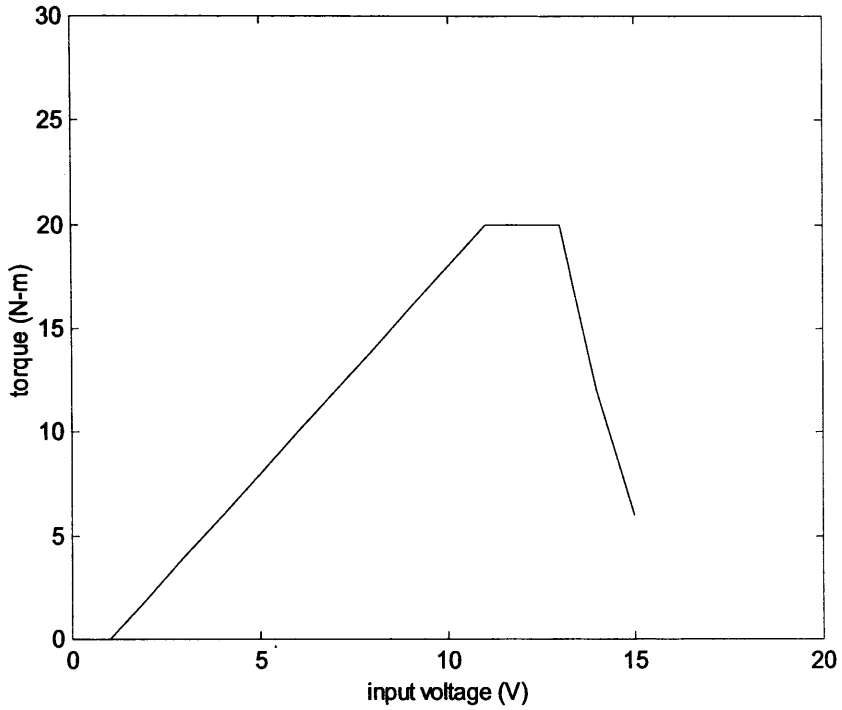


Figure 4.18. The relationship between input voltage and output torque at 74kHz.

# Chapter 5 Equivalent Circuit Estimation of the Ultrasonic Motor

## 5.1 Introduction

In Chapter 2, a new disc-type ultrasonic motor with a non-equal-triangular (120°-90°-150°) [17] boundary condition was described. The contacted point between the stator and the rotor is located at the middle of the circumferential edge of the 90° angle section. The operating mode relies on the use of non-equal-triangular boundary mechanism to produce a lateral elliptic motion at the contact point that drives the rotor by friction force. This motor has better stability than other surface surfing type ultrasonic motors introduced in Chapter 1 because the contact problem has been simplified from a large area to a single point.

In order to systematically analyze the behaviour of the proposed motor, an equivalent circuit model for the motor should be first derived. Because there are sufficiently applicable equivalent circuit models [136]-[141] to represent the practical operation of ultrasonic motors, it will be very useful for the prototype and the evaluation of motor characteristics. It is also more convenient to use the equivalent electrical circuit approach where both electrical and mechanical portions of the ultrasonic stator are represented by electrically equivalent impedances. This approach has distinct advantages over the direct equation of motion approach by virtue of the powerful methods of network theory. This approach is based on the analogy that exists between the electrical and the mechanical systems. In this method, the ultrasonic stator is no longer

described by the complex differential equation and boundary conditions, but by a lumped electrical circuit. The equivalent circuit offers an explanatory and quick way of gaining a deeper insight into the dynamic behavior of the ultrasonic stator, and makes it easier to visualize interactions of the ultrasonic stator with external systems, such as electrical driving devices and wave propagation medium. The equivalent circuits are particularly useful for the analysis of systems consisting of complex structural members and coupling subsystems with several electrical and mechanical ports. Berlincourt et al. [142] showed the equivalent circuits of simple piezoelectric bars. Shuyu [143] presented an equivalent circuit of the vibrator consisting of a slender piezoelectric rod and a thin circular plate. The equivalent circuits of the rod and the plate were separately constructed and they were combined to build the equivalent circuits of the entire vibrator, which had a single electric port. Ebenezer [144] presented a three-port equivalent circuit of a piezoelectric cylinder. Chubachi and Kim [145] showed a transmission line model of a thickness mode ultrasonic transducer using a simplified equivalent circuit. Impedance and admittance matrices, which represent the three-port parameters, were derived and the equivalent circuit was constructed from these matrices. This circuit was applied to a multistack transducer and finally a single electric port equivalent circuit of the multistack was obtained. Koike et al. [146] presented a single electrical port equivalent circuit of the Langevin flexural transducer. Only the symmetrical vibration mode of the unloaded transducer was considered and the rotational angular velocity of one face of the transducer was considered as the mechanical output. Sherrit et al. [147] presented an equivalent circuit of an unloaded ultrasonic vibrator in longitudinal mode. Mechanical, dielectric and piezoelectric losses were accounted for by the imaginary components of the circuit parameters instead of the resistance elements.

Chen et al. [148] presented an equivalent circuit of a stacked and segmented ultrasonic actuator and performed the analysis of the circuit with PSPICE. Wang et al. [149] derived the dynamic models of ultrasonic actuators bonded on a beam. The axial deflection was taken into account and then static and dynamic capacitances were calculated. Tanaka and Aoyagi [150] and Aoyagi and Tanaka [151] derived a 4×4 transmission matrix together with one electromechanical equation and presented a block equivalent circuit. By using the circuit, the multilayered ultrasonic stator was analyzed for these different type of geometric and boundary conditions. A piezoelectric bending accelerometer was also analyzed using of the equivalent circuit [152]. The accelerometer was divided into several subsections and each subsection was analyzed with the equivalent circuit model. Cho et al. [153] presented the electromechanical behavior of a three-layered piezoelectric bimorph beam by using an electrically equivalent circuit with impedance elements. Tilmans [154] analyzed an electromechanical system by using the equivalent circuit. The electromechanical system was simplified as a lumped-parameter system and then calculated using the electric network theory.

This chapter deals with the development of an equivalent circuit of the ultrasonic motor and its application to the evaluation of its frequency characteristics. The equivalent circuit analysis is based on the principle of ultrasonic motor operations and is conducted from the viewpoint of the mechanic vibration of the piezoelectric ceramic disk. When an external electric field is applied on a piezoelectric ceramic disk, two equivalent vibrations will, one in the thickness direction [see Figure 5.1(b)] [155] and the other in the radial direction [see Figure 5.1(a)], be observed. However, when the thickness-to-radius ratio is very small, the extensional vibration in the thickness can be ignored. On the other hand, the tangential vibration and coupled vibration are induced due to the

non-equal-triangular boundary condition of the stator. The two-dimensional equivalent circuit model for the new disc-type ultrasonic motor is derived based on the above considerations. The rotor is assumed as a rigid body, and its effect will be separately added into the equivalent circuit model. In this chapter, the equivalent circuits are admittance-type expression of a piezoelectric stator and focused on the contacted point between the stator and the rotor with the most significant lateral elliptic motion effect [156]. However, they can also be impedance-type expressions. The impedance-type equivalent circuits can clearly show the motor operation point of frequency, because its good load characteristics are obtained by operation at anti-resonance points. Therefore, the aim of this chapter is to derive an equivalent circuit model based on real conditions and to predict those equivalent circuit parameters. We assume that its rotor is rigid in order to simplify the equivalent circuit model. The analysis models are mainly focused on radial vibration, tangential vibration and coupling vibration modes due to the non-equal-triangular boundary condition of its stator. However, the equivalent circuits are better available for the contacted point between the stator and the rotor with the most significant lateral elliptic motion effect.

In this chapter, the equivalent circuit analysis is separated into three parts: firstly, the frequency switch of the piezoelectric membrane induced by the non-equal-triangular boundary condition of the stator; secondly, the elliptical motion of the metal back plate at the contacted point between the stator and the rotor; and, thirdly, the equivalent circuit of the rotor induced by friction force. The analysis models are verified and estimated by experimental measurements including resonance frequency, anti-resonance frequency, input and output currents, input and output voltages and resolution speed.

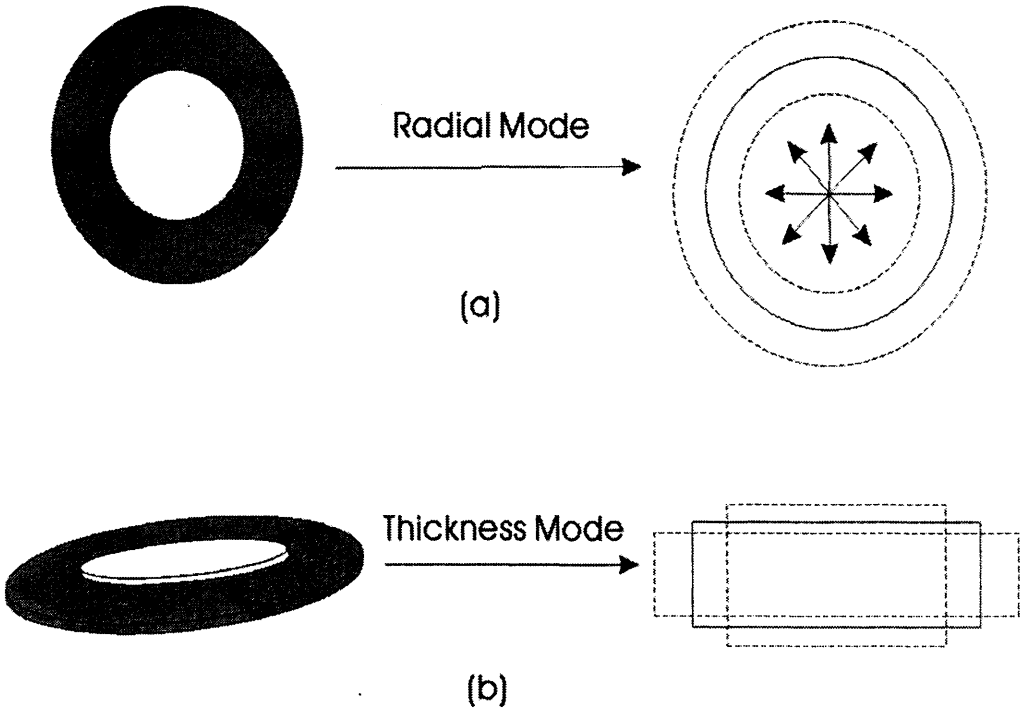


Figure 5.1. Resonance modes of the disc-type stator (a) radial mode (b) thickness mode.

## 5.2 Equivalent Circuit Models

### 5.2.1 Frequency Switch of Piezoelectric Membrane

When an external electric field is applied to the stator which includes a piezoelectric membrane and a metal back plate, the resonance modes observed are the planar mode, the thickness mode, and a number of lateral modes [155] related to the regular periodicity of the piezoelectric disk coating on the stator. For the case that we propose, the thickness resonance mode will be ignored due to the negligibly small thickness-to-diameter ratio. In our case, however, there exist tangential vibration mode and coupling vibration mode due to the non-equal-triangular boundary condition of the stator. Thus, tangential strains at edge need to be considered. For the equivalent circuit model of

the piezoelectric membrane, we assume, based on the experimental observations, which it is like a multi-frequency switch [see Figure 5.2]. These are driving frequencies, and resonance frequencies as well. The model is only available for the motor is running at these frequencies.

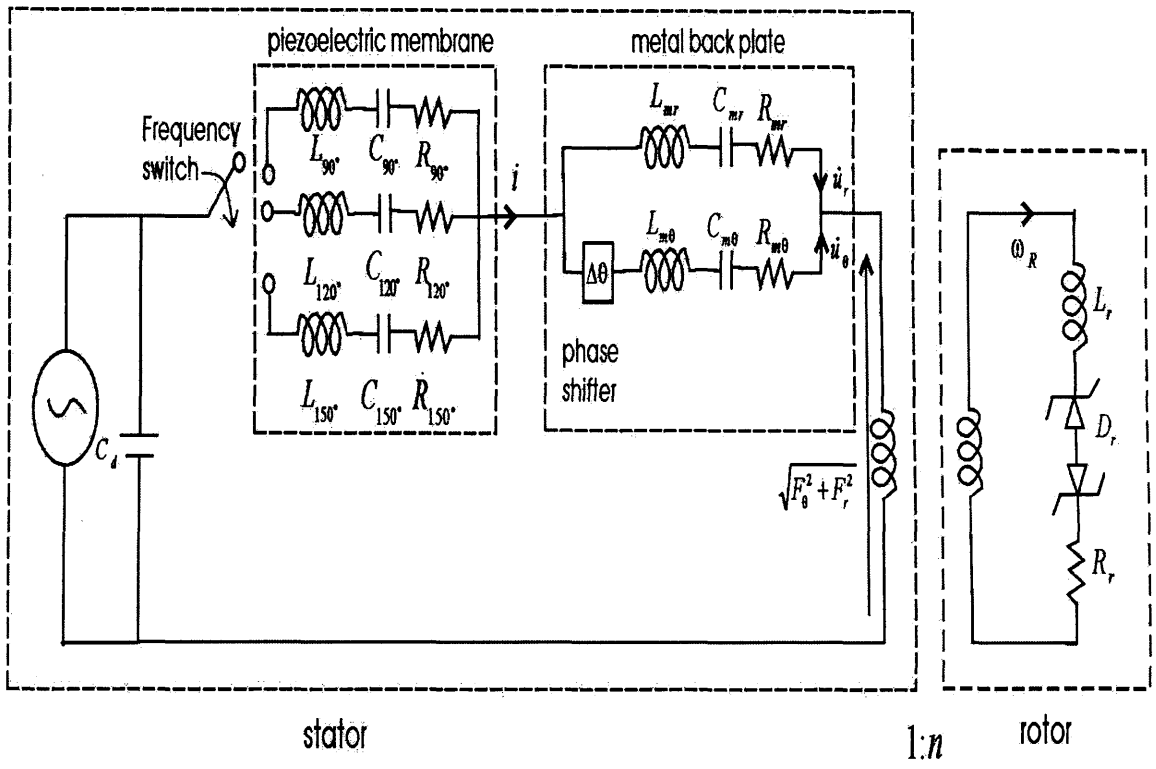


Figure 5.2. Equivalent circuit of the motor.

From the frequency response, we find that the resonance frequencies for 74kHz, 84kHz and 103kHz are caused by these standing waves induced from the included angels, i.e., 90°-103kHz, 120°-84kHz and 150°-74kHz. However, the analyses for these vibration modes are complex. The reason is that the modal interaction must be considered. In Figure 5.2, $L_\theta$, $C_\theta$ and $R_\theta$ ($\theta$=90°, 120°, 150°) represent equivalent inductor, capacitor and resistor for the pairs of 90°-103kHz, 120°-84kHz and 150°-74kHz, respectively, which are induced by wave reflecting from the edge of the metal back plate. These resonance and anti-resonance

frequency between 80kHz and 90kHz are these reflecting waves from the three fixed points and the three included angle sections, due to their heavy coupling effect and nonlinear behaviour, we will not include these frequencies into the linear equivalent circuit models. The $L_\theta$ and $C_\theta$ must satisfy the following relation,

$$L_\theta C_\theta = \frac{1}{4\pi^2 f_r^2}, \tag{5.1}$$

where $f_r$ is the resonance frequency obtained from experimental measurements.

### 5.2.2 Equivalent Circuit of the Metal Back Plate

The equivalent circuit of the metal back plate is also shown in Figure 5.2. It shall be noticed that the linear time-invariant model is valid under 10V applied voltage. $L_{mr}$, $C_{mr}$, and $R_{mr}$ represent the equivalent inductor, capacitor and resistor of radial vibration at the contact point, respectively, and $L_{m\theta}$, $C_{m\theta}$, and $R_{m\theta}$ represent, respectively, the equivalent inductor, capacitor and resistor of tangential vibration at the contact point. Meanwhile they must satisfy the following relations,

$$L_{mr} C_{mr} = \frac{1}{4\pi^2 f_r^2}, \tag{5.2}$$

$$L_{m\theta} C_{m\theta} = \frac{1}{4\pi^2 f_r^2}. \tag{5.3}$$

In addition, $\dot{u}_r$ and $\dot{u}_\theta$ are the radial and tangential velocities at the contacted point between the stator and the rotor, and the following lateral elliptic motion equation holds for their displacements:

$$\left[\frac{u_r}{(\overline{U}_r)}\right]^2 + \left[\frac{u_\theta}{(\overline{U}_\theta)}\right]^2 = 1, \tag{5.4}$$

where $\overline{U_r}$ and $\overline{U_\theta}$ represent normalized quantities, and $\overline{U_r} \neq \overline{U_\theta}$. It is noted that $r = a$ is the metal back plate radius. However, $u_r = 0, u_\theta = 0$ are at the three fixed points (120°-90°-150°) [17] locations. The lateral elliptic motion effect is most significant at the middle of the circumferential edge of 90° angle section, that is, the section with the contacted point. The effect reduces towards, and disappears at, those three fixed points. Thus the equivalent circuits of the radial and tangential vibrations are based on the contact point with the most significant lateral elliptic motion effect. In Figure 5.2, the phase shifter $\Delta\theta$ has to be equal to $\pi/2$. That is because when $\dot{u}_r$ and $\dot{u}_\theta$ have a phase difference of $\pi/2$, the elliptic motion of particle displacement can be formed. We use SCR equivalent circuit to simulate the phase shifter $\Delta\theta$ for its phase lag control.

### 5.2.3 Equivalent Circuit of the Stator

According to above assumptions, the complete equivalent circuit of the stator can thus be obtained as

$$L_{eq} = L_\theta + \frac{L_{mr} L_{m\theta}}{L_{mr} + L_{m\theta}}, \tag{5.5}$$

$$C_{eq} = \frac{C_\theta (C_{mr} + C_{m\theta})}{C_\theta + C_{mr} + C_{m\theta}}, \tag{5.6}$$

$$R_{eq} = R_\theta + \frac{R_{mr} R_{m\theta}}{R_{mr} + R_{m\theta}}, \tag{5.7}$$

where $L_{eq}$, $C_{eq}$ and $R_{eq}$ are the equivalent inductor, capacitor and resistor of the stator, respectively. Furthermore, the equivalent admittance

of the stator is given by

$$Y_{seq} = \frac{sC_{eq}}{s^2 L_{eq} C_{eq} + sC_{eq} R_{eq} + 1}, \tag{5.8}$$

where $Y_{seq}$ is the equivalent dynamic admittance under resonance frequency driving. So $s$ can be replaced by $j2\pi f_r$, where $f_r$ is the resonance frequency or driving frequency.

The mechanic force outputs of the stator can be obtained by

$$F_r = \frac{u_r}{C_{mr}}, \tag{5.9}$$

$$F_\theta = \frac{u_\theta}{C_{m\theta}}, \tag{5.10}$$

where $F_r$ and $F_\theta$ are the radial and tangential force of the stator at the contact point. It is noted that the vibration velocity and force have a phase difference of $\pi/2$ when $R_{eq} = 0$. The summary force is equal to $\sqrt{F_r^2 + F_\theta^2}$.

### 5.2.4 Equivalent Circuit of the Rotor

The complete equivalent circuit of the rotor is included in Figure 5.2. $L_r$ is the equivalent inductor of the rotor. Under consideration of the rotor transient response, it is as the following

$$L_r = A_r J, \tag{5.11}$$

where $A_r$ is the transfer factor, which is assumed as 1, and $J = \frac{mr^2}{2}$ the rotor moment of inertia with respect to its central axial, *m* the rotor mass and r the rotor radius. The equivalent capacitor of the rotor is neglected when the rotor is considered as a rigid body. $R_r$ represents the equivalent

resistor of the rotor. $D_r$ represents the direction restriction. $R_r$ and $D_r$ are used because the torsion vibration has the role of generating rotational force on rotor, and its energy is dissipated by rotor rotation.

The transfer ration between the stator and rotor is given by

$$n = \frac{\mu(F_r + F_c) + F_\theta}{\sqrt{F_r^2 + F_\theta^2}}, \tag{5.12}$$

where $\mu$ is the friction coefficient, which is assumed as 0.01, which is a typical value. It is noted that $F_c$, the pre-pressing force, must be included. The output torque of rotor induced by friction force can be obtained by

$$\tau_d = [\mu(F_r + F_c) + F_\theta]R. \tag{5.13}$$

Finally, the equivalent admittance of the rotor is given by

$$Y_{req} = \frac{\omega_R}{\mu(F_r + F_c) + F_\theta}, \tag{5.14}$$

where $\omega_R$ is the revolution speed of rotor. These equivalent admittance responses of the motor for both transient and stationary cases will be detail described by PSPICE equivalent circuit simulation at the following sections.

## 5.3 Motor Characteristics Estimation

The equivalent circuits are very useful to estimate the motor characteristics in coupling vibrations. To test whether the previously derived models are good mathematical descriptions of the actual motor, it is necessary to conduct numerical analysis and experiments for the proposed motor. A dynamic analyzer, power meter and photometer as shown in Figure 2.1 are used to measure these responses and parameters. The material of the piezoelectric ultrasonic stator is PZT-5H membrane

with metal back plate. In order to measure the admittance response, the input sinusoidal electric signal applied to the stator must be small and non-linear effect is to be avoided as much as possible. In our design, only driving frequencies are considered. The reason is that they have high electro-mechanical coupling efficiency, high sensitivity and low loss even they are not fundamental modes. Figure 5.3 shows the electrical admittance response from the dynamic analyzer results.

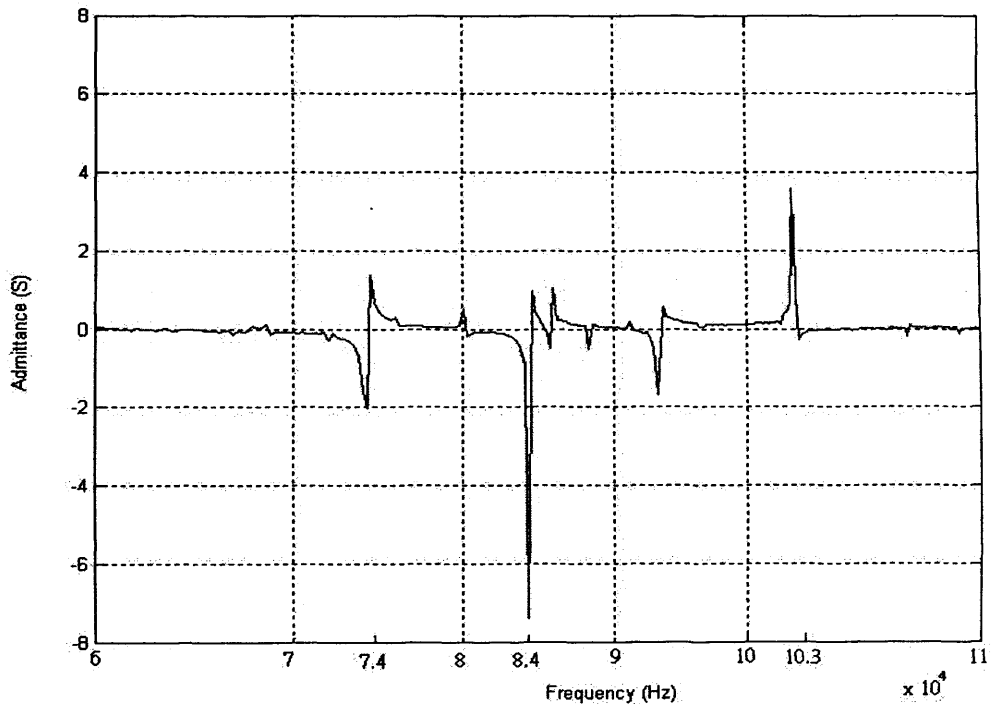


Figure 5.3. The electrical admittance response from dynamic analyzer measurement (x axial is algorithm scale).

First, the equivalent capacitance of stator from equivalent circuit analysis can be checked by the resonance frequency and anti-resonance frequency in Figure 5.3. The relationships are given by

$$C_{eq} = C_d \frac{f_r^2 - f_o^2}{f_o^2}, \tag{5.15}$$

where $f_o$ and $C_d$ are the anti-resonance frequency from measurement

and piezoceramic clamp capacitance, respectively. Furthermore, the equivalent admittance of stator is given by

$$Y_{seq} = \frac{i_{out}}{V_{out}}, \tag{5.16}$$

where $i_{out}$ is the measured output current, and $V_{out}$ the measured output voltage. Equation (5.16) is equivalent to (5.8). Thus $R_{eq}$ can be acquired from equation (5.8), (5.15) and (5.16). However $R_\theta$, $R_{mr}$ and $R_{m\theta}$ are the coupling effect of $R_{eq}$, and they cannot be obtained separately.

Secondly, $i_{out}$ has the following relation

$$i_{out} = A_i(\dot{u}_r + \dot{u}_\theta), \tag{5.17}$$

where $A_i$ is transfer factor, which is assumed as 1 so the vibration speed can be equivalent as a output current. $i_{out}$ is known, and $\dot{u}_r$ can be obtained from the experimental measurement [see Figure 5.4]. Therefore, $\dot{u}_\theta$ can be also obtained from Equation (5.17). In addition, $V_{out}$ also has the following relation

$$V_{out} = A_V\sqrt{F_r^2 + F_\theta^2}, \tag{5.18}$$

where $A_V$ is transfer factor, which is assumed as 1. $V_{out}$ is known, and $F_r$ can be acquired from the experimental measurement [see Figure 5.4]. Therefore, $F_\theta$ can be obtained from Equation (5.18). According to the above derivations, together with Equations (5.9) and (5.10), $C_{mr}$ and $C_{m\theta}$ can be calculated, then $L_{mr}$ and $L_{m\theta}$ can be obtained from Equations (5.2) and (5.3). Furthermore, substituting these parameters into Equations (5.5) and (5.6), $L_\theta$ and $C_\theta$ can be obtained. Substituting $L_\theta$ and $C_\theta$ into Equation (5.1), the resonance frequency can be calculated and verified. The computed and measured results are listed in Table 5.1. It shows that

the measured frequencies are in good agreement with the computed results.

Table 5.1. Driving frequency comparison between calculation and measurement.

| | Driving frequency | | |
|---|---|---|---|
| | $1^{st}$ (kHz) | $2^{nd}$ (kHz) | $3^{rd}$ (kHz) |
| Calculate | 73.52 | 83.41 | 102.31 |
| Measure | 74 | 84 | 103 |
| Error(%) | 0.65 | 0.70 | 0.67 |

Finally, the motor output power is given by

$$P_{out} = \tau_d \omega_R , \tag{5.19}$$

and its efficiency is calculated from the following

$$\eta = \frac{P_{out}}{i_{in} V_{in}} , \tag{5.20}$$

where $i_{in}$ is the measured input current, and $V_{in}$ the measured input voltage. Table 5.2 shows the motor efficiency value under its driving frequencies. The efficiency is very low due to it being one single contact point and just using one of all standing-wave-energy envelopes inside the stator, meanwhile the stator is a commercial buzzer device, in fact, itself has lots acoustic energy loss but it is cheap. It is noticed that possible errors exist in the parameter derivations in the above equivalent circuits. That may be due to the following reasons: (1) The standard material parameters are different from the actual values in the experiment; (2) The existence of the scattering effect comes from the non-equal-triangular

boundary locations. Table 5.3 lists the simulation parameter value for the equivalent circuit model of the stator. The parameter value for the equivalent circuit model of the rotor between calculation and measurement is shown in Table 5.4.

Table 5.2. Motor efficiency measurement value under driving frequency condition.

| Driving Frequency | Input Power(m VA) | Output Power(m W) | Efficieny $\eta(\%)$ |
|---|---|---|---|
| $1^{st}$ (74kHz) | 10 | 1.2 | 12 |
| $2^{nd}$ (84kHz) | 10 | 1.3 | 13 |
| $3^{rd}$ (103kHz) | 10 | 1 | 10 |

To show these results of the time evolutions of simulated responses for both transient and stationary cases, we use PSPICE circuit simulation to check the equivalent circuit of the motor for its transient and stationary response, Figure 5.5 shows the simulation result under 1 ms delay switch-on time for transient and stationary response of motor for 74kHz driving. The simulation results for 84kHz and 103kHz are similar to 74kHz. The simulation results show that the frequency switch on time would have only a effect of delay output, the stationary outputs still are sine output due to resonant driving.

Table 5.3. Simulation parameter value for the equivalent circuit model of the stator.

| Simulation parameter | |
|---|---|
| $C_d$ | 77nF |
| $L_{90°}$ | 2.2mH |
| $L_{120°}$ | 1.9mH |
| $L_{150°}$ | 1.6mH |
| $C_{90°}$ | 2.124nF |
| $C_{120°}$ | 1.8666nF |
| $C_{150°}$ | 1.5172nF |
| $R_{90°}$ | 675.0482Ω |
| $R_{120°}$ | 676.7037Ω |
| $R_{150°}$ | 678.965Ω |
| $L_{mr90°}$ | 770.95pH |
| $L_{mr120°}$ | 717.98pH |
| $L_{mr150°}$ | 511.63pH |
| $C_{mr90°}$ | 6mF |
| $C_{mr120°}$ | 5mF |
| $C_{mr150°}$ | 4.7mF |
| $R_{mr90°}$ | 238.97uΩ |
| $R_{mr120°}$ | 252.63uΩ |
| $R_{mr150°}$ | 220.74uΩ |
| $L_{m90°}$ | 101.54pH |
| $C_{m90°}$ | 45.6mF |
| $R_{m90°}$ | 31.475uΩ |
| $R_{r90°}$ | 23.897uΩ |
| $L_{m120°}$ | 122.68pH |
| $C_{m120°}$ | 29.3mF |
| $R_{m120°}$ | 43.167uΩ |
| $R_{r120°}$ | 30.315uΩ |
| $L_{m150°}$ | 78.039pH |
| $C_{m150°}$ | 30.6mF |
| $R_{m150°}$ | 33.67uΩ |
| $R_{r150°}$ | 28.696uΩ |
| $L_r$ | 5.6349uH |

Table 5.4. Parameter values for the equivalent circuit model of the rotor between calculation and measurement.

| | Calculation | Measurement |
|---|---|---|
| $\mu$ | 0.01 | |
| $F_\theta$(N)(90°) | $3.5\text{x}10^{-3}$ | |
| $F_\theta$(N)(120°) | $3.4\text{x}10^{-3}$ | |
| $F_\theta$(N)(150°) | $2.6\text{x}10^{-3}$ | |
| $F_r$(N)(90°) | | 0.05 |
| $F_r$(N)(120°) | | 0.04 |
| $F_r$(N)(150°) | | 0.03 |
| $F_c$(N) | | 0.1 |

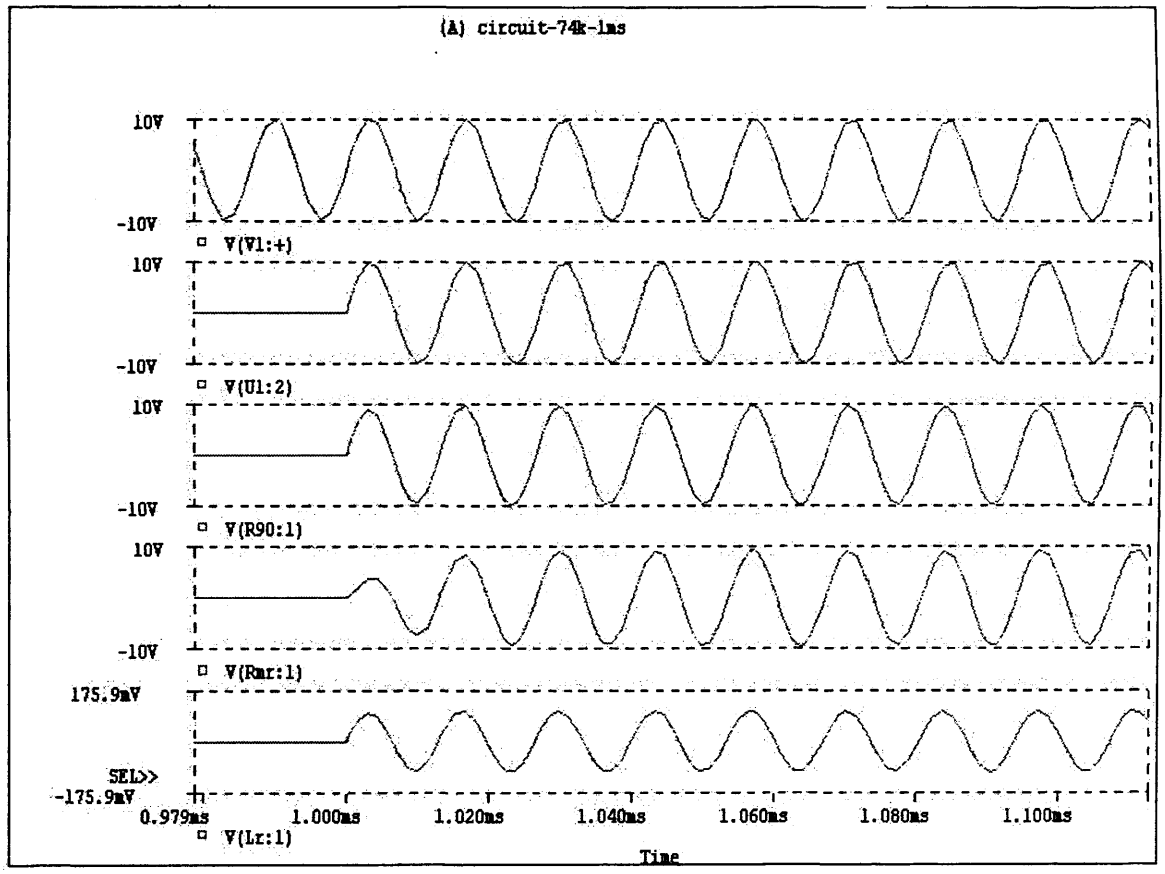


Figure 5.4. PSPICE circuit simulation of the motor for its transient and stationary response for 74kHz under 1ms delay switch-on time (V1: input voltage; U1: switch-on input voltage).

# Chapter 6 Speed Control of the Ultrasonic Motor by Using a Current Controller

## 6.1 Introduction

Ultrasonic motors usually are required to drive at low input power yet to produce maximum efficiency. However, ultrasonic motors inherit nonlinear speed characteristics that vary with driving conditions such as rising temperature and changing pre-load. Also the structure of the stator would cause speed fluctuation. Thus, it is necessary to exhibit the efficiency characteristic of an ultrasonic motor and to drive the motor at its maximum efficiency point with a control scheme. Use of adjustable speed drive system to raise the efficiency of an ultrasonic motor has been considered for a long time [157]. Reference [158] presented a speed control method for ultrasonic motors by using pulse width modulated (PWM) control scheme of dc voltage source combined with drive frequency control, in order to realize the speed control at maximum efficiency. [42] proposed some frequency tracking control plans for ultrasonic motors, which can keep revolving speed constant using relationship between the generated voltage and actual motor speed.

For rotors used in a high-speed, rotational experiment, the controllability and efficiency have to be taken into account. So a specific drive circuit control technique is required. [159] and [160] propose to design PI controllers with the features of simple structure, stability and reliability, which can be well tuned. However, those controllers may not maintain the performance results when the plant characteristics vary.

Several other driving circuits, using a two-phase half-bridge series-resonant inverter with an approximated unity switching frequency to resonant frequency ratio, have been reported in [35], [161]-[163]. However, good dynamic performance of the motor is difficult to obtain due to the unbalanced and peak value varying two-phase voltages. In recent years, some applications of fuzzy neural network systems in ultrasonic motor speed/position control have been reported [161]-[163]. For example, a hybrid adaptive-intelligent control system combining the adaptive control theories with fuzzy control techniques [163]-[164] or neural-network control approaches [165]-[166] can be used to deal with nonlinearities and uncertainties of the ultrasonic motor control systems. [167]-[168] proposed an adaptive fuzzy-neural-network control (AFNN) system using two inductances and two capacitances (LLCC) resonant techniques to control a rotary traveling wave-type ultrasonic motor. Their motor drive system is realized by a fuzzy-neural-network identifier (FNNI) to provide the sensitivity information for the drive system to their adaptive controller. The objective is to make the tracking error converge to zero to achieve a favorable control performance. However, these fuzzy-neural-network control models require more auxiliary circuits for signal processing and the algorithms will demand much DSP computing time. They may not be, therefore, suitable for real time industry applications.

In order to achieve high level of efficiency, ultrasonic motors should be driven at near resonant frequencies. Driving ultrasonic motors at the resonant and anti-resonant frequencies may reduce the load on the piezoceramic as well as on the power supply [12]. The parameters of an ultrasonic motor are all dependent on the operating temperature, running time, and mechanical quality factors. In addition, because an ultrasonic motor with two-phase construction is coupled mechanically and the

reaction from the electrical to the mechanical part is unbalanced for the two phases, the equivalent two-phase loads of the rotor are unbalanced and the equivalent resistor values vary for different rotating directions, rotor speeds, load torque, applied voltages, and static pressure force between the stator and the rotor. Due to the above reasons, the quality factors of the resonant inverter in the A and B phases are not equal. Moreover, they are time varying and load-condition dependent. [169] proposed that although the quality factors of two RLC tanks vary for different rotating speed and are not equal, the output voltage in phase A and B can be maintained at the same peak voltage when the inverter is operated closely to the geometric frequency. In that case, the rotor speed is smooth and constant. However, as a result, more complex circuits are needed for stabilizing the variation at the output.

The ultrasonic motor proposed in this thesis deals with the load-unbalanced problem well, but there still exist some other variations such as frequency deviation and temperature rise that will directly affect the motor speed and output efficiency. However, these drifts have a common origin, i.e. related to thermal factor. The temperature rise due to the internal losses and friction at rotor-stator interface causes an increase in the compliance as well as in the blocking capacitance, which generates a decrease of the resonance frequency. As a result, the motor speed decreases if the motor is driven at a fixed frequency. So a speed controller is necessary to avoid the fluctuation. The development of such a controller is the theme of this chapter. There are usually three approaches to adjust the motor speed: by setting the vibration amplitude of stator, by tracking the driving frequency or by tracking the phase. In this research, a controller consisting of a voltage-controlled oscillator (VCO), a compensated capacitor $C_s$, and a differential amplifier is used to maintain

the operation current so that the vibration amplitude of the stator can be maintained. Further, adjustment of the motor speed is implemented by a PI type speed controller which stabilizes the closed-loop system. It is shown that the degradation of tracking performance is significantly reduced by this error-driven mechanism.

## 6.2 Speed Characteristics of the Motor

### 6.2.1 Vibration Characteristics of the Stator

The driving principle of the motor is based on high frequency mechanical vibration, and the vibration force is generated by the piezoelectric ceramic located in the stator. A single-phase equivalent circuit model of the stator is shown in Figure 6.1. In Figure 6.1, $R_i$ is the mechanical loss, $C_i$ is the equivalent capacitance, $L_i$ is the equivalent inductance, $C_d$ is the damped capacitance, and $i$ the so-called motional current. To achieve high efficiency, the stator should be driven at an approximate frequency, which will create resonance between $C_i$ and $L_i$ in the equivalent circuit. In a complex notation, the damped admittance $Y_d$ and the motional admittance $Y_{eq}$ are given by equations (6.1) and (6.2)

$$Y_d = j\omega C_d, \tag{6.1}$$

$$Y_{eq} = \frac{1}{R_{eq}} = \frac{1}{j\omega L_i + \frac{1}{j\omega C_i} + R_i}, \tag{6.2}$$

in the resonant state, these admittance change as $Y_d = j\omega_o C_d$ and $Y_{eq} = \frac{1}{R_{eq}}\Big|_{\omega=\omega_o}$, where $\omega_o$ is the resonance frequency.

The transfer function of the stator can be obtained [156] from piezoelectric constitutive equation derivation as follows:

$$G(S)=\frac{u_r}{V}=\frac{Kd_{31}}{(S-\omega_o)(S-\omega_a)}, \tag{6.3}$$

where $K$ is the transfer coefficient , $d_{31}$ is the piezoelectric constant, $\omega_a$ the anti-resonance frequency, $u_r$ the radial vibration displacement, and $V$ the applied voltage. In addition, $u_r$ has to satisfy the lateral elliptic motion equation [126]:

$$\left[\frac{u_r}{(\overline{U_r})}\right]^2+\left[\frac{u_\theta}{(\overline{U_\theta})}\right]^2=1, \tag{6.4}$$

where $u_\theta$ is the circumferential displacement, and $\overline{U_r}$ and $\overline{U_\theta}$ are to normalize those two vectors. Notice that in general $\overline{U_r}\neq\overline{U_\theta}$. Equations (6.3) is linked to the transfer function model of the motor, equation (4.14), derived in Chapter 4. This is a second-order S domain function, in physical mean, it represents impendence response. So, equation (4.14) has to have two conjugative complex values, that is it can be separated as two first-order conjugative functions and their solutions must be resonance and anti-resonance frequency, $\omega_o$ and $\omega_a$, they are pair and conjugation. Driving ultrasonic motors at the resonant and anti-resonant frequencies may reduce the load on the piezoceramic as well as on the power supply. The detail has been described at Chapter 1.

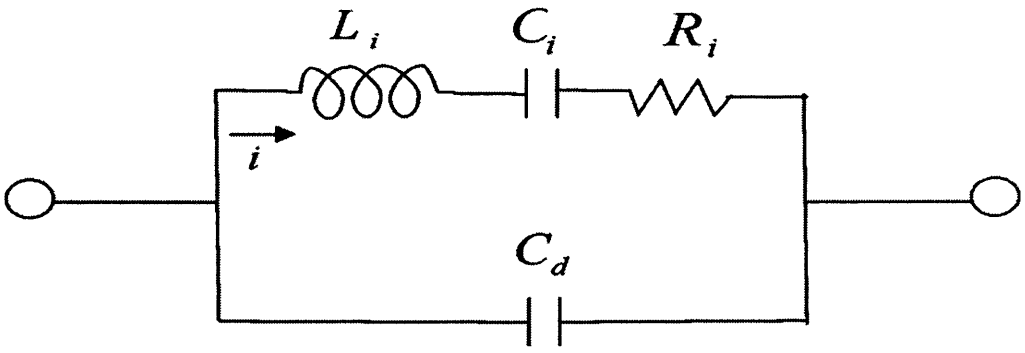


Figure 6.1. Equivalent circuit model of the stator.

### 6.2.2 Revolution Speed of the Rotor

Due to the induced motion, the region in Figure 1 with a 90° included angle will make contact with the rotor. As a result, a contact force $\vec{F}_d$ acts on the rotor edge. The contact force is given as

$$F_d = F_\theta + \mu(F_r + F_c), \tag{6.5}$$

where $F_r$ and $F_\theta$ are the radial and tangential forces of the stator at the contact point, and $\mu$ and $F_c$ are the kinetic friction coefficient and pre-pressing force. The angular displacement $\theta$ of the rotor is a function of the applied torque $\tau_d$, as follows:

$$J\ddot{\theta} = J\dot{\omega}_R = \tau_d = F_d r, \tag{6.6}$$

Where $J = \frac{mr^2}{2}$ is the rotor moment of inertia with respect to its central axial, m is the rotor mass and r is the rotor radius, and $\omega_R$ is the revolution speed of the rotor. The torque-angular displacement transfer function in S- domain can be obtained from equation (6.6) as follows:

$$\frac{\Theta}{T_d} = \frac{1}{JS^2}, \tag{6.7}$$

where $\Theta$ and $T_d$ are the Laplace transforms of $\theta$ and $\tau_d$, respectively. Furthermore, $\tau_d$ can be further simplified as

$$\tau_d = K_T u_r, \tag{6.8}$$

where $K_T$ is assumed as force factor. Equations (6.5)-(6.8) are linked to the transfer function model of the motor derived in Chapter 4.

## 6.3 The Control Method

### 6.3.1 Current Controller

For the motor under consideration, the relation between revolution velocity and operation current is not linear, contrary to the case of vibration velocity. This non-linear character is due to the presence of the parallel resonance phenomenon in the operation range. To obtain a good correlation between motor speed and operation current, a compensation capacitor can be added. The block diagram of the current controller of the motor is implemented as shown in Figure 6.2. This controller is composed of a voltage-controlled oscillator (VCO), a compensation capacitor $C_s$, and a differential amplifier. The voltage drop in the stator is divided into three parts: the voltage drop caused by the equivalent resistance, by the equivalent inductance and by the equivalent capacitance. A VCO is included here so as to maintain the output voltage at a constant peak value under the fluctuated-output frequency and current control. Because the main effect of the stator is a piezo capacitor effect, which always varies with frequency deviation and temperature rise that will affect the stator vibration velocity and cause the revolution speed fluctuation of the motor, the $C_s$ and differential amplifier are added to maintain an operation current. With the compensation effect, the total equivalent impedance is equal to

$$R = R_{eq} - \frac{1}{j\omega C_s}. \tag{6.9}$$

Due to inclusion of the compensation capacitor $C_s$, the variation of the total equivalent impedance caused by the total equivalent capacitor should be zero, that is,

$$\left.\frac{\partial R}{\partial C}\right|_{\omega=\omega} = \left.\frac{\partial R_{eq}}{\partial C_i}\right|_{\omega=\omega_o} + \frac{1}{j\omega_o C_s^2} = \frac{1}{j\omega_o}\left(\frac{1}{C_s} - \frac{1}{C_i}\right), \tag{6.10}$$

so that $C_s = C_i$. In addition, $C_i$, the equivalent capacitance of the stator, can be measured from the experimental resonance and anti-resonance frequency as follows

$$C_i = C_d \frac{\omega_n^2 - \omega_o^2}{\omega_o^2}. \tag{6.11}$$

As a result, the dynamic compensation capacitor $C_s$ can be obtained from Equation (6.11) and $C_d$ value is provided by manufacturer (see Table 2.1). In real condition, $C_s$ can be realize by attaching another same stator back-to-back the original stator and feedback signal from the original stator through a charge amplifier, which can change polarity, to the attached stator. After using the current controller, the variation of the displacement-voltage transfer function of the stator at a fixed driving frequency can be eliminated, due to its resonance and anti-resonance frequency being fixed. In that case, $G(S)\big|_{S=j\omega}$ is approximated to a constant gain $K_G$, where $\omega$ is a driving frequency, i.e., $G(S)\big|_{S=j\omega} \cong K_G$. In addition, to avoid sudden high operational current and/or overheat which could damage the stator, an over-current protection circuit system is implemented in the feedback-control drive circuit system as shown in Figure 6.3.

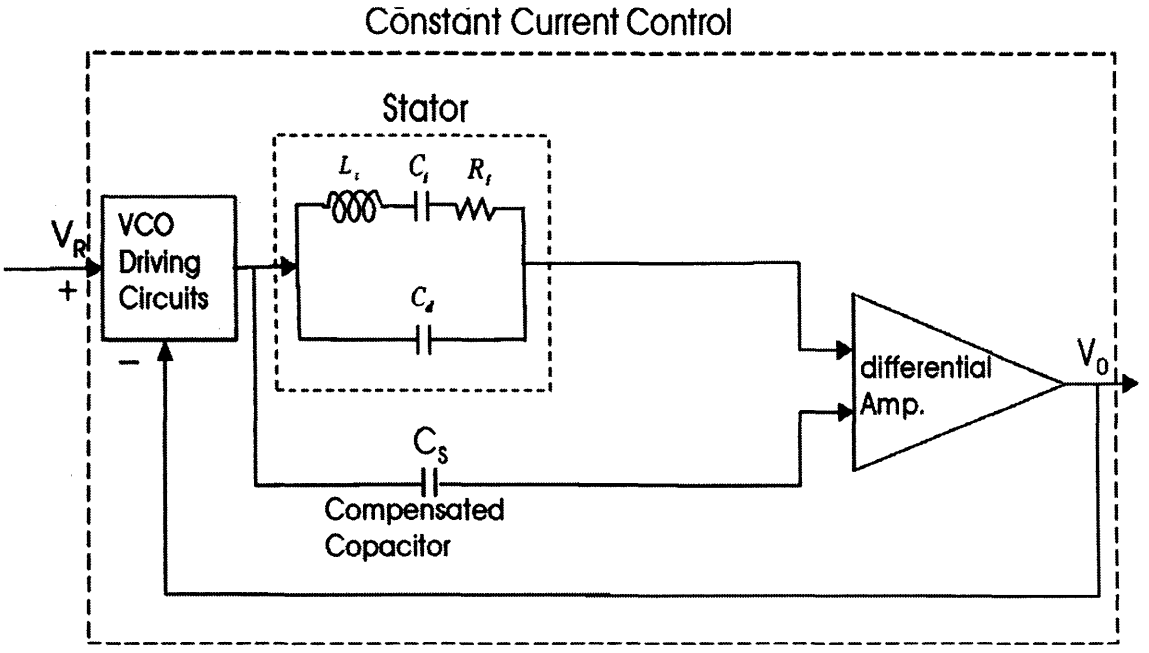


Figure 6.2. Block diagram of the current controller.

### 6.3.2 Speed Controller

Due to the fact that the speed fluctuation is time-varying and also depends on temperature condition, in order to effectively control the rotor speed of the motor, a controller is proposed in this section. Since the lumped dynamic model of the motor is unavailable, the gains of the speed controller are obtained by experimental observation and measurement. The configuration of the proposed speed controller for the motor is shown in Figure 6.3. For reliability and cost considerations in industry, a PI type control scheme is chosen. The parameters of the controller are tuned to meet the design performance specifications and stability requirement. Hence, when the plant parameter variations occur, the degradation of the tracking performance is significantly reduced by this error-driven mechanism set in the feedback loop. With the feedback compensation as shown in Figure 6.3, the forward-loop transfer function of the motor

control system can be obtained as

$$G'(S)=\frac{(K_PS+K_I)}{S}\times\frac{K_TK_G}{JS}=\frac{K_TK_G(K_pS+K_I)}{JS^2}, \tag{6.12}$$

where $K_P$ is the proportional gain and $K_I$ is the integral gain. Meanwhile, the speed error transfer function is obtained by

$$E(S)=\frac{\omega_R^*(S)}{1+G'(S)}=\frac{JS^2\omega_R^*(S)}{JS^2+K_TK_PK_GS+K_PK_IK_G}, \tag{6.13}$$

$$e_{SS}=\lim_{t\to\infty}e(t)=\lim_{S\to0}sE(S), \tag{6.14}$$

$e_{SS}=0$ , i.e., the steady-state response of the error function is zero corresponding to a step input. In the present design, the constants (parameters) of the controller are determined by experiences and via trial-and-error. For example, $k_p$ is always set as 1 due to that the main effect is the piezo capacitance, and $k_I$ and $k_G$ have been tried around about ten times of $k_T$ as the motor power efficiency is at most 10~15%.

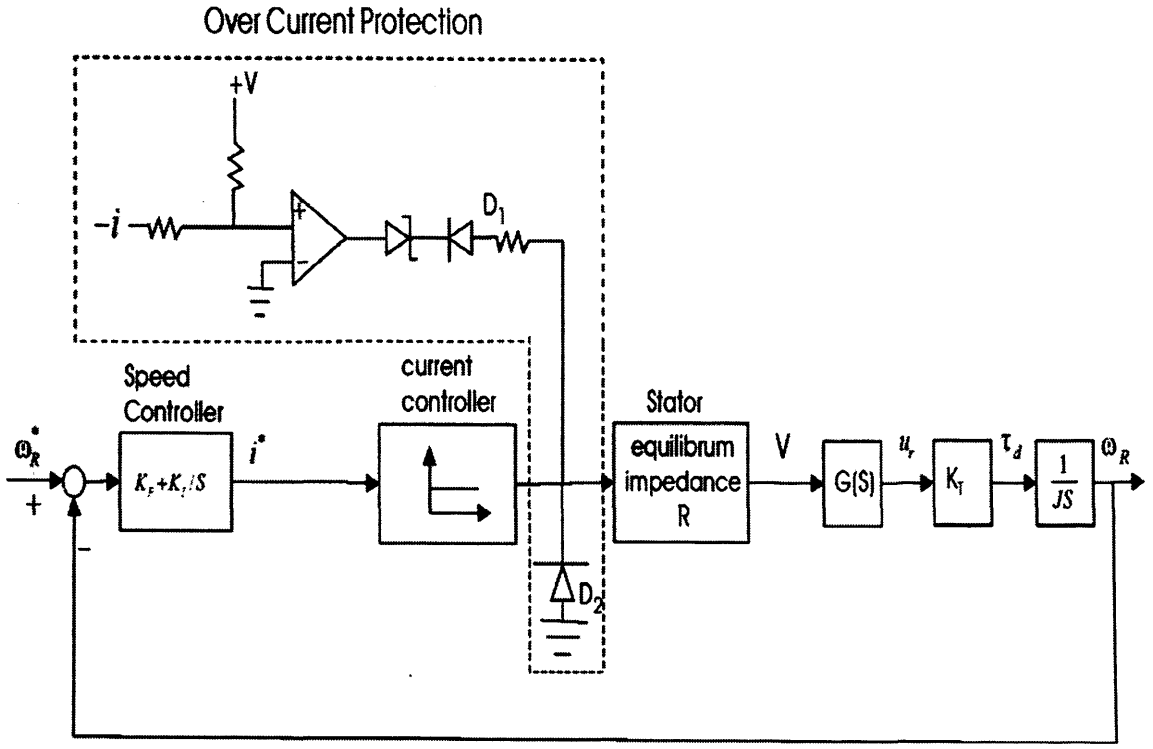


Figure 6.3. Block diagram of the speed-feedback control of the motor system.

## 6.4 Experimental Results and Discussions

Table 2.1 lists the parameters used in the verification of the performance response of the ultrasonic motor. Figure 6.4 shows the block diagram of the DSP-based computer control system for the motor drive. A TMS320C31 DSP is used to implement the closed-loop control system. A servo control card is installed in the control computer, which has multi-channels of D/A, PIO and detector interface circuits. The control signal processing is performed by the interrupt service routines (ISR) in the DSP. The interrupt intervals for the ISR'S are set at 2s. The ISR first reads the rotor speed from the photo detector, then obtains the Jacobian of the plant from the dual port RAM (DPRAM), sets the control signal and desirable rotor speed in the DPRAM, synchronizes the execution of the

DSP, and performs the closed-loop compensation. In Figure 6.4, the inverter is a single-phase AC-DC conversion driving circuit which is referenced to Chapter 2. The DSP hardware and software is a commercial build-in function PC-based digital servo control system and is developed by VisSim Technology Corporation, Taiwan. It is a lab instrument of Associate Professor Dr. Guo-Shing Huang at Department of Electronic Engineering National Chin-Yi Institute of Technology Taiping, Taichung, Taiwan. The control strategies of the current controller and the PI type speed controller are both tested. In the first batch of tests, the compensation capacitor is experimented for 74kHz, 84kHz and 104kHz driving frequencies and its values are calculated according to Equation (6.11). The results are shown in Table 6.1 and the capacitor parameters are of negative values that may be due to the need to balance the parasitic capacitance effect.

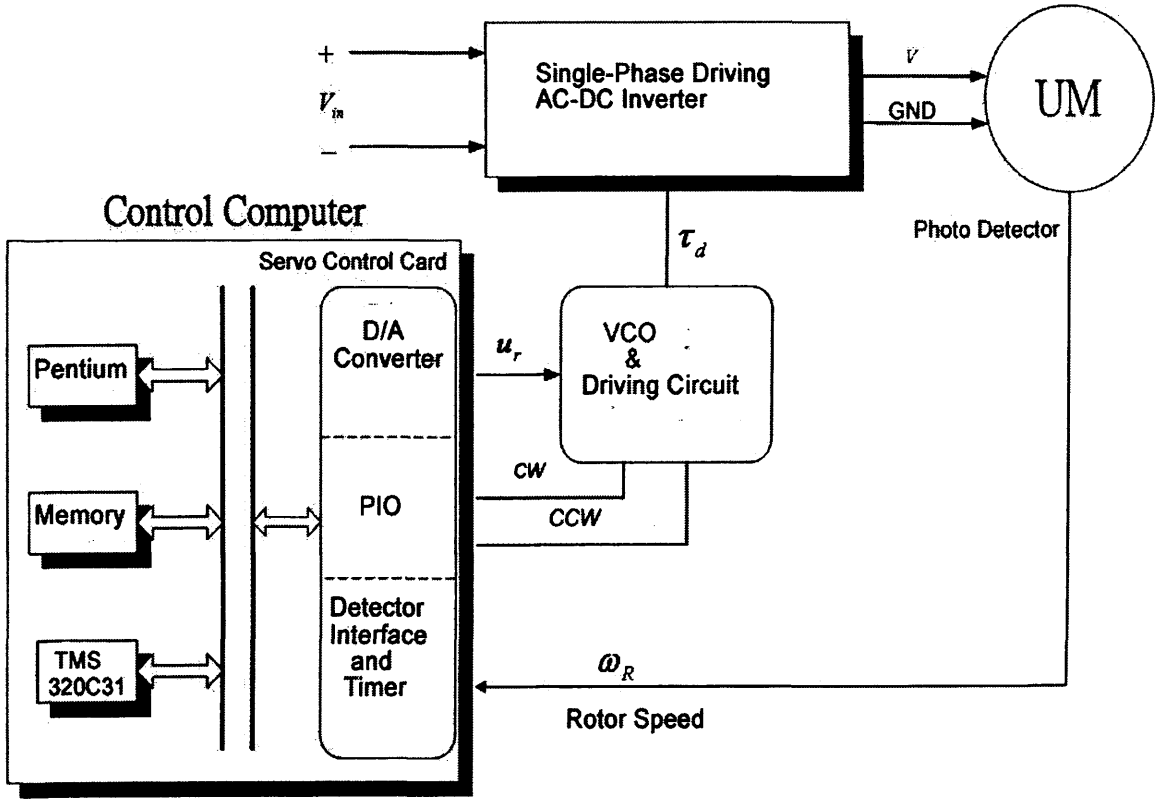


Figure 6.4. DSP-based computer control system.

In the second batch of tests, the current controller is experimented. The aim of the current controller is to remove these undesirable effects and minimize any steady state error for the stator. It shall be noted that the vibration velocity of the stator in the contact area with the rotor cannot be measured because the transverse direction measurement is not available. Figure 6.5 show the Nyquist plots of the stator with a current controller is in place. Using the Nyquist stability criterion, the system is shown to be stable driven at 74kHz, 84kHz and 104kHz driving-frequencies. So the idea of implementing an indirect current control by means of simple compensation capacitor principle has been found to be effective for the stability control of the stator.

Thirdly, the revolution-speed stability is tested. We set $K_T = 10$, $K_G = 100$, $K_P = 1$ and $K_I = 100$. The rotor-velocity performance derived through contact-friction force with and without the PI control is shown in Figure 6.6(a)-(c). These experiments are conducted with the current controller in the loop. The average speed of the rotor without speed-feedback control decreases with time; there exist speed fluctuations within a very wide range, for example about 10rpm at 74kHz, 12rpm at 84kHz and 8rpm at 104kHz in each periodic cycle. The rotor speed changes in step-like manner due to the intermit contact and detachment between the rotor and the stator. It should be pointed out that the rotor speed changes are not due to bad sampling effect. With the speed-feedback control scheme, the speed fluctuations have almost been eliminated. We thus can confirm that with a current control process already in place, a PI type speed controller will be powerful enough yet simple and thus suitable in industry to achieve transient performance requirements normally considered in practice. The input-output linearity of the total system, that is the minimal resolution of revolution speed, is near 0.1 rpm.

Finally, unit step transient responses are found to check the performance of the system. The ability of the controllers to attenuate a disturbance at the input and/or to a step change in the load is examined. Figure 6.7 shows the test results in the cases of with the current and PI controllers, with the PI control but without current control, and the case neither the PI control nor current control is used. The results show that the control schemes are efficient in reducing the overshoots up to a large percentage in comparison to the "open-loop" response, i.e. without using the control schemes.

Table 6.1. The compensated capacitor value for driving frequency.

| | compensated capacitor $C_s$ ($10^3$ pF) |
|---|---|
| Driving Frequency: (kHz) | |
| 74 | -4.1 |
| 84 | -4.7 |
| 104 | -3.6 |

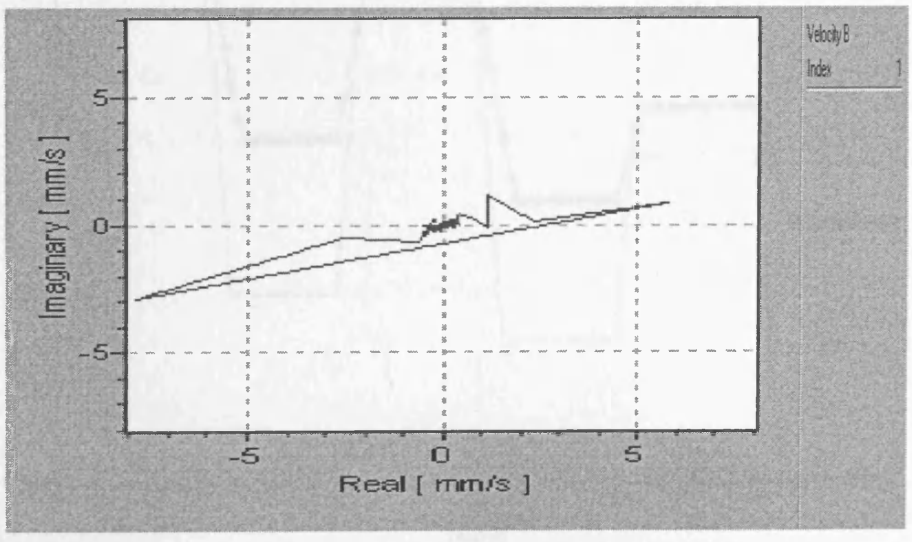


Figure 6.5. Nyquist plot of the stator with current controller at 74kHz.

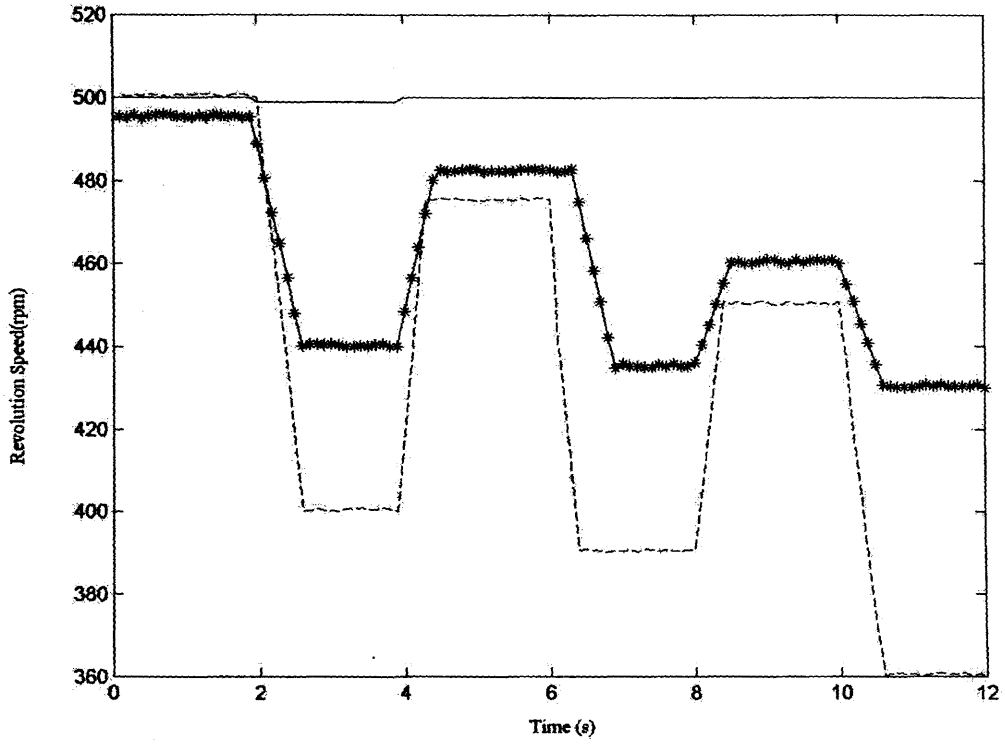
520
500
480
460
440
420
400
380
360
Revolution Speed(rpm)
0
2
4
6
8
10
12
Time (s)

(a)

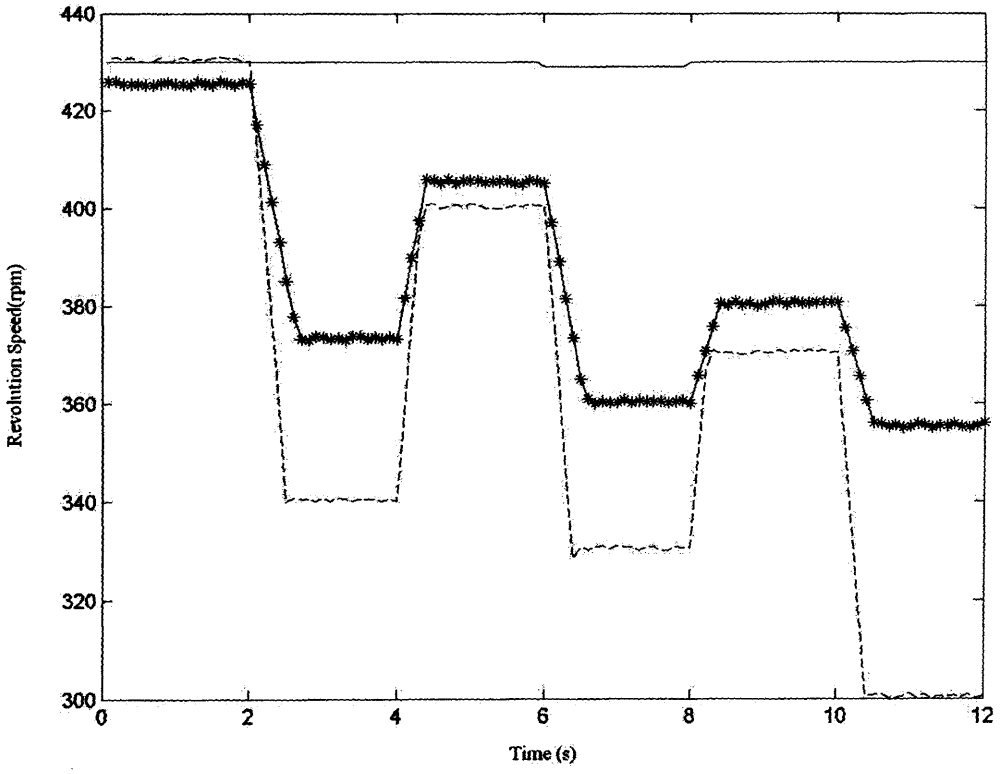
440
420
400
380
360
340
320
300
Revolution Speed(rpm)
0
2
4
6
8
10
12
Time (s)

(b)

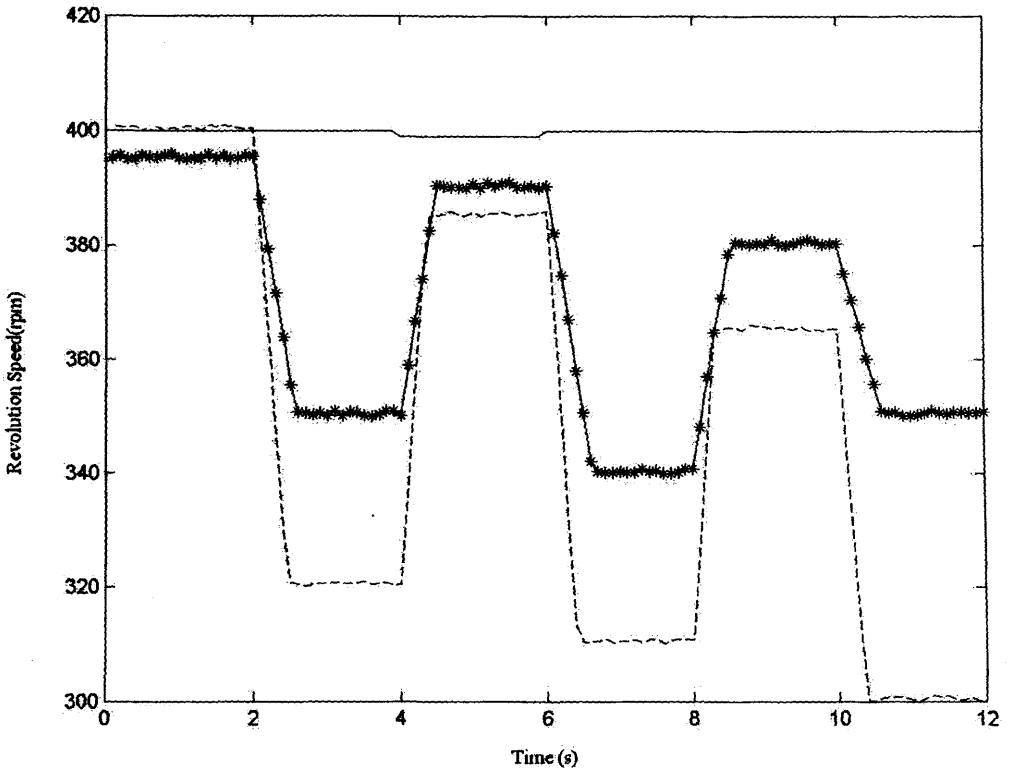


(c)

Figure 6.6. The rotor velocity with both the PI and current controls (solid line), with the PI control but no current control (line with stars), and with neither PI control nor current control (dash line), at (a) 74kHz, (b) 84kHz, and (c) 104kHz, respectively.

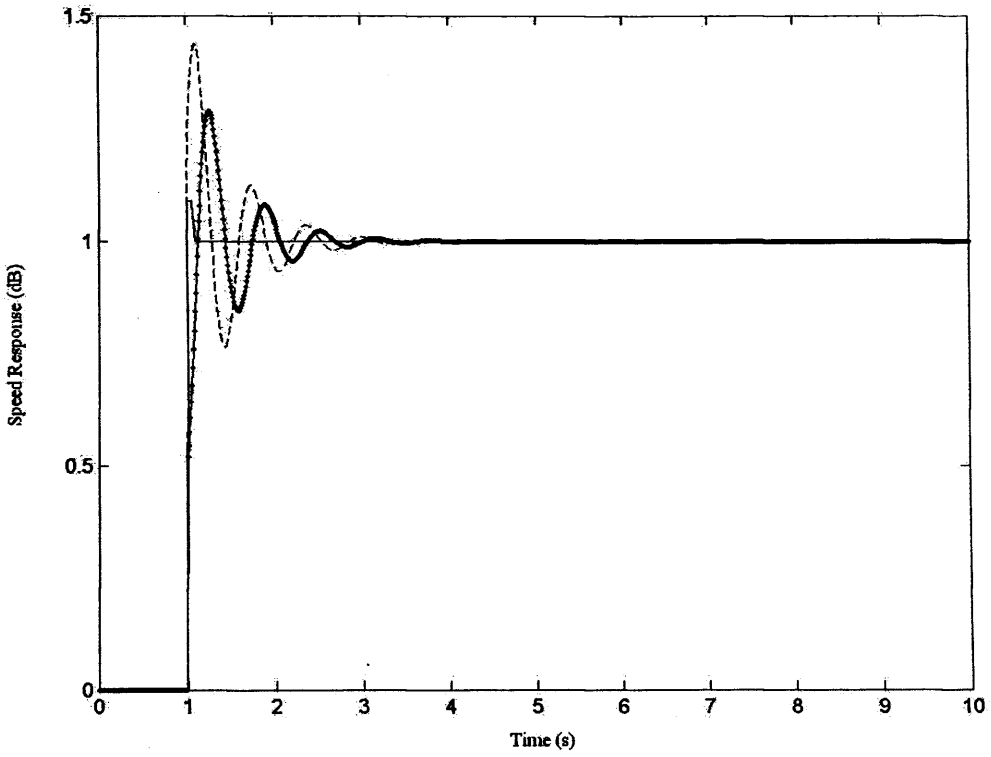


Figure 6.7. The transient response of motor speed at 74 KHz: with both the PI and current controllers (solid line), with the PI control but without current control (line with dots), and with neither PI nor current control (dash line).

# Chapter 7 Conclusions

## 7.1 Summary of the Work

The research work of the dissertation follows up a novel disc-type stator which was proposed by a published patent [17] for prototyping the ultrasonic motor. Its driving frequencies and driving force can be predicted by using some analyses and test method. Some theoretic models including finite element, transfer function, equivalent circuit model have been derived to estimate the characteristics of the motor. Experimental measurement was conducted to check the correctness and fidelity of the theoretic models. Finally, based on the theoretic models and the compensated capacitance technique and commercial DSP control method, the rotor speed fluctuation can be minimized.

The achievement of this research work can be summarized as follows:

1.Proof:

(1). According to the patent's modal analysis and test, and we used the precise laser vibrometer measurement of mode motion instead of using carbon powder and wave propagation concept, the asymmetrical simple-support boundary configuration (120°-90°-150°) for an adaptive mechanism was proven.

(2). The relationship between contact point (rotor location) and CW and CCW rotation, and the relationship between frequency and CW and CCW rotation were proven by finite element mode interaction together with real inspection.

2.Theory:

(1). By modelling the dynamic formulae of the new disc-type

piezoelectric stator in the finite element method, especially when the electrical term is treated as an extra mechanical degree of freedom, the related eigenvalue problem can be solved. The mechanical response under constant voltage excitation and the electrical impedance response and phase response are obtained. The experimental measurement has also been used to verify the response characteristics of the disc-type piezoelectric stator formulated by finite element analysis. It has been shown that the theoretical model can exactly examine the piezoelectric influence on a disc-type piezoelectric ultrasonic stator. It has great potential to serve as a design guideline for possible use in practical stator design, especially in the stator of an ultrasonic motor using its lateral motion. Boundary condition design is the successful key because it induces a standing wave but lets a traveling wave be partly reflected and mixed. It is useful in rotating the rotor.

(2). The transfer function models presented in this thesis incorporate these contact forces and predict the motor performance. Relative response measurements have been made to check the analysis results. From these results, the following conclusions can be drawn:

(a) The lateral displacement is determined according to the amplitude of the sinusoidal voltage applied to the piezoceramic.

(b) Fine-turning of input voltage amplitude, phase angle, and exciting frequency would yield better performance.

(c) The rotational orientation is determined by the frequency of the sinusoidal voltage

(d) Periodic interaction between the stator and the rotor will have significant influence on the trajectory of the contact point. Thus, to let the disc-type ultrasonic motor has better performance, the contact behaviour should be examined by experimental

measurements.

(3). In the equivalent circuit analysis, the radial vibration, tangential vibration and coupling vibration behaviour of a piezoelectric ceramic stator due to the non-equal-triangular boundary condition has been studied. An approximate analytic method has been developed to analyze the complex coupled vibration and the equivalent circuit models for the stator using have also been established. The resonance frequencies can be found from the characteristic equation of the equivalent circuit model. The PSPICE is used to build up the equivalent circuit models and simulate the equivalent circuit components. From the above analysis, the following conclusions can be drawn:

(a) The frequency switch is used to restrict the equivalent circuit model under driving frequency condition.

(b) The lateral vibration of the stator can be divided into two equivalent vibrations (axial vibration is not used at the lateral motion): one is the tangential vibration, and the other is the plane radial vibration. However, these two vibrations are interactive/coupled.

(c) The resonance frequencies for piezoelectric membrane, metal back plate and for the stator itself in the analytical method must be same.

(d) The present method shown in this thesis is an approximation method. The longitudinal vibration mode is not considered.

(e) The equivalent circuit models are based on the contact point between the stator and the rotor with the most significant lateral elliptic motion effect.

(f) The non-equal-triangular boundary condition of the stator induces more complicated mode-interactive behaviour and the

complication increases with the increase of driving frequency .

(4). The rotational speed of an ultrasonic motor is related to the vibration speed of its stator. Because drift of the piezostator characteristics will cause variation of the motor speed, a controller is thus necessary in order to produce a constant output speed. Variations of the motor output characteristics will also make it very difficult to obtain the efficiency of the motor. The analysis points out the origins of possible drifts in the new piezoelectric ultrasonic motor. The speed control scheme is implemented by using current modulation, so the revolutionary speed will be kept constant.

3. Experiment:

(1). The laser vibrometer system was set up to measure the stator vibration characteristic parameter. From it, three-dimensional displacement profile, frequency response and phase response (single frequency) can be acquired.

(2). In Appendix A, vibration displacement and velocity efficiency were measured in axial vibration measurement. The results showed that the vibration patterns were non-uniform with Bragg scattering. From axial vibration measurement, the sensitivity values were also obtained.

(3). In Appendix A, axial vibration measurement was made to investigate levitation motion on the stator surface. An axial vibration levitation motion can be applied to linear, surfing and shaft types of bearingless ultrasonic motor.

(4). Dynamic response was investigated and compared with several analytical results mentioned above.

(5). The revolution speed was measured. During the experiment, the average speed of the rotor showed a decrease in the time interval.

(6). The torque acting on the rotor was measured. Furthermore, the

measurements showed that torque appeared saturated above 10V.

(7). To drive the new disc-type piezoelectric ultrasonic motor effectively a current controller was used to provide a constant operation current with a constant amplitude voltage source by using a voltage-controlled oscillator for the motor. In the current controller, a compensated capacitor is added to enhance the transient response and to increase the robustness of the motor drive system. Furthermore, a commercial PI-type speed controller was implemented in the motor control loop to control the speed of the motor. In the closed-loop system for tracking, the error between the desired speed and the rotor actual speed can be asymptotically eliminated. The effectiveness of the controller has been demonstrated by experimental results.

Although the disc-type ultrasonic stator has some disadvantages such as the thrust force may not be steady due to friction and enclosed high heat from the mechanical standing waves, it may has a potential for application in small ultrasonic motor. It has a simple structure, simple driving electrical circuit and broadband operation frequency with good response and clockwise rotation and counter-clockwise rotation change by driving frequency modulation.

## 7.2 Future Research Direction

In the future, we plan to use thin-film PZT-on-silicon technology and incorporate the proposed motor into complete micro electromechanical systems, which will be able to upgrade ultrasonic motor speed for micro-robotic control application such as hard disk drive (HDD) and digital video drive (DVD) servo systems. The platters usually are driven

by a spindle motor. In addition to the control for the track seeking and following , the HDD or DVD needs to contain a spindle velocity control loop. The purpose of this loop is to control the airflow over the disk in order to guarantee the appropriate flying height of the read/write head. Further expansion of the closed-loop bandwidth of the HDD or DVD control system may be achieved by using the so-called dual stage servos which consist of a low bandwidth coarse actuator and a high bandwidth fine actuator. The fine actuator is with a small stroke and will be able to be implemented by using micro electromechanical ultrasonic motor.

# Bibliography


[1] Barth, H. V. Ultrasonic driven motor. *IBM Technical Disclosure Bulletin* 16 (1973), pp. 2263

[2] Ueha, S. ; Tomikawa, Y. ; Nakamura, N. Ultrasonic motors theory and applications. Clarendon Press (Oxford), 1993

[3] Sashida, T. ; Kenjo, T. An introduction to ultrasonic motors. Clarendon Press (Oxford), 1993

[4] Sashida, T. A prototype ultrasonic motor-principles and experimental investigations. *Oyobutsuri (Applied Physics)* 51 (1982), pp. 713-720

[5] Kumada, A. A piezoelectric ultrasonic motor. *Japanese Journal of Applied Physics* 24 (Supplement 2) (1985), pp. 739-741

[6] Fuda, Y. ; Yoshida, T. Piezoelectric torsional actuator. *Ferroelectrics* 160 (1994), pp. 323-340

[7] Nakamura, K. ; Ueha, S. An ultrasonic motor using a vibrator and multilayered piezoelectric actuators. *Japanese Institute of Electrocommunication Reports* US87-31 (1987), pp. 27-32

[8] Uchino, K. ; Kato, K. ; Tohda, M. Ultrasonic linear motors using a multilayered piezoelectric actuator. *Ferroelectrics* 87 (1988), pp. 331-334

[9] Ueha, S. ; Tomikawa, Y. Ultrasonic motors. Triceps Publishing, Tokyo, 1991

[10] Kurosawa, M. ; Ueha, S. ; Mori, E. Excitation conditions of flexural traveling waves for reversible linear motor. *Journal of the Acoustic Society of Japan* 77 (1985), pp. 1431-1439

[11] Sashida, T. Approach of development for the ultrasonic motor. *Mechanical Automation of Japan* 15 (1983), Nr. 12, pp. 31-35

[12] Uchino, K. Piezoelectric ultrasonic motors overview. *Smart Materials and Structures* 7 (1998), pp. 273-285

[13] Yoshida, T. Ultra-precise Positioning techniques and solid actuators for them. *Proceedings of the 2nd Memorial Symposium on Solid Actuators of Japan.* Japan, 1989, pp. 1-3

[14] Takahashi, S. ; Hirose, S. Vibration-Level characteristics for iro-doped lead-zirconate-titanate ceramic. *Japanese Journal of Applied Physics* 32 (1993), pp. 2422-2425

[15] Hirose, S. ; Takita, S. ; Takahashi, S. New design method of

piezoelectric transformer considering high power characteristics of various composition ceramics. *Proceedings of IEEE Ultrasonics Symposium.* Pittsburg, 1998, pp. 953-962

[16]Hirose, S. ; Takahashi, S. Measuring methods of high power characteristics on piezoelectric transducer and design method of piezoelectric transformer considering these results. *Transaction on Institute of Electronics, Information and Communication Engineers of Japan* J80-A (1995), pp. 1621-1636

[17]Ouyang, M. A thin-disc actuating type ultrasonic motor. Taiwan Patent 502488, September 11, 2002, (in Chinese)

[18]Kunkel, H. A. ; Locke, S. ; Pikeroen, B. Finite element analysis of vibrational modes in piezoelectric ceramic disks. *IEEE Transaction on Ultrasonics, Ferroelectrics and Frequency Control* 37 (1990), pp. 316-328

[19]Simson, E. A. ; Taranukha, A. Optimization of the shape of a quartz resonator. *Acoustic Physics* 39 (1993), pp. 472-476

[20]Silva-Nelli, C. E. ; Kikuchi, N. Design of piezoelectric transducers using topology optimization. *Smart Materials and Structures* 8 (1999), pp. 350-364

[21]Challande, P. Optimizing ultrasonic transducers based on piezoelectric composites using a finite-element method. *IEEE Transaction on Ultrasonics, Ferroelectrics and Frequency Control* 37 (1990), pp. 135-140

[22]Sato, J. ; Kawabuchi, M. ; Fukumoto, A. Dependence of the electromechanical coupling coeficient on the width-to-thickness ratio of plank-shaped piezoelectric transducers used for electronically scanned ultrasound diagnostic systems. *Journal of the Acoustic Society of American* 66 (1979), pp. 1609-1611.

[23]Diaz, A. R. ; Kikuchi, N. Solutions to shape and topology eigenvalue optimization problems using a homogenization method. *International Journal of Numerical Methods in Engineer* 35 (1992), pp. 1487-1502

[24]Meric, R. A. ; Saigal, S. Shape sensitivity analysis of piezoelectric structures by the adjoint variable method. *American Institute of Aeronautics and Astronautics Journal* 29 (1991), pp 1313-1318

[25]Smith, W. A. ; Auld, B. A. Modeling 1-3 composite piezoelectrics: thickness-mode oscillations. *IEEE Transaction on Ultrasonics, Ferroelectrics and Frequency Control* 38 (1991), pp. 40-47

[26]Hirata, H ; Ueha, S. Design of a traveling wave type ultrasonic motor. *IEEE Transaction on Ultrasonics, Ferroelectrics and Frequency Control* 42 (1995), Nr. 2, pp. 225-231

[27]Hosoe, K. An application of an ultrasonic motor to automatic focusing lenses. *Proceedings of 25th Tsuuken Symposium.* Tohoku University, 1989, pp. 117-122

[28]Hirata, H. ; Ueha, S. Characteristics estimation of a traveling wave type ultrasonic motor. *IEEE Transaction on Ultrasonics, Ferroelectrics and Frequency Control* 40 (1993), Nr. 4, pp. 402-406

[29]Nakamura, K. ; Kurosawa, M. ; Ueha, S. Design of a hybrid transducer type ultrasonic motor. *IEEE Transaction on Ultrasonics, Ferroelectrics and Frequency Control* 40 (1993), Nr. 4, pp. 395-401

[30]Iwamatsu, S. ; Ueha, S. ;Kuribayashi, M. ;Mori, E. Rotary ultrasonic motor using extensional vibration of a ring. *Japanese Journal Applied Physics* 25 (Supplement 25-1) (1986), pp. 174-176

[31]Ise, Y. Ultrasonic motor. *Journal of the Acoustic Society of Japan* 43 (1987), pp. 184-189 (in Japanese)

[32]Iula, A. ; Carotenuto, R. ; Lamberti, N. ; Pappalardo, M. A matrix model of the axle vibration of a piezoelectric motor. In *Ultrasonics* 38 (2000), pp. 41-45

[33]Wallaschek, J. Contact mechanics of piezoelectric ultrasonic motors. *Smart Materials and Structures* 7 (1998), pp. 369-381

[34]Wallaschek, J. Piezoelectric ultrasonic motor. *Journal of Intelligent Materials, Systems and Structures* 6 (1995), pp. 71-83

[35]Hagood, IV N. W. ; Mcfarland, A. J. Modeling of a piezoelectric rotary ultrasonic motor. *IEEE Transaction on Ultrasonics, Ferroelectrics and Frequency Control* 42 (1995), Nr. 2, pp. 210-224

[36]Marth, H. Untersuchungen zu Dimensionierung und zum Betriebsverhaten von Vibrationslinearmotren und deren Einsatz in Positioniereinrichtungen für Magnetköpfe, *Technische Universität Dresden, Dissertation*, 1980

[37]Ragulskis, K. Vibromotors for precision microrobotss. Hemisphere, 1988

[38]Fleischer, M. ; Stein, D. ; Meixner, H. Ultrasonic piezomotor with longitudinally oscillating amplitude-transforming resonator. *IEEE Transaction on Ultrasonics, Ferroelectrics and Frequency Control* 36 (1989), pp. 607-613

[39]Nakamura, K. ; Kurosawa, M. ; Ueha, S. Characteristics of a hybrid

transducer-type ultrasonic motor. *IEEE Transaction on Ultrasonics, Ferroelectrics and Frequency Control* 38 (1991), pp. 188-193

[40]Endo, A. ; Sasaki, N. Investigation of frictional material for ultrasonic motor. *Japanese Journal Applied Physics* 26 (supplement 1) (1986), pp. 197-199

[41]Kamano, T. ; Suzuki, T. ; Otoi, E. Characteristics and model of ultrasonic motor. *Japanese Journal Applied Physics* 27 (supplement 27-1) (1988), pp. 189-191

[42]Furuya, S. ; Maruhashi T. ; Izuno Y. ; Nakaoka M. Load-adaptive frequency tracking control implementation of two-phase resonant inverter for ultrasonic motor. *IEEE Transaction on Power Electronics* 7 (1992), pp. 542-550

[43]Kato, K. Friction between a rotor and a stator. *Proceedings of 25th Tsuuken Symposium.* Tohoku University, 1989, pp. 101-106

[44]Maeno, T. ; Tsukimoto, T. ; Miyake, A. The contact mechanism of an ultrasonic motor. *International Conference on Applications of Ferroelectrics*. Hamburg, 1990, pp. 535-538

[45]Maeno, T. ; Tsukimoto, T. ; Miyake, A. Finite-element analysis of the rotor/stator contact in a ring-type ultrasonic motor. *IEEE Transaction on Ultrasonics, Ferroelectrics and Frequency Control* 39 (1992), pp. 668-674

[46]Maeno, T. ; Bogy, D. B. FE analysis and LDA measurement of the dynamic rotor/stator contact in a ring- type ultrasonic motor. *Journal of Tribology* 115 (1993), pp. 625-631

[47]Flynn, A. M. Piezoelectric ultrasonic micromotors, Massachusetts Institute of Technology, Dissertation, 1995

[48]Zharii, O. Y. ; Ulitko, A. F. Smooth contact between the running Rayleigh wave and a rigid strip. *Journal of Applied Mechanics* 62 (1995), pp. 362-367

[49]Zharii, O. Y. Adhesive contact between the surface wave and a rigid strip. *Journal of Applied Mechanics* 62 (1993), pp. 368-372

[50]Zharii, O. Y. Frictional contact between the surface wave and a rigid strip. *Journal of Applied Mechanics* 63 (1996), pp. 15-20

[51]Buchaillot, L. ; Minotti, P. ; Le Moal, P. ; Ferreira, A. A comparative study of traveling wave and standing wave motor from the mechanical point of view. *Proceedings of 2nd Conference on New Actuator.* Bremen, 1996, pp. 4-6

[52]Kawai, Y. High power traveling-type ultrasonic motor. *Japanese*

*Journal Applied Physics* 34 (1995), pp. 2711-2714

[53]Cao, X. ; Wallaschek, J. Estimation of the tangential stresses in the stator/rotor contact of travelling wave ultrasonic motors using visco-elastic foundation models. *Proceedings of 2nd International Conference on Contact Mechanics.* Ferrara, 1995, pp. 53-61

[54]Cao, X. ; Wallaschek, J. Modelling and analysis of dynamic contact problems in travelling wave ultrasonic motors. *Proceedings of 3th International Congress on Industrial and Applied Mathematis.* Hamburg, 1995, pp. 564-566

[55]Guyomar, D. High torque/high power piezomotor—influence of the rotor vibration. *Proceedings of 2nd Conference on New Actuator.* Bremen, 1996, pp. 160-164

[56]Schmidt, J. P. ; Hagedorn, P. ; Bingqi, M. A note on the contact problem in an ultrasonic traveling wave motor. *Journal of Nonlinear Mechanics* 31 (1915), pp. 915-924

[57]Hagedorn, P. Modeling the ultrasonic traveling wave motor: the importance of the rotor flexibility. *Smart Materials and Structures* 7 (1998), pp. 301-310

[58]Maas, J. Simulation model for ultrasonic motors powered by resonant converters. *Proceedings of 1st Conference on New Actuator.* Orlando, 1995, pp. 111-20

[59]Maas, J. ; Ide, P. ; Grotstollen, H. Characteristics of inverter-fed ultrasonic motors — optimization of stator/rotor-interface. *Proceedings of 2nd Conference on New Actuator.* Bremen, 1996, pp. 241-244

[60]Ishii, T. Wear properties and life prediction of friction materials for ultrasonic motors. *Japanese Journal Applied Physics* 34 (1995), pp. 2765-2770

[61]Adachi, K. ; Kato, K. ; Sasatani, Y. The micro-mechanism of friction drive with ultrasonic wave. *Wear* 194 (1996), pp. 137-142

[62]Rehbein, P. ; Wallaschek, J. Friction and wear behaviour of polymer/steel and alumina/alumina under high frequency fretting condition. Wear 194 (1999), pp. 13-17

[63]Graff, K. F. Wave motion in elastic solids. Ohio State University Press, 1975

[64]Ugural, A. C. Stresses in plates and shells. McGraw-Hill Southeast, 1986

[65]Allik, H. ; Hughes, T. J. Finite element method for piezoelectric Vibration. *International Journal of Numerical Methods in*

*Engineering* 2 (1970), pp. 151-157

[66]Kagawa, Y. A new approach to analysis and design of electromechanical filter by finite element technique. *Journal of the Acoustic Society of American* 49 (1971), pp. 1348-1356

[67]Cowdrey, D. R. ; Willis, R. J. Application of the finite element method to the vibrations of quartz plates. *Journal of the Acoustic Society of American* 56 (1974), pp. 94-98

[68]Allik, H. ; Webman, K. M. ; Hunt, J. T. Vibration response of sonar transducers using piezoelectric finite elements. *Journal of the Acoustic Society of American* 56 (1974), pp. 1782-1791

[69]Naillon, M. ; Coursant, R. H. ; Besnier, F. Vibration response of sonar transducers using piezoelectric finite elements. *Acta Electronica* 25 (1983), pp. 341-362

[70]Armstrong, B. A. ; McMahon, G. W. Discussion of the finite-element modeling and performance of ring-shell projectors. *IEE Proceeding* 131. Hamburg, 1984, pp. 275-279

[71] Yamaguchi, M. ; Hashimoto, K. ; Makita, H. Finite element method analysis of dispersion characteristics for 1-3 type piezoelectric composites. *Proceedings of IEEE Ultrasonics Symposium.* Japan, 1987, pp. 657-661

[72] Lerch, R. Simulation of piezoelectric devices by two- and three-dimesional finite elements. *IEEE Transaction on Ultrasonics, Ferroelectrics and Frequency Control* 37 (1990), pp. 233-247

[73] Hladky-ennion, A. C. ; Decarpingny, J. N. Finite element modeling of active periodic structure Applictions to 1-3 piezocomposites. *Journal of the Acoustic Society of American* 94 (1993), Nr. 2, pp. 621-635

[74] Smith, R. R. ; Hunt, J. T. ; Barach, D. J. Finite Element Analysis of acoustically radiating structures with application to sonar tranducer. *Journal of the Acoustic Society of American* 54 (1971), Nr. 1, pp. 1277-1288

[75] Kagawa, Y. ; Yamabuchi, T. Finite element approach for piezoelectric circular rod. *IEEE Transaction on Sonics and Ultrasonics* 23 (1976), Nr. 4, pp. 379-385

[76] Ostergaard, D. F ; Pawalak, T. P. Three-dimensional finite element for analyzing piezoelectric structure. *Proceedings of IEEE Ultrasonics Symposium.* London, 1986, pp. 639-644

[77] Guo, N. ; Cawley, P. The finite element analysis of the vibration

characteristics of piezoelectric discs. *Journal of Sound and Vibration* 159 (1992), Nr. 1, pp. 115-137

[78] Juang, P. A. ; Hardtke, H. J. A new disc-type piezoelectric ultrasonic motor. *Journal of Sensors and Actuators A* 94 (2001), pp. 102-111

[79] Lim, Y. H. ; Varadan, V. V. ; Varadan, V. K. Finite-element modeling of the transient response of MEMS sensor. *Smart Materials and Structures* 6 (1997), pp. 53-61

[80] Varadan, V. V. ; Chin, C. L. ; Varadan, V. K. Finite-element modeling of flextensional electrcacoustic transducers. *Smart Materials and Structures* 2 (1993), pp. 201-207

[81] Rolt, R. D. History of the flextensinal electrcacoustic transducer. *Journal of the Acoustic Society of American* 87 (1990), pp. 1340-1349

[82] Sugawara, Y. ; Onitsuka, K. ; Yoshikawa, S. ; Xu, Q. C. ; Newnham, R. E. A new composite piezoelectric actuator. *93rd Annual Meeting of American Ceramic Society*. Ohio, 1991, pp.1-3

[83] Xu, Q. C. ; Yoshikawa, S. ; Belsick, J. R. ; Newnham, R. E. Piezoelectric composite with high sensity and high capacitance for use at high pressure. *IEEE Transaction on Ultrasonics, Ferroelectrics and* Frequency *Control* 38 (1991), pp. 634-639

[84] Gass, V. ; van der Schoot, B. H. ; de Rooij, N. F. Handling by micro-flow-sensor based on drag force measurements. *Proceedings of IEEE MEMS Workshop*. Fort Lauderdale, 1993, pp.167-172

[85] Kim, J. ; Varadan, V. V. ; Varadan, V. K Finite element-optimization methods for the active control of radiated sound from a plate structure. *Smart Materials and Structures* 4 (1995), pp. 318-326

[86] Seshu, P. ; Naganathan, N. G. Finite-element analysis of strain transfer in an induced strain actuator. *Smart Materials and Structures* 6 (1997), pp. 76-88

[87] Lim, Y. H. ; Varadan, V. V. ; Varadan, V. K. Closed loop finite element modeling of active structural damping in the time domain. *Smart Materials and Structures* 8 (1999), pp. 390-400

[88] Tzou, H. S. ; Tseng, C. I. Distributed piezoelectric sensor/actuator design for dynamic measurement/control element approach. *Journal of Sound and Vibration* 138 (1990), Nr. 4, pp. 17-34

[89] Varadan, V. V. ; Lim, Y. H. ; Varadan, V. K Closed loop finite element modeling of active/passive structural damping in structural vibration control. *Smart* Materials *and Structures* 5 (1996), pp. 685-694

[90] Ha, S. K. ; Kleiler C. ; Chang, F. K. Finite element analysis of composite structures containing distributed piezoelectric sensors and actuators. *American* Institute *of Aeronautics and Astronautics Journal* 30 (1992), pp. 772-780

[91] Lim, Y. H. ; Varadan, V. V. ; Varadan, V. K Closed loop finite element modeling of active structural damping in the frequency domain. *Smart Materials and Structures* 6 (1997), pp. 161-168

[92] Peelamedu, S. M. ; Yu, Y. ; Naganathan, N. G. ; Dukkipati, R. V.; Active strain-transfer analysis in a piezoceramic system using a finite-element method and experimental investigation. *Smart Materials and Structures* 8 (1999), pp. 654-662

[93] Bernadou, M. ; Haenel, C. Modelization and numerical analysis of active thin shell structures. *European Congress on Computational Methods in Applied Sciences and Engineering.* Barcelona, 2000, pp. 1-14

[94] Krome, J.W. ; Wallaschek, J. Influence of the piezoelectric actuator on the vibrations of the stator of a traveling motor. *Proceedings of IEEE Ultrasonics Symposium.* Pittsburg, 1995, pp. 413-416

[95] Kadokura, M. ; Hirashima, T. ; Sasaki, Y. Analysis and design of AT-cut quartz resonators by three dimensional finite element method. *Proceedings of the Advanced in Electronic Packaging.* 1997, pp. 1101-1108

[96] Kim, J. ; Varadan, V. V. ; Varadan, V. K Finite element modeling of structures including piezoelectric active devices. *International Journal of Numerical Methods in Engineer* 2 (1996), pp. 685-694

[97] Boucher, D. ; Lagier, M. ; Maereld, C. Computation of the vibrational modes for piezoelectric array transducers using a mixed finite element-perturbation method. *IEEE Transaction on Sonics and Ultrasonics* 28 (1981), Nr. 5, pp. 318-329

[98] Kagawa, Y. ; Tsuchiya, T. ; Kataoka, T. Finite element simulation of dynamic responses of piezoelectric actuators. *Journal of Sound and Vibration* 191 (1996), Nr. 4, pp. 519-538

[99] Fung, R. F. ; Tseng, C. R. Dynamic simulation of a bimodal ultrasonic motor by new hybrid Laplace transform/finite element method. *Journal of Sound and Vibration* 226 (1999), Nr. 4, pp. 625-644

[100] Sze, K. Y. ; Pan, Y. S. Hybrid finite element models for piezoelectric materials. *Journal of Sound and Vibration* 226 (1999), Nr. 3, pp. 519-547

[101]Jeng, J. H. ; Bao, X. ; Varadan, V. V. ; Varadan, V. K Complete finite element eigenmode analysis for 1-3 type of piezoelectric composite transducer including the effect of fluid loading and internal losses. *Proceedings of IEEE Ultrasonics Symposium.* Santiago, 1988, pp. 685-688

[102]Hossack, J. A. ; Hayward, G. Finite element analysis of 1-3 composite transducers. *IEEE Transaction on Ultrasonics, Ferroelectrics and Frequency* Control 38 (1991), pp. 618-627

[103]Hwang, W. S. ; park, H. C. Finite element modeling of piezoelectric sensors and actuators. American *Institute of Aeronautics and Astronautics Journal* 31 (1993), pp. 930-937

[104]Moetakef, M. A. ; Lawerence, K. L. ; Joshi, S. P. ; Shiakolas, P. S. Closed form expressions for high order electroelastic tetrahedral elements. *American Institute of Aeronautics and Astronautics Journal* 33 (1995), pp. 136-142

[105]Heyliger, P. ; Ramirez, G. ; Saravanos, D. Coupled discrete-layer finite elements for laminated piezoelectric plates. *Communication and Numerical Methods in Engineering* 10 (1994), pp. 971-981

[106]Lammering, R. The application of a finite shell element for composites containing piezo-electric polymers in vibration control. *Computers and Structures* 41 (1991), pp. 1101-1109

[107]Koko, T. S. ; Orisamolu, I. R. ; Smith, M. J. ; Akpan, U. O. finite element based design tool for smart composite structures. *Smart Materials and Structures 1997: Mathematics and Control in Smart Structures, Proceedings of SPIE* 3039. New York, 1997, pp. 125-134

[108]Saravanos, D. A. ; Heyliger, P. R. ; Hopkins, D. H. Layerwise mechanics and finite element for the dynamic analysis of piezoelectric composite plates. *International Journal of Solids and Structures* 34 (1997), pp. 817-832

[109]Tzou, H. S. Piezoelectric shells: Distributed sensing and control of continua. Kluwer Press, 1993

[110]Tzou, H. S. ; Tseng, C. I. ; Bahrami, H. A thin piezoelectric hexahedron finite element applied to design of smart continua. *Finite Elements in Analysis and Design* 16 (1994), pp.27-42

[111]Tzou, H. S. ; Ye, R. Analysis of piezoelectric structures with laminated piezoelectric triangle shell element. *American Institute of Aeronautics and Astronautics Journal* 34 (1996), pp. 110-115

[112]Pian, T. H. H. ; Tong, P. Basis of finite elements for solids continua.

*International* Journal *of Numerical Methods in Engineering* 1 (1969), pp. 3-28

[113] Yang, J. S. Variational formulations for the vibration of a piezoelectric body. *Journal of Applied Mathematics* 53 (1995), pp. 95-104

[114] Ghandi, K. ; Hagood, N. W. A hybrid finite element model for phase transitions in nonlinear electro-mechanically coupled material. *Smart Materials and Structures 1997: Mathematics and Control in Smart Structures, Proceedings of SPIE* 3039. New York, 1997, pp. 97-112

[115] Im, S. ; Atluri, S. N. Effects of a piezo-actuator on a finitely deformed beam subject to general loading. *American Institute of Aeronautics and Astronautics Journal* 27 (1989), pp. 1801-1807

[116] Tomikawa, Y. ; Ogasawara, T. ; Takano, T. Ultrasonic motors—Construction/characteristics/applications. *Ferroelectrics* 91 (1989), pp. 163-178

[117] Fleischer, M. ; Stein, D. ; Meixner, H. Novel ultrasonic motors with mono- and bimodal drives. *Sensors and Actuators* A21-A23 (1990), pp. 357-361

[118] Carotenuto, R. ; Lamberti, N. ; Iula, A. ; Pappalardo, M. A new low voltage piezoelectric micromotor based on stator precessional motion. *IEEE Transaction on Ultrasonics, Ferroelectrics and Frequency Control* 45 (1998), pp. 1427-1435

[119] Lamberti, N. ; Iula, A. ; Pappalardo, M. A piezoelectric motor using flexural vibration of a thin piezoelectric membrane. *IEEE Transaction on Ultrasonics, Ferroelectrics and Frequency Control* 45 (1998), pp. 23-29

[120] Hagood, N ; Chung, W. ; von Flotow, A. Modeling of piezoelectric actuator dynamics for active structural control. *Journal of Intelligent Materials, Systems and* Structures 1 (1990), pp. 327-354

[121] Hagerdon, P. ; Wallaschek, J. Travelling wave ultrasonic motors. Part I: Working principle and mathematical modelling of the stator. *Journal of Sound and Vibration* 155 (1992), Nr. 1, pp. 31-46

[122] Yang, B. ; Mote, C. D. On time delay in non-collocated control of flexible mechanical systems. *Journal of Dynamics Systems, Measurement and Control* 114 (1992), pp. 409-415

[123] Yang, B. ; Mote, C. D. Active vibration control of the axially moving sring in the S domain. Journal *of Applied Mechanics* 58 (1991), pp.

189-196

[124]Hatman, V. G. ; Haque, I. ; Bagchi, A. Dynamics of a flexible rotating beam interacting with a flat rigid surface Part I: Model development. *Journal of Sound and Vibration* 194 (1996), Nr. 5, pp. 653-669

[125]Hatman, V. G. ; Haque, I. ; Bagchi, A. 1996 Dynamics of a flexible rotating beam interacting with a flat rigid surface Part II: Numerical solution. *Journal of Sound and Vibration* 194 (1996), Nr. 5, pp. 671-683

[126]Uchino, K. Piezoelectric Actuators and Ultrasonic Motors. Boston, Kluwer, 1997

[127]Lin, W. W. ; Shih, S. T. ; Chen, M. H. ; Huang, S. C. The transfer function of PZT phase modulators in optical fiber sensors. *Proceedings of National Science Council.* Taiwan, 1994, pp. 570-575

[128]Chung, C. H. ; Tan, C. A. Active vibration control of the axially moving string by cancellation. ASME *on Vibration and Control of Mechanical Systems* 61 (1993), pp. 21-28

[129]Datko, R. ; Lagnese, J. ; Polis, M. P. An example on the effect of time delays in boundary feedback stabilization of wave equation. *Siam Journal on Control and Optimization* 24 (1986), pp. 152-155

[130]Wie, B. ; Bryson, R. L. Modelling and control of flexible space structure. *Proceedings of 3rd conference on Dynamics and Control of Large Structure.* Virginia, 1981, pp. 153-174

[131]Alli, H. ; Singh, T. Exact time optimal control of the wave equation. *AIAA Guidance, Navigation and Control Conference.* Baltimore, 1995, pp. 102-111

[132]Pan, C. T. ; Chao, K. S. A computer-aided root-locus method. *IEEE Transaction on Automatic Control* 23 (1978), pp. 856-860

[133]Alli, H. ; Singh, T. On the feedback control of the wave equation. *Journal of Sound and Vibration* 234 (2000), Nr. 4, pp. 625-640

[134]Schulte, T. ; Frohleke, N. Parameter identification of ultrasonic motors. *Proceedings of IEEE/ASME International Conference on Advanced Intelligent Mechatronics.* Atlanta, 1999, pp. 97-102

[135]Maas, J. ; Schulte, T. ; Grotstllen, H. Optimized drive control for inverter-fed ultrasonic motors. *Proceedings of IEEE/ASME International Conference on Advanced Intelligent Mechatronics.* Louisiana, 1997, pp. 690-698

[136]Schnabel, P. Dispersion of thickness vibrations of piezoelectric disk resonators. *IEEE Transactions on Sonics and Ultrasonics* 25 (1978), pp. 16-24

[137]Aoyagi, M. ; Tomikawa, Y. Simplified equivalent circuit of ultrasonics motor and its application to estimation of motor characteristics. *Japanese Journal Applied Physics* 34 (1995), pp. 2752-2755

[138]Lebrun, L. ; Petit, L. ; Briot, R. ; Gonnard, P. Electromechanical conversion in an ultrasonic motor using a non-axisymmetric (1,1) mode. *Smart Materials and Structures* 6 (1997), pp. 47-53

[139]Petit, L. ; Briot, R. ; Gonnard, P. A multi-mode piezomotor using a flextensional coupler. *Smart Materials and Structures* 8 (1999), pp. 167-174

[140]Lebrun, L. ; Gonnard, P. ; Guinet, M. A low-cost piezoelectric motor using a (1,1) non-axisymmetric mode. *Smart Materials and Structures* 8 (1999), pp. 469-475

[141]Shuyu, L. Analysis of the equivalent circuit of piezoelectric ceramic disk resonators in coupled vibration. *Journal of Sound and Vibration* 231(2000), pp. 277-290

[142]Berlincourt, D. A. ; Curran, D. R. ; Jaffe, H. Piezoelectric and piezomagnetic materials and their function in transducers. *Physical Acoustics* Academic Press, 1 Part A, 1964, pp. 169-267

[143]Shuyu, L. Vibration analysis and frequency equation for an ultrasonic transducer consisting of a longitudinal vibrator and a flexural circular plate. *Acoustica* 81 (1995), pp. 53-57

[144]Ebenezer, D. D. Three-port parameters and equivalent circuit of radially polarized piezoelectric ceramic cylinders of finite length. *Journal of the Acoustic Society of American* 99 (1996), pp. 2908-2912

[145]Chubachi, N. ; Kim, M. J. Transmission line model equivalent circuit for piezoelectric transducers including the effect of electrical terminal impedance. *Japanese Journal of Applied Physics* 35 (1996), pp. 3231-3235

[146]Koike, Y. ; Tamura, T. ; Ueha, S. Electrical equivalent circuit of loaded thick Langevin flexural transducer. *Japanese Journal of Applied Physics* 36 (1997), pp. 3121-3125

[147]Sherrit, S. ; Wiederick, H. D. ; Mukherjee, B. K. ; Sayer, M. An accurate equivalent circuit for the unloaded piezoelectric vibrator in

the thickness mode. *Journal of Physics* D: Applied Physics 30 (1997), Nr. 16, pp. 2354-2363

[148]Chen, Y. C. ; Wu, L. ; Chang, K. K. ; Huang, C. L. Analysis and simulation of stacked-segment electromechanical transducers with partial electrical excitation by PSPICE. *Japanese Journal of Applied Physics* 36 (1997), pp. 6550-6557

[149]Wang, X. Elhers, C. ; Neitzel, M. Dynamic analysis of piezoelectric actuator bonded on beam. *Proceedings of the Third International Conference on Intelligent Material.* Lyon, 1996, pp. 883-890

[150]Tanaka, H. ; Aoyagi, R. Derivation of equivalent circuit of multilayered bending vibration. *Proceedings of Acoustic Engineering.* Japan, 1992, pp. 262-263

[151]Aoyagi, R ; Tanaka, H. Equivalent circuit analysis of piezoelectric bending vibrators. *Japanese* Journal *of Applied Physics* 33 (1995), pp. 3010-3014

[152]Tanaka, H. ; Aoyagi, R. Analysis of piezoelectric bending accelerometer using the equivalent circuit. *Japanese Journal of Applied Physics* 35 (1996), pp. 3035-3037

[153]Cho, Y. S. ; Pak, Y. E. ; Han, C. S. ; Ha, S. K. Five-port equivalent electric circuit of piezoelectric bimorph beam. *Sensors and Actuators* 84 (2000), pp. 140-148

[154]Tilmans, H. A. C. Equivalent circuit representation of electromechanical transducers: I. Lumped-parameter systems. *Journal of Micromechanics and Microengineers* 6 (1996), pp. 157-176

[155]Gururaja, T. R. ; Schulze, W. A. ; Cross, L. E. ; Newnham, R. E. ; Auld, B. A. ; Wang, Y. J. Piezoelectric composite materials for ultrasonic transducer applications. Part I: resonant modes of vibration of PZT rod-polymer composits. *IEEE Transactions on Sonics and Ultrasonics* 32 (1985), Nr. 4, pp. 481-498

[156]Juang, P. A. ; Brenner W. The transfer function of a new disc-type ultrasonic motor. *Journal of Sensors and Actuators A* 100 (2002), pp. 272-280

[157]Sousa, G. C. D. ; Bose, B. K. ; Gleland, J. G. Fuzzy logic based on-line efficiency optimization control of an indirect vector-controlled induction motor drive. *IEEE Transaction on Industry Electronics* 42 (1995), Nr. 2, pp.192-198

[158]Senjyu, T. ; Miyazato, H. ; Uezato, K. Adjustable speed control of

ultrasonic motor by adaptive control. *IEEE Transaction on Power Electronics* 10 (1995), Nr. 5, pp. 532-538

[159]Takeishi, H. ; Mitarai, R. Dual mode position control of ultrasonic motor. *Proceedings of the 31th Society of Instrument and Control Engineers Annual Conference,* 1992, pp. 401-402, (in Japanese)

[160]Izumi, T. ; Yasutsune, H. ; Kim, Y. J. ; Nakaoka, M. ; Furuya, S. ; Maruhashi, T. New inverter-fed power ultrasonic motor for speed tracking servo application and its feasible evalutions. *Proceedings of 1995 International Conference on Power Electronics and Drive Systems*, 1995, pp. 776-773

[161]Senjyu, T. ; Uezato, K. Adjustable speed control of ultrasonic motor by adaptive control. *Proceedings of IEEE PESC'94*, 1994, pp. 1237-1242

[162]Izuno, Y. ; Nakaoka, M. High performance and high precision ultrasonic motor-actuated positioning servo drive system using improved fuzzy reasoning controller. *Proceedings of IEEE PESC'94*, 1994, pp. 1269-1274

[163]Lin, F. J. Fuzzy adaptive model-following position control for ultrasonic motor. *IEEE Transaction on Power Electronics* 12 (1997), Nr. 2, pp. 261-268

[164]Wang, L. X. Adaptive Fuzzy Systems and Control: Design and Stability Analysis. Englewood Cliffs, Nj Prentice-Hall, 1994

[165]Sastry, P. S. ; Santharam, G. ; Unnikrishnan, K. P. Memory neuron networks for identification and control of dynamical systems. *IEEE Transaction on Neural Networks* 5 (1994), Nr. 2, pp. 306-319

[166]Noriega, J. R. ; H. Wang. A direct adaptive neural-network control for unkown nonlinear systems and its application. *IEEE Transaction on Neural Networks* 9 (1998), Nr. 1, pp. 27-34

[167]Lin, F. J. ; Wai, R. J. ; Lin, H. H. An adaptive fuzzy-neural-network controller for ultrasonic motor drive using the LLCC resonant technique. *IEEE Transaction on Ultrasonics, Ferroelectrics and Frequency Control* 46 (1999), Nr. 3, pp. 715-727

[168]Lin, F. J. ; Wai, R. J. ; Duan, R. Y. Fuzzy neural networks for identification and control of ultrasonic motor drive with LLCC resonant technique. *IEEE Transaction on Industry Electronics* 46, (1999), Nr. 5, pp.999-1011

[169]Lin, F. J. ; Kuo, L. C. Driving circuit for ultrasonic motor servo drive with variable-structure adaptive model-following control. *IEE*

*Proceedings of Electric and Power Application* 144 (1997), Nr.2, pp.199-206

[170]Yamayoshi, Y. ; Hirose, S. Ultrasonic motor not using mechanical friction force. *International Journal of Applied Electromagnetic Materials* 3 (1992), pp. 179-182

[171]Hashimoto, Y. ; Koike, Y. ; Ueha, S. Noncontact substance transportation using flexural traveling wave. *Institute of Electric and Communication Engineers, Janpan* 95 (1995), pp. 37-44

[172]Hu, J. H. ; Nakamura, K. ; Ueha, S. Characteristics of a noncontact ultrasonic motor using acoustic levitation. *IEEE Ultrasonics Symposium.* San Antonio, TX, 1996, pp. 373-376

[173]Yamazaki, T. ; Hu, J. H. ; Nakamura, K. ; Ueha, S. Trail construction of a noncontact ultrasonic motor with an ultrasonically levitated rotor. *Japanese Journal of Applied Physics* 35 (1996), pp. 3289-3288

[174]Hashimoto, Y. ; Koike, Y. ; Ueha, S. Magnification of transportation range using non-contact acoustic levitation by connecting vibration plates. *Japanese Journal of Applied Physics* 36 (1997), pp. 3140-3145

[175]Hashimoto, Y. ; Koike, Y. ; Ueha, S. Near field acoustic levitation using flexural vibration mode. *Ultrasonics World Congress Proceedings*. Berlin, 1995, pp. 835-837

[176]Hashimoto, Y. ; Koike, Y. ; Ueha, S. Near-field acoustic levitation of planar specimens using flexural vibration. *Journal of the Acoustic Society of Japan* 100 (1996), pp. 2057-2060

[177]Ueha, S. ; Hashimoto, Y. ; Koike, Y. Non-contact transportation using near-field acoustic levitation. *Ultrasonics* 38 (2000), pp. 26-32

[178]Hatano, H. ; Kanai, Y. ; Ikegami, Y. ; Fujii, T. ; Saito, K. Ultrasonic levitation and positioning of sample. *Japanese Journal Applied Physics* 21 (Supplement 3) (1982), pp. 202-206

[179]Moroney, M. ; White, R. M. ; Howe, R. T. Ultrasonic micromotors. *IEEE Ultrasonics Symposium.* Montreal, 1989, pp. 745-747

[180]Kurosawa, M. ; Yamada, H. ; Ueha, S. Hybrid transducer type ultrasonic linear motor. *Japanese Journal Applied Physics* 28 (Supplement 28-1) (1988), pp. 156-160

[181]Schadegrodt, G. ; Salomon, B. The piezo traveling wave motor-a new element in actuation. *Control Engineer* 5 (1990), pp. 10-18

[182]Kurosawa, M. ; Ueha, S. Hybrid transducer type ultrasonic. *IEEE Transaction on Ultrasonics, Ferroelectrics and Frequency Control* 38 (1991), pp. 89-92

[183]Fleischer, M. ; Stein, D. ; Meixner, H. New type of piezoelectric ultrasonic motor. *IEEE Transaction on Ultrasonics, Ferroelectrics and Frequency Control* 36 (1989), pp. 614-619

[184]Goto, H. ; Sasaoka, T. Vertical micro positioning system using PZT actuators. *Bulletin of Japanese Society of Precise Engineer* 22 (1988), pp. 277-282

[185]Ohnishi, O. ; Myohga, O. ; Uchikawa, T. ; Tamegai, M. ; Inoue, T. ; Takahashi, S. Piezoelectric ultrasonic motor using longitudinal torsional composite vibration of a cylindrical resonator. *Proceedings of IEEE Ultrasonics Symposium. Japan*, 1989, pp. 739-743

[186]Niedermann, P. ; Emch, R. ; Descouts, P. Simple piezoelectric translation device. *Review of Scientific Instrument* 59 (1988), pp. 368-368

[187]Burleigh Instruments Incorporation. Piezoelectric electromechanical translation apparatus. *US Patent* 3902084, 1975

[188]Newton, D. ; Garcia, E. ; Horner, G. C. A linear piezoelectric motor. *Smart Materials and Structures 6* (1997), pp. 295-304

[189]Helin, P. ; Sadaune, V. ; Druon, C. ; Tritsch, J. B. linear ultrasonic motors using surface acoustic waves mechanical model for energy transfer. *International Conference on Solid-State Sensors and Actuators*. Chicago, 1997, pp. 1047-1050

[190]Kurosawa, M. ; Takahashi, M. ; Higuchi, T. Ultrasonic linear motor using surface acoustic waves. *IEEE Transaction on Ultrasonics, Ferroelectrics and Frequency Control* 43 (1996), pp. 901-906

[191]Helin, P. ; Druon, C. ; Sadaune, V. A microconveyer using surface acoustic waves in the HF band. *Proceedings of IEEE Mechatronics Symposium*. Paderburg, 1996, pp. 580-5825

[192]Viktorov, I. Rayleigh and Lamb waves. Plenum Press, 1967

[193]Kurosawa, M. ; Takahashi, M. ; Higuchi, T. Ultrasonic X-Y stage using 10MHz surface acoustic waves. *Proceedings of IEEE Ultrasonics Symposium*. Cannes, 1994, pp. 534-538

[194]Kurosawa, M. ; Takahashi, M. ; Higuchi, T. Operation condition and output force of surface acoustic wave motor. *Technical Report Institute of Electronics, Information and Communication Engineers*

*of Japan* US97-76 (1996), pp. 43-50

[195]Kurosawa, M. ; Takahashi, M. ; Higuchi, T. A surface acoustic wave motor using V-shape groove guide. *Transaction on Institute of Electronics, Information and Communication Engineers of Japan* J80-A (1997), pp. 1711-1717

[196]Takahashi, M. ; Kurosawa, M. ; Higuchi, T. Direction frictional driven surface acoustic wave motor. *International Conference on Solid-State Sensors and Actuators*. Stockholm, 1995, pp. 401-404

[197]Kurosawa, M. ; Takahashi, M. ; Higuchi, T. Optimum pre-load of surface acoustic wave motor. *Proceedings of IEEE Ultrasonics Symposium*. San Antonio, 1996, pp. 369-372

[198]Kurosawa, M. ; Ueha, S. High speed ultrasonic linear motor with high transmission efficiency. *Ultrasonics* 27 (1989), pp. 39-44

[199]Kuribayashi, M. ; Ueha, S. Study of ultrasonic linear motor IV—electrical method of energy back flow. *Proceedings of Annual Meeting of Acoustic Society of Japan*. Japan, 1985, pp. 585-586

# Publications


[1] Juang, P. A. ; Gu, D. W. Speed Control of a New Disc-type Ultrasonic Motor by Using Current Controller. *IEEE Transaction on Power Electronics.* (Accepted in May 2005).

[2] Juang, P. A. ; Gu, D. W. Equivalent Circuit Estimation of a New Disc-type Ultrasonic Motor. Submitted to *IEEE Transaction on Mechatronics.* (Finished revising).

[3] Juang, P. A. ; Gu, D. W. Analysis, Measurement and Control of a New Disc-type Ultrasonic Motor System. Submitted to *International Journal of Mechatronics.* (To appear in January 2006.)

[4] Huang, G. S. ; Juang, P. A. ; Gu, D. W. Theoretical and Experimental Studies for a New Disc-Type Ultrasonic Stator. *Proceedings of IEEE International Conference on Mechatronics.* Taipei, 2005, pp. 428-433.

[5] Juang, P. A. ; Gu, D. W. Operational Verification of a New Disc-type Ultrasonic Motor by Finite Element Simulations. *Proceedings of IEEE International Conference on Mechatronics.* Taipei, 2005, pp. 663-668.

[6] Juang, P. A. ; Gu, D. W. Finite Element Analysis of a New Disc-type Ultrasonic Stator. *IEEE Transaction on Ultrasonics, Ferroelectrics and Frequency Control* 50 (2003), Nr. 4, pp. 368-375.

[7] Juang, P. A. ; Brenner W. Vibration Characteristic Identification of a New Disc-type Ultrasonic Stator by Experiment. *Journal of Micromechanics and Microengineerings* 12 (2002), p.598-603.

[8] Juang, P. A. ; Brenner W. The transfer function of a new disc-type ultrasonic motor. *Journal of Sensors and Actuators A* 100 (2002), pp. 272-280.

[9] Juang, P. A. ; Hardtke, H. J. A new disc-type piezoelectric ultrasonic motor. *Journal of Sensors and Actuators A* 94 (2001), pp. 102-111.

# Appendix A Explore Axial Vibration Levitation of the Ultrasonic Stator

## A.1 Introduction

Piezoelectric ultrasonic stators have been routinely used as driving sources of ultrasonic motors. Their driving characteristics result from the frictional contact force between the stator and rotor. However, in addition to rotating a stator by contact friction, piezoelectric ultrasonic stators can also levitate and transport objects [170]-[174] by non-contact ultrasonic radiation. Hashimota and co-workerss [175]-[177] have proven that a 10kg planar object can be levitated without a reflector. Hatano et al. [178] have reported that small objects of a few grams were levitated on the nodal points by the excitation of a standing acoustic field. Moroney et al. [179] have proposed levitating and transporting small objects using 4MHz ultrasonic driving frequency.

As known, the use of a contact bearing will reduce the performance of the ultrasonic motor due to friction loss. Through ultrasonic levitation, a stator can be made into a non-contact bearing-less structure with linear or planar motion [180]-[186]. So, the efficiency of the ultrasonic motor can also be raised . Since the linear ultrasonic motor has few moving parts and is lightweight and bearing-less, it is ideal for space applications where problems of bearing seizure, reliability and weight are key concerns [188]. Newton et al [188] have developed a type of linear hybrid transducer piezoelectric motor. The motor consists of a longitudinal actuator, which provides output displacement and force, and two alternating clamping actuators, which provide the holding force. This

motor has the advantages of being lightweight, and having macro- and micro-positioning, large force/velocity output and less contact.

This new variation of the linear motor has numerous other applications. The Kurosawa linear motors [180], [182] that incorporate piezoelectric stacks can be driven with sinusoidal voltages at high frequencies to achieve a reported maximum speed of 50mm/sec and a maximum force output of 0.5kgf. The force outputs of both these designs are limited by the inability of a piezoceramic to withstand shears forces due to less contact. The Burleigh linear motor has been proposed [187], which can operates well as a micro-positioner with a maximum speed of 2mm/sec and a maximum force output of 1.5kgf. Speed improvements are realized by the ability to drive lower voltage at higher frequencies. Helin et al [189] have presented theory, simulation results and experimental study of a slider displacement at a nanometer scale in a linear ultrasonic motor using Lamb and Rayleigh waves. They made the first attempt to describe the energy transfer from the acoustic wave to a slider. Their analysis model has shown that the mechanism is sequential with alternative phases of levitation and contact with step-like behavior of the slider velocity. Kurosawa et al [190] have demonstrated the first success of a linear ultrasonic motor with 10MHz Rayleigh waves. The slider moved in the opposite direction of the propagation through a frictional drive. Helin et al [191] fabricated several linear ultrasonic motors using Lamb and Rayleigh waves with the highest frequencies. The positioning of a levitated object can be accurate by means of time-controlled electrical excitation. A detailed description can be found in [192] of an interdigital transducer for Rayleigh wave excitation and Lamb waves. The propagation of these surface acoustic waves generates a retrograde elliptic motion of surface particles (see [191], [192]). By contacting a slider onto the substrate surface, it is pulled by the surface

particles through friction force in the opposite direction of the wave propagation. Kurosawa et al [192] have proposed an X-Y linear motor that operates at 10MHz in two dimensions and uses a $LiNbO_3$ wafer of three inches in diameter. Kurosawa et al [193]-[185] have demonstrated the operation of an HF band (3-30MHz) ultrasonic motor at 20MHz, which was made possible by operating the Rayleigh wave; a type of surface acoustic wave was applied to the linear ultrasonic motors. Takahashi et al [196]-[197] have experimentally investigated the operation conditions and basic performance of linear ultrasonic motors under high-frequency operation. The most significant result of this research was the discovery of the high output force density of the friction drive. The output force density is $50N/mm^2$. However, the actual output force was 1 mN because the tested slider was one steel ball. The maximum speed and maximum acceleration were 0.8m/s and $900m/s^2$. Kurosawa and Ueha [198] and Kuribayashi and Ueha [199] have succeeded in the circulation of the power flow in a vibration system of a travelling wave type linear motor having two longitudinal vibrators and a flexural vibrating bar for a wave guider using an electric circuit.

In this appendix, the simple-support-structure disc-type stator (see Figure A.1) with three non-equal-triangular (120°-90°-150°) [17] fixed points at the near edge (the lateral effect of 120°-90°-150° has been discussed at Chapter 2) is to be studied for axial vibration levitation motion. An axial vibration levitation motion can be applied to linear, surfing and shaft types of bearingless ultrasonic motor. As shown in Figure A.2 [177], when a movable object is put on the stator subject to a travelling wave (see Figure A.3), the ultrasonic radiation between them can induce a levitation motion between the two. The travelling wave for levitation motion is obtained in a circular plate using a combination of several standing waves. These standing waves correspond to a degenerate

vibration due to asymmetrical boundary reflection. Figure A.4 shows the displacement flow vector of the stator under 75kHz excitation from finite element analysis. As shown in Figure A.4, due to the circular symmetry being disturbed, a degenerate mode is split into several vibration modes.

Here, the appendix is to acquire the axial vibration characteristics of the stator by experimental measurement, and then explore the effect of 120°-90°-150° [17] boundary configuration on the axial vibration characteristics, the detail about the lateral effect (radial and tangential) of 120°-90°-150° [17] has been discussed at Chapter 2. It is noted that the levitation phenomena are caused from acoustic or ultrasonic radiation by driving the stator at acoustic or ultrasonic frequency range but the levitated objects are not fixed. In this research, we focus on the axial vibration characteristics of the stator, so no levitated object has been used. But it can be attempted by one finger touching. The axial vibration displacement and velocity patterns are acquired using the laser heterodyne technique. The sensitivity is also obtained from the measured data. Finally, we state whether it is possible to produce a levitation motion on the stator.

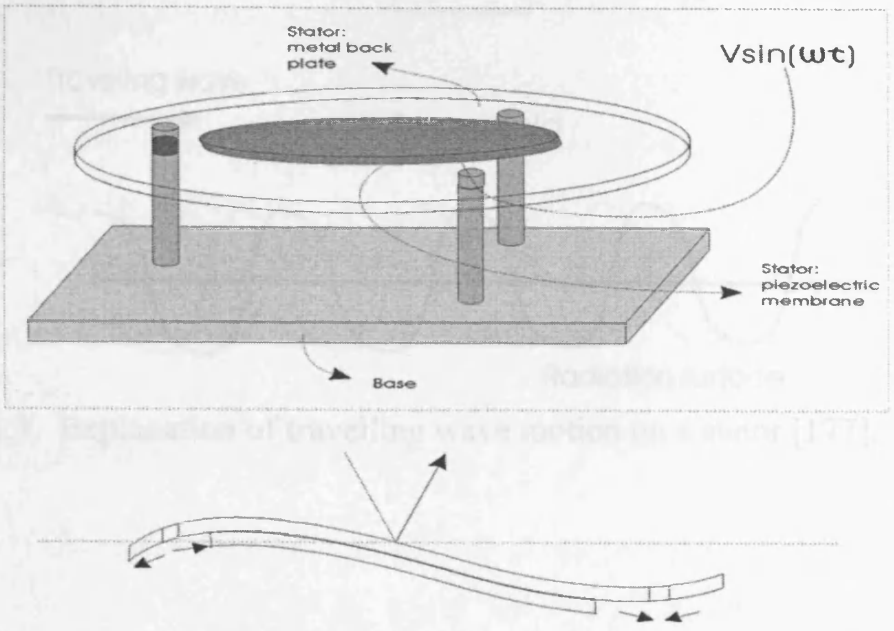


Figure A.1. Configuration of the stator.

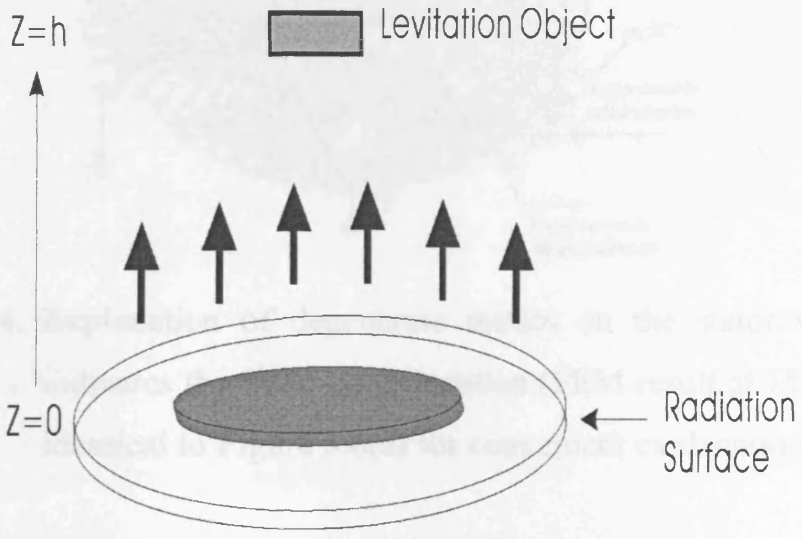


Figure A.2. Schematic diagram of ultrasonic levitation [177].

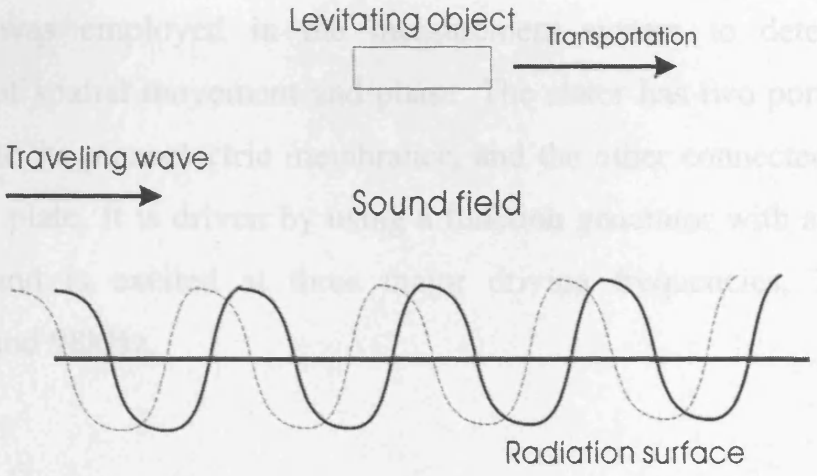


Figure A.3. Explanation of travelling wave motion on a stator [177].

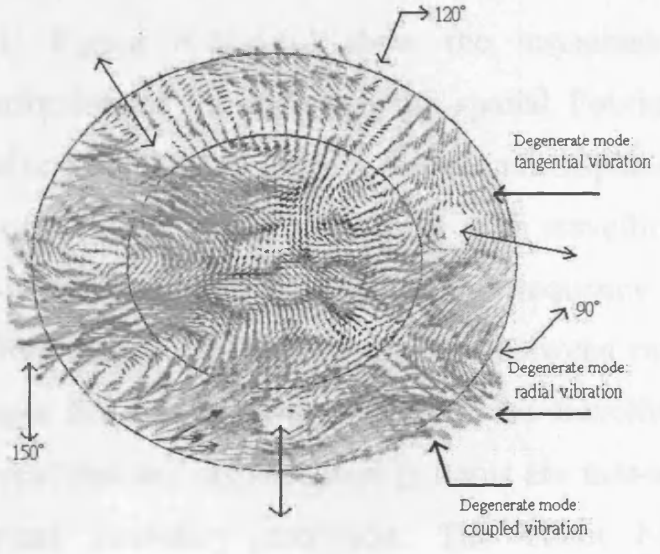


Figure A.4. Explanation of degenerate modes on the stator where ↔ indicates the fixed-point location (FEM result at 75kHz, it is identical to Figure 3.6(a) for convenient explanation).

## A.2 Axial Vibration Characteristics

The laser vibrometer was used to explore the surface vibration characteristics of the stator, as shown in Figure 2.12. The heterodyne

technique was employed in the measurement system to detect the variations of spatial movement and phase. The stator has two ports: one connected to its piezoelectric membrance, and the other connected to its metal back plate. It is driven by using a function generator with a signal amplifier and is excited at three major driving frequencies, 75kHz, 83.81kHz and 98kHz.

### A.2.1 Axial Displacement Pattern

The vibration displacement of the stator surface is induced by flexural vibration caused from shear force and bending interaction between the piezoelectric membrane and the metal back plate, as shown in Figure A.1. Figure A.5(a)-(c) show the instantaneous vibration amplitude distribution of the stator in the spatial Fourier spectrum at 75kHz, 83.81kHz and 98kHz. These z-directional displacement patterns are the result of standing waves combining with travelling waves. The travelling wave is obtained from the driving frequency. The standing waves result from the circumferential distance between two fixed points being the integer time of the wavelength of the travelling wave. The results also reveal that the displacement patterns are non-uniform due to the asymmetrical boundary condition. The effect becomes more significant with the increase in driving frequency. The instant maximal vibration amplitudes of 75kHz, 83.81kHz and 98kHz are 500nm, 400nm and 80nm, respectively. All of the input voltages are 20V.

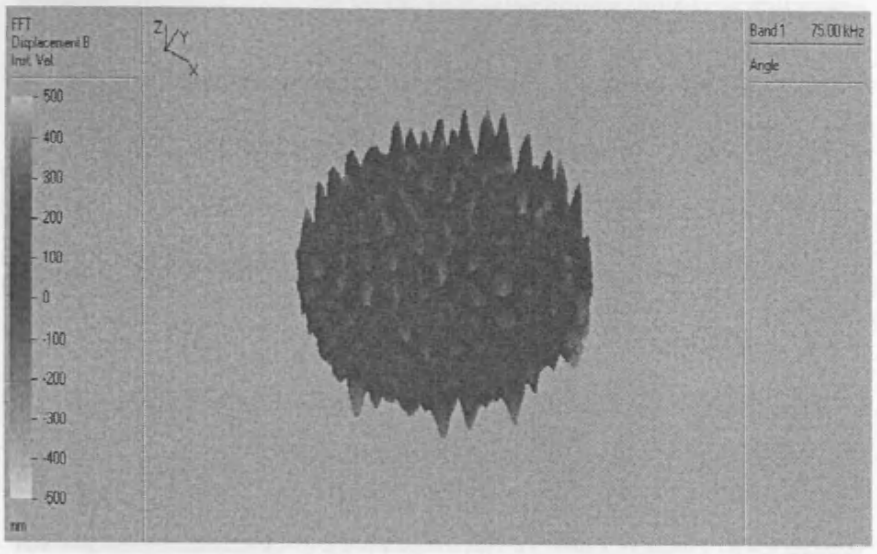
FFT
Displacement B
Inst. Val.
500
400
300
200
100
0
-100
-200
-300
-400
-500
nm
Z
Y
X
Band 1
75.00 kHz
Angle

(a)

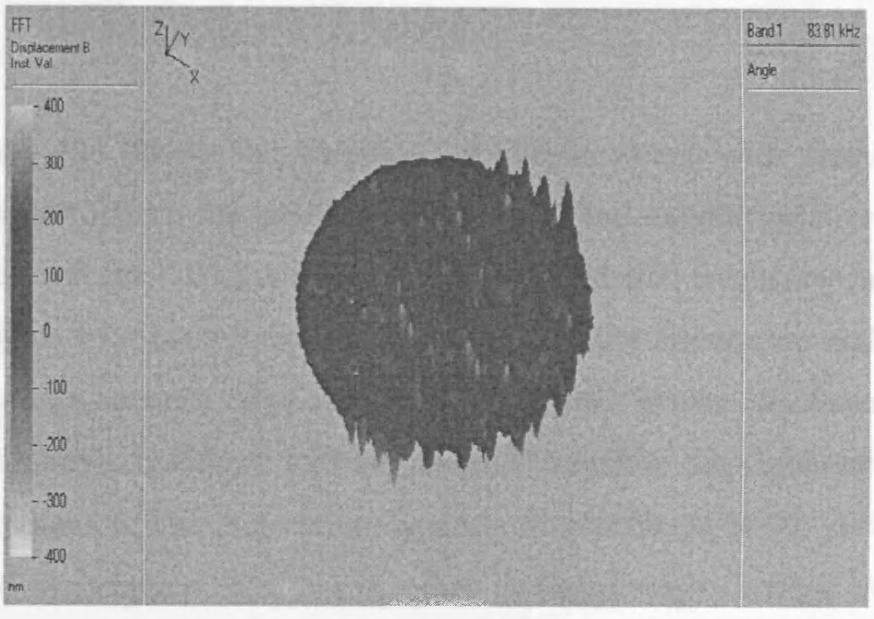
FFT
Displacement B
Inst. Val.
400
300
200
100
0
-100
-200
-300
-400
nm
Z
Y
X
Band 1
83.81 kHz
Angle

(b)

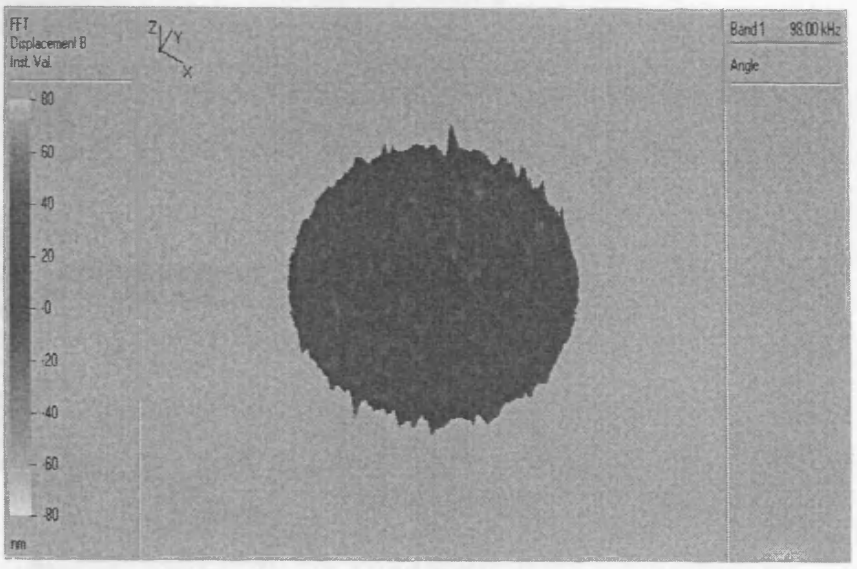


(c)

Figure A.5. Vibration amplitude distribution of the stator for (a) 75kHz, (b) 83.81kHz and (c) 98kHz.

Figure A.6 shows the variation of displacement with frequency increase (z dir.) from the analysis (Chapter 3) and experimental results, the applied voltage (10V) is fixed for all of the desired frequency ranges, and the place of measurement is located around the circumferential (90° included angle section) edge fro getting maximal instant displacement. The result shows that there will be maximal dynamic displacement near driving frequency. The z direction dynamic displacement of 90° included angle section is larger than that of other included angle sections due to traveling waves generated from the input signal being partly reflected and mixed near the stator edge.

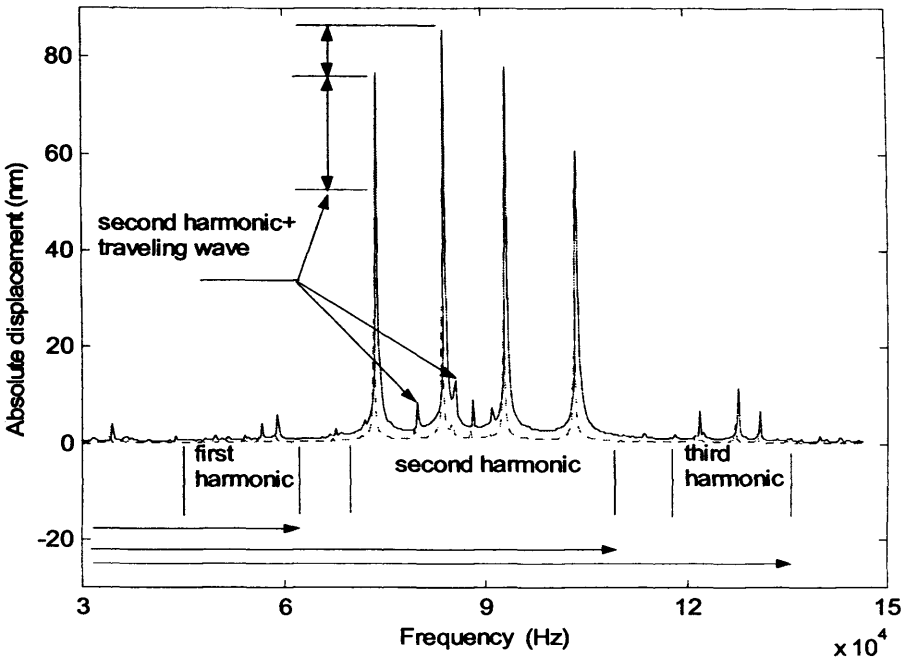


Figure A.6. The variation of displacement with frequency increase (z dir.) (—, experiment; ---, analysis, it is identical to Figure 3.2 for convenient explanation).

## A.2.2 Axial Vibration Velocity

The z-direction and intensity of the particle speed at the maximum instantaneous amplitude of each point of the surface is shown in Figure A.6(a)-(c) for 75kHz, 83.81kHz and 98kHz. These velocity patterns also tend towards non-uniformity. The velocity variations of 83.81kHz and 98kHz are small due to attenuation with the increase of driving frequency. The results also reveal that the vibration velocity has radial and tangential velocity components because the trajectory of the velocity at each point of the surface is not circular. From Figure A.6(b), 83.81kHz, the Bragg scattering effect seems to have occurred due to a tendency of random velocity distribution. The instant maximum velocities of 75kHz, 83.81kHz and 98kHz are 250mm/s, 140mm/s and 50mm/s, respectively.

Furthermore, Figure A.7(a)-(c) show the variations of vibration velocity at 75kHz, 83.81kHz and 98kHz along three different circumferential curves (120°-90°-150°). They have different tendencies due to asymmetrical boundary conditions. The results also reveal that the vibration velocities for the three included angle sections always oscillate rapidly and forcefully at the three driving frequencies. This matches the displacement vector flow of Figure A.4, which is caused by the vibration mode being degenerated and coupled. The direction and intensity of the particle speed on the stator surface are key factors for levitating capability.

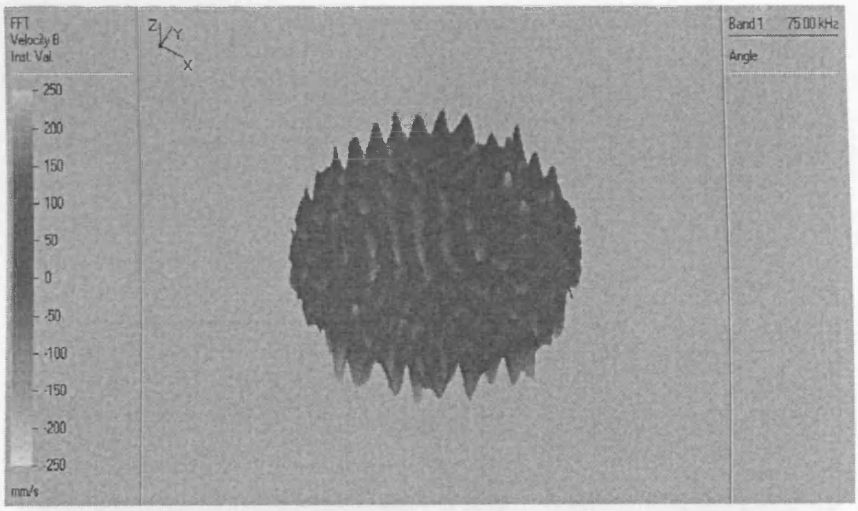


(a)

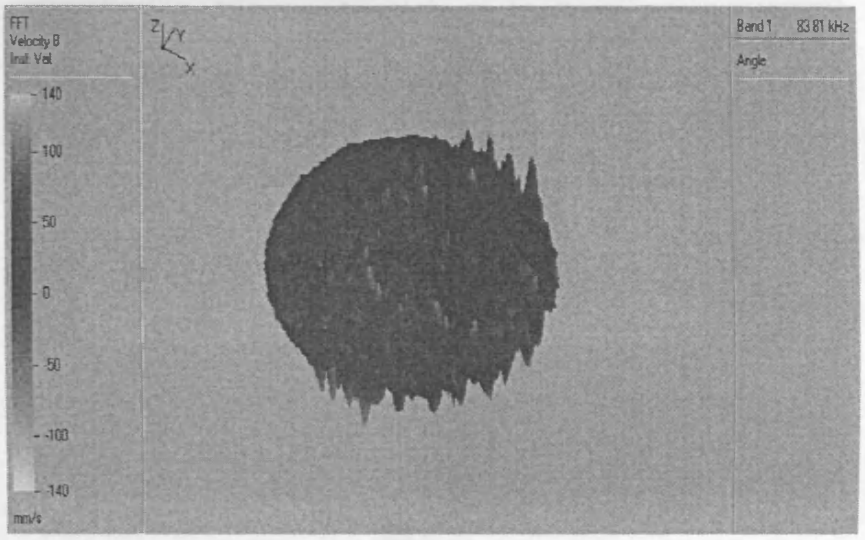


(b)

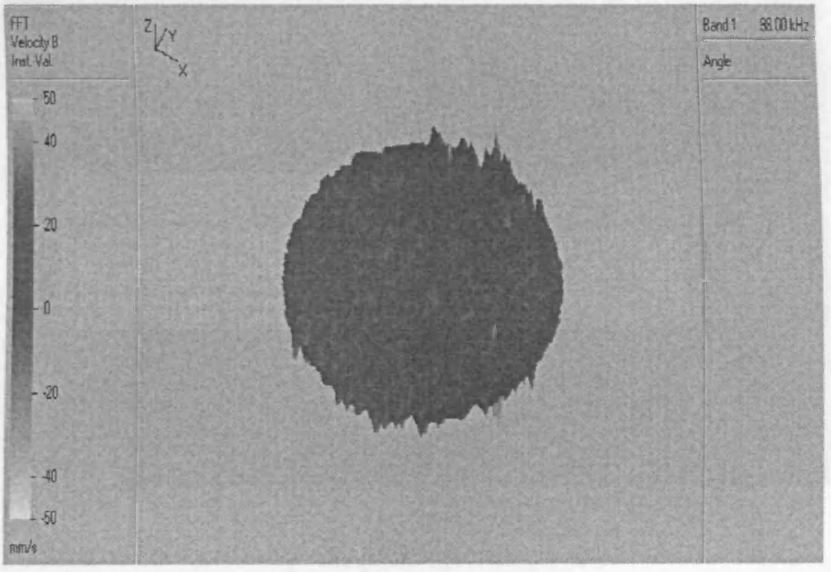


(c)

Figure A.7. Vibration velocity distribution of the stator for (a) 75kHz, (b) 83.81kHz and (c) 98kHz.

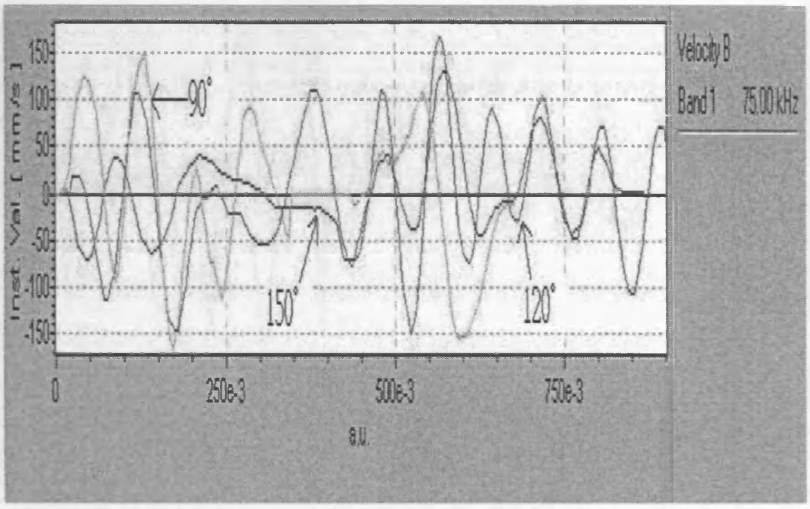
Velocity B
Band 1 75.00 kHz
Inst. Val. [ mm/s ]
150
100
50
0
-50
-100
-150
90°
150°
120°
0
250e-3
500e-3
750e-3
a.u.

(a)

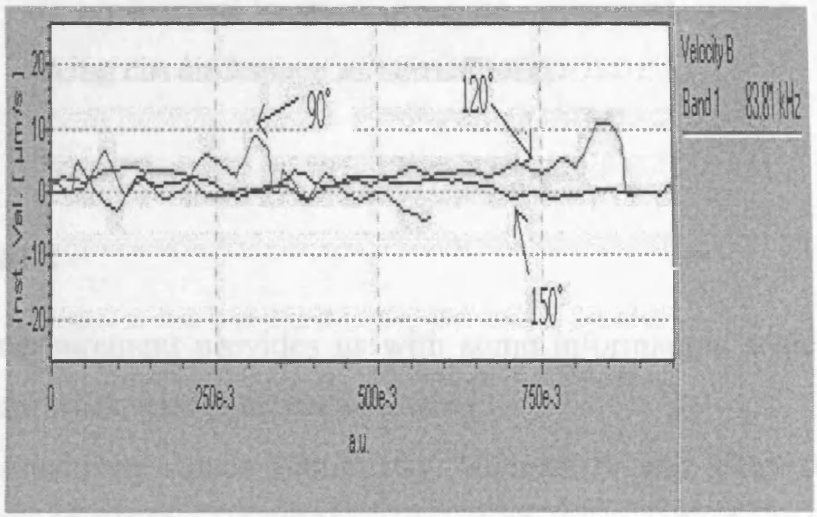
Velocity B
Band 1 83.81 kHz
Inst. Val. [ µm/s ]
20
10
0
-10
-20
90°
120°
150°
0
250e-3
500e-3
750e-3
a.u.

(b)

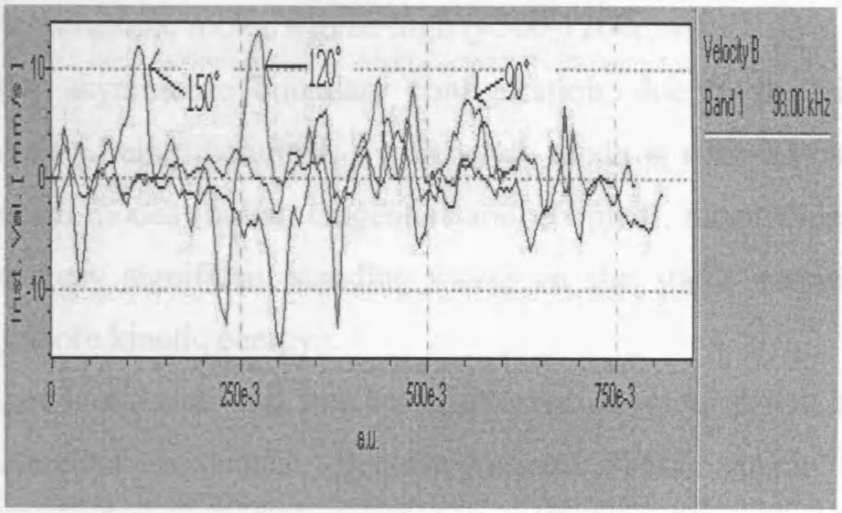


(c)

Figure A.8. Variation of the vibration velocity at (a) 75kHz, (b) 83.81kHz and (c) 98kHz corresponding to three different circumferential locations(here a.u., a=around, u=unit, means taking circumference as normal unit).

## A.3 Remark

The measurement provides us with some information, which may help in future work, including the following:

(a) The sensitivity values 500nm/10V, 400nm/10V and 80nm/10V for 75kHz, 83.81kHz and 98kHz, respectively, are useful for analysing the transfer function of the stator.

(b) The vibration information reveals that the stator seems to be ill-suited for application on the linear and surfing types of bearingless ultrasonic motor due to the axial vibration patterns are non-uniform.

(c) The axial vibration velocity is high for a single particle speed. Thus, if the contact between the stator and rotor occurs on one point of the stator surface, that is a shaft-driving type, the revolution speed

of the ultrasonic motor will be high (≈500-1200rpm).

(d) In the asymmetric boundary configuration, due to the circular symmetry being disturbed, a degenerate mode is split into several vibration modes (radial, tangential and coupled), meanwhile there exist many significant standing waves on the stator surface that carry more kinetic energy.

(e) A same stator but with free boundary configuration, it will have a fundamental resonance frequency(about 7kHz) much below ultrasonic frequency, however, by a specific boundary constraint on the stator surface, the resonance frequency will be switched to much high ultrasonic frequency. It means that the asymmetric boundary configuration will affect its resonance frequency.

(f) Due to its higher mechanical resonance frequencies, the stator surface will have higher acoustic radiation although it is non-uniform.

# Appendix B Principle of Piezoelectric Material Properties

## B.1 Piezoelectric Effect

Piezoelectric materials possess the ability of producing mechanical work when they are electrically excited or generating energy if they are mechanically stressed. Elements such as tourmaline and quartz are inherently piezoelectric. Other ceramic elements that are not naturally piezoelectric, such as barium titanate, can be transformed to quasi-piezoelectric by poling. An ultrasonic actuator utilizes this unique property of piezoelectric materials and converts the ultrasonic mechanical energy to the mechanical thrust motion by a friction force.

J. Curie and P. Curie discovered the piezoelectric effect in 1880. There are certain types of crystals, when subjected to tensile or compressive force (or stresses) results in the crystal. Conversely, if the crystal is being polarized by an electric field, strains along with resulting stresses are created. Together, these two effects are known as the piezoelectric effect. In crystals which show piezoelectric properties, mechanical quantities, such as stress ($T$) or strain ($S$), and electrical quantities such as electric field ($E$), electric displacement (flux density) or polarization ($P$), are interrelated. This phenomenon is called electromechanical coupling.

### B.1.1 Longitudinal and Transverse Effects

Longitudinal and transverse effects in the piezoelectric phenomena

are particularly important. In the longitudinal effect, deformations take parallel to the electric axis as shown in Figure B.1(a). Figure B.1(b) illustrates the transverse effect deformations occurring at right angles to the electric axis. In practice, these two types of effect take place at the same time.

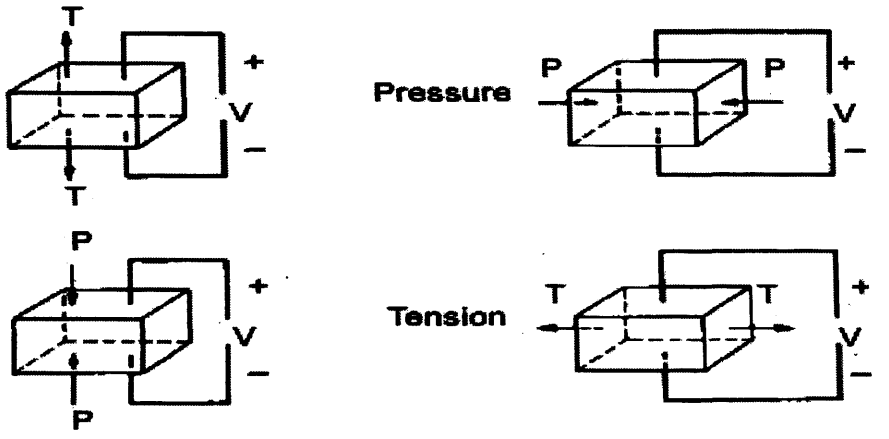


Figure B.1. The piezoelectric effect: (a) Longitudinal; (b) Transverse [3].

## B.1.2 Piezoelectricity

When a crystal is placed in an electric field, two types of strain can be observed, one is proportional to the field strength and the other is proportional to the square of the field strength. Strictly speaking, the former represents the piezoelectric effect while the latter is sometimes distinguished as the electrostrictive phenomenon. Practical piezoelectric ceramics have a complex multi-domain structure under the microscope and exhibit quite complex behavior. Figure B.2 is a plot of strain in the

direction of the applied electric field (longitudinal effect) for a PLZT materials (the material main composites are (Pb, La)(Zr, Ti)$O_3$ [3]. This property is referred as hysteresis as the material state is determined by its previous history, $S$ is the strain and $E_c$ is the coercive electric field.

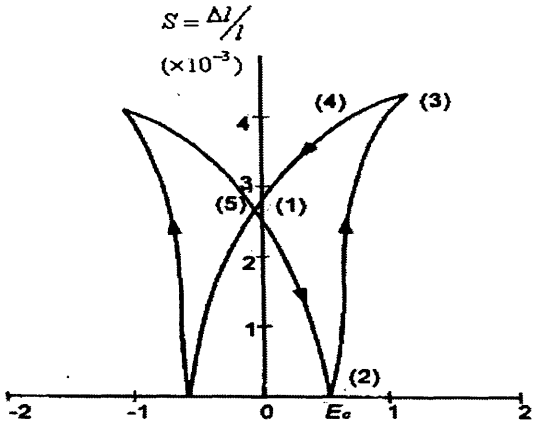


Figure B.2. The dielectric strain characteristics for a PLZT piezoelectric ceramic [3].

## B.1.2 Terminology

*Polarization* ($P$): Related to the electric displacement (electric flux density) $D$ through the linear expression

$$D_i = P_i + \varepsilon_0 E_i, \qquad \text{(B.1)}$$

Where the subscript $i$ represents any of the three coordinates $x$, $y$, and $z$, $\varepsilon_0$ is the permittivity of free space, equal to $8.854 \times 10^{-12}$ F/m and $E_i$ is electric field.

*Permittivity* ($\varepsilon$): Defined as the incremental change in the electric

displacement per unit electric field when the magnitude of the measuring is very small compared with the coercive electric field denoted by $E_c$ in Figure B.2.

*Remanent polarization*: The value of the polarization that remains after an applied electric field is removed.

*Poling and switching*: Poling is process by which a D.C. electric field exceeding the coercive field is applied to a specimen of multi-domain ceramic to produce a net remanent polarization. To understand this process in more detail, let us examine a few grains of crystal as shown in Figure B.3. The crystal has been initially polarized in the negative direction and each domain is polarized in the downward direction. If an electric field in the positive direction is gradually applied, the block will contract initially since the field opposes the polarized direction. As strength of the electric field increases, some of the poles in the grains will begin to reverse their direction. At strength of the electric field increases, some of the poles in the grains will begin to reverse their direction. At a certain voltage, the block will no longer be able to contract further. This electric field is known as the coercive field $E_c$ as indicated in Figure B.3(2). If the field continues to increase, the ceramic block will start to expand. When all the poles have been reversed and the block can expand no further, this field is known as the $E_{\max}$ as shown in Figure B.3(3). If the electric field is reduced, the strain will keep decreasing until the electric field reaches zero. In the final state, the poles in all grains are reversed from the initial state and now the block has been polarized in the positive direction.

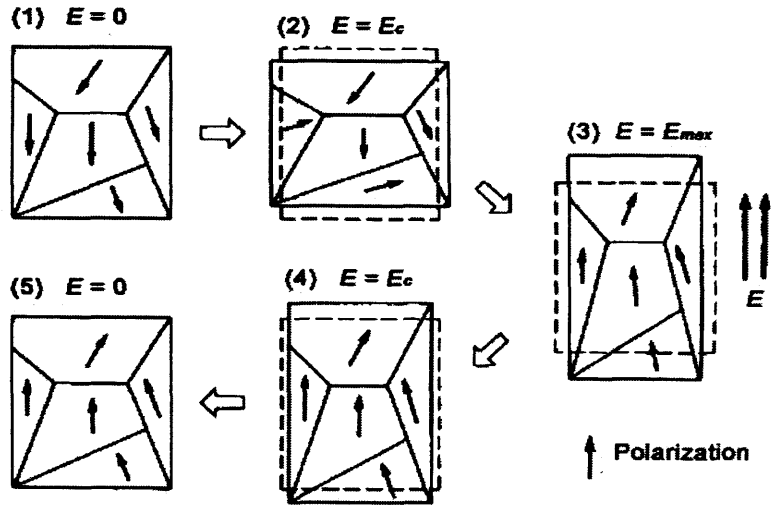


Figure B.3. Diagrammatic representation of strain induced by pole reversals in ceramic materials [3].

## B.2 Parameters of Piezoelectric Effect

### B.2.1 Piezoelectric Strain Constant

Strain and applied voltage are proportional in a polarized crystal. Ignoring hysteresis effect, their relationship can expressed as

For positive polarized state

$$\frac{\Delta l}{l} = dE . \tag{B.2}$$

For negative polarized state

$$\frac{\Delta l}{l} = -dE . \tag{B.3}$$

The proportionality constant $d$ is known as the piezoelectric strain constant.

## B.2.2 Poisson Ratio

Piezoelectric strain are generally small. Strain constant ($d$) ranges typically from $10^{-10}$ to $10^{-12}$ m/V. Taking $d$=$10^{-9}$ for example, a voltage of 10,000V applied on a ceramic specimen 1cm thick creates a mere elongation of 0.1 $\mu$m. Poisson's ration is a parameter which indicates relative deformations in the longitudinal and transverse direction. Specifically, it is the ration of transverse elongation to longitudinal contract when a pressure is applied to a solid at a constant voltage.

$$\nu^E = \frac{S_{31}}{S_{33}}. \tag{B.4}$$

The superscript denotes a non-varying parameter during state changes, $\nu^E$ is Poisson's ration when the applied voltage is kept constant. Subscripts indicate axis directions for cause and effect. The numbers 1, 2, and 3 correspond to axes $x$, $y$, and $z$ respectively shown in Figure B.4. $S_{33}$ represents a pressure in the $z$ direction creating a strain $\frac{\Delta z}{z_0}$ in the $z$ direction, and $S_{31}$ is the strain in the $x$ direction caused by a pressure in the $z$ direction.

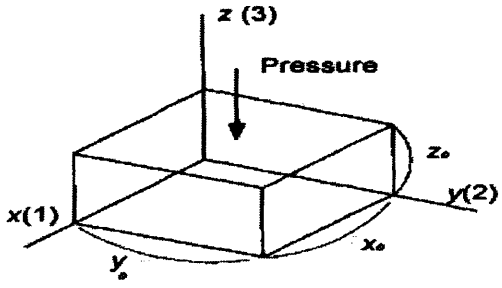


Figure B.4. Coordinate axes and corresponding subscript numbers [3].

## B.2.3 Directionality of Piezoelectric Strain Constant

If deformations are caused by an electric field, Poisson's ration can not be used for determining the relative deformations. In this cause, the piezoelectric strain constant in the $z$ direction is usually represented by $d_{33}$,

$$\frac{\Delta z}{z_0} = d_{33} E_z . \tag{B.5}$$

The elongation in the x direction is given by $d_{31}$.

$$\frac{\Delta x}{x_0} = \frac{\Delta y}{y_0} = d_{31} E_z . \tag{B.6}$$

## B.2.4 Voltage Output Coefficients

The reverse piezoelectric effect is formulated as

$$E_z = -g_{33} T_z = -g_{31} T_{x,y} . \tag{B.7}$$

Where T is stress and $g$ is called the voltage output constant (V/mN) and is related to $d$ constant with the following relationship:

$$g_{33} = d_{33} / \varepsilon_{33}^T , \tag{B.8}$$

$$g_{31} = d_{31} / \varepsilon_{31}^T . \tag{B.9}$$

Where $\varepsilon$ is the permittivity of the ceramics.

## B.2.5 The e-form Piezoelectric Equations

These equations express the characteristics of piezoelectric ceramics

$$\begin{aligned} \Delta D &= eS + \varepsilon \Delta E \\ \Delta T &= cS - e\Delta E \end{aligned}, \qquad \text{(B.10)}$$

Where $\Delta$ represents variation, $D$ is electrical displacement, $S$ is strain, $T$ is stress, $E$ is electrical field, $c$ is Young's Modulus, and $e$ is piezoelectric constant.

## B.2.6 Coupling Coefficients k

Electromechanical coupling describes the conversion of energy from mechanical form to electrical form or vice versa. It is the square root of the ratio between the input and output energy.

## B.2.7 Voltage and Stress Limits

If the applied voltage exceeds a certain level, the voltage-strain relationship will lose its linearity. In general, the limitation on field strength is typically between 500V/mm and 1000V/mm depending on the poling process, the operating temperature and the duration. Shown in Figure B.5 is the stress-strain relation at the positive and negative voltage limits respectively. The parallelograms show the limits for voltage and force. The theoretical maximum output is obtained when the stress or strain follows the parallelogram's perimeter in the plot.

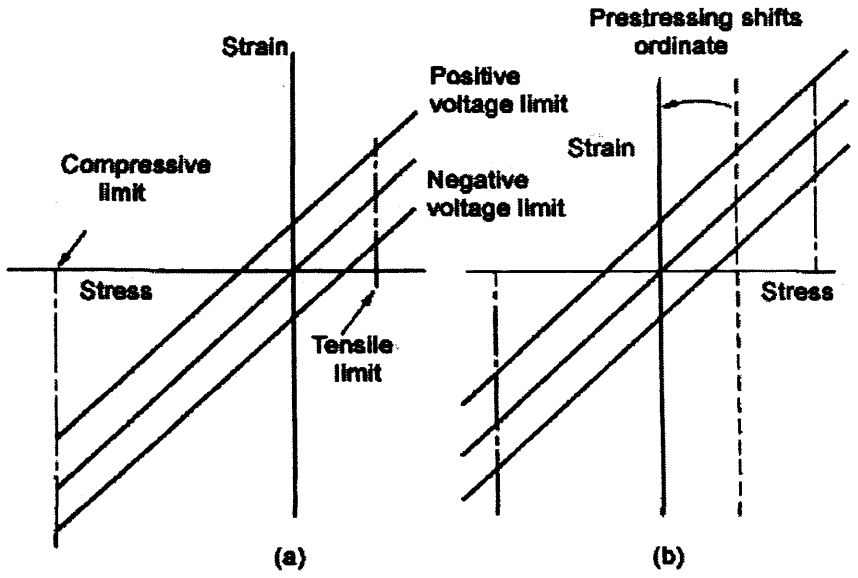


Figure B.5. Piezoelectric stress vs strain characteristics (a) without prestressing (b) stress limit is increased with prestressing [3].